Una nova tècnica de microscòpia de forces atòmiques per a l'estudi de les propietats nanoelèctriques de les cèl·lules

Martí Checa Nualart

Universitat de Barcelona

Facultat de Física

Departament d'Enginyeria Electrònica i Biomèdica

Una nova tècnica de microscòpia de forces atòmiques per a l'estudi de les propietats nanoelèctriques de les cèl·lules.

Programa de Doctorat:

Nanociències

Línia de recerca:

Nanobiotecnologia

Director i tutor de tesi:

Dr. Gabriel Gomila Lluch

UNIVERSITAT DE BARCELONA

Autor:

Martí Checa Nualart

“El fútbol es así”

“Yes... pasa que...”

Statement of Originality

The author of this thesis, Martí Checa Nualart, claims it to be considered original and that it complies with the ethical codes and good practices without containing plagiarism. Stating that he is aware that it will be subjected to a procedure to check its originality.

Then, I declare the following elements of this thesis to be considered a contribution to knowledge:

- **Checa, M.**, Millan-Solsona, R. & Gomila, G. Frequency-dependent force between ac-voltage-biased plates in electrolyte solutions. *Phys. Rev. E* **100**, 022604 (2019).

- **Checa, M.**, Millan-Solsona, R. & Gomila, G. Mapping the Dielectric Constant of a Single Bacterial Cell at the Nanoscale with Scanning Dielectric Force Volume Microscopy. *Nanoscale* **11**, 20809-20819, (2019).

- **Checa, M.**, Millan-Solsona, R. & Gomila, G. Modeling Electrostatic Force Microscopy in electrolyte solutions. *In preparation.*

- Millan-Solsona, R., **Checa, M.**, & Gomila, G. Dielectric properties of sub-nanometer ultrathin molecular layers at the metal/electrolyte interface by electrochemical force microscopy. *In preparation.*

- Kyndiah, A., Leonardi, F., Di Muzio, M., **Checa, M.**, Millan-Solsona, R. Mas-Torrent, M., & Gomila, G. Nanoscale electrical characterization of Electrolyte Gate Organic Field-Effect Transistor. *In preparation.*

- **Checa, M.**, Glinkowska, A., Millan-Solsona, R. & Gomila, G. Electrosttic force microscopy of HeLa cells in lquid enviroment. *In preparation.*

Signed:

Table of contents

Structure of the thesis

This work of thesis is organized into 8 different chapters:

- **Chapter 1:** introduces the nanoscale electrical properties of cells and their relevance in the different fields of science in order to establish a framework for the objectives of the project.
- **Chapter 2:** introduces the Scanning Probe Microscopy techniques, with a special interest in its electrical modes. It mainly focuses the interest on Electrostatic Force Microscopy as it is the technique used during the project.

Motivation and objectives of the thesis: Once the introductory chapters have established a framework for the realization of the thesis, its motivation, and its main goals are exposed.

- **Chapter 3:** covers the theoretical modeling of electrostatic force measurements in electrolyte solutions for 1D geometry.
- **Chapter 4:** extends the theoretical modeling of electrostatic force measurements in electrolyte solutions to 3D realistic geometries, and their implications regarding EFM in liquid media are discussed.
- **Chapter 5:** presents and validates a new SPM technique called *Scanning Dielectric Force Volume Microscopy (SDFVM)* designed specially to deal with topographically complex and heterogeneous samples like cells.
- **Chapter 6:** exposes the application of SDFVM to obtain the first (to our knowledge) local dielectric constant map of a cell at the sub-cellular level.
- **Chapter 7:** uses the developed technique to obtain EFM images of different interesting systems in nanotechnology, showing the power of method by achieving nice images in a wide range of systems going from small nanowires to big eukaryotic cells.

- **Chapter 8:** presents the steps performed towards implementing SDFVM into liquid environments, and some preliminary results for fixed and living eukaryotic cells in physiological conditions.

Then the conclusions of the project and its future perspectives are exposed. The references can be found at the end of the document.

1. Nanoscale electrical properties of cells

This chapter contains an introduction to the nanoscale electrical properties of cells and their relevance in the different fields of science in order to establish a framework for the realization of the goals of the project.

1.1 Introduction to nanoscale electrical properties of cells

Cells are the morphologic and functional units of every living organism[1]. In fact, cells are the smallest elements that can be considered to be alive, allowing scientists to classify the different living organisms according to the type and number of cells that they have. Mainly they can be separated into two big groups: prokaryotic cells and eukaryotic cells (Figure 1.1).

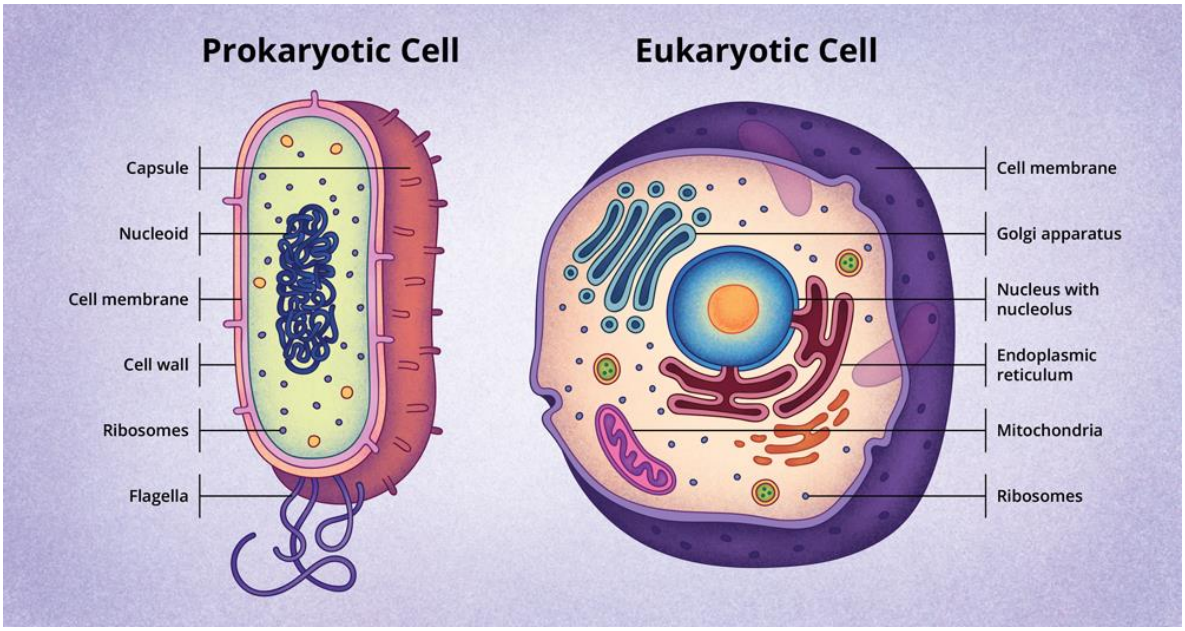

Figure 1.1: Basic scheme of prokaryotic and eukaryotic cells. Image © National Institute of Health.

On the one hand, prokaryotic cells are, in general, smaller and simpler than eukaryotic ones. They contain ribosomes, but they lack organelles or endomembrane systems, like the nucleus. That is why they have their genetic material spread in the cytosol. On the other hand, eukaryotic cells are much more complex, with a lot of internal structure between which the nucleus (containing its genetic information) stands out.

The ability of cells to perceive and respond to different external and internal stimuli, allows them to function and to communicate with the exterior and with other cells of the same organism. Such stimuli can be of many different types: a physical force or pressure, a chemical reaction, an electric current… and can be at many different timescales and length scales, ranging from very quick and small to very long-lasting and big processes.

In this work of thesis, we are interested in studying, which are the electric properties of cells at the sub-cellular level. Among the different properties that one can study from an electrical point of view, mainly two big groups are found, the conducting properties (active) and the capacitive properties (passive). Namely the ability of cells and cell components to conduct electricity and the ability of cells and cell components to polarize or accumulate charges under the application of an externally applied field.

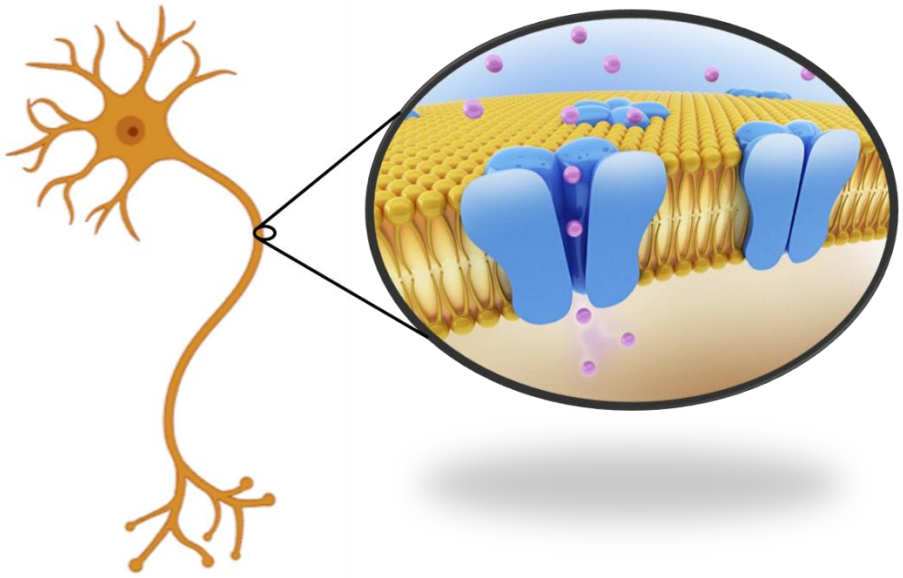

Figure 1.2: Sketch of the ionic channel proteins present in the cell membrane of a neuron.

Cell components (especially the cell membrane) can change their conductance and capacitance depending on different stimuli present. The cell membrane is a lipidic bilayer that delimits all the cells. In brief, it is structured by two sheets of phospholipids, glycolipids, and proteins that maintain the equilibrium between the interior and exterior of the cell. It regulates the entrance of substances to the cell. Not only substances but also the membrane is used to separate the charge between the intracellular and extracellular compartments. Stuck in the membrane, there are several proteins and other biomolecules with diverse structural and biological functionalities. Ionic channels and ionic pumps are part of those families of proteins[2]. They can change their physical structure allowing the flow of ions through them and so changing the conductance of the membrane (Figure 1.2). Thus, when the ion channels are closed, the membrane acts as an insulator able to achieve a charge separation by maintaining a different ionic concentration between the intracellular and extracellular compartments. However, when ionic channels open, the cell membrane is not an insulator anymore and behaves like a conductor allowing the flow of current through it. Accordingly, the electrophysiological signals will depend strongly on the conductive and insulator behavior of its molecular sub-components. An example of it is the length and time constants of a neuron (used to quantify the distance that an electric potential will extend upon a point stimulus), which will specifically depend on its membrane capacitance.

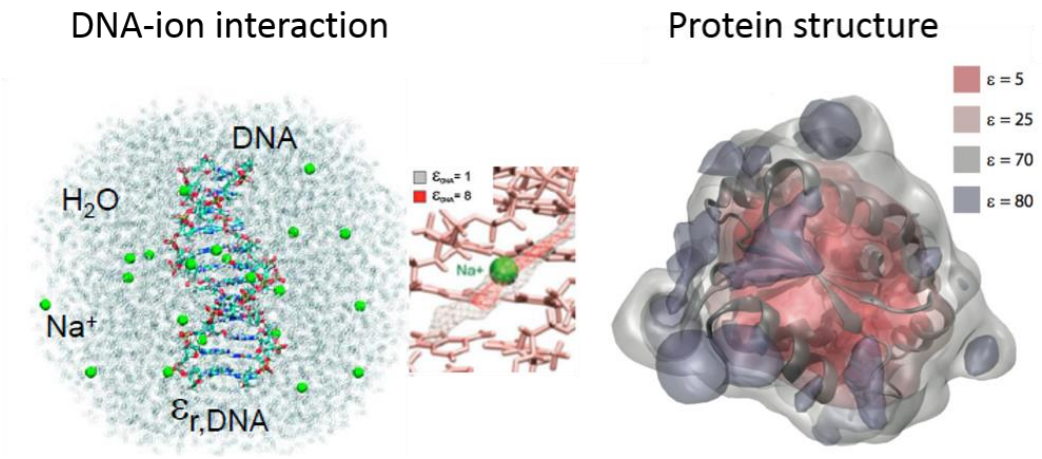

Figure 1.3: Examples of biochemical processes where the dielectric constant of its components can be relevant for its outcome. Images extracted from[3,4].

On the other hand, several physicochemical and biological phenomena occurring inside the cell (see Figure 1.3) are also ruled by electrostatic forces (protein-protein interaction, protein structure, protein folding, DNA-ion interaction, etc.). This fact gives an important relevance to how the charges and dipoles present in the biomolecules individually and collectively behave under the application of electric fields and chemical forces. Thus, the surface charge or the dielectric constant of such biological structures will be a key factor in how they interact.

1.2 Cell Electrophysiology

Electrophysiology is the field of science that studies the electrical activity of cells and biological tissues. It includes measurements of current and voltage at a different time and length scales, from full organ activity to single-molecule recordings. Excitable cells contain ion channels that under voltage or chemical modifications change their probability of opening abruptly, inducing, in turn, an abrupt change in membrane conductance and, consequently, on transmembrane ionic current. Electrical recordings on single cells offer, then, crucial information to understand the physiology of cells and constitute the basis for understanding more complex multicellular systems such as nerves or full organs (although the relationship between single-cell recordings and organ activity is highly nontrivial). Electrophysiology advances can contribute to a better diagnostic in medical electrical techniques, such as electrocardiography, electroencephalography, or electromyography.

Most of our current understanding of the electrical activity of single excitable cells, and their main components (e.g., ionic channels) is based on whole-cell intracellular recordings[5,6], single/few ion channel recordings[7] or whole-cell extracellular recordings[8] (Figure 1.4). The first two are techniques that use sharp or patch microelectrode pipettes that can be inserted into the cell body or sealed to its membrane to record whole-cell activity or (in advanced systems) even single or few ion channel activities. The third technique uses a free-standing micromanipulated pipette with a microelectrode (like the ones used for whole-cell

intracellular recordings) or arrays of integrated electrodes or transistors to record the extracellular electric potential surrounding the cell created by the cell activity.

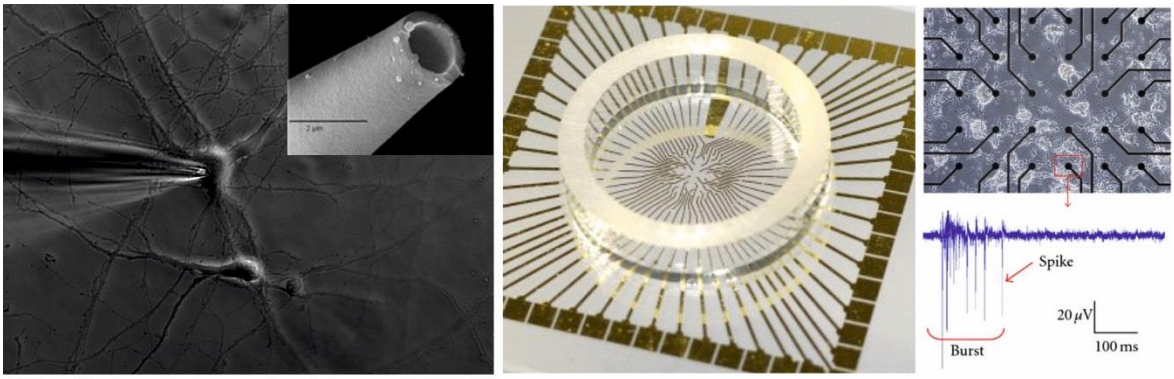

Figure 1.4: Left: Attachment of a patch electrode to a single cell body. Inset: SEM image of the tip of the micropipette. Middle: Integrated microelectrode array device used for extracellular recordings. Right: integrated microelectrode arrays for extracellular recordings and an example of the type of signals recorded. Images obtained from the webpage of New Biotechnology Ltd and from[9].

Other electrophysiological experimental techniques include optical measurements such as the so-called calcium imaging[10], which take advantage of the calcium indicators: fluorescent dyes that, when binding to a Ca^{2+} ion, can change their fluorescence emission.

The main limitations of such techniques refer mainly to the long-time stability of the measurements, the small size dimensions of some cell parts (like dendrites or axons that can be smaller than the pipette or electrode itself), the damage to the cells under study, or in the case of the extracellular recording, the poor electrical coupling with the specimen. Some alternatives to microelectrode or optical techniques based on using nanowire-based systems for the recording or modifications of the Scanning Ion Conductance Microscopy (SCIM, which explained in more detail later) have been able to overcome some of the drawbacks mentioned above of microelectrode technology[11].

1.3 Cell dielectric properties

In addition to the conduction properties of cells and cell membranes probed by electrophysiological techniques, the dielectric properties of cells are also of great interest[12]. One of the most important properties of insulator materials is its dielectric constant or

relative permittivity (ε_r). Under the application of an external electric field, the permanent or induced dipoles present on a material, reorient (see Figure 1.5), and so they generate an additional electric field in the material (called polarization) that screens the external one. How much such dipoles react to the application of an external electric field or how strong that additional electric field generated by the dipoles is, it is reflected in the dielectric constant value of the material. The dielectric constant in linear systems is defined as:

$$\vec{D}=\varepsilon_0\varepsilon_r\vec{E}=\varepsilon_0\vec{E}+\vec{P} \qquad \text{(eq.1.1)}$$

where $\vec{D}$ is the electric displacement field, $\vec{E}$ the electric field, $\vec{P}$ the polarization vector and ε_0 the vacuum permittivity.

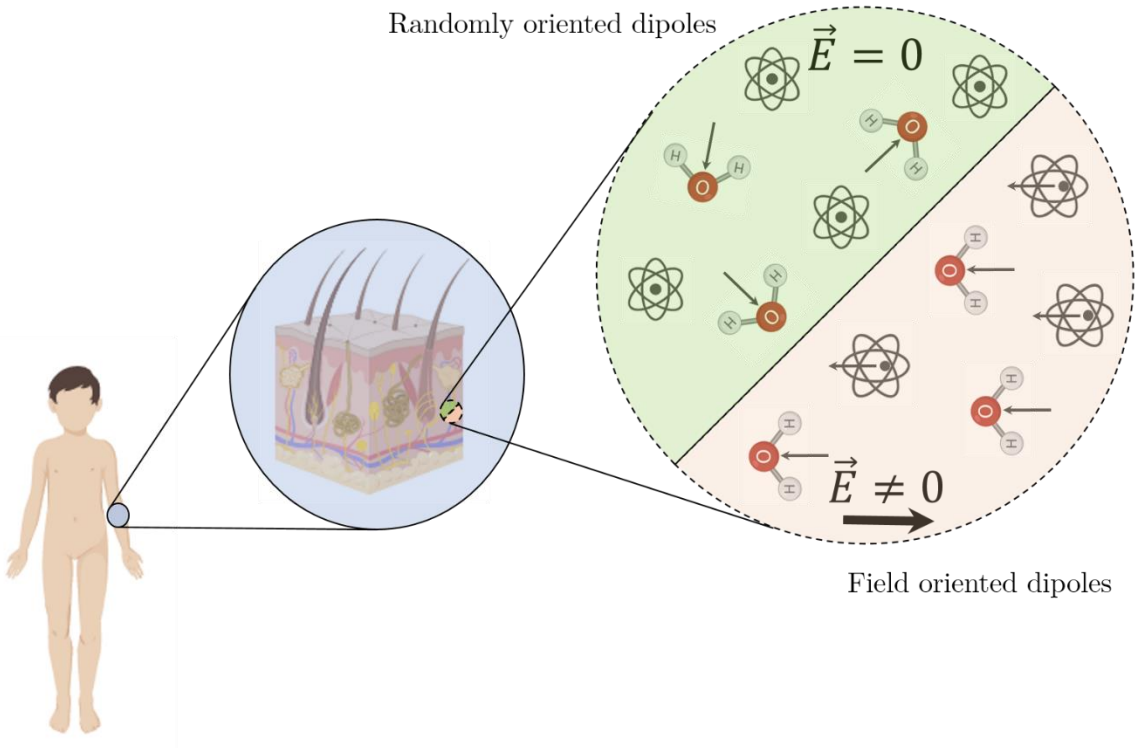

Figure 1.5: Schematic representation showing that even if relative permittivity is a bulk property, its physical nature comes from the behavior of its microscopic components.

The relative permittivity of a material is a frequency-dependent magnitude showing that the different types of dipoles that form the material have different relaxation times. Therefore, we can distinguish between the electronic polarization in the PHz range (when dipole is formed by the electron cloud of the atom that is displaced from its nucleus), the ionic

polarization in the THz range (when the dipoles are formed from oppositely charged ions in the material structure), the orientation polarization in the GHz range (where the dipole that reorients is the whole molecule, like in the case of water for instance) and the interface polarization in the kHz range (where mobile charges at the interface of different materials, form different space charges, being the Electric Double Layer a good example of it).

The frequency dependence of the relative permittivity is often represented in the literature as a complex number ($\varepsilon_r \rightarrow \widehat{\varepsilon_r}(\omega)$) the modulus of which has to do with its strength, and the phase of which has to do with the phase difference between the externally applied field and the polarization field, usually related to the losses in the material.

Many different types of experimental techniques are available for the characterization of dielectric materials in its bulk macroscale form[13]. Examples include the measurements of reflecting radiation[14], its electromagnetic resonating modes[15], or its impedance[16]. In Figure 1.6, there is an example of a table of bulk relative permittivity values at MHz frequency for different common materials. Regarding the nomenclature, the low frequency values of the relative permittivity are referred to as dielectric constant.

Material	**Dielectric constant, ε_r**
Acetone	20.9
Air	1
Benzene	2.3
Clay (dry)	2-6
Clay (wet)	15-40
Ethanol	22.4
Ice	3.4
Mica	6.4
Paper	3
Quartz	4.5
Sand (dry)	3-6
Sand (wet)	10-30
Teflon	2.1
Water	80

Figure 1.6: Table of bulk dielectric constant values of common materials at the MHz range, values are extracted from[17].

Since the relative permittivity is one of the main actors governing the electrostatic interaction, its relevance in the dielectric behavior of matter is very high in many different fields of science, such as material science, physics, chemistry or biology. Examples where the relative permittivity plays a key role, are extensive, from radars in geology to the performance of optoelectronic devices, the efficiency of solar cells, or the transmission speed of an action potential in a neuronal cell. All those phenomena have in common that an electric field is present and that the material polarizes in response to it, screening it on different degrees.

Also, studies on the frequency dependence of the relative permittivity (related to the different components of the total polarization), and on temperature, are found in the literature[18].

How do the electric fields affect the polarization in the different structures of a living organism? This is a non-trivial question, that nowadays turns even more important to answer, as electric fields of any kind increasingly surround us. Its relevance comes not only from the possibility to unravel possible damages that such fields can induce to biological structures but as well as a possible tool for medical diagnosis[19] or treatment of pathologies.

Bulk measurements of the dielectric behavior of biological tissues have been performed since a long time ago, and tables with the corresponding values of each different biological structure present in our body are available[20]. An example of the relative permittivity measurements and its frequency dependence for some relevant biological tissues is found in Figure 1.7.

Even if the relative permittivity is defined usually as a bulk property, it has a lot of sense to study it at the nanoscale level. First, because even if it is defined as a macroscopic property, its physical nature comes from its microscopic components. Second, because it is quite unknown how the nanometric dimensions of nanomaterials and its higher surface to volume ratios affect the polarization properties of matter. Not only that but also the confinement of a certain material inside a nanometric structure can be extremely relevant

for its polarization like it has been recently shown by L. Fumagalli *et al.*[21] for the case of nano-confined water. And third, because there are materials that are only present in its nanometric form like DNA, for example.

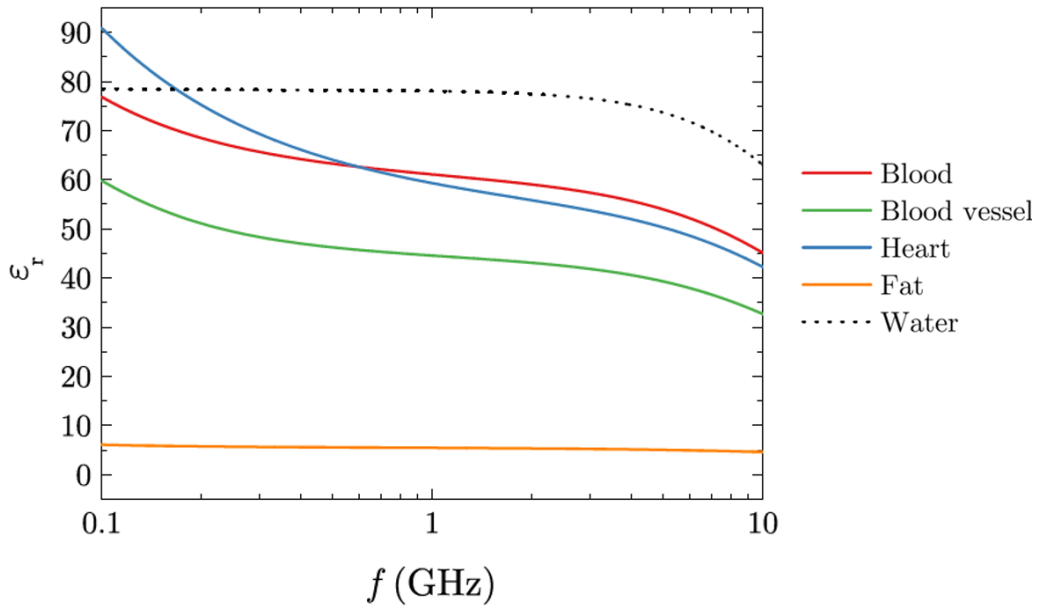

Figure 1.7: Table of frequency dependence of the bulk relative permittivity of some biological tissues of relevance. Figure extracted from[19].

Regarding the physical meaning of defining a macroscopic property (like ε_r) at the nanoscale, we have to say that its meaning is the same as at the macroscale: an effective quantitative value for the electric screening of the polarization field inside the material (as we are never going to study properties at the subatomic level, we do not need the consideration of quantum mechanics).

Theoretical studies where the effective dielectric constant of materials is calculated exist, both from first principles[22] and through molecular dynamics simulations[23–25]. However, there is a lack of experimental techniques able to check the validity of such theoretical studies in the case of small systems (at nanoscale).

Although different techniques are available for the characterization of the dielectric properties at the macroscale, none of them are suitable for nanoscale measurements. There are optical methods (which involve labeling), that use fluorescent probes, that have

demonstrated to report the polarizability of certain functional sample locally[26]. This kind of technique has been used to image the local dielectric properties of cells[27], obtaining nice images, but its quantification in terms of realistic values of the intrinsic dielectric constant of the specimen under study has not been possible. First, because such techniques, have important crosstalk effects, as they are not only sensitive to polarization, but stress and another physical magnitude can affect them, and second because there is a lack of comprehensive theoretical expressions for the calculation or prediction of solvent effects on chemical reactivity, and inadequacy of defining solvent polarity in terms of simple physical solvent characteristics.

Scanning probe microscopy (SPM) related techniques are the only existing techniques capable of characterizing the relative permittivity quantitatively with nanoscale spatial resolution[28]. Not only that, but they are non-invasive microscopies that can work under many kinds of experimental environments: vacuum, air, liquid, temperature control, etc. This fact makes them able to measure most nanoscale samples regardless of their structure, origin, properties, or topographical complexity. Among them, our group has specialized during the last decade on the use of Electrostatic Force Microscopy (EFM), for nanoscale relative permittivity characterization. The possibility to measure the intrinsic dielectric constant at the nanoscale level allows scientists to address multiple scientific open problems.

Some examples of physical systems that have been characterized through this technique are studies on the efficiency of solar cells[29], probing the different charge transport in semiconductors[29], sensing the electrical properties of graphene and its water absorption[30], label-free compositional mapping of biomolecules such as protein[31], lipid layers[31,32], DNA[3] or different polymer blends[33] and nanoparticles[34] or label-free structural mapping of differences in internal structure of gram-positive and gram-negative bacteria[35]. As well, different hydration and hygroscopicity properties of bacteria as compared with endospores[36], subsurface characterization of nanoparticles or carbon nanotubes embedded inside polymeric matrices[37–39] or size determination of nanoscale objects like metal NWs through its

polarization forces[40]. Also, the different interface capacitance at the solid/liquid interface, and more recently, even dielectric behavior of confined water[21], has been characterized using this technique.

1.4 Nanoscale dielectric properties of biological samples

We (the Nanoscale Bioelectrical Characterization Group) are focused on the study of polarization properties of biological components and structures at the nanoscale level employing EFM. During the last decade, a deep study of how the main biomolecules present in the biological structures polarize has been carried out, and it is summarized in Figure 1.8.

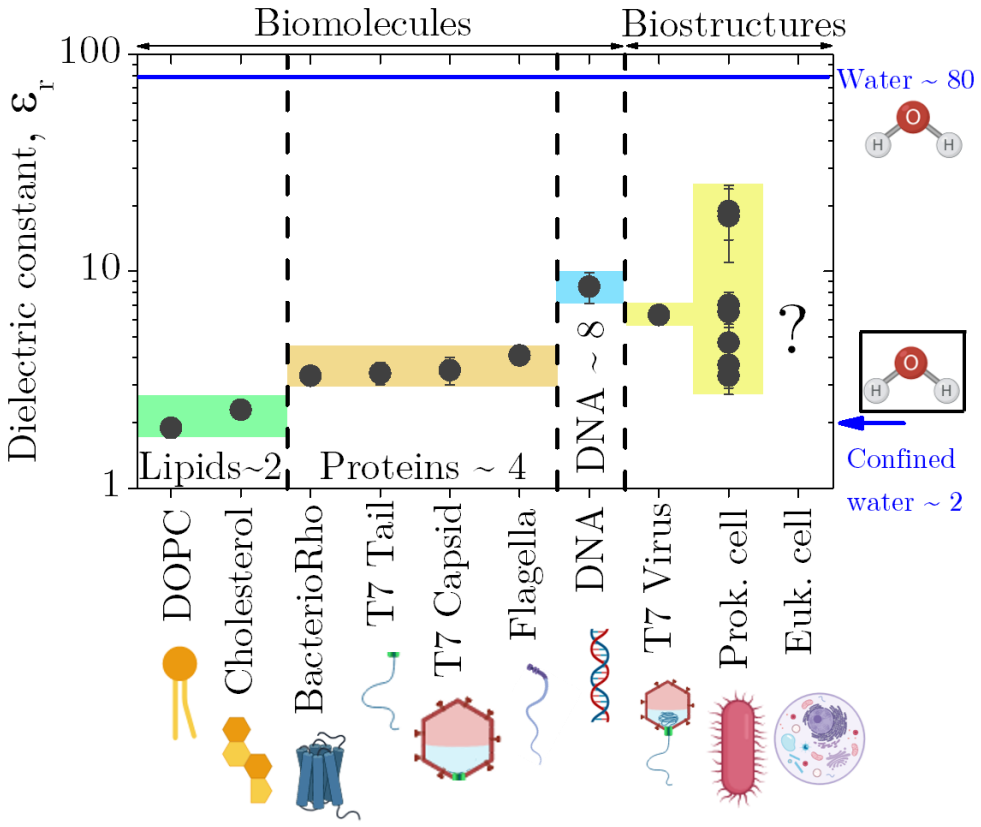

Figure 1.8: Summary of the dielectric constant values calculated by EFM related techniques of the main biomolecules present in the biological structures. Values are obtained from the following references[3,21,30,31,33,34].

Cells, which are the smallest structural and functional units of a living organism, are mainly formed by lipids, proteins, nucleic acids, and water. Those different biomolecules have turned to give different intrinsic dielectric responses. Going from lower to higher polarizability, we have the lipids ($\varepsilon_r \sim 2$), the proteins ($\varepsilon_r \sim$ 3-4), and finally, the nucleic acids ($\varepsilon_r \sim 8$). On its

side, water is well known to have high polarizability ($\varepsilon_r \sim 80$) mainly attributed to their polar molecule free to orient its dipolar moment with the externally applied field. Nevertheless, as is has been said before, water dramatically decreases its polarization ($\varepsilon_r \sim 2$) when it is confined at the nanoscale level due to the loss in the degree of freedom for the rotation of its molecules.

Such results have been achieved after proper quantification of EFM measurements with non-trivial procedures that will be explained deeply in the following sections. But they are mainly measurements on thin homogeneous layers of a certain biomolecule, or single point measurements on heterogeneous samples like bacterial cells, that do not fully represent its different local polarization properties. In both cases, the measurements performed have low statistical relevance. This fact is a consequence of the difficulty of obtaining good data without any unwanted artifact with the state-of-the-art techniques available, and to the costly procedure to analyze and quantify them. The only studies available dealing with more complex heterogeneous systems such as eukaryotic cells are performed in air and lack of quantification, only showing images full of topographic crosstalk contributions[41,42], or if they are quantified, they use parallel-plate models which do not take into account the geometry of the system[43]. Thus, there is still room for improvement in the use of SPM techniques in order to achieve locality of the dielectric mapping of heterogeneous and topographically complex samples, as well as increasing its statistical significance.

Following next, you will find a review of SPM techniques for electric characterization, and more in detail Electrostatic Force Microscopy.

2. Scanning Probe Microscopy

This chapter contains an introduction to the Scanning Probe Microscopy techniques, with a special interest in its electrical modes. We are focused mainly on Electrostatic Force Microscopy, which is the chosen technique for our project.

2.1 Introduction to Scanning Probe Microscopy

In 1981, Gerd Binnig and Heinrich Rohrer invented the Scanning Tunneling Microscope (STM)[44], the first Scanning Probe Microscope (SPM). Only five years later, they received the Nobel Prize for its invention. Also, in 1986, Binnig and Christoph Gerber invented the Atomic Force Microscope (AFM)[45]. The emergence of Scanning Probe Microscopies is considered as one of the main boosts for the field of nanotechnology. For the first time, scientists all around the world had a tool with sub-nanometric resolution, able to work in liquid conditions and useful to characterize with nanoscale spatial resolution different physicochemical properties of materials, devices, biological tissues, etc.

A Scanning Probe Microscope is an instrument able to analyze a sample's surface by tracking it with a sharp probe, similarly to a braille writing system for visually impaired people. The instrument is composed of three parts: the scanner, the probe, and the controller (Figure 2.1).

The scanner is responsible for the movement of the probe during the image acquisition. It is formed by three piezoelectric actuators (X, Y, Z), that can change their length with sub-nanometric precision under the application of a certain electric potential difference. This allows controlling both probe location (X, Y) and probe-sample distance (Z). The scanner

can be located under the sample (acting as a sample stage in sample-moving SPMs) or on top of the sample, mounted on the tip (acting as a scan-head in probe-moving SPMs).

The probe is responsible for sensing the sample's surface. Very different types of probes are found depending on the SPM technique used, but most common ones are needle-like shaped, ending with a sharp apex. The probe is located on top of the sample's surface, and its sharp end is brought to very close proximity with it. In that configuration, the probe can "feel" different interactions with the surface. Those interactions change depending on the probe-sample distance, probe type, and local sample's physicochemical properties.

The controller is responsible for driving the scanner's movement through the sample and recording the probe-sample interaction. The (X, Y) movement of the scanner is normally performed at constant rates and with one of the two axes called fast and another one called as slow (as one is scanned faster than the other one). The Z movement is of special importance in such systems as is normally dominated by a feedback loop that depending on the probe-sample interaction recorded, will change the Z length of the scanner to maintain constant the desired interaction strength. Thus, the movement of the Z piezo is recorded and correlated with the (X, Y) position of the tip, generating a topographical image of the sample's surface.

Nowadays, a whole tree of different SPM techniques exists, depending on the probe-sample interaction felt by the probe and/or the feedback or recording system used. As previously said, the first one to be invented was the STM[44], which relies on the tunneling current recorded by the probe when it is placed at a nanometric distance (below 10nm) to the sample. As the tunneling current sensed by the tip is highly dependent on the tip-sample distance, the Z-piezo of the scanner will be extended or retracted to maintain constant de real-time recorded tunneling current. The main limitation of STM is the fact that a tunneling current is only found between conductive materials, and so it was restricting STM to work only with conductive samples or very thin insulating films. That fact leads to the early development of AFM[45] in 1986 as a more versatile version of the STM.

2.2 Atomic Force Microscopy

AFM is based on the use of a small cantilever (tens of µm wide, and hundreds of µm long) with a sharp tip at its free end that has an apex in the nanometer range, whose deflection is measured while the tip scans the sample. In its beginnings, the deflection of the cantilever was detected using an STM, but it was quickly removed by a much easier system as it is the reflection of a laser onto a four-quadrant photodiode (Figure 2.1). The deflection of the cantilever is normally caused by the interaction of the tip's apex with the sample (depending on the interaction, it can also affect the whole tip and the cantilever itself). The deflection can be used to map that interaction itself locally or as a magnitude to maintain constant for the controller to extract the sample's topography.

The change in the deflection of the cantilever (ΔD) is measured as a voltage difference in the output of the photodiode. That signal is converted into length units (through the sensitivity factor) to know the real distance that the cantilever has bent. Later, the realistic deflection of the cantilever is converted into force (F) through Hooke's law:

$$\text{Force} = k \cdot \triangle D \qquad \text{(eq. 2.1)}$$

where k is the spring constant of the cantilever.

The AFM development opened a whole new world of possibilities, as its way of working (laser detection of cantilever deflection) can perform measurements regardless of the nature of the sample (valid for insulating samples) and in vacuum, air, or liquid environments. Not only that but the extremely good force resolution of AFM (~pN) together with its extremely good nanoscale spatial resolution allowed scientists to study (Van der Waals forces[46], capillary forces[47], solvation forces[48] or chemical affinity[49]) that remained inaccessible until its arrival (surface force apparatus[50] had similar force resolution, but not nanoscale resolution). Besides, functionalization of the tip with different molecules and coatings, together with the application of external physical fields, enabled the study of unknown phenomena like protein

folding[51], ligand-receptor interactions[52], DNA hybridization[53], cell surface interactions[54], magnetization domains[55] or ferroelectricity.

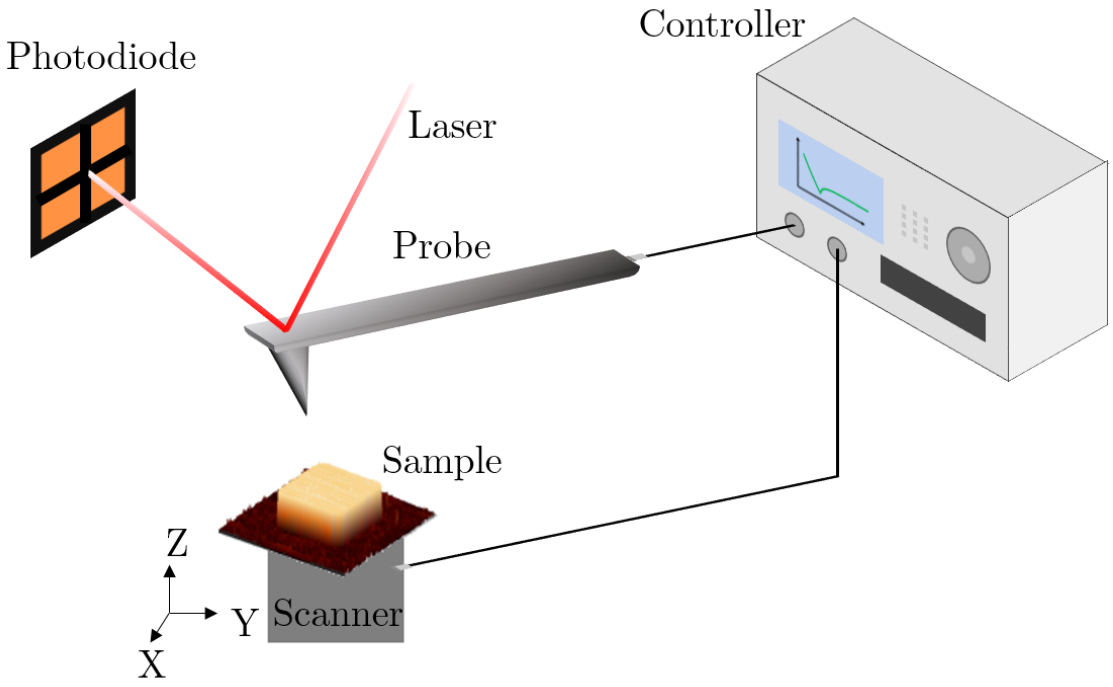

Figure 2.1: Schematic illustration of the Atomic Force Microscope.

Classically, the main disadvantages of AFM are: first, the fact that it is normally restricted to surfaces (some AFM electrical and mechanical techniques can achieve sub-surface imaging[56]) and second, that as a scanning technique, it is considered to be slow (this was sorted out in 2001 with the invention of High-Speed AFM[57]) as compared with electron microscopies for example. Moreover, other disadvantages can be tip or sample damage during scanning, and artifacts appearing in the obtained images coming from the different parts of the system (piezo scanners, tip convolution, etc.).

2.3 Force regimes and imaging modes

Among all the AFM capabilities, the possibility to acquire topographic images of the sample surface with extremely good resolution (down to the atomic level), remains as its main use. Probe-sample interaction arises from different phenomena depending on the probe-sample distance. At long distances, the probe and the sample do not interact (Figure 2.2). As the

tip gets closer to the surface, the short-range Van der Waals forces (< 10 nm) appear to be relevant and cause the (negative) deflection of the cantilever towards the sample until apex-sample contact is made (in the so-called "snap-in" point) (Figure 2.2). As the probe keeps approaching the surface, the repulsive forces increase until the attraction forces are balanced, and hence, the cantilever goes back to a zero-deflection state (Figure 2.2). Finally, as the probe is further pushed towards the sample, we enter into the repulsive regime, where the repulsive forces cause the (positive) cantilever deflection. In the last sentences, we have referred to a negative deflection as the one where the cantilever is bent towards the sample (downwards), and to a positive deflection as the one where the cantilever is bent upwards.

The interaction landscape shown in Figure 2.2 is a general one, in the sense that it can change upon many different things. For instance, electrostatic repulsion can appear, and the tip can start bending up positively due to static electric charges present in the surface of the tip and the sample. In that case, the contact is made with the tip bent positively, and no "snap-in" point is found. This situation is very relevant in liquid imaging, where many other physicochemical factors (i.e., pH, an electric field applied, etc.) can also make that interaction landscape change.

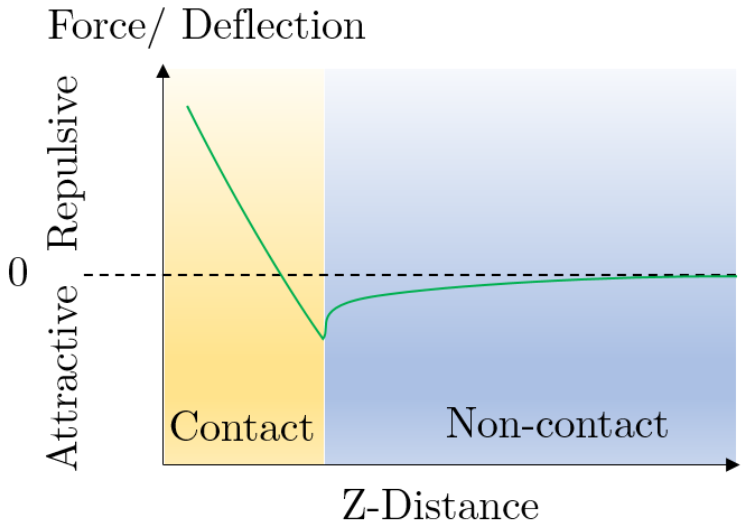

Figure 2.2: Schematic illustration of AFM force regimes as a function of tip-sample distance.

The scenario shown in Figure 2.2, allows us to work in 3 different regions of such interaction landscape. The non-contact region, where tip and sample are not in physical contact. The intermittent contact region, where tip and sample are sometimes in physical contact and sometimes out of physical contact. And the contact region, where tip and sample are in physical contact. Those regions also define the different imaging modes normally used in AFM, known as contact mode, dynamic mode (otherwise named as AC mode or Tapping mode), and non-contact mode.

In contact mode, the static bending of the cantilever in the repulsive regime is recorded and maintained constant during all the scanning process at a certain fixed valued named as setpoint (Figure 2.3a). The feedback loop will tell the Z-piezo to elongate (shortening the probe-sample distance) when the controller reads a deflection value lower than the setpoint, and to shorten (enlarging the probe-sample distance), when a deflection value higher than the setpoint is acquired. Therefore, the setpoint is the parameter that will tell us how much we are pressing our sample. Ideally, a 0 force setpoint would be the best choice to make (to minimize sample and tip damaging), but due to the high instability of such a situation, images are normally obtained applying a higher force. Here, the topographic image is obtained from the Z-piezo displacement value for each pixel. To reduce perturbation, usually soft cantilevers (k <1 N/m) are used. Furthermore, lateral forces are to be as well avoided. This is normally achieved by lowering the scanning velocities.

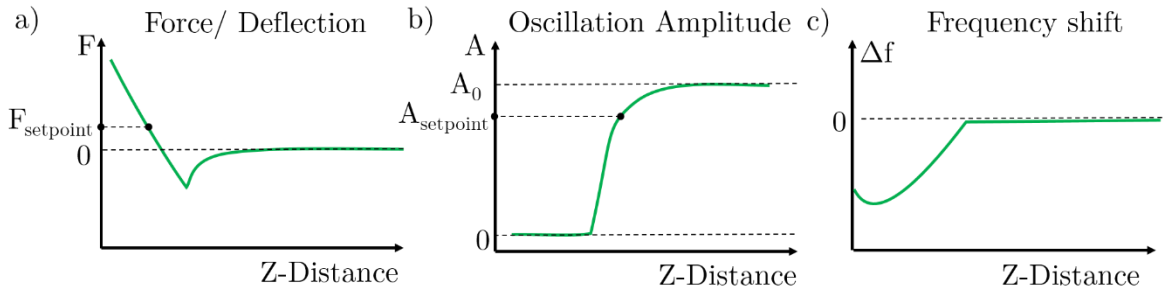

Figure 2.3: Setpoint values in the different imaging modes. a) Contact mode. b) Dynamic mode. c) Non-contact mode.

In dynamic mode (also known as AC mode, Amplitude modulation mode, or Tapping mode, depending on the AFM brand), the cantilever is mechanically oscillated close to or at its resonance frequency (to maximize the oscillation amplitude) and usually operates in intermittent contact. Normally this mechanical oscillation is performed with a piezoelectric actuator mounted on the probe holder, but other methods like the so-called MAC-mode[58] (using magnetic forces), the application of an AC bias inducing electrostatic oscillation, or the induction of an oscillation through a pulsed laser (photothermal method) are often used. A lock-in amplifier records the oscillation amplitude, that has as an input signal, the photodiode signal coming from the reflection of the laser in the cantilever. The lock-in amplifier is also able to record the phase difference between the oscillation of the probe and the excitation of the piezoelectric actuator. The recorded oscillation amplitude will be reduced as the probe is approached towards the sample (Figure 2.3b). A given amplitude (A_s) is defined as a setpoint, and it is normally expressed in terms of the free-oscillation amplitude (A_0), as a percentage of it. Therefore, the feedback loop will tell the Z-piezo to elongate (shortening the probe-sample distance), when an oscillation amplitude lower than A_s is read by the controller, and to shorten (enlarging the probe-sample distance), when an oscillation amplitude higher than A_s is acquired. Here, apart from the topographic image (extracted as usually from the Z-piezo displacement for each pixel), we also have the amplitude or error image (oscillation amplitude value for each pixel), which is normally highlighting the edges of the sample's features, and the phase image (phase shift value for each pixel). The phase image has additional information about the sample and can be used to unravel material composition or adhesion, as the phase shift is a fingerprint of the dissipation energy during the cantilever damping (usually strongly dependent upon material composition)[59].

Finally, the non-contact mode (or frequency modulation mode) works similarly to the dynamic mode but takes advantage of the resonance frequency shift that appears when the tip is very close to the sample in the attractive regime. Here, the feedback loop makes the

Z-piezo elongate or retract to maintain the cantilever oscillating at its resonance frequency (Figure 2.3c). This is achieved normally by feedbacking the phase signal of the lock-in amplifier to maintain it constant (at 90º). Because of the short tip-sample distance between the probe and the sample, small oscillation amplitudes must be used. The main advantage is that since the probe is flying above the sample without getting in contact with it, nor the probe nor the sample suffer any damage. The main disadvantage is the difficulty of maintaining good feedback, which makes this mode very challenging to use on topographically tall samples.

2.4 Scanning Probe Microscopy for nanoscale electrical characterization

One of the main advantages of SPM techniques as compared with other types of microscopies is the possibility to obtain relevant qualitative and quantitative information about the physicochemical properties of the specimen under study. This ability comes first, from the fact that the probe can have different uses: as a lever to sense forces, as an electrode to detect currents, as a nanomanipulation tool to move objects at the nanoscale, etc. and second from the fact that different local properties of the system can change the physical interaction that we are sensing.

On what follows, I will make a summary of the main SPM techniques used for electrical characterization, dividing them into two groups depending on whether the physical magnitude measured is an electrical current or an electrical force.

2.4.1 Current detection SPM techniques

In this first group of techniques or modes, the physical magnitude that it is measured is an electrical current flowing between tip and sample in order to study the behavior of the sample qualitatively or to extract a physical property of interest quantitatively. We find:

1. **Scanning Tunneling Microscopy**[44] **(STM)**, as explained before, it relies on the tunneling current recorded by the probe when it is placed at a nanometric distance (below 10 nm) to the sample. As the tunneling effect is restricted to

metallic materials, only metallic surfaces or very thin insulating layers can be studied. It was initially invented for its performance in topographic imaging, but as the tunneling current is sensitive to both geometry of the sample, and local density of states of the electrons in the sample, it can be used to map the local density of states[60]. Even though STM can be used in liquid environments, it was not until recently that high-resolution imaging (compared to the one in air) has been achieved[61]. The added difficulty when STM is used in liquid relies on the electrochemical congestion and external noise interference, which results in low-resolution images, as local tunneling current is masked.

2. **Conductive Atomic Force Microscopy (C-AFM)** relies on the simultaneous detection of topography and electric current flow at the contact point of a conductive tip with the specimen's surface. The electric current is detected through a preamplifier located close to the tip when a DC biased is applied between tip and sample. The fact that both topography and electric current are obtained independently (topography from deflection and electric current from preamplifier), constitutes an advance with respect to STM, as there is not any electrical crosstalk in the topographic images. It is operated in contact mode, and both voltage-current measurements in a single point of the image, or current measurements at constant voltage as the tip scans the surface, can be obtained[62].
3. **Scanning Capacitance Microscopy (SCM)** is also operated in contact mode but now under the application of a high frequency (GHz) AC bias between the tip and the sample, forming a capacitor. The changes in the sample's capacitance are detected through an external electronic resonance circuit. Charge storage[63], semiconductor dopant profiling[64], or local dielectric properties[65] of materials are some examples of studies carried out with SCM. The topography is again obtained independently with the optical acquisition of the deflection of the cantilever.

4. **Nanoscale Impedance Microscopy (NIM)**, is a technique that investigates the electrical properties and processes in the frequency regime[66]; having an AC bias applied, but in this case, the current sensed between tip and sample is passed through an impedance analyzer, that directly measures the local impedance of the resistive-capacitive system. In this manner, both impedance images at a constant frequency and local studies of the frequency behavior in certain points of the image can be acquired. The topography is again obtained independently with the optical acquisition of the deflection of the cantilever. Contrary to C-AFM, now both the resistive behavior (conductivity properties) and the capacitive behavior (dielectric properties) of the sample are explored. Contrary to the DC measurements, in AC measurements, spurious contributions to the global capacitance of the system appear. These contributions (also known as stray capacitances) appear as a big part of the acquired signal and come from the fact that the whole tip, the cantilever, and even the chip of the cantilever are part of the whole capacitor system. Normally this is solved by imaging, not the total signal, but only the contrast from point to point (highly affected by the local properties of the sample) or subtracting the stray capacitances as if they were a background offset of the measurement, but extremely precise amplifiers are needed in order to achieve the needed resolution in terms of capacitance (down to the aF level with tens of fF background noise).
5. **Scanning Microwave Microscopy (SMM)**, consist of the interconnection of an AFM setup with a vector network analyzer. A high frequency microwave wave (in the range of 0.1GHz to 100GHz) is sent from the network analyzer to the sample through the tip, that acts as an antenna. The microwave scattering parameters (S11, S22: reflection, and S12, S21: transmission), are recorded. The local impedance properties of the sample induce changes in the S-parameters, and so, conductivity and capacitance images can be obtained at the nanoscale. Other

configurations (not AFM-based) of SMM also exist. Mainly the problem when working with microwave signals is that the shielding of the signal from the microwave generator to the sample must be well done to avoid internal reflections at the connections or circuit resonances. Multiple different waveguides are available to perform such a procedure in a good manner. High frequency waves are expected to have deeper penetration lengths, so also subsurface studies have been carried out with SMM[67]. Its interaction with biological tissues[68] and specifically its quantification[69] are also of major interest.

The techniques explained until now are normally restricted to air or vacuum environments. Many additional complications appear when running electric current measurement through liquid environments. Those can arise from many different causes. First, if the current that is recorded not only flows through the apex of the probe, but it also flows through all the cone and cantilever, lots of unwanted artifacts appear, enormous background current noise, provoking a loose in the locality. Furthermore, scattering of the radiation can be found when there is a medium change or spurious electrochemical reactions can happen and normally, a potentiostat is needed to control the potential of the solution. The formation of Electrostatic Double Layers (EDL), and the appearance of new forces acting on the tip like surface stress[70] or osmotic force, can also affect the current detected (these phenomena will be explained in more detail further on). However, this has not stopped SPM techniques to be able to record currents under liquid environments, and the two main techniques available in that space are:

6. **Scanning Electrochemical Microscopy (SECM)** was developed in 1989[71] and is used to measure the local electrochemical behavior of different interfaces such as liquid/solid, liquid/gas, or liquid/liquid. The local changes in the current flowing to the probe, that is generated by a redox-active couple (i.e., Fe^{2+}/Fe^{3+}) present in the solution, are recorded as the surface is scanned. Normally SECM probes are platinum or other metal microwires that are sealed in a glass capillary.

The use of a bipotentiostat (normally in the standard four-electrode configuration) is needed, where the tip normally acts as a working electrode. The adhesion of a tuning fork to the ultramicroelectrode performing the measurement allows obtaining the topography of the sample as well simultaneously[72].

7. **Scanning Ion Conductance Microscopy (SICM)**[73] detects the small current changes through a capillary probe, originated by a change in the flow of ions through its small aperture when the tip gets very close to a surface. The technique allows extracting the topography of insulating samples like cells, as the flow of ions through the probe is dependent upon the distance between probe and sample. The principle underlying SICM is the fact that the closer the aperture of the probe and the sample are, the smaller the region with liquid between probe and sample, therefore fewer ions can flow inwards. Lastly, its high-speed version has been developed, able to acquire sub-second topography imaging of living cells[74]. It is also a promising tool to use for electrophysiology[11] at the single-cell level, with a principle of working similar to patch-clamp techniques. In recent years it has also been used to map the surface charge[75].

2.4.2 Electric Force detection SPM techniques

In this second group of techniques or modes, the physical magnitude that the probe measures it is a force, that is related to some electrical property of the sample of interest. Most of those techniques have very similar experimental setups, based on the application of a voltage between a conductive AFM probe and the sample's conductive substrate.

In a general form, when an external bias of form $V(t)=V_{DC}+V_{AC}\cos(\omega_{el}t)$ is applied, there is an electric force acting on the probe given by:

$$F_{el}(t)= \frac{1}{2}\frac{dC(z)}{dz}(V(t)-V_{CP})^2 \qquad \text{(eq. 2.2)}$$

Where V_{CP} is the so-called contact potential and dC(z)/dz is the capacitance gradient. By expanding eq. 2.2 one obtains three components, namely, a "static" DC bending, and two oscillatory components at the frequencies ω_{el} and $2\omega_{el}$:

$$F_{el,DC}(t)= \frac{1}{2}\frac{dC(z)}{dz}\left[(V_{DC}-V_{CP})^2+\frac{V_{AC}^2}{2}\right] \qquad \text{(eq. 2.3)}$$

$$F_{el,\omega}(t)= \frac{dC(z)}{dz}(V_{DC}-V_{CP})V_{AC}\cos(\omega_{el}t) \qquad \text{(eq. 2.4)}$$

$$F_{el,2\omega}(t)= \frac{1}{4}\frac{dC(z)}{dz}V_{AC}^2\cos(2\omega_{el}t) \qquad \text{(eq. 2.5)}$$

Depending on the harmonic recorded, different electric force modes have been developed:

1. **Kelvin Probe Force Microscopy (KPFM)**[76], uses a lock-in amplifier to measure the ω component of the tip movement. A feedback loop is applied to the system driving the DC potential applied to the tip (V_{DC}) to nullify the ω component of the force (eq. 2.4). As this condition is satisfied only when $V_{DC} = V_{CP}$, the local distribution of the contact potential (otherwise named surface potential) can be measured. KPFM is a common technique for material science characterization and semiconductor industry, but also studies on bio-samples have been performed[77].
2. **Electrostatic Force Microscopy (EFM)** is divided between DC-EFM or AC-EFM, depending on whether the static contribution (eq. 2.3) or the oscillating contributions (eq. 2.4 and eq. 2.5) are measured (through the static deflection or through a lock-in amplifier respectively). Basically, the capacitance gradient dC(z)/dz is measured through one of the components of the electrostatic movement induced to the cantilever. Local dielectric properties of the specimens under study, as well as subsurface characterization, can be achieved with EFM. A more detailed explanation of EFM is found further on in the thesis as it is the main technique used in this work.

3. **Scanning Polarization Force Microscopy (SPFM)** is a technique where a feedback loop is performed on the 2ω component of the electric force (eq. 2.5), forcing it to feel a certain polarization force during the scan that is modulated by moving the tip up and down. SPFM images have information about the polarization of the sample, but an important contribution of the total acquired signal comes from the topographic features, which makes its quantification, strongly challenging coupling topographic information with its dielectric response.
4. **Piezoresponse Force Microscopy (PFM)**, allows imaging and manipulation of piezoelectric and ferroelectric materials. In summary, an AC bias is applied to the tip (when it is in contact with the sample), that induces a deformation in the sample through the converse piezoelectric effect. The amplitude and phase of the tip are recorded, employing lock-in techniques, and the different domains of the sample can be imaged[78].

Similarly to what happens for current-based techniques, the application of electrostatic force-based measurements in liquid environments is highly problematic. The formation of Electrostatic Double Layers (EDL), at the close vicinity of the solid surfaces immersed in an electrolyte, screens the electrostatic interaction and turns it short range. Not only that, but the appearance of new forces acting on the tip like surface stress or osmotic force prevents the detection of pure electrostatic interaction and adds complication to the quantitative studies. If the frequency of the voltage applied is not sufficiently high, or the bias is too high, electrochemical reactions tend to happen, that mask the signal that is measured, or damage the tip or the sample. Furthermore, the high value of the dielectric constant of water ($\varepsilon_r \sim 80$) and other polar liquids (more often used), as compared to the one of air ($\varepsilon_r \sim 1$), can be an issue to achieve locality in the measurements.

Even if force-based techniques in liquid environments are not so extended as current-sensing techniques, different works have been done on this topic. Here I summarize the most important ones:

1. **Double Layer Force Microscopy**[i] measures the short-range electrostatic forces induced in the tip's charged surface by the EDL formed at the solid-liquid interface in liquid environments. Normally non-conductive probes are used. Nevertheless, also conductive tips can be used to study such forces and how tip surface chemistry affects the total force felt by the tip[79]. The surface of the tip gets charged when immersed in a liquid. Usually, the surface charge accumulated into the tip can be tuned with the pH of the solution or other chemical methods. That charge can feel the electric field distribution in the close surroundings of the surface of interest when the EDL overlap. Molecular structure of the EDL, as well as the surface charge of materials or biomolecules[80], can be analyzed with such techniques, that depending on the case of study, may need the use of potentiostatic control of the system[81] or not. The advantages of using dielectric tips rely on the fact that electrochemical reactions are avoided at the tip surface, which enhances the stability of the measurements. The main drawback of such techniques is that it is restricted to a very short-range distance, and the tip-sample interaction vanishes after few nanometers of separation (Debye length, λ_D, in 1 mM solution of 1:1 electrolyte in water is around 10 nm). Quantification is normally performed with analytical models that do not consider normally topographical effects on the electrostatic signal.
2. **Surface Stress Sensor**[ii] measures the bending of the cantilever when immersed in a solution due to a change in its surface free energy. Different charge accumulation at the solid-liquid interface, or adsorption of molecules at the surface, induce the cantilever bending as the free energy landscape changes. Ion adsorption[82] or surface charge[83] can be studied with this technique, that more

[i] The nomenclature of this mode is not clear inside the forest of names of the different SPM techniques. So, I choose myself that name to join them together.

[ii] The nomenclature of this mode is not clear inside the forest of names of the different SPM techniques. So, I choose myself that name to join them together.

than a microscope, it can be seen as a cantilever-based sensor. The lack of locality is the main drawback of such a group of techniques, as the force is felt normally by the whole cantilever, and not only by the tip.

3. **Open-loop Kelvin Probe Force Microscopy (OL-KPFM) or Dual Harmonic Kelvin Probe Force Microscopy (DH-KPFM),** is a multifrequency technique, that allows performing KPFM measurements into liquid environments. Traditionally, KPFM uses closed-loop feedback that applies a DC bias to the tip to nullify the first harmonic (eq. 2.2) of the electrostatic oscillation induced to the tip. Takeuchi *et al*[84], developed a new method (in dry conditions) where the contact potential (V_{CP}) is determined in open-loop conditions by measuring both the first (eq. 2.4) and second harmonic (eq. 2.5) of the tip oscillation and dividing them (which allows to eliminate the derivative of the capacitance term), leaving as a unique unknown parameter, the V_{CP}. Conventional KPFM cannot be used in liquid environments, as both electrochemical reactions and screening of the potential distribution happen in such conditions during its closed-loop operation. The use of a high frequency of the voltage bias applied (preventing electrochemical reactions and redistribution of ions into the liquid), allowed Kobayashi *et al*[85] to extend OL-KPFM to liquid environments. Further discussion about the reliability of OL-KPFM in liquid is found in the modeling chapters.
4. **Electrochemical Force Microscopy (EcFM)**, introduced by the group of Sergei V. Kalinin in the last decade[86], is based on the measurement of the time and voltage dependence of the electrostatic force felt by a conductive tip at very short times after the application of a voltage excitation (normally in the form of a voltage pulse). This "trick" allows studying the electrochemical system dynamics. For short time acquisitions after the excitation, it avoids the formation of the EDL or the appearance of the osmotic or surface charge forces. Also, the

dynamics of the electrochemical processes happening at the solid-liquid interface can be probed as a function of the magnitude of the bias applied.

5. **Electrochemical strain microscopy (ESM)**[87] is based on the detection of the strain induced at the tip-sample junction due to electrochemical processes when an electric field is applied. This technique allows imaging with nanoscale spatial resolution, electrochemical processes that are of great interest for many fields of science such as energy storage and production[88], or ionic diffusion[89] in electrolytes. Even though the mechanical stress is measured here (not an electrostatic force itself), the strain is induced by an external applied electric field and allows to study electrochemical phenomena at the nanoscale.
6. **Electrostatic Force Microcopy in Liquid (In liquid-EFM)**, this technique will be further explained in the following section as it is one of the main techniques studied during this work of thesis. Mainly, it relies on the application of a high frequency bias to avoid electrochemical reactions, EDL formation, osmotic forces, and surface stress to recover the pure electrostatic interaction that is found in vacuum or air environments. It faces the challenge that sometimes the frequency required to avoid all this phenomenon needs to be on the tens of MHz range, and conventional AFM probes normally cannot oscillate that fast (and even less in liquid). Our group developed the low frequency modulation of the high frequency bias applied to the tip[90] to be able to perform EFM in liquid environments (especially crucial for the application to biological samples[91]). Also, high resonance frequency probes have been used to perform measurements in low-molarity environments and with different types of liquid media (non-polar media are easy to work with) to study both EFM and KPFM[92].

2.5 Electrostatic Force Microscopy

EFM is the technique used in this work of thesis to study the dielectric properties of the samples of interest, and so it will be explained in more detail below.

2.5.1 EFM in dry environment

We have seen that different harmonics of the electrostatic force appear on a conducting AFM tip when it is biased with a voltage wave of form $V(t)=V_{DC}+V_{AC}\cos(\omega_{el}t)$ (eq. 2.3, 2.4 and 2.5). We observe that the two first harmonics ($F_{el,DC}$ and $F_{el,\omega}$), provide information about both the dielectric properties of the samples (through the derivative of the capacitance) and the surface potential (through the surface potential term), and they appear mixed. As the interest of our group is mainly the dielectric properties of matter, we use the second harmonic ($F_{el,2\omega}$) for our measurements, where only the derivative of the capacitance term (containing the information about the dielectric properties of our sample), appears:

$$F_{el,2\omega}(t)= \frac{1}{4}\frac{dC(z)}{dz}V_{AC}^2\cos(2\omega_{el}t) \qquad \text{(eq. 2.5)}$$

EFM can also be performed using the DC term (eq. 2.3) in the so-called DC-EFM mode[93], but the mixed contribution from dielectric and surface potential information and the lower signal to noise ratio makes the second harmonic EFM (AC-EFM) be our choice.

Depending on the detection system used, the AC-EFM measurements can be performed either in amplitude modulation (AM-EFM) or in frequency modulation (FM-EFM). While AM-EFM detects the changes in the amplitude oscillation of the cantilever, the FM-EFM detects the frequency shifts on the resonance frequency of the cantilever (as electrostatic force modifies its effective spring constant). While FM-EFM has, in theory, slightly better spatial resolution[94], it is more challenging to implement and perform measurements with. That is why our choice in this work of thesis is AM-EFM.

In Figure 2.4a, I show the time variation of the deflection of the probe when an AC voltage is switched on (recorded by myself). We observe that the three terms mentioned above appear (Figure 2.4b and c). Another experimental aspect to consider is which frequency of the applied voltage is suitable for EFM experiments. In Figure 2.4d, we show the spectra of the 2ω oscillation amplitude as a function of the frequency, and we can clearly see that the response is not flat, but strongly convoluted by the mechanical resonance spectra of the

cantilever. One could find optimal to select an electrical frequency (ω) close or at the resonance frequency of the cantilever (f_r), as the signal is maximum there. But we must consider that f_r is shifted when brought close to the sample and can suffer changes depending on other sample's properties. As we do not want such effects to affect our electrical signal, we always choose an electrical oscillation frequency in the flat region of the spectra (Figure 2.4d), well below f_r, where the signal is only affected by the terms appearing in eq. 2.5.

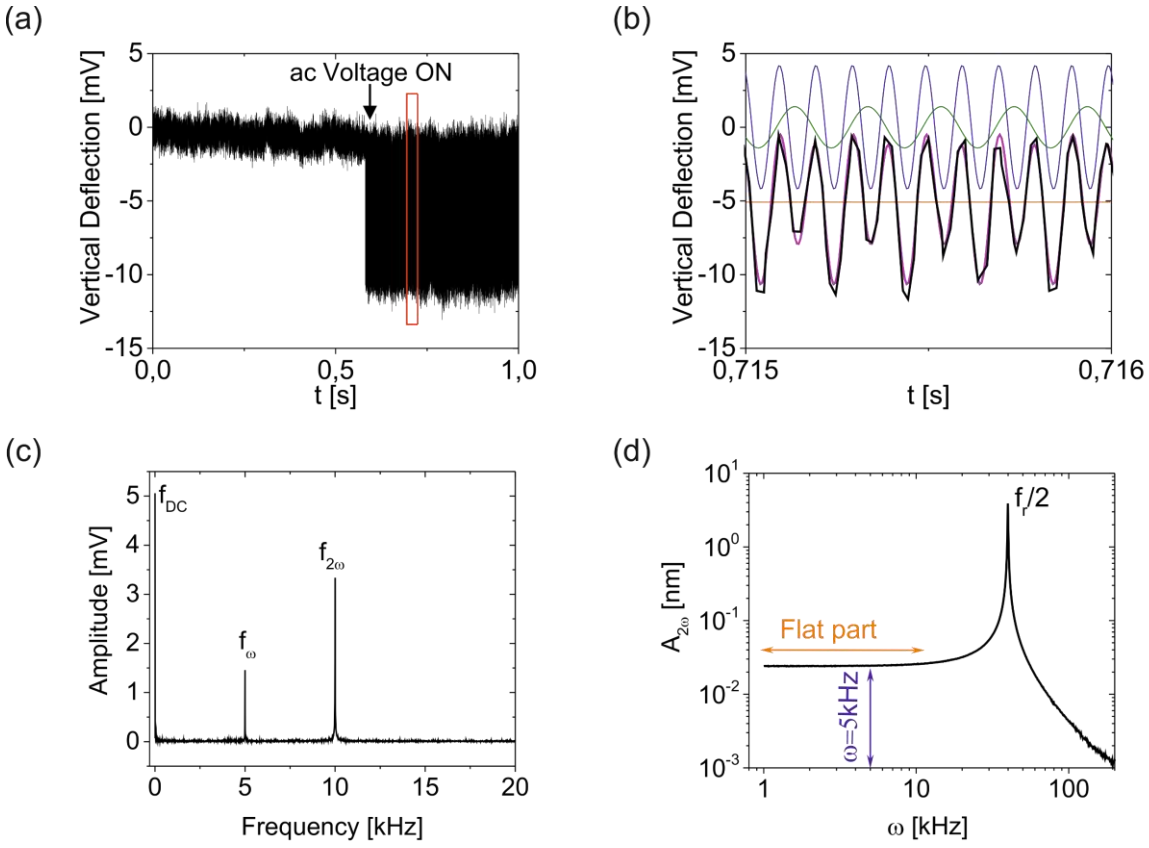

Figure 2.4: (a) Time response of the vertical deflection of one of AFM probes when an ac voltage of frequency f_{el}= 5 kHz and amplitude 3 V is applied. (b) (black line) Zoom-in of the time response of the vertical deflection around the red square area marked in (a). (pink line) The fit of the experimental time response of the vertical deflection with the theoretical time response predicted by eq. 2.1. (orange, green and blue lines) Decomposition of the time response of the vertical deflection into the DC, ω, and 2ω components, respectively. (c) Fourier transform of the vertical deflection time response shown in (b). Three peaks corresponding to the DC, ω, and 2ω components are clearly identified, whose amplitude matches with those of the components shown in (b). (d) Dependence of the $2\omega_{el}$-oscillation amplitude with the frequency of the electric voltage applied. A peak appears at $\omega=f_r/2$=40 kHz. Parameters: lock-in gain, G=200, photodiode sensitivity, m=40 mV/nm, equivalent spring constant k=1.7 N/m.

In Figure 2.5a, we show a scheme of how an EFM setup works. A lock-in amplifier is used to excite the tip through a sinusoidal voltage wave and records the oscillation induced to the tip (recorded by the photodiode). It extracts the amplitude and phase of the tip oscillation in the desired harmonic. Classically, EFM measurements are recorded in two-pass mode, meaning that on a first pass, the topography is recorded (with the electrical oscillation switched off), and in the second pass, the electric oscillation is recorded as the tip hovers the sample in the desired way. Depending on the hovering mode (which trajectory does the tip follow in the second pass), we find two different EFM imaging modes: lift mode or constant height mode.

Lift mode: in this mode (Figure 2.5b), the second pass is performed by lifting the tip a desired distance from the sample topography and maintaining the tip-sample distance constant during all the scan (by following the topography line acquired in the first pass). It is an "easy to use" mode, as the user only has to select the lift distance, but the fact that the tip moves up and down during the electrical pass introduces topographic crosstalk artifacts (these will be explained further on), that hinders the intrinsic properties of the sample.

Constant height mode: in this mode (Figure 2.5b), the second pass is performed by scanning parallel to the metallic substrate at the desired distance. This mode allows the user to obtain polarization images, that are not affected by the topographical crosstalk effect, but that is not directly showing the intrinsic polarization properties of the samples, as the geometry of it needs to be considered (the highest or biggest objects give more signal than the shortest or smallest ones). The mode is not suitable for highly non-planar samples, as the tip could easily crash with the sample.

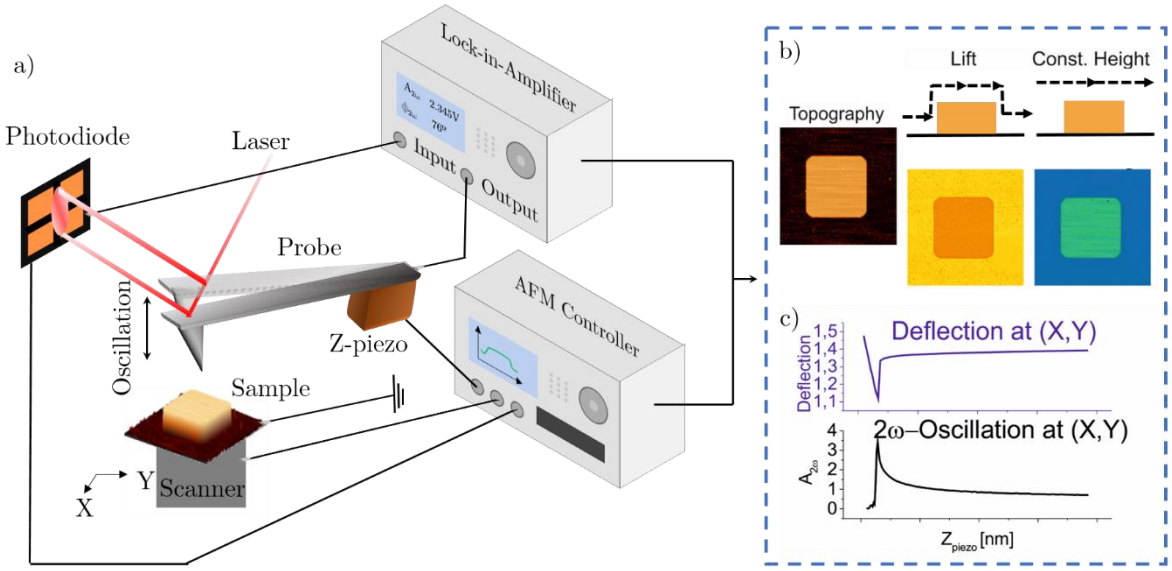

Figure 2.5: a) Scheme of EFM setup. b) Qualitative examples of the topography and different imaging modes of EFM. c) Example of vertical deflection and 2ω electric oscillation approach curves.

The signal from the EFM measurements is strongly tip-sample distance-dependent, as the capacitance gradient in a capacitor depends on the distance between the plates[iii]. EFM force-distance curves are acquired to study such dependence. Such curves consist of the recording of the amplitude of the 2ω electrostatic force component as the tip approaches the surface (Figure 2.5c), together with the vertical deflection (normally recorded in classical AFM force-curve measurements).

2.5.2 Scanning Dielectric Microscopy

EFM images and force-distance curves give qualitative information about the dielectric properties of the samples under study, but the full power of such measures comes from the possibility to quantify them and extract quantitative information such as the intrinsic dielectric constant of the sample. EFM quantification is not trivial, and lots of different aspects must be considered[28].

[iii] It is relevant to point out that even if in KPFM measurements, also find this dependence in the signal detected by the first harmonic term, it has no relevance. The irrelevance comes from the fact that KPFM tries to nullify the ω term, and this is only achieved when the external DC applied is equal to the surface potential, regardless of the value of the capacitance gradient.

The first aspect to be considered is the fact that the probe geometry plays a key role in the measured force. The force that we measure is related to the total derivative of the capacitance of the probe-sample system. Nevertheless, the different contributions coming from the apex, the cone, and the cantilever can have different dependencies with the tip-sample distance and dielectric constant of the sample:

$$\frac{\partial C_{Total}}{\partial z} = \frac{\partial C_{Apex}}{\partial z} + \frac{\partial C_{Cone}}{\partial z} + \frac{\partial C_{Cantilever}}{\partial z} \qquad \text{(eq. 2.6)}$$

On the one hand, even if the area of the cantilever is much bigger than those of the cone and apex, the variation of the cantilever contribution for nanometric displacements of the probe, has shown to be negligible[95] (as the cantilever is far ~15μm from the substrate). Thus, $\frac{\partial C_{Cantilever}}{\partial z}$ can be treated as the background signal offset in the measurement. On the other hand, there is a lack of analytical expressions for the main contributions (apex and cone). Those are only available for two cases: a probe interacting with a plane metallic surface[96], or a probe interacting with a very thin dielectric film[97]. Therefore, in general, one has to use finite element numerical simulations to disentangle the contribution of each part of the probe[34,35].

Secondly, the raw data that comes out from the experimental setup needs to be passed to units with a physical meaning. To perform that operation, the 2ω tip oscillation that comes from the output channels of the lock-in amplifier in volts must be converted into units of capacitance gradient (Farad/meter). This is done with the following expression:

$$\frac{\partial C}{\partial z}\left[\frac{F}{m}\right] = \frac{2\sqrt{2}}{V_{AC}^2} k \frac{(A_{2\omega}[V] - A_{2\omega,offset}[V])}{m \cdot G} \qquad \text{(eq. 2.7)}$$

where k is the spring constant, m the sensitivity, G the lock-in gain, and V_{AC} the RMS value of the excitation applied to the tip.

The third aspect is what we call topographic crosstalk. The topographic crosstalk is an artifact that the lift mode images have, which comes from the fact that in such modes, the

tip moves up and down following the tip topography. As the signal is strongly z dependent, such images can lead to misleading information, as the points of the image where the tip is further away from the metallic substrate will show a lower 2ω oscillation. Even though methods to remove this contribution from the total signal are developed[98], it makes lift mode images very difficult to analyze and quantify.

Finally, the conversion of EFM measurements to direct quantification of dielectric constant value of the sample is strongly dependent not only on the tip geometry (as explained before) but also on the sample geometry[99]. The same experimental signal quantified with different geometric models for the sample will lead to a different intrinsic dielectric constant of the sample. As said before, analytical expressions derived from first principles for the EFM signal are only present in two cases with very easy geometries: (tip-metal)[96] and (tip-insulator thin film)[97] (other pseudo-phenomenological models have also been derived for the tip-sphere case[34]). Therefore, we use finite-element numerical simulations to quantify our measurements that are normally not showing planar geometries.

The procedure for the quantification of the dielectric constant consists of two parts: tip calibration and dielectric constant extraction. The tip calibration procedure consists of finding the geometric parameters for the tip that we are using (sometimes they can differ from the ones in the commercial specifications). To do so, one uses an experimental EFM approach curve acquired on a bare metallic part of our sample to fit the radius and angle to different finite element simulated EFM curves containing different combinations of radius and angles (see Figure 2.6a)[28]. Once the radius and angle of our tip are determined, one can pass to the second part: dielectric constant determination. In that second part, a realistic geometric model of our sample needs to be built up in the finite-element simulator, and again a table of simulated EFM approach curves for different values of the dielectric constant of our sample is built (see Figure 2.6b). Finally, the dielectric constant of our sample is determined by fitting an experimental EFM approach curve on top of the sample to the different approach curves generated with the simulation.

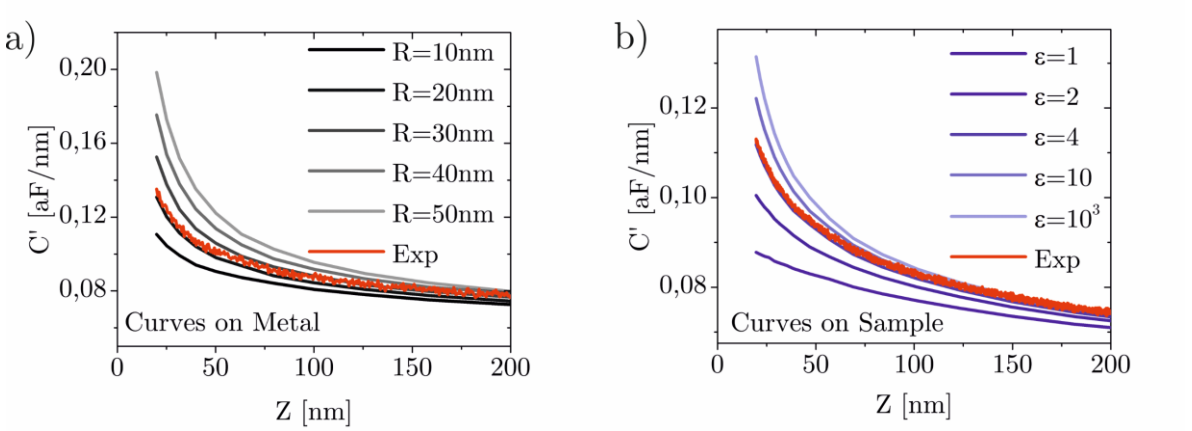

Figure 2.6: Example of the quantification process in SDM for a calibration sample of SiO_2 pillar on top of a metallic substrate. a) Tip geometry calibration: we show an example of simulated EFM force-distance curves (black) with different tip radius, like the ones we use to fit the experimental EFM curve (red) on the bare metal part of the sample. b) Dielectric constant extraction: we show an example of simulated EFM force-distance curves with a different dielectric constant (blue) value for the sample (SiO_2 pillar), like the ones we use to fit the experimental EFM curve taken on top of the sample (red).

The combination of EFM measurements quantified with finite-element numerical simulation to extract intrinsic dielectric constant values of the sample has been developed by our group in the last decade, and we refer to as Scanning Dielectric Microscopy (SDM)[28]. The fact that the quantification of EFM data is not easy turns into very few studies where the intrinsic quantitative values of the dielectric constant obtained are realistic and in good agreement with the literature. Scientists must pay attention to EFM data when reading papers, as there are plenty of works where some of the relevant quantification aspects commented during this section are not considered that may lead to wrong conclusions[43,100].

One of the objectives of this work of thesis is to develop a general experimental setup and quantification platform to be able to map the intrinsic dielectric properties of any sample, regardless of its geometric shape, dielectric properties, or any other aspect.

2.5.3 EFM in liquid environment

As it has been explained before, one of the main advantages of SPMs is their ability to perform measurements in liquid conditions, without losing its nanoscale spatial resolution. This fact becomes especially relevant for biological systems, as it opens the door for characterization of living organisms in their natural environments. Nevertheless, when we

move to the liquid environment (especially polar electrolytes), the subject complicates quite a bit. Different interactions related to the application of a voltage bias to a conductive tip in such environments appear and can mask partially or totally the electrostatic force of interest in EFM. A deeper study of such forces and their dependences with frequency, voltage, solute concentration, etc. will be explained further on in this thesis (see modeling chapters), but mainly, the development of the Electrostatic Double Layer (EDL) at the vicinity of the probe and sample, is the responsible of them.

Such layers develop when a charged surface or a biased electrode is exposed to an electrolyte solution. The mobile charges present in the liquid (mainly ions), feel the electric field generated by the surface charges or the application of a bias and form a space charge region in the close vicinity of the solid surface. If the system is closed and no electrochemical reactions occur at the electrode, the mobile charges on the liquid accumulate until they reach the thermodynamic equilibrium. In equilibrium, the EDL has a certain structure with different layers (Figure 2.7):

Inner Helmholtz Plane (IHP): is composed of a compact layer where ions or solvent molecules are chemically absorbed onto the surface.

Outer Helmholtz Plane (OHL): is composed of the solvated molecules interacting electrostatically with the surface charge.

Diffusive Layer: is a more diluted and thicker layer of ions and molecules that electrically screen the surface charge of the electrode, causing an exponential decay of the potential (a linear decay of the potential is found at the Helmholtz layers). The characteristic length of that exponential decay is called Debye Length (λ_D). The λ_D is well described by the present theory in the literature[101] and is mainly dependent on the electrolyte concentration (normally in the range of few nanometers, i.e., 10 nm for 1 mM 1:1 electrolyte):

$$\lambda_D = \sqrt{\frac{k_B T \varepsilon_0 \varepsilon_r}{2 z^2 e^2 n_0}} \qquad \text{(eq. 2.8)}$$

where k_B is the Boltzmann constant, T the temperature, z is the number of charges per ion, e is the elementary charge, and n_0 is the ionic concentration.

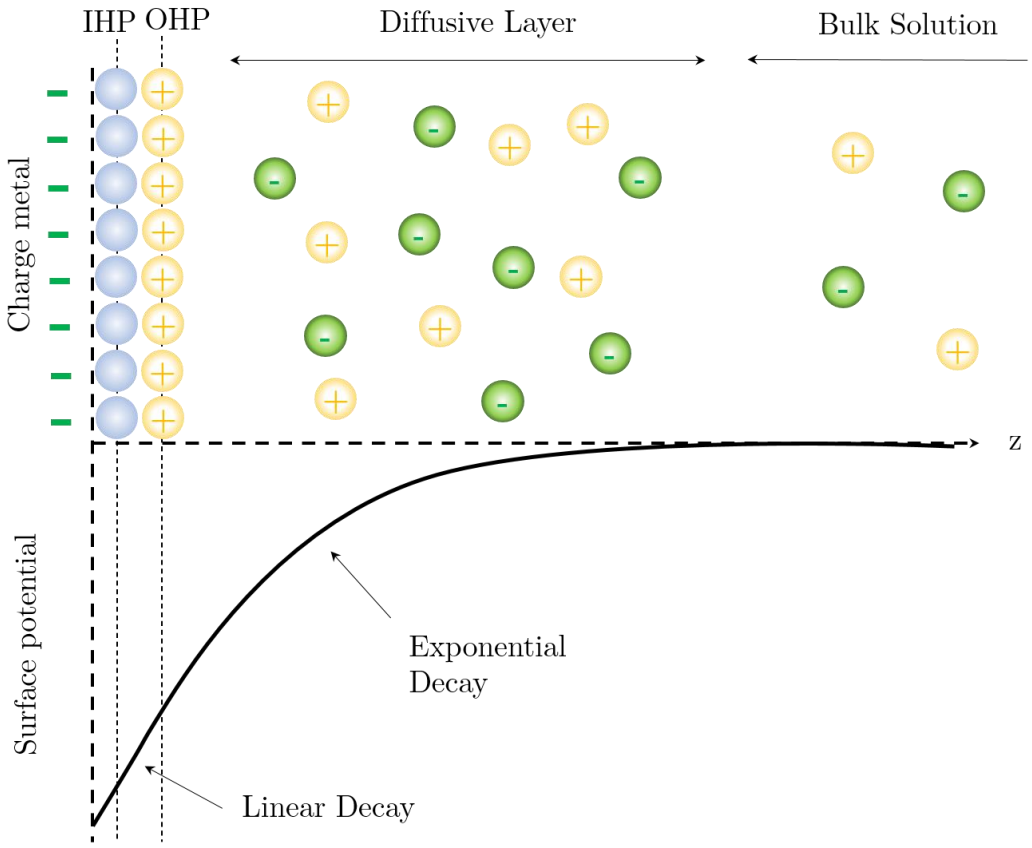

Figure 2.7: EDL structure.

On the one hand, the charge accumulation leads to change into the energy landscape of the probe surface that induces a surface stress bending of the tip (see surface stress interaction[81,83]). On the other hand, the charge accumulation leads as well to a diffusive osmotic force that tends to homogenize the ion concentration everywhere at the surface. The strategy that was developed by our group[90] to avoid such interactions, together with the exponential potential decay induced by the EDL, was to use high frequency electrical excitations (higher than the EDL formation time). The threshold frequency needed to avoid EDL formation is concentration-dependent but goes from several hundreds of kHz to the

tens of MHz. The main issue here is that commercially available probes cannot oscillate fast enough to follow the high frequency electric oscillation in liquid, and if they do so, the electric oscillation falls very close to the resonant frequency of the cantilever, what brings to the unwanted mechanical convolution of the electrostatic force.

Therefore, the trick for the implementation of EFM in liquid not only relies on the application of a high frequency wave but also on the modulation of the voltage amplitude by a low frequency signal. In dry conditions, an EFM tip is biased with $V(t)=V_{AC}\cos(\omega_{el}t)$ (where the DC term is normally not needed as the 2ω term is not dependent on V_{DC}).

However, in liquid, a low frequency (ω_m) amplitude modulated high frequency (ω_{el}) wave is sent to the tip (Figure 2.8a,b):

$$V(t)=V_0(1+\cos(\omega_m t))\cos(\omega_{el}t) \qquad \text{(eq. 2. 9)}$$

Then if we consider the quadratic dependence of the electrostatic force with respect to voltage (only valid for high frequency case, see modeling chapters), and substitute eq. 2.9 into the eq. 2.2, we can calculate the 8 force harmonics of this case (Figure 2.8c,d). Five of those harmonics are located in the high frequency range (where the tip cannot oscillate), so they will not suppose any tip deflection. Nevertheless, three of them (DC, ω_m, and $2\omega_m$) are located in the low frequency range (where the tip is able to oscillate), so they will induce a deflection or oscillation to the tip. Of the 3 prefactors that accompany that 3 low frequency components, the higher one is the ω_m. The expressions for the low frequency components are now:

$$F_{el,DC,\,liquid}(t)=\frac{3V_0^2}{8}\frac{dC(z)}{dz} \qquad \text{(eq. 2.10)}$$

$$F_{el,\omega_m,liquid}(t)=\frac{V_0^2}{2}\frac{dC(z)}{dz}\cos(\omega_m t) \qquad \text{(eq. 2.11)}$$

$$F_{el,2\omega_m,liquid}(t)=\frac{V_0^2}{8}\frac{dC(z)}{dz}\cos(2\omega_m t) \qquad \text{(eq. 2.12)}$$

That is why we choose that one (ω_m) for EFM performance in liquid.

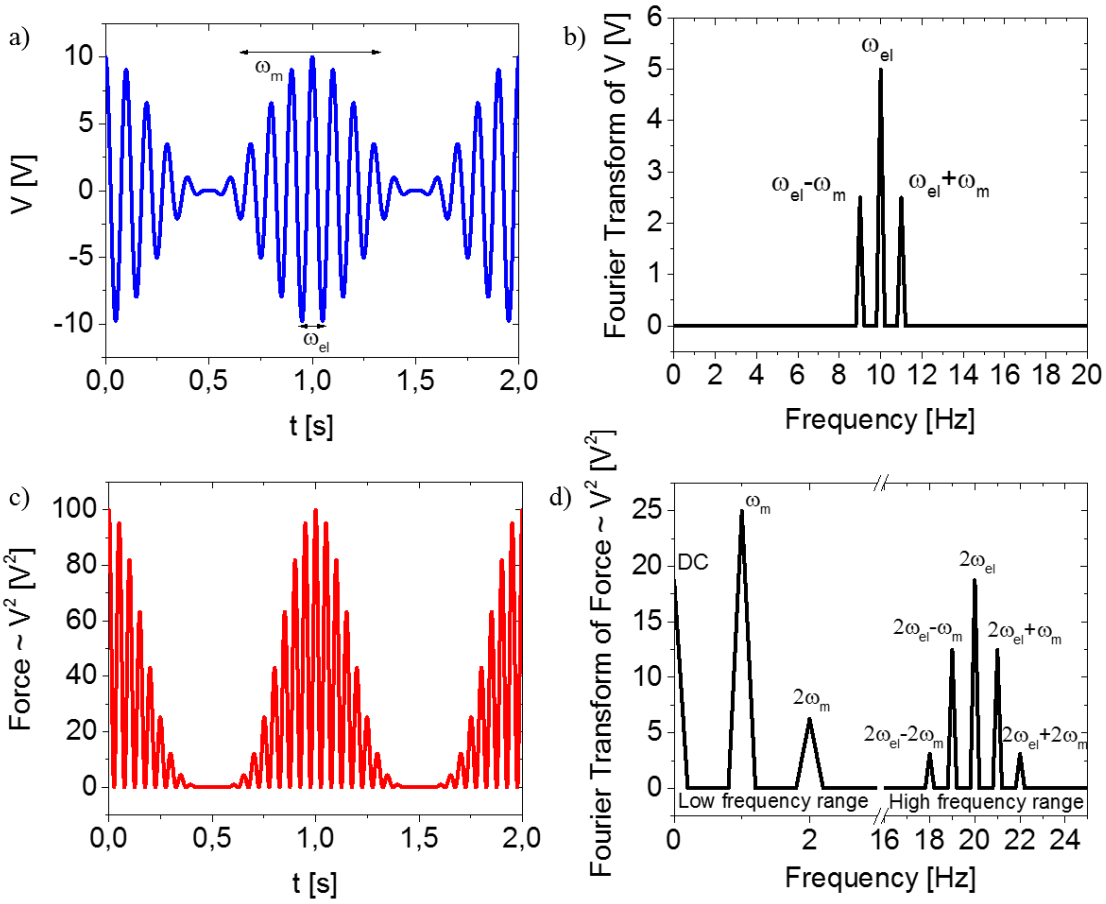

Figure 2.8:a) Time evolution of the voltage wave applied to the tip to perform EFM in liquid. b) Fourier transform of the voltage wave in a). c) Time evolution of the voltage squared (proportional to the force that the tip will suffer. d) Fourier transform of the voltage squared in c), where the different harmonics for the force will appear. For those plots, an unrealistic value of $\omega_m = 1$Hz and $\omega_{el} = 10$Hz is chosen in order to see better the waveform.

All that theoretically imposed changes necessary for EFM implementation under liquid conditions, turn into a different experimental setup (see Figure 2.9), where a function generator is used to send a high frequency voltage signal to the tip. Here the lock-in amplifier sends its output signal as the modulation input signal for the function generator, which sends the voltage wave of the eq. 2.9 to the tip. The vertical deflection of the cantilever is recorded and set as the input for the lock-in amplifier to be able to detect the different harmonics of the tip oscillation.

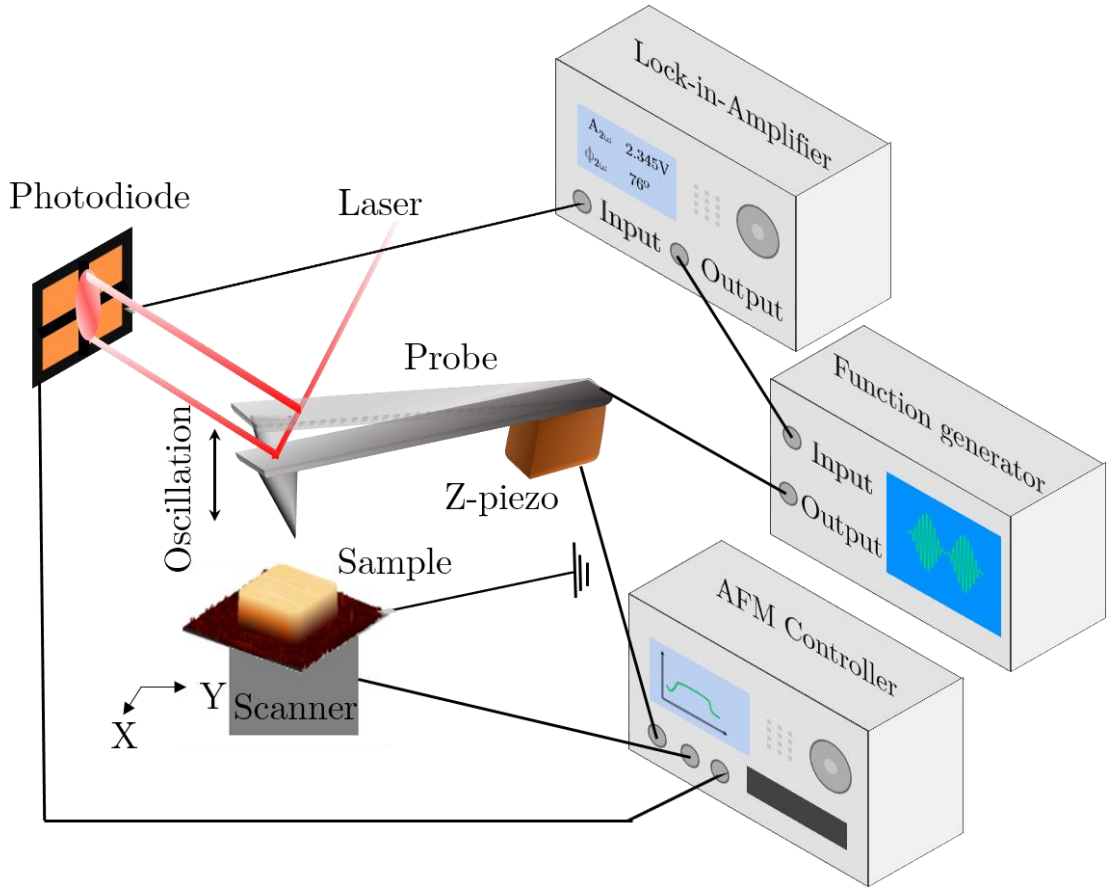

Figure 2.9: Scheme of EFM in liquid setup.

With respect to the full theoretical framework for EFM in liquid, a further explanation will be done in the following chapters, focusing specifically in the modeling, but until this work of thesis there was not a full theoretical model including all the forces acting on the tip. The existing theoretical analysis had been mostly based on quasi-electrostatic current models or equivalent circuit models, which generally neglect the contribution of the osmotic force[86,102,103].

Since the measurements of EFM in liquid are done at high frequencies where the EDL formation is avoided, regarding their quantification, the idea is to follow a similar procedure to the one used in dry conditions: first a tip geometry calibration, and second a dielectric constant determination, through fitting the experimental data to finite-element simulations for different parameters of the tip geometry and dielectric properties of the sample.

Nevertheless, the physics of the models used for the simulation, must suffer some modifications, as they must take into account the high dielectric constant of the solutions ($\varepsilon_r \sim 80$), and the possible capacitances generated by the molecules chemically absorbed onto the Helmholtz planes of the electrodes (the formation of those layers cannot be avoided by applying a high frequency field), which highly increase the complexity of the quantification, by adding new fitting parameters to the models.

2.6 Multidimensional SPM modes

Since the invention of the AFM[45], classically SPM images are 3D data sets (X, Y, A) where the tip is moved laterally in the fast (X) and slow (Y) scanning axis while recording a third (A) variable (Piezo displacement, Vertical Deflection, Amplitude of Oscillation…) that is plotted in a color scale generating an image (see Figure 2.10 Left). Nevertheless, since the invention of SPM techniques, also the so-called force-distance curves have been used to generate spatially resolved data sets that can be used to generate topographical images or to map another physical variable that is extracted by analyzing pixel by pixel each force-distance curve. These kind of imaging modes are normally referred to as Force Volume modes, where now the Z-axis is a third scan axis (faster), and 4D data sets (X, Y, Z, A) are generated (see Figure 2.10 Right). In this last way, maps of mechanical properties such as tip-sample adhesion or Young modulus[104] had been generated since a long time ago.

The main limitation of force volume-based measurements has always been the acquisition time. As a force-distance curve must be acquired in every single pixel of our image, very long times were normally needed to record the force-volume data sets. Longer timescales are not only a problem for the user in terms of time consumption, but also for the system itself, as drifting effects will be increased, or unwanted sample degradation can be found. This fact was normally solved by acquiring low-resolution images of $32 \cdot 32$ pixels instead of the classical $128 \cdot 128$ or $256 \cdot 256$ of SPM images.

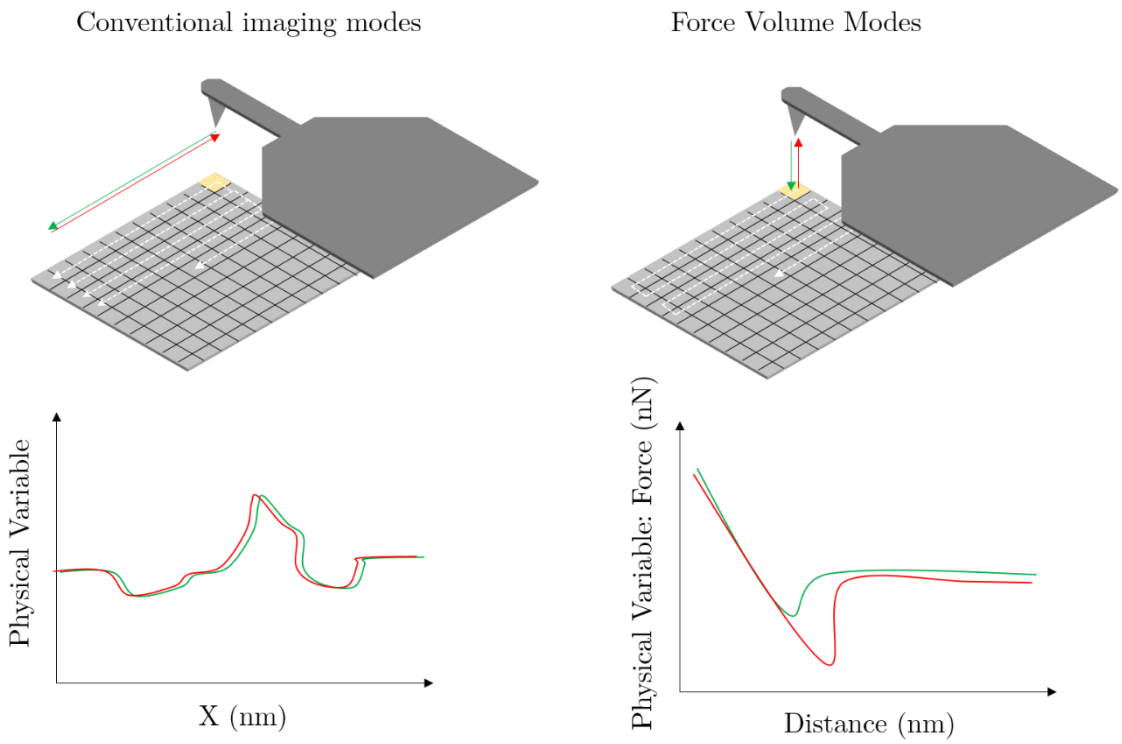

Figure 2.10: (Left) Scheme of conventional imaging modes in AFM. (Right) Scheme of Force Volume mode.

The main advantage of force volume-based measurements is the fact that now 2 variables (Z, A) are measured in each pixel, which allows scientists to extract physically relevant parameters at each pixel of the image by post-processing the 4D data sets generated. Depending on which is the physical magnitude of interest, different fitting models must be applied to the data acquired in each pixel. The two most common fitting models used are, the Hertz model to extract local Young Modulus of the sample in under study[105–107], and the adhesion maps, that are generated by looking for the maximum tip-sample adhesion force in the retraction curve[108].

Force-distance based modes have also been widely used for molecular recognition and chemical mapping, as the appearance of binding events between tip and sample in each force-distance acquired can be the parameter of fitting[109]. Also, the low lateral force applied to the sample has always appeared as an advantage for the use of such modes in weakly adhered samples, which makes force-distance based imaging modes more interesting for biological samples.

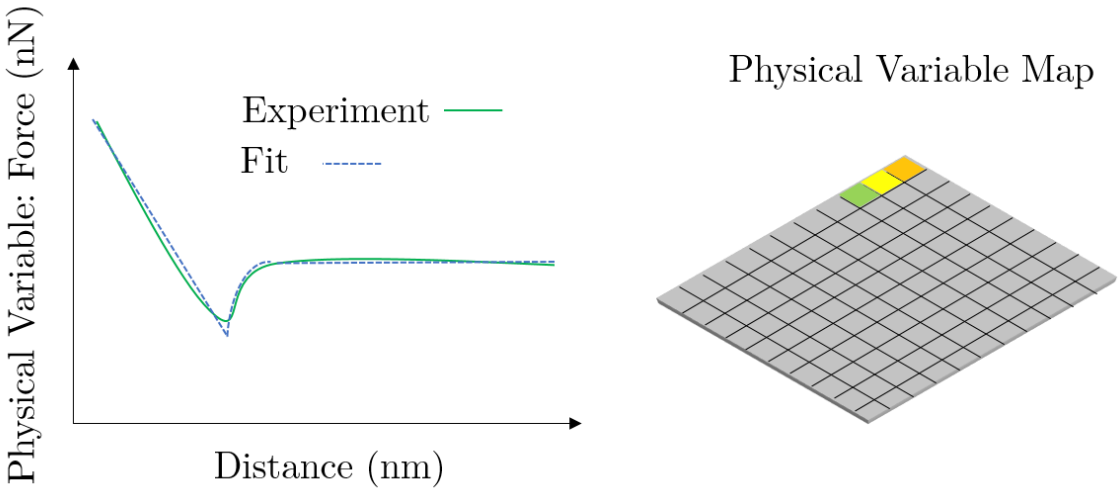

Figure 2.11: (Left) 2D data set collected in each pixel (X, Y) of the image. (Right) After post-processing and extracting the desired parameters from fitting a model to each pixel data, one can generate a map of the fitted physical variable.

In the last decade, improvements to solve the long acquisition time of force volume techniques have been made. The fast electronics of current commercial AFMs, together with the improvement in the piezoelectric materials used for the scanners, the closed-loop systems, and the low-drift equipment built, make the possibility to acquire fast force-distance curves, largely dropping the time required for of such techniques in a big way. Not only that, but also the present immense data storage capacity, the strong computing power, and the new deep data processing techniques make the data treatment and storage, not a limitation anymore[110]. Therefore, such techniques have suffered a boost, and new techniques based not only on force-distance curves but in multidimensional datasets have appeared. Nowadays, systems can not only record the measured variable (A) when sweeping the Z distance but also when sweeping whatever other variables of the system such as temperature, voltage, time, applied frequency etc. generating N-dimensional data sets ($X,Y,Z,A_1,A_2,...A_N$) that can map (even simultaneously[111]) different physicochemical properties. Most AFM companies have developed even new modes of their systems that, in an automatic way, allow the user to collect all these data sets. PeakForce mode of Bruker systems or QI Advanced Mode of JPK (now together) are some examples of this. These new imaging modes are not only

making SPM techniques easier to use or less time consuming but mainly allow scientists to characterize physical, chemical, and biological structures that remained uncharacterized.

High resolution mechanical maps[112], physicochemical native protein characterization[113], defect detection in crystalline structures[114], characterization of the hydration layers in the solid-liquid interfaces[115–123], surface charge in DNA[124], living cells imaged at different setpoints[125], or conductivity maps[126], are only some of the examples of physical problems where the development of such multidimensional modes has been crucial.

Nevertheless, it has not been yet implemented on force-based dielectric characterization modes like scanning dielectric microscopy.

Motivation and objective of this thesis

As it has been shown during the two introductory chapters, EFM constitutes a very good tool to characterize the electrical properties of samples locally with nanoscale spatial resolution. Not only that, but the ability of EFM to work in liquid conditions makes it suitable for dealing with biological samples in physiological conditions. To achieve it, non-trivial computational quantification methods to extract relevant electrical parameters of the specimen under study have been developed. The combination of EFM measurements with computational models for their quantification is known as Scanning Dielectric Microscopy (SDM). Nevertheless, there are still some developments needed to apply these methods to single-cell systems both from the experimental and the modeling side.

From the experimental part, a big issue in EFM measurements on cells is that a lot of *a-priori* considerations must be taken into account before doing the experiment: how tall is my sample? Which lift height should I take my images at? Which is the best imaging mode (lift mode or constant height) for my sample? How fragile is my sample? Which scanning mode (tapping mode, constant mode, etc.) should I use? With the existing methods, no *a-priori* answers are most often available.

From the modeling part, a big issue is how to take into account the topographical features of cells (which strongly affect the quantification process[99]). This process is not automated, costly (as it needs the work of a specific person in the design and reconstruction of a specific sample's geometry), and uses non-fully realistic geometries for the quantification. Also, the different forces that act on a voltage biased tip in liquid are not fully understood as their nature comes from different time and length scales ranging from hundreds of nanoseconds to seconds or from few nanometers to few micrometers.

These issues are the main responsible for the low statistical significance of the studies regarding dielectric constant quantification at the nanoscale with SDM on cells and for the lack of applications of such techniques to physiological conditions.

Thus, the main goal of this work of thesis is to develop theoretically and experimentally an Scanning Force Microscopy technique (based in the multidimensional SPM approach explained previously) able to perform EFM measurements of "whatever" samples (irrespectively of their topography, mechanical properties, and environment they are in), focusing particularly on cells, which are topographically complex, structurally interesting and show heterogeneous dielectric properties.

Not only that, but as EFM is capable of measuring the electric properties surrounding the sample under study, our aim is to open new avenues in the nanoscale electrical characterization field, ranging from dielectric constant mapping to exploring alternatives to microelectrode technology in the electrophysiology field.

3. Modeling the forces in 1D AC voltage biased plates in electrolyte solutions

This chapter describes the forces acting on voltage biased plates in electrolyte solutions in a 1D geometry. It is mainly based in the article: "Frequency-dependent force between ac voltage biased plates in electrolyte solutions"[127]*. In the article, M. Checa did the simulations, R. Millan-Solsona helped to analyze the data, G. Gomila developed the analytical model, wrote the manuscript, and supervised the work.*

3.1 Introduction

The forces acting on a voltage biased electrode in an electrolyte solution are of great interest for various scientific fields, such as colloidal science[101], microelectrochemical systems[128–130], or some of the novel SPM electrical characterization modes available in liquid environments[85,86,90,92,103,131–135] that we use. Those forces have been widely studied under the Poisson-Boltzmann theory, mainly when the applied voltage is constant (DC voltage). Nevertheless, the study of such forces under AC fields is still not fully understood, especially considering the different possible contributions to the total force and its dependence in all the different parameters of such systems (frequency, voltage, ionic concentration, geometry…). The complex nature of such phenomena (diffusion of ions, dynamics of formation of space charge layers, electrical conduction, etc.) makes them challenging systems to model and the existing theoretical analysis found in the literature are normally based on quasi-electrostatic current models or equivalent circuit models, that in general only count for the pure electric contribution to the force and do not include the osmotic one[86,92,128].

We wanted to establish a comprehensive theoretical analysis of all the forces acting in voltage biased electrodes in electrolyte solutions. To do so, we worked in the framework of the

Nernst-Planck-Poisson (NPP) transport model, solved its full non-linear time-dependent equations for a 1D model system by means of finite-size numerical calculations and calculated the force acting on the plates and its dependencies. Also, a 1D analytical solution was calculated for the linear regime, and its results were in good agreement with the simulated ones. Nevertheless, as the development of the analytical solution was done by other members of the research group, it is not shown itself in this work of thesis (it can be checked in[127]).

3.2 Model system

We consider the case of a 1D system of total length 2L containing a symmetric 1:1 electrolyte with blocking electrodes and without the presence of compact (Stern) layers (for the full analysis with compact layers see[127]). We do not assume the presence of any electrolyte reservoir in contact with the system under study, as it is usually done in the context of Poisson-Boltzmann treatments[101]. This means that the number of ions in between the plates will be assumed to remain constant. For DC voltages, this assumption is justified in situations in which the electrolyte is really enclosed by the plates, or a small amount of solution is in between them as it is the case in some electrical actuation approaches in microelectromechanical systems or some "in-liquid" electric SPM modes. For AC voltages, this assumption can be rather general due to the lack of effectiveness of the electrolyte reservoir as the frequency of the applied voltage increases.

The model consists of the continuity equations for the ion number densities $n_{\mp}(x,t)$, coupled to the Poisson equation for the electric potential $\psi(x,t)$:

$$\frac{\partial n_{\mp}}{\partial t}+\frac{\partial J_{\mp}}{\partial x}=0 \qquad \text{(eq. 3.1)}$$

$$-\varepsilon_0\varepsilon_r\frac{\partial^2\psi}{\partial x^2}=e(n_+-n_-) \qquad \text{(eq. 3.2)}$$

where ε_0 is the vacuum permittivity, ε_r the relative dielectric constant of the electrolyte (assumed to be frequency and electric field independent), $J_{\mp}$ are the ion number flux densities, which in the dilute concentration limit, can be expressed as:

$$J_{\mp}=-D\frac{\partial n_{\mp}}{\partial x}+\mu n_{\mp}\frac{\partial \psi}{\partial x} \qquad \text{(eq. 3.3)}$$

where D is the ion diffusion coefficient, μ the ion mobility (assumed to be the same for both ionic species and independent from concentration as we are in the dilute concentration limit). The diffusion coefficient and mobility are assumed to be related by Einstein's relation for dilute electrolytes $D=\frac{k_B T \mu}{e}$, with k_B as the Boltzmann's constant, T the temperature and e the elementary charge. The plates are situated at the coordinates ±L and are assumed to show blocking properties (no ion or charge exchange with the electrolyte). They are described by means of no-flux boundary conditions:

$$J_{\mp}(\mp L,t)=0 \qquad \text{(eq. 3.4)}$$

The voltage of the plates is fixed externally and so gives:

$$\psi(\mp L,t)=\mp V(t) \qquad \text{(eq. 3.5)}$$

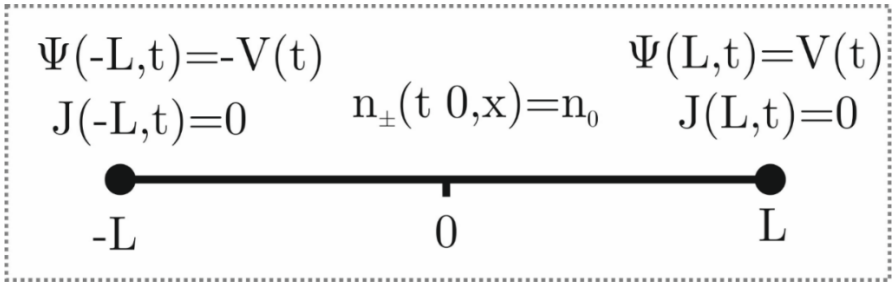

Figure 3.1: Sketch of the boundary conditions for the 1D model system.

In the present case, we will take the general form $V(t)=V_{DC}+V_{AC}\cos(\omega t)$. The initial condition for the ionic concentration before the application of the potential corresponds to a uniform ionic density distribution:

$$n_{\mp}(t\leq 0,x)=n_0 \qquad \text{(eq.3.6)}$$

A sketch of the boundary conditions is found in Figure 3.1. The continuity equation (eq. 3.1), together with the blocking boundary condition (eq. 3.4), impose that the total number of ions of each type remains constant in the system.

From the electric potential distribution, ψ, and the ion number density distributions, $n_{\pm}$, obtained by solving the NPP model, the force acting on the plates can be calculated as[101]:

$$F(t)=F_{el}(t)-F_{os}(t) \qquad \text{(eq. 3.7)}$$

where

$$F_{el}(t)=\frac{\varepsilon_0 \varepsilon_r}{2}\left(\frac{\partial \psi(L,t)}{\partial x}\right)^2 \qquad \text{(eq 3.8)}$$

is the electric force component, which corresponds to the Maxwell stress tensor projected onto the normal of the plate electrode, and

$$F_{os}(t)=\pi(L,t)-\pi_0 \qquad \text{(eq. 3.9)}$$

is the osmotic force component, which is the projection onto the normal of the plate of the difference between the equilibrium and the non-equilibrium Van't Hoff pressure, $\pi=k_B T(n_+ + n_-)$, where $\pi_0=2k_B T n_0$.

Finally, it is also interesting to define the Debye screening length, L_D

$$L_D=\sqrt{\frac{2n_0 e^2}{k_B T \varepsilon_0 \varepsilon_r}} \qquad \text{(eq. 3.10)}$$

which gives us an effective screening length that the electrostatic interaction covers in such systems (strongly dependent on the ionic concentration and independent of the applied voltage).

Unless it is otherwise specified, the parameters used to solve the NPP system are: a total length $2L=100$nm, an ion concentration $n_0=1$mM, and an applied DC and AC voltages $V_{DC}=5$mV and $V_{AC}=10$mV respectively. The remaining set of independent parameters are the ion diffusion, $D=10^{-9}$ m^2/s, and temperature, $T=298$ K. For these parameters, the thermal voltage is $V_T=k_B T/e=26$ mV, the ion mobility $\mu=D/V_T=3.9\ 10^{-8}$ m^2/V $\cdot$ s, the electrolyte conductivity $\sigma=2e\mu n_0=7.4\ 10^{-3}$ S/m and the Debye screening length $L_D=9.6$ nm. The full nonlinear time-dependent NPP system of equations and its boundary conditions

presented above are carried out with the corresponding built-in model in COMSOL MULTYPHISICS 5.3a.

3.3 Electric potential and charge density

The spatial and frequency dependence of the electric potential and charge density are calculated and shown in Figure 3.2. Both analytical and simulated data are in perfect agreement.

For $L>L_D$, the DC voltage and charge density profiles show the presence of DC space charge diffusive layers at the plate surfaces, which decay exponentially with distance, with a characteristic length L_D (Insets in Figure 3.2 a and b). For $L<L_D$, the space charges fully overlap, the DC potential decays linearly, and the electric charge increases linearly (data not shown). These results coincide with those obtained from the resolution of the Poisson-Boltzmann theory for plates at constant voltages, in the presence of an electrolyte reservoir[101]. This coincidence is peculiar to the 1D geometry and does not occur in general.

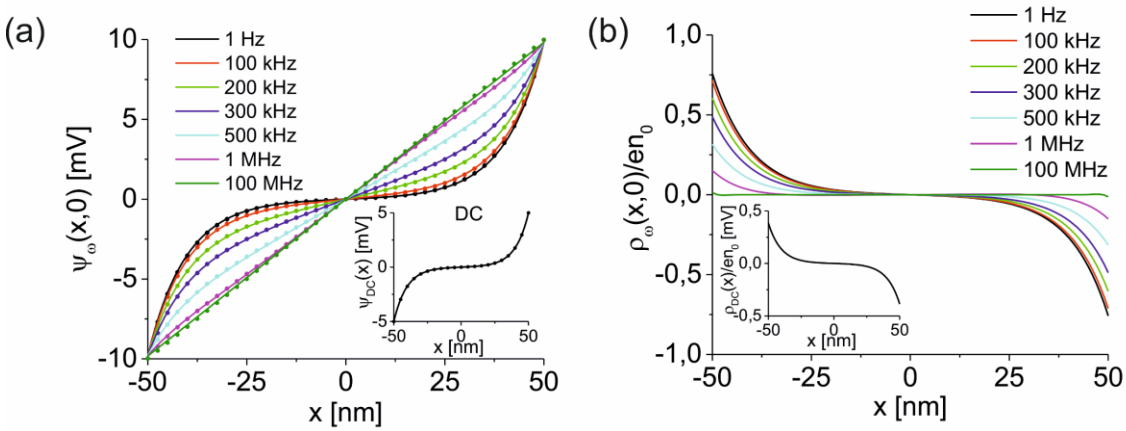

Figure 3.2: AC component of the (a) electric potential and (b) charge density distribution predicted by the analytical solution as a function of space for a fixed time multiple of the period of the applied ac voltage and for different frequencies. The distribution is shown for 1 Hz, and it is indistinguishable from the DC voltage distribution for an applied voltage $V_{DC}=V_{AC}$. Insets in (a) and (b): DC components of the electric potential and normalized electric charge as a function of space predicted by the analytical solution. The symbols refer to the numerical results obtained from the resolution of the full non-linear Nernst-Planck-Poisson model. Parameters: $V_{DC}=5$ mV, $V_{AC}=10$ mV, $2L=100$ nm, $n_0=1$ mM, $D=10^{-9}$ m^2/s, $T=298$ K. Derived parameters: $V_T=k_BT/e=26$ mV, $\mu=D/V_T=3.9\ 10^{-8}$ m^2/V$\cdot$s, $\sigma=2e\mu n_0=7.4\ 10^{-3}$ S/m, $L_D=9.6$ nm.

On the other side, the AC voltage and AC charge profiles evolve continuously from "DC-like" profiles at low frequencies, up to linear voltage, and zero charge density profiles at very high frequencies (Figure 3.2). This behavior is the equivalent in the frequency domain to the behavior described in the time domain for the transient response to a DC voltage step[136].

The characteristic frequencies that determine the evolution of the AC voltage and charge density can be identified by analyzing the system impedance or its analytical expression. In Figure 3.3, both modulus (black) and phase (red) are shown. The impedance (for $L>L_D$) shows three different frequency regimes:

$$|Z(f)|\approx\begin{cases}\dfrac{2}{2\pi f C_{dl}} & f<f_{RC_{dl}}\\ R_{sol} & f_{RC_{dl}}<f<f_{RC}\\ \dfrac{1}{2\pi f C_{sol}} & f_{RC}<f\end{cases} \qquad \text{(eq. 3. 11)}$$

Here, C_{dl} is the double-layer capacitance, and R_{sol} and C_{sol} are the electrolyte resistance and capacitance, respectively defined as:

$$C_{dl}=\frac{\varepsilon_0\varepsilon_r}{L_D}; \qquad R_{sol}=\frac{2L}{\sigma}; \qquad C_{sol}=\frac{\varepsilon_0\varepsilon_r}{2L} \qquad \text{(eq. 3. 12)}$$

The factor 2 appearing in the double layer capacitance term of the impedance comes from the fact that there are two double layers in series so that its equivalent capacitance is half the double layer of one of the plates. Instead, the factor 2 in the definitions of R_{sol} and C_{sol} comes from the fact that the total length of the system is 2L. According to this description, the equivalent circuit for the system consists of two double-layer capacitances in series with the parallel combination of the electrolyte resistance and capacitance (Inset in Figure 3.3). The two characteristic crossover frequencies are given by the inverse of the charging times of the double layer capacitance ($f_{RC_{dl}}$), and of the whole electrolyte capacitance (f_{RC}):

$$f_{RC_{dl}}=\left(\frac{2\pi R_{sol}C_{dl}}{2}\right)^{-1}=f_{RC}\left(\frac{L_D}{L}\right)$$
$$f_{RC}=(2\pi R_{sol}C_{sol})^{-1}=\frac{\sigma}{2\pi\varepsilon_0\varepsilon_r} \qquad \text{(eq. 3. 13)}$$

For the data used in Figure 3.2, one obtains $f_{RC_{dl}}$=330kHz and f_{RC}=1.7MHz.

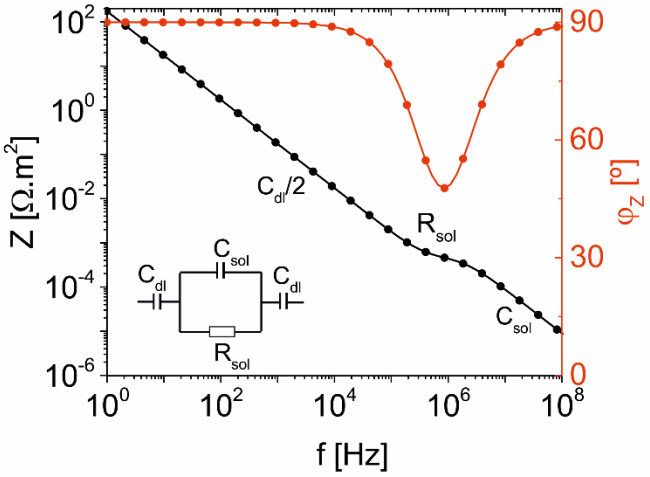

Figure 3.3: Modulus (black line, left axis) and phase (red line, right axis) of the impedance of the two-plate system predicted by the analytical solution. Inset: the equivalent circuit for the system. The symbols refer to the numerical results obtained from the resolution of the full non-linear Nernst-Planck-Poisson model. Parameters: V_{DC}=5 mV, V_{AC}=10 mV, 2L=100 nm, n_0=1 mM, D=10^{-9} m^2/s, T=298 K. Derived parameters: $V_T=k_BT/e$=26 mV, $\mu=D/V_T$=3.9 10^{-8} $m^2/V\cdot s$, $\sigma=2e\mu n_0$=7.4 10^{-3} S/m, L_D=9.6 nm.

According to this description, in the low frequency range ($f < f_{RC_{dl}}$), the system shows a capacitive behavior, with an equivalent capacitance $\frac{C_{dl}}{2}$. In this frequency regime the AC voltage and charge density show a quasi-static "DC-like" voltage and charge density distributions, with the presence of AC space charge layers at the plate surfaces that fully screen the applied AC voltage with a nearly null AC electric field and charge density outside the double layers (see Figure 3.2).

At the intermediate frequencies ($f_{RC_{dl}} < f < f_{RC}$), the system shows a resistive behavior, with equivalent resistance R_{sol}. The AC voltage and charge density profiles show partially developed AC space charge layers that do not fully screen the applied voltage. Hence, a non-null AC electric field appears outside the AC space charge layers (see Figure 3.2), which induces an AC resistive current.

Finally, at high frequencies $f > f_{RC}$, the system shows a capacitive behavior again, but this time determined by the electrolyte capacitance C_{sol}. No AC space charge layers are formed in this frequency range (see Figure 3.2); thus, the AC electric field is constant between the plates and the AC charge density null everywhere. Note that in the steady-state, neither the voltage and charge distributions nor the system impedance depends on the inverse diffusion time.

3.4 Forces

Once the electric potential and the charge density are calculated in all the space and for all the different cases of study, we are ready to calculate the forces acting on the plates. As mentioned before, the force acting on the plates has two different contributions, namely the electrostatic force, and the osmotic force.

The first one comes from the fact that where there is an electric field different from zero, the electrically charged surfaces will feel a force. The second one arises from the concentration gradient present in the system, which acts as a driving force for the solution that tries to homogenize the concentration everywhere. They will normally have opposite signs as the homogenization will try to compensate for the accumulated charge instead of being favorable to it.

The fact that the excitation of our system is a cosine function of angular frequency ω, and the two different components of the force are not linear with the voltage, induces the appearance of higher harmonic terms. The way we will proceed is to calculate the full temporal dependence of the different components (see Figure 3.4a), as expressed in eq. 3.14 and 3.15, and then Fourier transform the response to get the different harmonic responses (see Figure 3.4b):

$$F_{el}(t)=F_{el,DC}+F_{el,0\omega}+F_{el,\omega}(t)+F_{el,2\omega}(t) \qquad \text{(eq. 3. 14)}$$

$$F_{os}(t)=F_{os,DC}+F_{os,0\omega}+F_{os,\omega}(t)+F_{os,2\omega}(t) \qquad \text{(eq.3. 15)}$$

The total force acting on the plates is the sum (with the correct signs) of the electric and osmotic forces:

$$F(t)=F_{DC}+F_{0\omega}+F_{\omega}(t)+F_{2\omega}(t) \qquad \text{(eq.3. 16)}$$

With:

$F_{DC}=F_{el,DC}-F_{os,DC}$; (eq. 3. 17) $F_{0\omega}=F_{el,0\omega}-F_{os,0\omega}$; (eq. 3. 18)

$F_{\omega}(t)=F_{el,\omega}(t)-F_{os,\omega}(t)$; (eq. 3. 19) $F_{2\omega}(t)=F_{el,2\omega}(t)-F_{os,2\omega}(t)$ (eq. 3. 20)

In the harmonic separation, we differentiate from the DC and the 0ω terms (both static), as the first one is the one arising from the DC term of the voltage excitation (V_{DC}), and the second one is the static contribution of the AC term of the voltage excitation (V_{AC}).

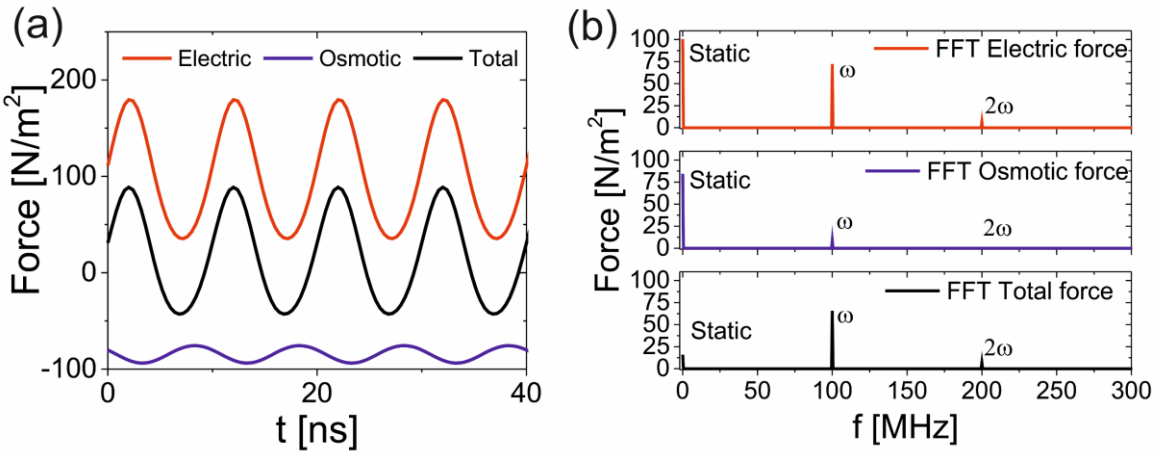

Figure 3.4: (a) Example of the temporal evolution of the total (black line), electric (red line) and osmotic (blue line) forces as a function of time for an applied voltage frequency of 100MHz. The positive sign indicates attraction forces, while the negative sign indicates repulsive forces. (b) Fourier transform of the total (black line), the electric (red line) and the osmotic (blue line) forces, and appearance of the different harmonic peaks in the frequency range. The value of the peak in the Fourier transform is the amplitude of that harmonic.

The dependences of all the DC forces on the plate separation are shown in Figure 3.5a. The dependences of the 0ω, ω, and 2ω force harmonics on frequency are shown in Figure 3.5b-f. The parameters used in the calculations are those used in the previous figures of this chapter. For the AC components (ω and 2ω), we plot both the moduli and the phases. In all graphs, we plot the electric (red), osmotic (blue), and total (black) force contributions separately.

The symbols represent the results of the numerical calculations, which show a perfect match with the analytical solution derived and valid in the linear regime[127].

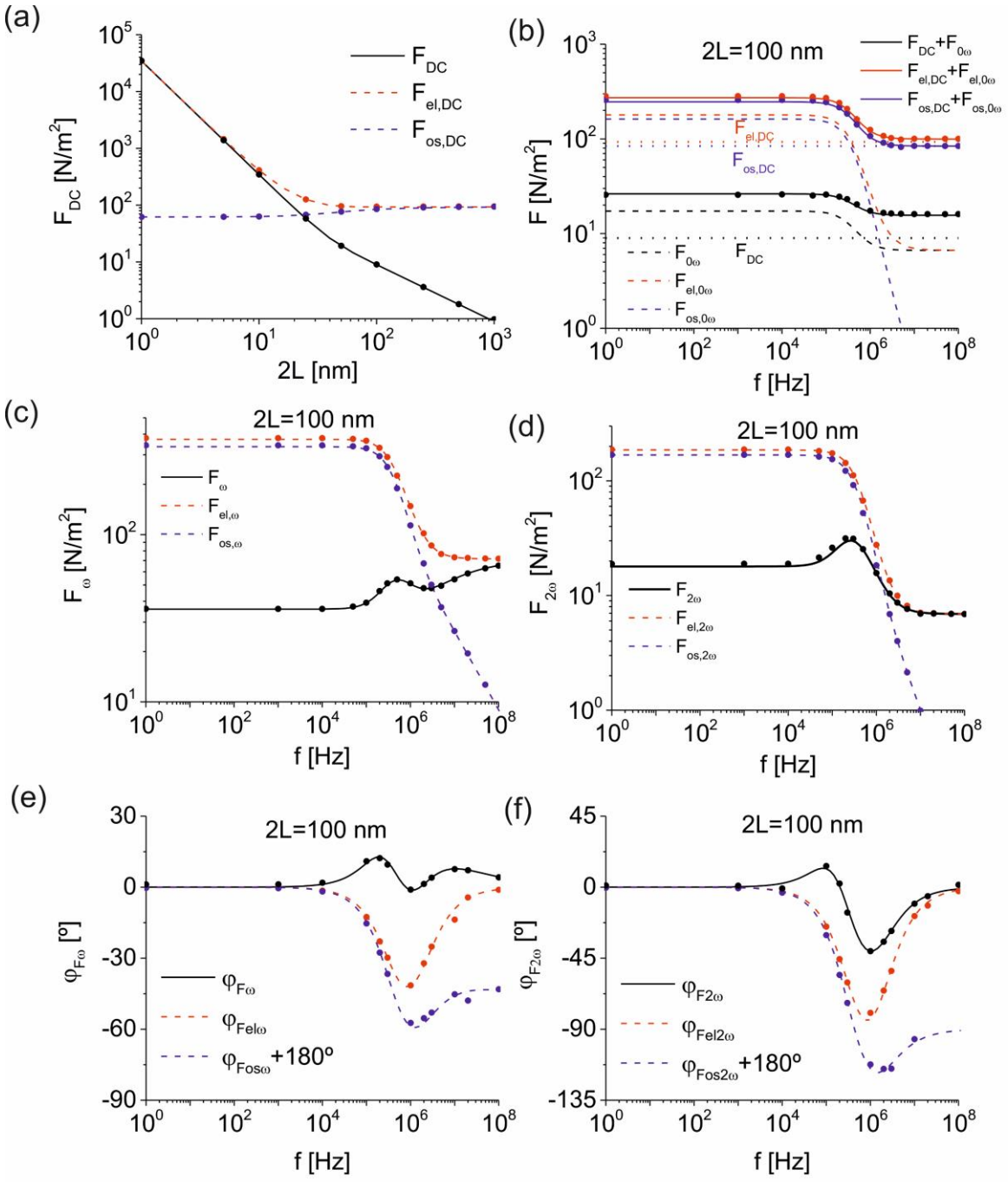

Figure 3.5: (a) Total (continuous black line), electric (red dashed line) and osmotic (blue dashed line) DC forces predicted by the analytical solution as a function of the separation between plates. Symbols represent the results of the numerical calculation of the full non-linear NPP model. (b) Total static force, which includes the DC contribution (dotted lines) and the 0ω contribution (dashed lines) of the forces as a function of frequency for a plate separation $2L$=100 nm. (c) and (d) Idem for the moduli of the ω and 2ω harmonics of the forces, respectively.

(e) and (f) Idem for the phase of the ω and 2ω harmonics forces (a few numerically calculated points for the osmotic phase at the highest frequency are not included due to a lack of numerical accuracy). Note that the osmotic phase is shifted by 180º for easier comparison with the electric phase.

In general, we observe that the osmotic force contribution vanishes in the high frequency range (above the dielectric relaxation time, where the charge density tends to be null everywhere), and that is the only range where the electrostatic interaction itself, matches with the total net force felt by the plate. Below that time, generally, both forces play an important role in the total force.

Regarding the DC force component (Figure 3.5a), two distinct regimes are observed with a characteristic cross-over length at around $2L \sim 4L_D$ appear. On the one hand, at very large separations, the total DC force tends to zero. This is a consequence of the perfect balance between the electrostatic and osmotic DC forces at very large plate separations. The DC force decays towards zero as $\sim L_D/L$, and not exponentially as predicted for plates at a constant voltage in systems in contact with electrolyte reservoir[137]. Therefore, the range of interaction is here much longer (tens of times L_D). On the other hand, at short separations ($L<L_D$), the electric force dominates over the osmotic force, as the electric field is not fully screened at any region in between the plates.

The 0ω term (Figure 3.5b) shows a monotonic behavior with a transition found at the intermediate frequencies, which goes from the low to the high frequency asymptotic values. At high frequencies, the electric force dominates (as we will see, this behavior is always found, as charge density tends to null as frequency increases, so osmotic force vanishes). At low frequencies, both electric and osmotic forces are very large due to the presence of the space charge layers, but the resulting net force is relatively small (orders of magnitude smaller sometimes), as they cancel each other similar to what happens in the DC component. We note that only in the high frequency range, we recover the expression valid for the air case, where the total force can be expressed in terms of the derivative of the electrolyte capacitance, as predicted by equivalent circuit theories in the absence of ionic diffusive effects[138]: $F_{0\omega} \approx \frac{1}{4}\frac{dC_{sol}}{dL}V_{AC}^2$. This fact is crucial for our work, as it allows us to measure the

derivative of the capacitance of the system, which is the physical magnitude needed to perform Electrostatic Force Microscopy in electrolyte solution experiments and quantify them.

The ω term (Figure 3.5c), on its side, shows a non-monotonic behavior when passing from the low to the high frequency regimes. At low frequencies, both electric and osmotic force are very large, but is cancellation again makes the total force orders of magnitude smaller. The characteristic frequency limit for the low frequency regime is the inverse of the diffusion time: $f_D=\left(\frac{2\pi L^2}{D}\right)^{-1}$, which are usually much longer than the electric relaxation times, therefore the corresponding frequencies are much smaller. For the data used in Figure 3.5c, the diffusion frequency is f_D=64 kHz. In the intermediate frequencies, we find a broad peak. That peak is the consequence of the interplay of electric and osmotic forces. Its different decay function with frequency induces the appearance of such a peak. The peak is centered at the frequency corresponding to the inverse of the charging time of the Debye layer (f_{RCdl}), which for our parameters is 330kHz. Finally, we note that the asymptotic value of the high frequency range is found at much higher frequencies (in the GHz range), than for the 0ω and 2ω terms. The osmotic force decay is slower than in the other terms, as the ω term is crossed with the static components making diffusion play a more important role. This fact has important implications as it makes the ω term impossible to express in terms of the derivative of the capacitance as it happened with the 0ω harmonic. This fact might indicate that further efforts have to be made for the implementation of open-loop Kelvin probe force microscopy approaches in electrolyte solutions[132,133,139].

Last, the 2ω force component (Figure 3.5d) shows also a non-monotonic behavior in its pass from the low to the high frequency asymptotic regimes. As for the ω term, in the low frequency case, the net force is the result of the unbalance between the quasi-static values of the electric and osmotic forces, giving a value that is much smaller than any of the individual forces. The characteristic frequency limit for the low frequency regime is again

the inverse of the diffusion time: $f_D=\left(\frac{2\pi L^2}{D}\right)^{-1} = 64\text{KHz}.$ In the intermediate frequency range, again a broad peak is found (centered around $f_{RC_{dl}}$), where both electric and osmotic force play a role. In this case, the decaying of the peak is faster than in the ω case. As a result, the high frequency crossover for the 2ω (where only the electric contribution matters) is attained at frequencies around f_{RC}, and we can recover an expression in terms of the capacitance gradient. The behavior of the phases for the ω and 2ω components is shown in Figure 3.5e and Figure 3.5f, respectively. The characteristic frequency ranges are approximately the same ones as those discussed above for the moduli.

3.5 Non-linearities

The voltages used until now to study the frequency and distance dependence of the force are in the linear regime (below the thermal voltage V_T). We did that, firstly, because the analytical model derived in[127] is only valid in such case, secondly for simplicity in the numerical simulations, and thirdly because for high voltages applied other physical interactions need to be accounted in the modeling (like the finite size of the ionic species).

Next, we show (Figure 3.6) the results of the simulations for higher voltages (between 3- and 6-times V_T).

We note that the results obtained with the analytical model, describe to a good approximation, the numerically calculated ones and that by entering the non-linear regime, higher-order force harmonics can appear (e.g., 3ω and 4ω harmonics of Figure 3.6c and d). The study of the physical meaning of such higher-order terms goes beyond the interest of this work.

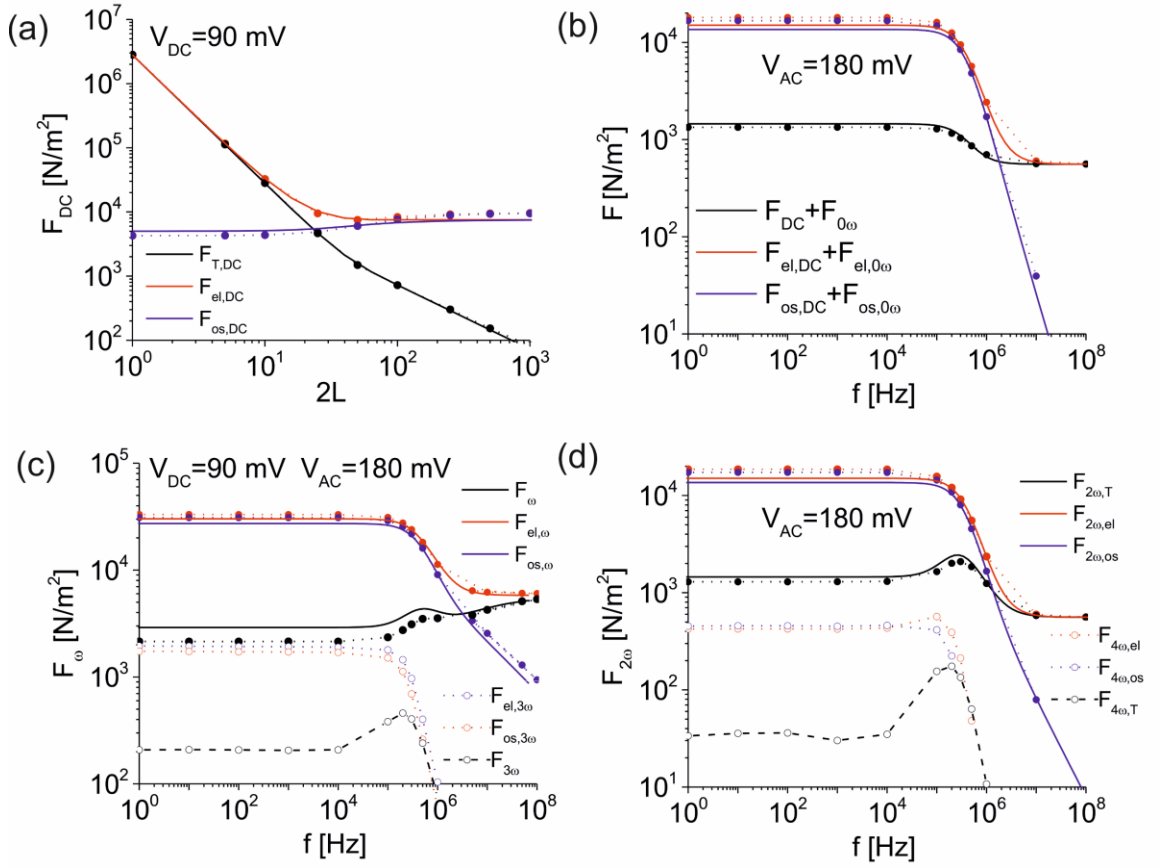

Figure 3.6: (a) Total (continuous black line), electric (continuous red line), and osmotic (continuous blue line) DC forces predicted by the analytical solution as a function of the length of the system for a voltage in the non-linear regime eV_{DC}/k_BT~3. Symbols represent in all figures the results of the numerical calculation of the full non-linear NPP model (dotted lines are guides to the eyes). (b) Total static force, which includes the DC and the 0ω contribution of the forces as a function of frequency for a sample length L=100 nm and applied potentials in the non-linear regime eV_{DC}/k_BT~3 and eV_{AC}/k_BT~6. (c) and (d) Idem for the ω and 2ω components of the amplitude of the forces, respectively. In (c) and (d), the empty symbols represent the amplitude of the 3ω and 4ω force harmonics, respectively.

3.6 Conclusions

We have presented a comprehensive theoretical analysis of the frequency and distance dependence of the electric, osmotic and total forces acting on a voltage biased plates in electrolyte solutions in the framework of the Nernst-Planck-Poisson (NPP) transport model for the case of blocking electrodes. The dependence of the different force harmonics (DC, 0ω, ω, and 2ω) on plate separation, frequency, and ion concentration has been analyzed. We have shown that, in general, the osmotic force contribution cannot be neglected in front of the electric force contribution, thus rendering the total force usually well apart from either

the two forces separately. Only for very high frequencies, above the dielectric relaxation time, or for short plate separations, the osmotic force contribution can be neglected.

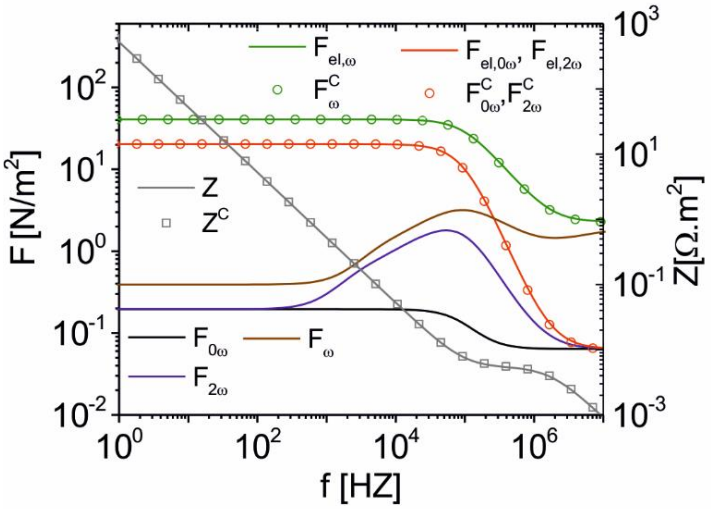

Figure 3.7: (Right axis) Modulus of the impedance predicted by the analytical solution of the NPP model (gray line) and by the pure electrostatic model (gray squares). (Left axis) 0ω, ω and 2ω amplitudes of the electric force (red and green lines) predicted by the NPP model, and of the electric force predicted by the pure electrostatic model (red and green circles). For comparison, we also show the 0ω, ω, and 2ω amplitudes of the total force (black, brown, and blue lines, respectively).

In Figure 3.7, we show that the different harmonics of total force (lines) calculated in the NPP framework (considering the osmotic contribution), only match with the equivalent pure electrostatic model (circles) that contains only the electrostatic interaction, in the very high frequency range. That happens because it is only in this range, when the density charge distribution is very close to being homogeneous, that the osmotic force vanishes. In this case, the electrostatic model has been parameterized by fitting the impedance of the system to be the same as the one in the NPP model.

We have also shown that higher harmonic terms can appear when we enter in the non-linear regime. The results reported in this chapter can be of interest for a better understanding of electrically actuated plates in microelectromechanical systems operating in electrolyte solutions and (most importantly for this work of thesis) it allows us to have a theoretical framework to study the electric scanning force microscopy techniques working in electrolyte solutions (see next chapter).

4. Modeling 3D Electrostatic Force Microscopy in electrolyte solutions

This chapter is the extension of the description of the forces acting on voltage biased electrodes to the realistic 3D geometry of an EFM experimental setup. It is based on the article in preparation: "Modeling Electrostatic Force Microscopy in electrolyte solutions." In the article, M.Checa did the modeling, and G.Gomila supervised the work.

4.1 Introduction

Why are there hundreds of studies regarding electrostatic force microscopy in dry/air conditions, but only a few of them regarding electrostatic force microscopy in liquid environment? The answer is simple, electrostatic force microscopy is a complex technique, but its operation is well known both experimentally and theoretically when operated in dry conditions and has been widely used to characterize nanoscale electric properties of samples of interest. Nevertheless, the difficulty of performing meaningful measurements in electrolyte solutions is strongly increased, and there is not a clear full theoretical understanding of it, which is needed to extract qualitative and quantitative information.

During this chapter, we will extend the theoretical modeling developed for 1D geometries in chapter 3 to 3D realistic geometries, and the implications for EFM in liquid media will be discussed. To show in a practical way the importance of achieveing a correct modeling for the EFM in liquid measurements, we have Figure 4.1.

In Figure 4.1a, we show the topography of a silicon oxide pillar on top of highly doped silicon acquired by myself. In Figure 4.1b, we show the EFM constant height image in dry conditions, where a clear dielectric contrast is found on top of the oxide film. Next to it in Figure 4.1c, we can see that if conventional EFM is operated in liquid conditions, it doesn't show any dielectric contrast. Moreover, in Figure 4.1d, we see that under the application of a high frequency electric field, and with the help of some experimental tricks (see the explanation of EFM in liquid in the introduction section), the dielectric contrast can also be recovered in electrolyte solutions but with an inverted sign and higher lateral size effect (see color gradient inside the oxide film). Thus, a clear understanding of such complex behaviour found experimentally is needed for the theoretical point of view.

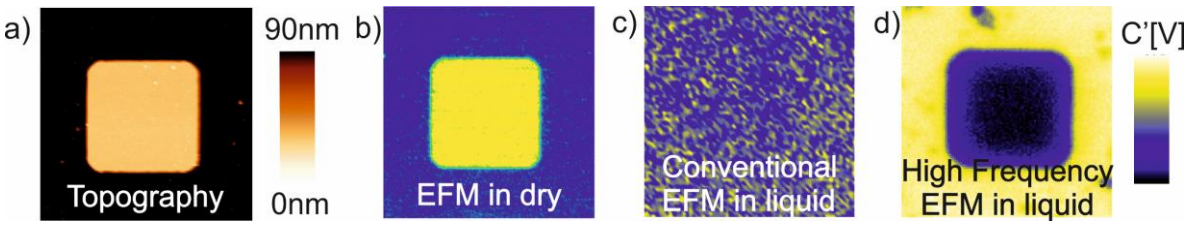

Figure 4.1: a) Topography of a silicon oxide pillar. b) Constant height EFM image in dry conditions. c) Constant height EFM image in an electrolyte solution. d) Constant height EFM image in electrolyte solutions with high frequency applied.

As said commented previously, the complexity of EFM in liquid measurements arises from many different factors: the appearance of surface stress forces, the formation of surface charge layers, the role of the interfacial capacitances appearing at every interface, the presence of the osmotic force contributions, etc. The relevance of being able to detect nanoscale dielectric changes under liquid environment extends beyond the scope of this work of thesis, being important for many fields of science: electrochemistry, bioelectricity, biosensing, organic electronics, energy storage.

As already stated, the majority of the theoretical models that are used to understand such phenomena are based on quasi-electrostatic current models or equivalent circuit models, that in general only account for the pure electric contribution to the force and not the osmotic one[86,92,128]. In our case, we are interested in modeling a system more similar to a realistic in

liquid EFM setup. To approach such a situation, we considered two different systems. First, a simple one, based on a sphere simulating the tip and a plane simulating the metallic substrate, which allows us to achieve a better understanding of the physics of the system. Second a fully realistic EFM in liquid tip-metal and tip-thin film geometry. In both cases, we will probe the locality and dielectric resolution of the system in the different frequency regimes by adding a thin dielectric film as a sample of study.

4.2 Sphere-Plane model

The first system that we consider is the case of a 2D-axisymmetric system containing a symmetric 1:1 electrolyte with two blocking electrodes: a spherical one (which will be the first approximation to an AFM tip) and a planar one (which will be simulating the metallic substrate in EFM measurements). Everything was simulated inside a cylindrical domain that contains the electrolyte solution. Here we will consider the case without the presence of compact (Stern) layers (similarly to the previous chapter). Nevertheless, in this case, we will add a dielectric film to the simulation that will be placed between the sphere and the plane and will serve us to probe the ability of EFM in liquid to detect dielectric changes in the specimens under study.

In a similar way to the previous chapter, the model consists of the continuity equations for the ion number densities $n_{\mp}(x,t)$, coupled to the Poisson equation for the electric potential $\psi(x,t)$:

$$\frac{\partial n_{\mp}}{\partial t} + \vec{\nabla} \cdot \overrightarrow{J_{\mp}} = 0 \qquad \text{(eq.4.1)}$$

$$-\varepsilon_0 \varepsilon_r \nabla^2 \psi = e(n_+ - n_-) \qquad \text{(eq. 4.2)}$$

where ε_0 is the vacuum permittivity, ε_r the relative dielectric constant of the electrolyte (assumed to be frequency and electric field independent), $J_{\mp}$ are the ion number flux densities, which in the dilute concentration limit, can be expressed as:

$$\overrightarrow{J_{\mp}} = -D\nabla n_{\mp} + \mu n_{\mp} \nabla \psi \qquad \text{(eq. 4.3)}$$

Where D is the ion diffusion coefficient, μ the ion mobility (assumed to be the same for both ionic species and independent from concentration as we are in the dilute concentration limit). The diffusion coefficient and mobility are assumed to be related by Einstein's relation for dilute electrolytes $D=\frac{k_B T \mu}{e}$, with k_B as the Boltzmann's constant, T the temperature and e the elementary charge. The sphere and plane electrodes are separated a certain distance Z and are assumed to show blocking properties (no ion charge exchange with the electrolyte, the same as the dielectric film). They are described by means of no-flux boundary conditions:

$$\begin{cases} \hat{n} \cdot \vec{J}(r=\text{electrodes},z=\text{electrodes},t)=0 \\ \hat{n} \cdot \vec{J}(r=\text{film},z=\text{film},t)=0 \end{cases} \qquad \text{(eq. 4.4)}$$

where $\hat{n}$ is the unit vector perpendicular to the surface. The voltage of the plates is fixed externally so that:

$$\psi(r=\text{electrode}, z=\text{electrode} ,t)=\mp V(t) \qquad \text{(eq. 4.5)}$$

which for our case will take the general form of $V(t)=V_{AC}\sin(\omega t)$. The reason to focus on the AC case and not in the DC case is due to the goal of the modeling, which is to fully understand the EFM in liquid dynamics during the application of an AC voltage wave (like the one we apply experimentally). The initial condition for the ionic concentration before the application of the potential corresponds to a uniform ionic density distribution:

$$n_{\mp}(r,z,\ t\leq 0)=n_0 \qquad \text{(eq. 4.6)}$$

A sketch of the boundary conditions is found in Figure 4.2.

From the electric potential distribution, ψ, and the ion number density distributions, $n_{\pm}$, obtained by solving the NPP model, the z component of the forces acting on the spherical electrode (which simulates the EFM tip) can be calculated as[101]:

$$F_z(t)=F_{z,\ el}(t)-F_{z,os}(t) \qquad \text{(eq. 4.7)}$$

where

$$F_{z,\,el}(t)=\left(\int_S \frac{\varepsilon_0\varepsilon_r}{2}\left(\nabla\psi(L,t)\right)^2\cdot dS\right)\cdot n_z \qquad \text{(eq 4.8)}$$

is the electric force component, which corresponds to the Maxwell stress tensor on the sphere electrode surface, projected onto the z-direction, and

$$F_{z,\,os}(t)=\left(\int_S (\pi(L,t)-\pi_0)\cdot dS\right)\cdot n_z \qquad \text{(eq. 4.9)}$$

is the osmotic force component, which is the projection onto z-direction of the difference between the equilibrium and the non-equilibrium Van't Hoff pressure, $\pi=k_BT(n_++n_-)$ on the surface of the spherical electrode, where $\pi_0=2k_BTn_0$.

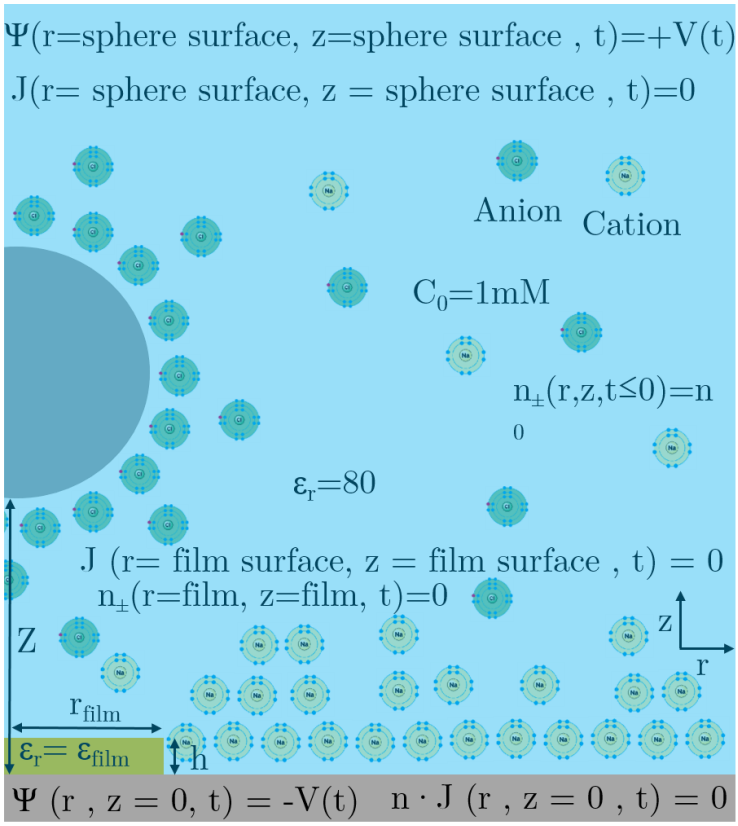

Figure 4.2: Sketch of the model and the boundary conditions for the sphere-plane model.

Finally, the Debye screening length (L_D) is defined as:

$$L_D=\sqrt{\frac{2n_0e^2}{k_BT\varepsilon_0\varepsilon_r}} \qquad \text{(eq. 4.10)}$$

which gives us an effective screening length that the electrostatic interaction covers in such systems (strongly dependent on the ionic concentration and independent of the applied voltage).

Unless it is otherwise specified, the parameters used to solve the NPP system are distance between electrodes Z=100nm, ion concentration n_0=1mM and AC voltages V_{AC}=10mV. The remaining set of independent parameters are the ion diffusion, D=10^{-9} m^2/s, and temperature, T=298 K. For these parameters, the thermal voltage is $V_T=k_BT/e$=26 mV, the ion mobility $\mu=D/V_T$=3.9 10^{-8} $m^2/V \cdot s$, the electrolyte conductivity $\sigma=2e\mu n_0$=7.4 10^{-3} S/m and the Debye screening length L_D=9.6 nm. The full nonlinear time-dependent NPP system of equations and its boundary conditions presented above are carried out with the corresponding built-in model in COMSOL MULTYPHISICS 5.3a.

As every finite element numerical simulator, we have to discretize the spatial and temporal domain. In our system, this is a key point, as the different length scales and time scales involved in the system are very broad: they go from few nanometers to hundreds of micrometers, and from tens of nanoseconds for the conduction processes to the seconds for the diffusion processes. Therefore, the meshing has to be fine enough to resolve all the physical relevant phenomena, but coarse enough to reduce the simulation time to the minimum. This brings us to have to set up different meshing structures and sizes for the different structures present in the system. Normally, the spatial meshing will be finer closer to the solid/electrolyte interfaces and coarser further away from the electrodes. The concrete specifications for meshing elements, element sizes, and so on are not shown in the thesis as they are not giving any relevant information.

First, we will study the system without a dielectric film (for an easier understanding of the physics behind). Later on, we will move to the system with a dielectric film, to probe the EFM capabilities of detecting dielectric changes in the samples under study.

4.2.1 Electric potential and charge distribution

The spatial and frequency dependence of the electric potential and charge density are calculated and shown in Figure 4.3. For $Z>L_D$, the DC voltage and charge density profiles (Figure 4.3 f and l) show the presence of DC space charge diffusive layers at the sphere surface (and to a much less extent on the plane electrode), which decay exponentially with distance, with a characteristic length of L_D. For $Z<L_D$. The space charges fully overlap, the DC potential decays linearly, and the electric charge increases linearly (data not shown).

Such results are different from the ones shown in the 1D geometry, where an equal space charge layer was found in each one of the electrodes. Here the space charge layer is dependent on the charge density at the electrode surface. That means that the space charge layer size will depend on the electrode size. The density of charge of the sphere will be much higher than the one on the substrate, as the sphere's surface is much smaller than the substrate area but will accumulate the same electrical charge. This implies that the charge layer in the sphere will be larger than the one on the substrate.

In our case, as the sphere area is much smaller than the substrate area ($A_{sphere}<<A_{substrate}$), the charge layer is only observed in the sphere surface and not on the substrate. This is a consequence of the lack of an infinite electrolyte reservoir, which would act as a reference electrode in an experimental setup (fixing the potential of the solution to a certain value).

On the other side, the AC voltage and AC charge profiles evolve continuously from "DC-like" profiles at low frequencies, up to linear voltage, and zero charge density profiles at very high frequencies (Figure 4.3 e and k). This behavior is the equivalent in the frequency domain to the behavior found in the time domain for the transient response to a DC voltage step[136].

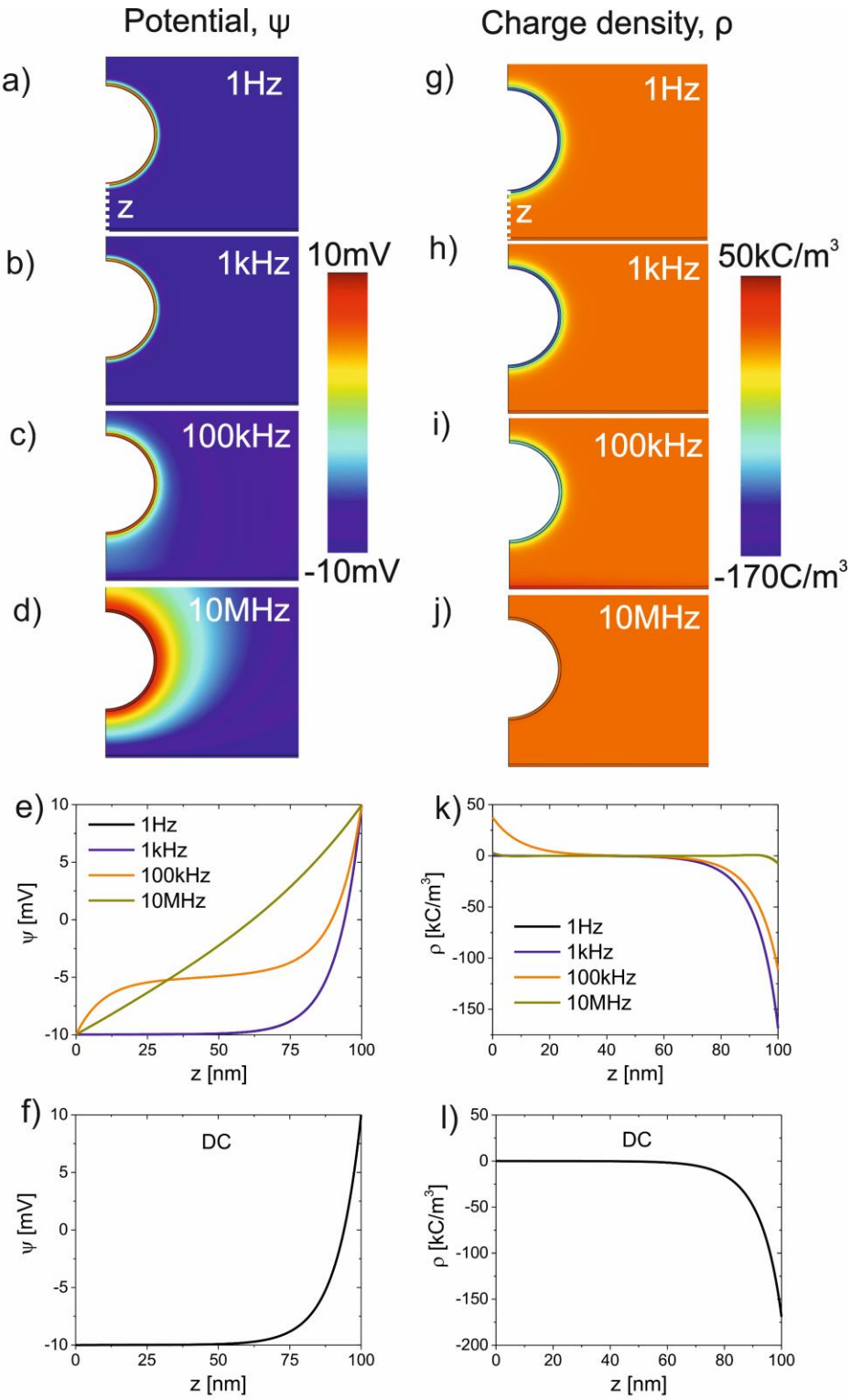

Figure 4.3: AC component of the electric potential (a)-(d) and charge density distribution (g)-(j) as a function of space for a fixed time multiple of the period of the applied AC voltage for different frequencies. e) Electric potential profile along the z-axis (white dotted line in (a)) between the sphere and the plane. k) Charge density profile along the z-axis (white dotted line in (g)) between the sphere and the plane. DC component of the electric potential (f) and charge density distribution (l) as a function of space for the case where V_{DC}=V_{AC}.

In Figure 4.4, we find the modulus and phase of the impedance of the system, were one can identify the 3 different regimes: the low frequency regime ("DC-like, charge space layers"), the intermediate frequency regime, where the ions are still able to move but they cannot completely follow the frequency of the applied voltage and an offset between the applied voltage and the AC current appears, and the high frequency regime ("frozen electrolyte, no space layers") where the ions do not have time to follow the applied potential, so they do not move, playing a neglectable role in the dynamics of the system (from here we refer to them as "frozen").

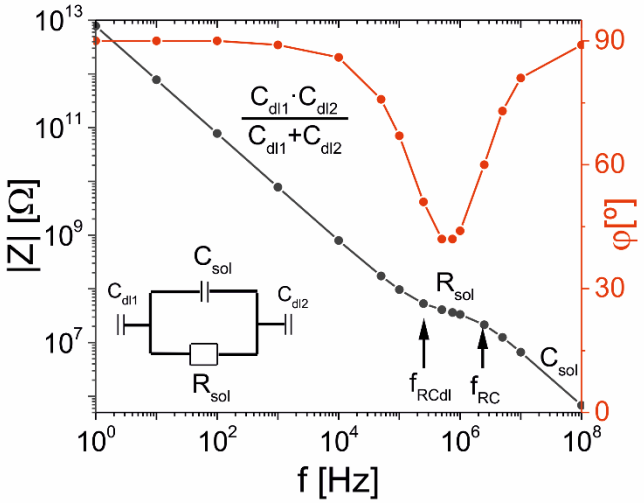

Figure 4.4: Modulus (black line, left axis) and phase (red line, right axis) of the impedance of the system. Inset: the equivalent circuit for the system.

According to this description, in the low frequency range ($f < f_{RC_{dl}}$), the system shows a capacitive behavior, with an equivalent capacitance $\frac{C_{dl1} \cdot C_{dl2}}{C_{dl1}+C_{dl2}}$. In this frequency regime the AC voltage and charge density show a quasi-static "DC-like" voltage and charge density distributions, with the presence of AC space charge layers at the surfaces that fully screen the applied AC voltage with a nearly null AC electric field and charge density outside the double layers (see Figure 4.3a, b, g, h). Note that for our case, as $C_{dl1} >> C_{dl2}$ (because $A_{sphere} << A_{substrate}$), the expression for the equivalent capacitance is reduced to C_{dl2}.

At the intermediate frequencies ($f_{RC_{dl}} < f < f_{RC}$), the system shows a resistive behavior, with equivalent resistance R_{sol}. The AC voltage and charge density profiles show partially developed AC space charge layers that do not fully screen the applied voltage. Hence, a non-null AC electric field appears outside the AC space charge layers (see Figure 4.3c,i), which induces an AC resistive current.

Finally, at high frequencies $f > f_{RC}$, the system shows a capacitive behavior again, but this time determined by the electrolyte capacitance C_{sol}. No AC space charge layers are formed in this frequency range (see Figure 4.3d, j); thus, the AC electric field is constant between the plates and the AC charge density null everywhere. Note that in the steady-state, neither the voltage and charge distributions nor the system impedance depends on the inverse diffusion time.

4.2.2 Forces on bare electrodes

Once the electric potential and charge distributions are calculated, we are ready to calculate the forces acting on the sphere. We will proceed the same way that we did in the previous chapter (for the 1D case), but this time due to the 3D dimensionality of the system, we have to solve the numerical integration of each force through the sphere surface. Not only that, but as we are trying to mimic the EFM-like system, we are interested in only the Z component of the force (which would be the measured one in an EFM setup). Therefore, we have to multiply each force by the z unit vector (see previous sections).

In the same way, as we proceed for the 1D case, we will calculate the full temporal force series, and then we will Fourier transform to obtain the amplitude of each harmonic separately (similarly to what the lock-in amplifier does experimentally). We will focus on the 2ω-component of the force, as it is the one normally acquired experimentally in EFM measurements for dielectric characterization.

In general, in the force behavior, we can distinguish the 3 different regimes that we saw in the impedance (see Figure 4.4). With the same data, a further study of the DC and ω components could be done, but it goes beyond the interests of this thesis.

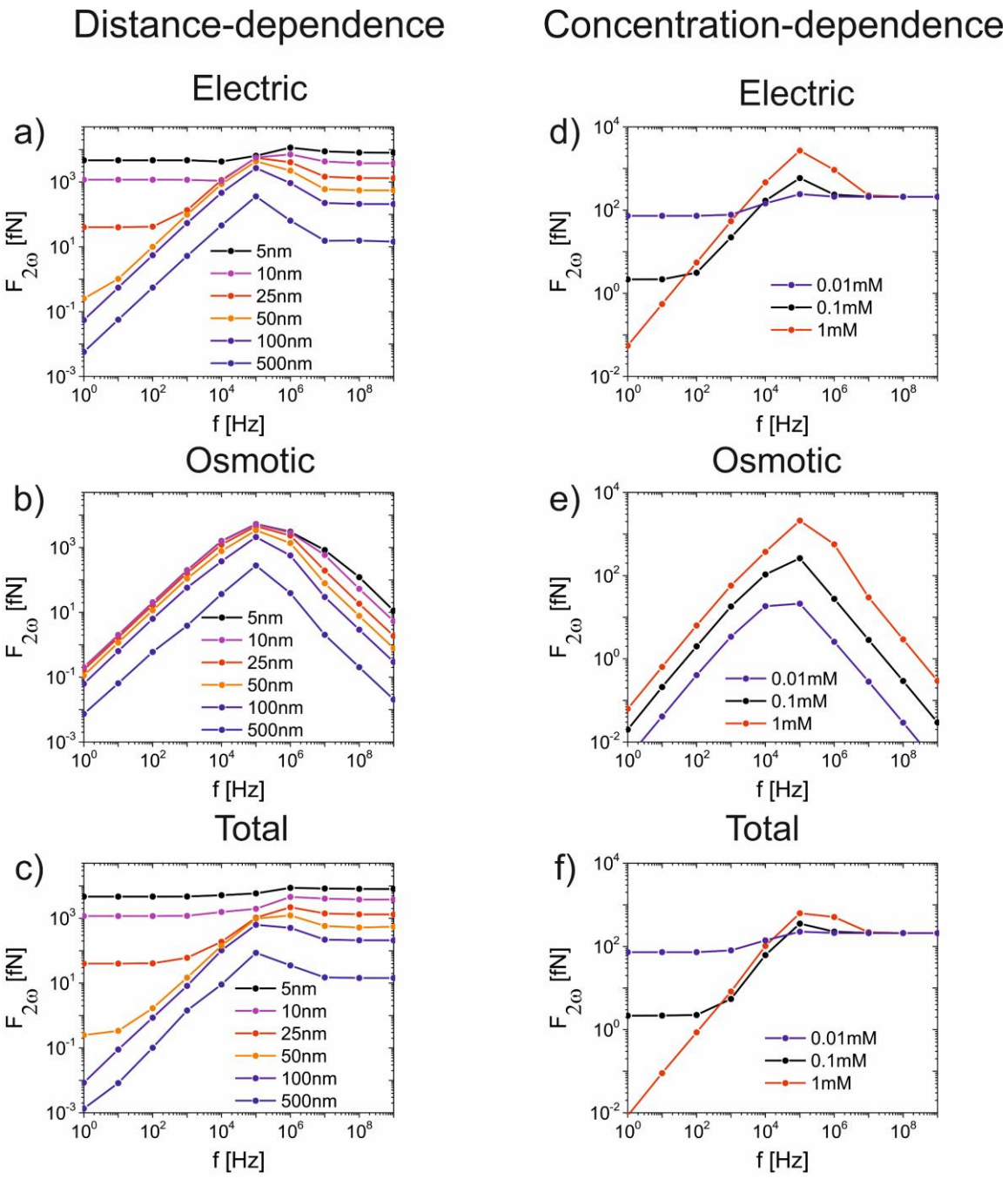

Figure 4.5: a) Electric force as a function of the applied frequency for different sphere-plane distances. b) Osmotic force as a function of the frequency for different sphere-plane distances. c) Total force as a function of the frequency for different sphere-plane distances. d) Electric force as a function of the applied frequency, for different

ionic concentrations of the electrolyte. b) Osmotic force as a function of the for different ionic concentrations of the electrolyte. c) Total force as a function of the frequency for different ionic concentrations of the electrolyte.

For the low frequency regime, the space charge layers produce an electrostatic and osmotic force onto the sphere. On the one hand, if $Z>L_D$, this force is canceled point-by-point due to the symmetry of the sphere. This means the upper surface of the sphere will suffer a force of the same magnitude but opposite sign to the force found in the down part of the sphere. On the other hand, if $Z<L_D$, this force is not canceled point by point as the down part of the sphere, will feel the interaction with the substrate (as the space charge layers of sphere and plane will overlap), but the upper part of the sphere will not be overlapping its space charge layer with the one of the substrate (see Figure 4.5c).

In the intermediate regime, ions can still move, but they are not able to fully form the space charge layers, and this induces a phase difference between the ions movement and the applied potential, that turns into the bump found in the forces in the intermediate range (see Figure 4.5c). This bump is again a consequence of the different forces acting on the upper and lower parts of the sphere, which have different distances to the substrate, and so different characteristic time dynamics.

Finally, in the high frequency regime, the osmotic force vanishes (see Figure 4.5b), as the ac charge space layers do not have time to form, and the total force is only given by the electric component. The distance dependence of the force is now extended to distances much larger than L_D, which allows having distance dependence interaction in EFM in liquid at large distances (if the applied frequency is high enough, see Figure 4.5c).

The effect of the electrolyte concentration on the force acting on the tip (see Figure 4.5 d-f), are two. First, it induces a change in the Debye screening Length (L_D), as this one is highly dependent on the electrolyte concentration: $L_D=\sqrt{\frac{2n_0e^2}{k_BT\varepsilon_0\varepsilon_r}}$. Thus, we find that for 1 mM concentration: L_D~10 nm. For 0.1 mM: L_D~30 nm. And for 0.01 mM: L_D~100 nm. Second, it shifts to higher frequencies the high frequency regime threshold (f_{RC}), as it changes the medium conductivity. The force dependence with the concentration is of extreme

relevance to our work, as it is setting a maximum threshold concentration for the electrolyte that we can use in the experimental measures if we do not want to overcome certain frequency values (experimentally going beyond 100MHz can be problematic as the shielding of EFM systems is not prepared for such high frequency waves). This is a drawback from the cells' point of view, as cells normally live in environments that are rich in ions and other charged molecules (see the last chapter).

4.2.3 Local sensitivity to a dielectric film

Once we have understood the physical phenomena ruling our system, we are going to probe the in liquid EFM capability for local dielectric resolution. To do so, we will place a finite size thin dielectric layer of h=4 nm, r_{film}=100nm, and $\varepsilon_{r,\,film}$=2 (see Figure 4.2). We will again calculate the electric potential distributions in the different frequency range for different sphere-plane distances and compare them with the case without the dielectric film.

In Figure 4.6 a-d, we show the electric potential distribution for the low frequency regime (1 Hz) where we can see that the ac space charge layers are formed (Figure 4.6 a-b) and high frequency regime (10 MHz) where we observe that the ions are not playing any role and the charge distribution is homogeneous (Figure 4.6 c-d). We compare two different scenarios: when the sphere-plane distance is shorter than the Debye screening length ($Z<L_D$, Z=5 nm, Figure 4.6 a,c), and when the sphere-plane distance is longer than the Debye screening length ($Z>L_D$, Z=100 nm, Figure 4.6 b,d).

In Figure 4.6 e-f, we show the electric potential profile between the sphere and plane (along the white dashed line in Figure 4.6b for the four cases above), and we compare it with the case without the dielectric film (dashed lines). In all the cases, there is a linear potential drop in the film. In the case of the low frequency regime, after the film, there is an exponential potential drop due to the space charge layers. In the case of the high frequency regime, after the film, there is as well a potential drop but with a different slope (because of the different relative permittivity, $\varepsilon_{r,solution}$ =80 of the solution as compared with the film, $\varepsilon_{r,film}$ =2). The different potential distributions turn into different forces acting on the tip.

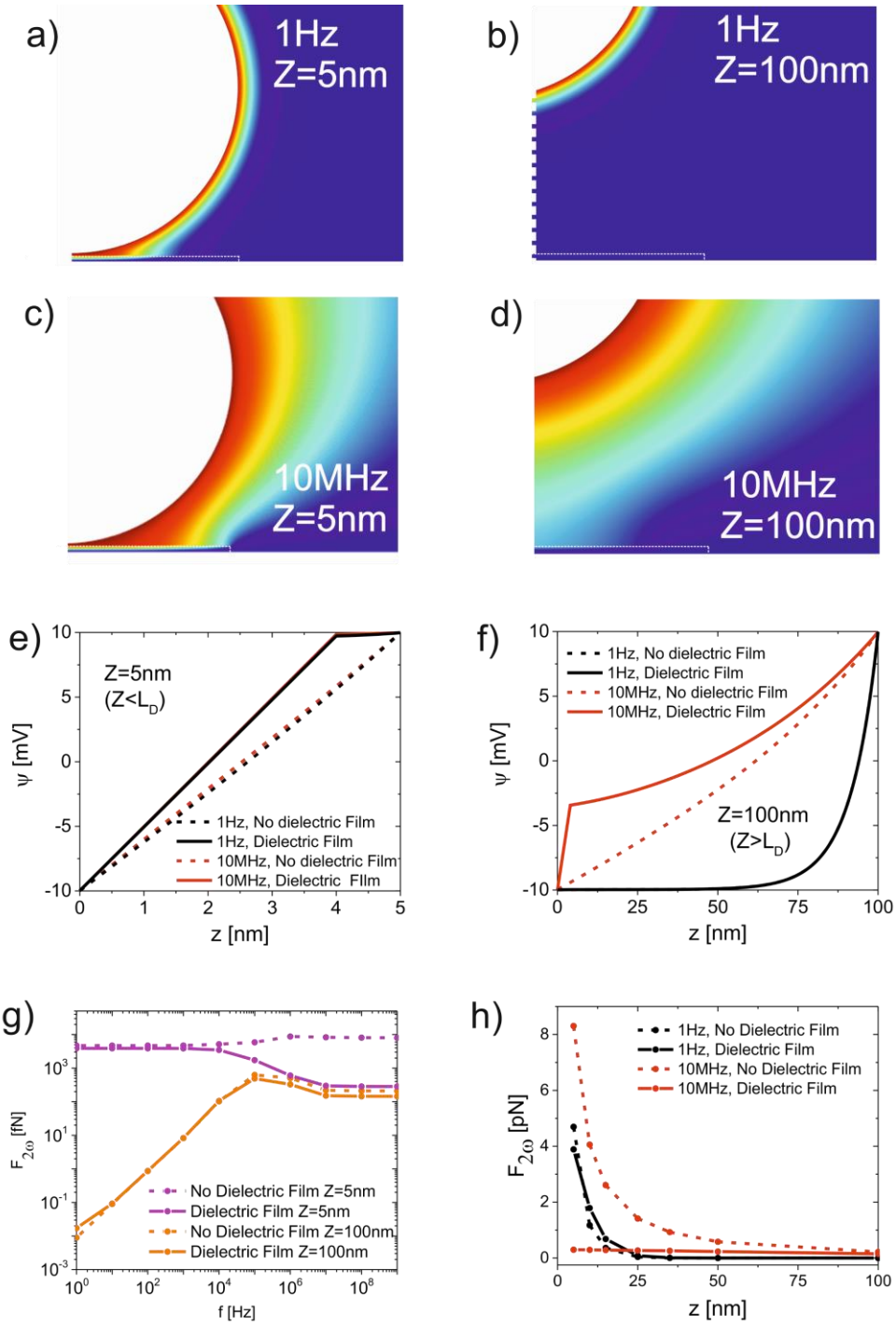

Figure 4.6: Electric potential distribution of the sphere-plane system with a dielectric layer of h=4nm, r_{film}=100nm, and $\varepsilon_{r,\ film}$=2 for the following cases: a) 1Hz applied frequency and 5nm sphere-plane distance (Z<L_D), b) 1Hz applied frequency and 100nm sphere-plane distance (Z>L_D), c) 10MHz applied frequency and 5nm sphere-plane distance (Z<L_D), d) 10MHz applied frequency and 100 nm sphere-plane distance (Z>L_D). Potential profile along the z-axis between the sphere and plane for the case of the dielectric film and compared as well with the case of no dielectric film, e) for the sphere-plane distance of 5nm (Z<L_D), and f) for the sphere-plane distance of 100nm (Z>L_D). g) The total force acting on the sphere as a function of the frequency for the

cases under study (with and without dielectric film). h) Approach curves for the low frequency (1Hz) and high frequency (10MHz) with and without the dielectric film.

The frequency dependence of the total force acting on the sphere is shown in Figure 4.6g and compared with the case of no dielectric film (dashed lines). Finally, we also show (Figure 4.6h) the distance dependence for the high and low frequency regimes of the total force acting on the sphere in all the cases.

The relevant information that we can extract from this analysis is that both in the low frequency and high frequency regimes, a voltage biased sphere can feel the presence of a dielectric field (as the total force acting on the sphere is different from the case without a film). Nevertheless, in the low frequency regime, the dielectric resolution is restricted to the case where the space charge layers overlap, which implies very short ($Z<L_D$) sphere-substrate distances. On the other hand, for the high frequency case, as the screening space charge layers do not form, the electrostatic interaction is expanded to a long-range interaction, and we have not only a higher dielectric contrast but as well a longer interaction range.

4.3 Tip-plane model

The second system that we considered is identical to the sphere-plane model system but changing the sphere for a realistic AFM tip geometry. The boundary conditions are the same as the ones explained in the previous section (see Figure 4.2). The main difference apart from the shape of the tip itself is the size of it. The sphere we were simulating previously, had a radius of 100 nm while the full AFM tips have a characteristic length much larger than that. The apex radius itself can be on the order of magnitude of tens or hundreds of nanometers, but the whole cone and cantilever are on the tens of μm size.

The AFM probe is modeled as a truncated cone with half-angle θ and height H_{cone} terminated with a tangent hemispherical apex of radius R, as shown in[97]. The cantilever is modeled as a disk of height H_{cant}, thickness W_{cant}, and length L_{cant}. The forces are calculated over all the surface of the AFM probe.

As we already described the (frequency, concentration and distance) dependence of the different force regimes for the case of the sphere-plane model, in this case, we are going to go directly to analyze the possibility to detect dielectric changes in a sample under study.

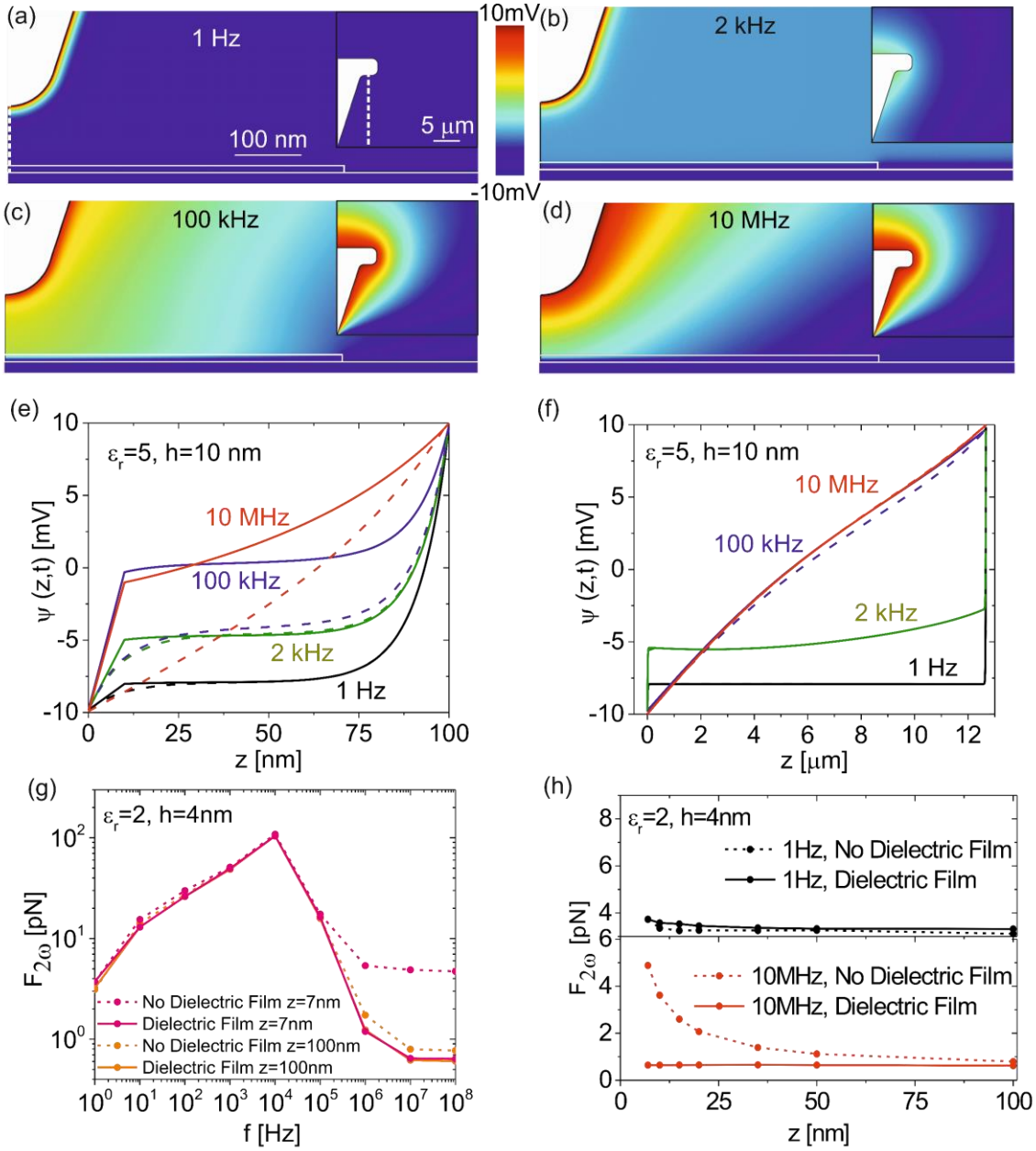

Figure 4.7: Electric potential distribution of the tip-plane system with a dielectric layer of height h, and dielectric constant ε_r for the following cases: a) 1Hz, b) 2kHz, c) 100kHz, and d) 10MHz applied frequency and 100 nm tip-plane distance (z>L_D). Insets show the whole tip and cantilever disc. Potential profile along the z-axis (white dotted line in a) between the tip and plane for the case of the dielectric film (continuous lines) and compared as well with the case of no dielectric film (dashed lines), e) for the tip-plane and f) for the cantilever-plane distance. g) The total force acting on the tip as a function of the frequency (with and without dielectric film) for z=7nm

(z<L_D) and z=100nm (z>L_D). h) Approach curves for the low frequency (1Hz) and high frequency (10MHz) with and without the dielectric film.

As we saw in the case of the sphere-plane system, for low frequency applied voltages, space charge layers form at the electrode/liquid interfaces of the tip and substrate (Figure 4.7a), screening the electrostatic interaction between tip and sample unless the distance between them is smaller than the Debye screening length[140]. In this case, as the area of the tip is larger than the one of the sphere, we observe a space charge layer in both electrodes. As we increase the frequency, we move to the intermediate frequency regime, where the ions present in the electrolyte, can still move with the externally applied field, but the electrostatic potential distributions differ from the quasi-static ones (like DC or low frequency), as diffusion has no time to reach the steady-state of the system (Figure 4.7b,c). Finally, when we are in the high frequency range (Figure 4.7d), ions do not play any role, and the electrostatic distribution is equivalent to the one in dry conditions, but with the only difference of a higher relative permittivity of the solution (ε_r~80). In the insets of the figure, the potential distribution of the whole tip (including the cone and the cantilever) illustrates the fact that different temporal dynamics of the EDL formation are found for the different parts of the tip, as their characteristic distance with respect to the substrate changes.

In Figure 4.7e, we show the potential profiles between the apex-substrate and in Figure 4.7f the potential profiles between cantilever-substrate with continuous line and compare it with the case without the dielectric layer (dashed line). We show that the high frequency range is the optimal one for dielectric detection, as the potential distribution with and without the dielectric films is much more different in that regime that in the other ones.

In Figure 4.7g we show the frequency dependence of the total force acting on the tip for distances longer (Z=100nm) and shorter (Z=7nm) than L_D as well as their comparison with the case without dielectric film. We can observe that the maximum contrast as well as the maximum interaction range is obtained for the high frequency regime. These facts are as well illustrated in Figure 4.7h, where the 2ω component of the force-distance curves is plotted and as well compared with the case without dielectric film.

Regarding the locality of the measurements, one can clearly see that only in the high frequency regime, in the apex profiles, the potential difference between the case with and without the dielectric layers is different, showing that the forces are local (apex probed).

We can then state that, even if also in the low frequency regime and for distances shorter than L_D the tip also feels dielectric changes of the sample, it is the high frequency range the optimal regime for nanoscale dielectric characterization. First, because in the high frequency range, the contrast (the difference between thin layer force and metal force) extends to the long-range (longer than the Debye length), which solves a lot of problems experimentally (otherwise, the measurements should be done at very close distances). Second, because the contrast also appears to be larger than in the low frequency case. We also have to say that (even if we have not considered this aspect in our model) experimentally at low frequency applied voltages, chemical reactions can occur at the electrode, and huge surface stress interactions appear, avoiding the possibility to perform good measurements.

Therefore, we will use high frequency voltages for our experimental work, and we will focus on the high frequency case (10 MHz) for the study of the feasibility of achieving dielectric resolution in electrolyte solutions (see[90,91] for experimental works already published on that, but lacking a full theoretical model[102]). With that aim, in Figure 4.8, we show the possibility to distinguish between different dielectric layers, by showing the force acting on the tip in the high frequency range (the one we use experimentally) for different film radius (Figure 4.8a), dielectric constants (Figure 4.8b) and thicknesses (Figure 4.8c).

For the case of the radius, we can see that the signal decreases to a *plateau* value as the radius gets big (Figure 4.8a). This *plateau* is reached when the lateral size effects are not seen anymore. For the case of the relative permittivity, similar behavior is found, a *plateau* value is reached when we increase a lot the permittivity of the layer(Figure 4.8b). Nevertheless, in this case, the *plateau* is reached when the dielectric layer is not an insulator anymore but acts like a conductor surface, and zero voltage drop happens inside the layer. Finally, for the case of the thickness, we observe that as we increase the thickness, the force

value tends to decrease, as a higher potential drop happens in the dielectric layer(Figure 4.8c).

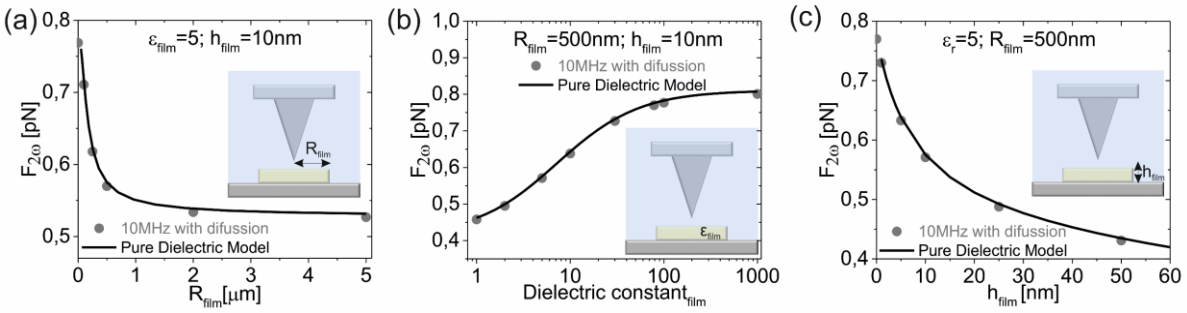

Figure 4.8: Total force measured on an EFM measurement at high frequency of a thin dielectric film as a function of a) the radius of the film, b) the relative permittivity of the film, and c) the thickness of the film. The tip-metal distance is kept constant for all the cases at z=100nm.

This shows us that we can detect dielectric changes for certain values of film radius, dielectric permittivity, and thickness. Then if the geometry of our tip (r and ϴ), together with the topography of sample (R_{film} and h_{film}), are known parameters, one can use the modeling to fit the best relative permittivity to the experimental EFM in liquid data.

It is interesting to highlight the fact that under liquid environment (as the dielectric constant of water is much higher), the contribution of the cone force to the total force is more important as compared with the case in air, this fact is transduced into higher lateral size effects for EFM in liquid (see Figure 4.8a, where the saturation value for the thin film radius is not achieved until this has reached the 4 or 5 μm in size).

As we have seen, the measurements of EFM in liquid have to be performed at high frequency, where ions do not play any role on the force acting on the tip. Therefore, as the modeling of the Nernst-Plank-Poisson system is complex and solving its equations is computationally demanding, one can use a simple Poisson model for the quantification in liquid as well (taking advantage of the fact that ions are frozen in such circumstances).

In Figure 4.8 we can see the good matching between the two models in the high frequency range (black line Poisson model and grey dots NPP model), which ensures for the usage of

a pure electrostatic model for the quantification of the EFM in liquid data, where the relationship (valid in air) between the force felt by the tip and the derivative of the capacitance of the system is recovered ($F_{2\omega}=\frac{1}{4}\frac{dC}{dz}{V_{AC}}^2$). Here it is important to remark that this equivalence found in the high frequency regime is not necessary recovered for the low and intermediate frequencies, where ions play an important role in the forces acting on the tip. Such fact could have important implications for the performance of open-loop techniques both in EFM and KPFM, which sometimes take for granted that the relationship between the force acting on the tip and the derivative of the capacitance is the same for all the frequency ranges.

4.4 Discussion

The first important aspect to comment is the range of validity for our theoretical modeling. Even if the model is (to our knowledge) the first complete modeling of the forces acting on voltage biased electrodes in electrolyte solution applied to EFM, it still has some room for improvement to achieve the validity in the full range of applied voltages and frequencies. In our model, the pure electrostatic force and the osmotic force have been considered. Nevertheless, especially for the low frequency regime, other forces can act on the electrodes. The space charge layers can induce huge surface stress interactions[70] at the solid/liquid interface that are not negligible experimentally. I would say that this is the main limitation of performing voltage biased EFM measures in liquid at low frequencies. Next, chemical reactions can also occur at the surface of the electrodes (especially for high voltages and low frequencies applied), and a degrading of the sample's quality or bubble formation can be found. Therefore, the analysis of the forces acting on the electrodes for the low frequency regime, at high voltages, has a limited validity to systems not showing the interactions listed before.

Secondly, I also wanted to comment that the term “liquid” has been used in this chapter to refer only to polar liquids (like water-based solutions). EFM measurements on other non-

polar liquids (like fluorocarbon liquid) are possible without the need considering all the aspects explained during this chapter[92].

Even though in-liquid EFM can look easy to implement after the modelling analysis is made (only a high frequency applied voltage is needed as compared with the state of the art EFM in dry setup), experimentally, it is not so simple. The high frequencies needed to avoid surface stress and spurious osmotic forces are too high for the commercial AFM probes to oscillate in liquid environments. In the last years, with the development of high-speed AFM[57], higher resonant frequency tips are needed and have been developed, but first, not all of them are conductive, and second, commercially availability of such probes is not well established yet. That explains the experimental need of modulating the high frequency signal with a low frequency signal (see EFM in liquid explanation in the introduction chapter) for the in liquid EFM setup.

It is also important to comment on the low value of the forces that come out during this chapter. Without any further comment on that, it would seem that the forces measured in EFM in liquid are close to de detection limits of an AFM setup, as they are sometimes below the pN range, which starts to be challenging even for lockin techniques like EFM. This is a consequence of performing the simulations in the linear regime for the voltage. We do so to avoid ionic finite-size effects which would arise in the low frequency regime if higher voltages are used. We also do it to shorten the computing time, as higher applied voltages seem to need more computational power. Nevertheless, experimentally, the force values that are found are much higher than the ones shown in the simulations, as the voltages needed to have a nice signal to noise ratio (SNR) are on the order of magnitude of 1V. As we perform the experiments in the high frequency range, where the ions do not play an important role on the force, we can still use the well-known quadratic force-voltage dependence that we find in dry environments: $F_{2\omega}=\frac{1}{4}\frac{dC}{dz}{V_{AC}}^2$. Here it is important to remark that this relationship can only be used in the high frequency range, as the space charge layers formed in the intermediate and low frequency ranges can induce changes in the force-voltage dependence.

Therefore, as most simulations have been calculated for the 10mV case, a factor $\alpha = \frac{1000^2}{10^2} = 10^4$ has to be added to all the force values in the high frequency range to obtain the value of a realistic experiment with the same parameters but performed at 1V.

To show that the EFM force dependence on the concentration and the applied frequency probed during this chapter, match with the experimental trend, in Figure 4.9b, we show experimentally acquired constant height images for different frequencies and two different solutions. It is clearly seen that the dielectric contrast decreases and finally vanishes as the applied frequency is lowered, which is showing the need of high frequency for the EFM measurements in liquid environment. The threshold frequency for dielectric detection is strongly dependent on the conductivity (or solute concentration) of the solution, finding that for more conductive solutions, higher frequencies are needed to recover the dielectric contrast.

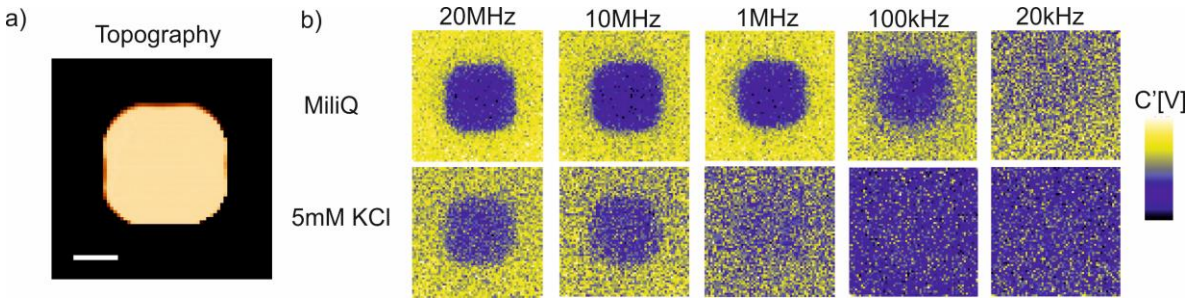

Figure 4.9: a) Topography of the silicon oxide pillar. b) Table of Constant height EFM in liquid images at 350nm from the metallic substrate, for different applied frequencies in MiliQ and 5mM KCl solutions. XY scale bar is 4μm.

4.5 Conclusions

We have developed a model in the frame of Poisson-Nernst-Plank equations to analyze the electrostatic and osmotic force acting on an EFM in liquid setup. We have been able to differentiate between three different interaction regimes and their feasibility for nanoscale dielectric imaging in liquid environment has been discussed. As a conclusion, the high frequency regime is the best one to perform EFM in liquid, as it has the longest interaction range (not restricted to the short Debye screening length), the highest contrast, and experimentally it has no spurious interactions like surface stress, chemical reactions or

osmotic forces. Nevertheless, experimentally, it is necessary to modulate the signal with a low frequency wave in order to perform the detection (too fast for commercially available metallic cantilevers). More complex models are still needed to achieve the quantification of the experimental measurements for the local dielectric properties in such environments. Briefly, due to the interfacial capacitances generating at the electrodes and sample interfaces with the solution, which add more fitting parameters to the quantification of scanning dielectric microscopy in liquid. Those models are being developed by other group members and will be soon published, allowing to complete also the quantification of the measurements performed in liquid during my thesis, that will be shown in the last chapter.

5. Scanning Dielectric Force Volume Microscopy

This chapter explains the experimental technique developed during this work of thesis: Scanning Dielectric Force Volume Microscopy to deal with complex samples like cells. It reproduces almost literally parts of the article: "Mapping the Dielectric Constant of a Single Bacterial Cell at the Nanoscale with Scanning Dielectric Force Volume Microscopy"[141]*. Regarding the contributions of the different authors, M.Checa developed the experimental technique, prepared the samples, did the experiments, and build a software for its data analysis, R. Millan-Solsona developed the quantification methods, and G. Gomila supervised the work.*

5.1 Introduction

Mapping the local dielectric constant of non-planar samples with nanoscale spatial resolution is of major interest in fields of science and technology ranging from Materials to Life Sciences and Nanomedicine. Examples include dielectric nanocomposites[142,143], whose energy storage capability strongly depends on the local dielectric properties of the interfaces between the nanomaterial and the matrix[144]; the response of cells to electromagnetic fields[145], which depends on the local cell composition[146] and cell state[147], and their corresponding dielectric properties[148,149]; the biophysics of bioelectric phenomena, such as action potential propagation, membrane ion transport[150] or electroporation[151], which depend on the local dielectric properties of the cell membrane; and the development of novel label-free imaging methods for Nanotoxicity studies[152–154], which could be based on the different dielectric properties of cells and of nanoengineered materials. In most of the cases, the non-planar nature of the samples and the nanoscale variations of their dielectric properties make them not appropriate for conventional macroscale or microscale dielectric techniques.

Scanning Dielectric Microscopy (SDM) techniques have been developed over the years to overcome this limitation, following earlier works at the microscale[155]. SDM techniques combine Scanning Probe Microscopy (SPM) imaging techniques sensitive to the local electric polarization[156], such as Scanning Capacitance Microscopy (SCM)[32,157], Nanoscale Impedance Microscopy (NIM)[66,158], Scanning Microwave Microscopy (SMM)[159,160] or Electrostatic Force Microscopy (EFM)[21,33,34,161–165], with theoretical methods and calibration procedures able to quantify and map the dielectric constant at the nanoscale[28]. Despite its widespread use, the application of these techniques to the case of heterogeneous and topographically complex samples still constitutes a formidable challenge. On the one side, the existing dielectric imaging modes, such as constant height with respect to the substrate, constant distance with respect to the sample surface (or lift-mode), or at constant magnitude (e.g., electric force), all present important limitations when applied to samples with complex topographies. Lift-mode, for instance, introduces topographic crosstalk contributions in the dielectric image[166], which cannot always be completely removed by post-processing[167,168]. Constant height imaging[32], on its side, is not adequate for samples showing large topographic variations since the tip-substrate distance must be set too high, and the sensitivity to the small scales is, then, lost. Finally, imaging at constant magnitude (e.g., force[161]) provides images that mix dielectric and topographic information, which are, again, difficult to separate by post-processing. These facts introduce artifacts in the dielectric images that severely compromise its direct interpretation in terms of the local dielectric properties. To overcome these drawbacks, a quantitative analysis of the dielectric images is needed in order to obtain nanoscale dielectric constant images. This step in the case of non-planar samples is hampered by the fact that the local electric polarization depends, apart from the local dielectric constant on the local geometry of the sample[99]. This means that the actual sample geometry and physical dimensions need to be considered in the theoretical models to obtain quantitatively correct dielectric constant values, as it has been demonstrated for samples showing simple geometries, such as nanoparticles, nanowires or whole bacterial cells[34,35,169]. However, for topographically complex samples no simple approach has been developed, yet.

In these cases, simple local thin film models have been used to derive the dielectric constant maps[42,43,170,171], which, in general, give rise to dielectric constant values that are not realistic, except, of course, for thin film-like samples[32,97,165]. Therefore, until now, reliable and quantitatively accurate nanoscale dielectric constant measurements with SDM techniques have been performed only on either planar samples such as oxide thin films[97] , polymer blends[33,162] and lipid bilayers[32], or non-planar samples with simple geometries, such as, macromolecular protein complexes[3,169], liquid droplets[161], nanoparticles[34,172], whole bacterial cells[35], viruses[34], nanotubes[165], nanowires[170] or water confined in nanochannels[21]. Samples showing complex topographies, such as non-planar nanocomposite materials or single cells, have been left out of scrutiny due to the lack of appropriate nanoscale dielectric techniques.

Here we overcome the limitations of existing SDM techniques by introducing Scanning Dielectric Force Volume Microscopy (SDFVM). SDFVM is based on the acquisition of Electrostatic Force Microscopy (EFM) approach curves at each point of a sample and its post-processing and quantification by using theoretical models that include the real measured sample topography. We show that with this approach, realistic nanoscale dielectric constant maps can be derived with an unparalleled spatial resolution, accuracy, and statistical significance irrespectively of the complexity of the sample topography. SDFVM constitutes the dielectric counterpart of modern force volume nanoscale mechanical mapping methods developed in recent years[173] and is fully in line with the modern approach to functional SPM imaging based on big data analysis and processing[174]. The potential of the technique is demonstrated here by reporting dielectric constant images of single-bacterial cells with sub-cellular composition sensitivity, without the use of any labeling or staining agents.

In this chapter, we will present SDFVM from the experimental point of view, and we will as well show how to analyze and quantify the data to obtain the corresponding nanoscale dielectric constant map. To that end we will use a simple sample containing SiO_2 pillars micropatterned on top of a highly doped silicon surface. In chapter 6, we will show the application of SDFVM to the label-free compositional mapping of a bacterial cell from its

nanoscale local dielectric constant map. In chapter 7, we will show the ability of the method to obtain EFM images in a variety of nanometric systems of interest, challenging to image with the state-of-the-art EFM modes.

Last, the experimental development of Electrostatic Force Microscopy in liquid (see introduction chapter), together with its theoretical comprehension (see modelling chapters), makes it suitable for the application of SDFVM in liquid conditions. This fact is what makes the technique really interesting and promising for its application to the study of nanoscale electrochemical processes in living cells: dielectric mapping, capacitive/resistive changes during an action potential, cell-nanoparticle interaction, etc. There is a lot of work to be done, concerning possible applications in liquid of the technique developed in this thesis, from both theoretical and experimental points of view. The first steps towards the application of SDFVM to liquid is made in chapter 8.

5.2 Scanning Dielectric Force Volume Microscopy

Scanning Dielectric Force Volume Microscopy (SDFVM) is based in acquiring deflection, D(X,Y;Z), and 2ω-oscillation amplitude, $A_{2\omega}$ (X,Y;Z), EFM approach curves at all points (X,Y) of a sample (Figure 5.1 a). The EFM approach curves (Figure 5.1 b) are acquired with an applied ac voltage of amplitude v_{ac} and angular frequency ω_{el}, which generates both the static bending (deflection) and the $2\omega_{el}$ oscillation of the cantilever[156] (also a ω_{el}oscillation of the cantilever is produced, which is not considered in our studies, Figure 2.4). An appropriate trade-off between approach curve velocity, cantilever resonance frequency, frequency of the applied voltage, and sensitivity needs to be achieved for the proper implementation of SDFVM (see discussion section). The 2ω-oscillation amplitude is represented through the capacitance gradient, dC/dz(X,Y;Z), given by[34] $dC/dz(X,Y;Z)=4kA_{2\omega}(X,Y;Z)/v_{ac}^2$, where k is the equivalent spring constant of the probe (see eq. 2.7). A total of $N \cdot M$ EFM approach curves are acquired in a set of data, where N and M are the number of lines and pixels per line, respectively (for instance, for a 128x128 image $N \cdot M=16394$ approach curves are included, see Figure 5.5.

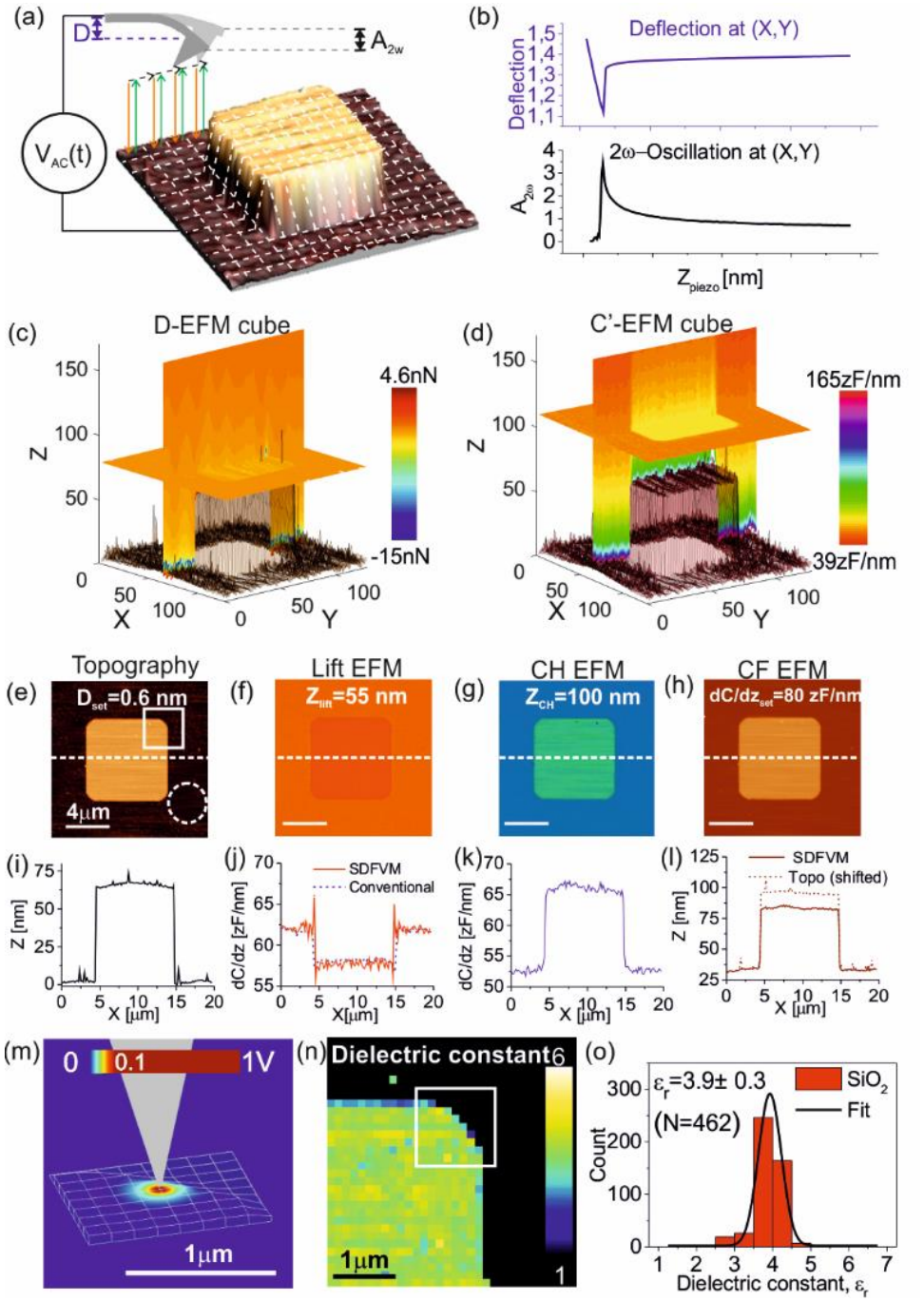

Figure 5.1: (a) Schematic representation of Scanning Dielectric Force Volume Microscopy. (b) Examples of deflection and capacitance gradient approach curves obtained simultaneously in a sample position. (c) Deflection and (d) capacitance gradient (2ω-oscillation amplitude) EFM cubes of data containing the ensemble of measured data (128x128x300 voxels) for a sample consisting of a silicon dioxide pillar ~60 nm thick and ~10 μm wide micropatterned on a highly doped silicon substrate. Experimental parameters: range and duration of each curve 200 nm and 150 ms, respectively; ac applied voltage amplitude and frequency 3V and 5 kHz, respectively; HQ:NSC/Cr-Au probe with equivalent spring constant k=1.7 N/m and resonance frequency 80 kHz. (e) Topographic image obtained from the D-EFM cube for D_{set}=0.6 nm (corresponding to a force ~1 nN). The dashed circle represents a clean region of the substrate and the square the region quantitatively analyzed. (f)-(h) Lift-mode, constant height and constant force (capacitance gradient) EFM images obtained from the C'-EFM cube

of data for Z_{lift}=55 nm, Z_{CH}=100 nm and dC/dz_{set}=80 zF/nm (force amplitude ~0.25 nN), respectively. (i)-(l) Corresponding cross-section profiles along the dashed lines in (e)-(h). In (j), the dashed line corresponds to a capacitance cross-section profile obtained from an EFM image directly acquired in conventional two-pass lift mode at Z_{lift}=55 nm. In (l), the dashed line represents the shifted cross-section topography. (m) The local geometric model with 9x9 pixels used to calculate the force acting on the tip when located at the pixel position (89,92) of the whole image, with the calculated electric potential superimposed on its surface. Tip geometry calibrated on the circular dashed area of (e): R=18 ± 1 nm, θ=14º and C'_{offset}= 0.45 ± 2 zF/nm (N=441). The remaining tip parameters take their nominal values: H=12.5 µm, W=3 µm, L=3 µm. (n) Dielectric constant map of a 32x32 pixels region corresponding to the squared area in the topographic image in (e), obtained by fitting the theoretically calculated EFM approach curves to the experimental curves in the C'-EFM cube at those positions. Pixels for which the EFM approach curve does not depart from the curve used for the tip geometry calibration are set to unity (air). The white square represents the area of the local geometrical model shown in (m). (o) The statistical distribution of N=462 dielectric constants values measured on top of the SiO_2 pillar region in (n). The continuous line represents a Gaussian fit to the data, with a mean of ε_r=3.9±0.3 (N=462).

The post-processing and quantification of the acquired approach curves enables obtaining topographic and EFM images (in all desired modes), as well as dielectric constant maps of the sample (see quantification section). This approach follows and generalizes to any type of sample geometry, and any position in the sample, previous single point quantifications approaches on geometrically simple samples[34,175].

We illustrate the procedure for the case of a test sample consisting of SiO_2 thin film square pillars ~60 nm thick and ~10 µm wide micropatterned on a highly doped silicon substrate. Figure 5.1c and d show, respectively, the deflection and capacitance gradient EFM data cubes representing the ensemble of the 128x128 recorded EFM approach curves (see Figure 5.5). At each position *(X,Y,Z)* of the cubes, the value of the corresponding magnitude (deflection or capacitance gradient) is given through a color scale. The *Z* coordinate in the cubes represents the flattened value of the recorded *Z* piezo value (see Data analysis section). Figure 5.1e shows the topographic image obtained from the D-EFM cube for a set point D_{set}=0.6 nm (corresponding to a force of ~1 nN), while Figure 5.1i shows the corresponding topographic cross-section profile along the dashed line in Figure 5.1e. The topographic image shows the presence of one micropatterned SiO_2 pillar and displays a quality like conventional AFM topographic images. Figure 5.1f-h shows examples of lift-mode, constant height, and constant force EFM images obtained by setting Z_{lift}=55 nm, Z_{CH}=100 nm, and dC/dz_{set}=80 zF/nm in the C'-EFM cube of data, respectively (see Figure 5.5). The corresponding cross-

section profiles along the dashed lines are shown in Figure 5.1 j-l (additional EFM images are provided in Figure 5.3). The lift-mode EFM image obtained from the C'-EFM cube of data is identical to the image measured with the conventional two-pass EFM lift-mode (dashed line in Figure 5.1j).

Note, that the EFM constant height image (Figure 5.1g) shows a positive dielectric contrast, as expected when reasoning in terms of the local electrical polarization properties of the sample. Instead, the lift-mode EFM image shows a negative contrast, which is due to the contribution of topographic crosstalk effects, as mentioned above, and discussed elsewhere[166,168]. Finally, we note that the constant force (capacitance gradient) EFM height image (Figure 5.1h) differs from the (shifted) topographic image in Figure 5.1e, as can be seen in Figure 5.1l, where the corresponding cross-section profiles are compared, as should be. The difference between them reflects, precisely, the electric polarization response of the sample[161], but also includes some topographic crosstalk contributions.

We highlight that with SDFVM, we can obtain EFM images that cannot be obtained directly from conventional EFM imaging modes. This is what we call "real tip-sample imaging." It consists of adding the deflection of the tip during the image reconstruction to correct the tip-sample distance for the realistic tip-sample distance.

Figure 5.1m shows a local geometrical model used to derive the local dielectric constants. The geometrical model has been imported directly from the measured topography in Figure 5.1e so that geometric effects on the local electric polarization properties are automatically incorporated into the model. To reduce the computing time, we used local geometrical models consisting of nxm pixels ($n<N$, $m<M$) that are constructed dynamically at around each position of the tip. In Figure 5.1m, for instance, we show a local 9x9 geometric model corresponding to the pixel position (89,92) in the topographic image in Figure 5.1e.

The probe is represented, as in previous works[97], as a truncated cone of height H and half cone angle θ ended with a tangent sphere of radius R. The tip radius and half cone angle

are determined by fitting the numerically calculated capacitance gradient EFM approach curves to the experimental EFM approach curves measured on a bare conductive part of the substrate[175]. In the present case, we chose a 21x21 pixels region inside the dashed circle in Figure 5.1e, giving R=18±1 nm, θ=14º and an offset C'_{offset}= 45 ± 2 zF/nm, where the errors represent the standard deviation of the values obtained from the fitting of N=441 curves in this region (see Figure 5.2).

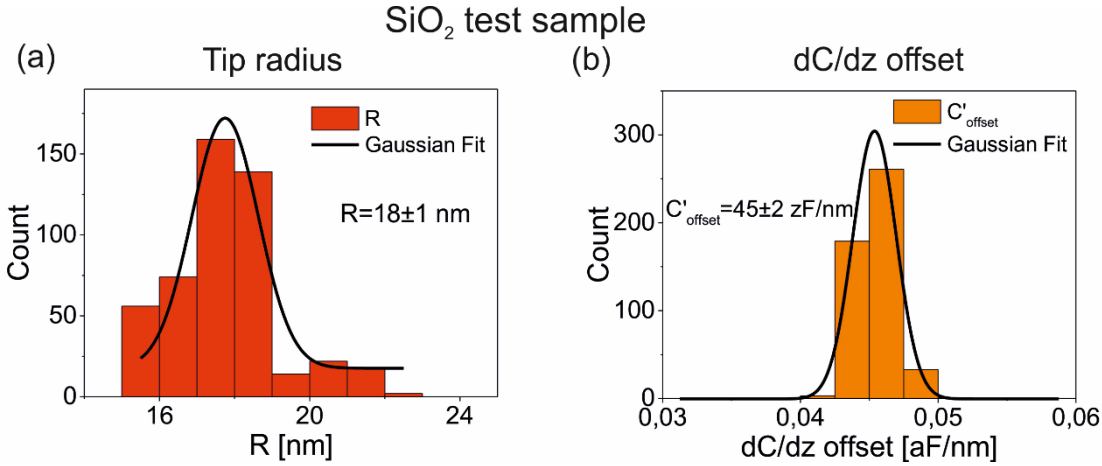

Figure 5.2: (a) and (b) Statistical distribution of the radii and capacitance gradient offsets obtained by calibrating the tip geometry in the 21x21 area inside the highlighted dashed circle in Figure 5.1e. From a Gaussian fit of the data, we obtain the mean values R=18 ± 1 nm, θ=14º and C'$_{offset}$= 45 ± 2 zF/nm.

We note that in the whole analysis, we use Gaussian fits to parametrize the statistical distribution of quantified parameters since it constitutes a good approximation to the actual distributions due to the low noise level of the measurements. Figure 5.1n shows the resulting dielectric constant map for the 32x32 pixels region enclosed by the square in Figure 5.1e (in the dielectric constant map, the pixels on the substrate are set to 1 (air)). The dielectric constant map is nearly uniform on the SiO_2 thin film. This fact is explicitly shown by the sharp distribution of dielectric constant values obtained (see Figure 5.1o). A Gaussian fit to the distribution of dielectric constant values gives the mean value ε_r =3.9±0.3 (N=462), where the error corresponds to the standard deviation of the Gaussian distribution. This value fully agrees with the dielectric constant value reported for SiO_2 (~4), thus validating the quantitative accuracy of SDFVM. We highlight the excellent spatial resolution of the

dielectric constant map, which is reflected in the well-defined dielectric values at the edges of the pillar.

Next, in Figure 5.3, I show in more detail the power of SDFVM with plotting the different possible topographies and EFM cuts of the capacitance gradient Data Cubes. I want to remark again, that all those images are just reconstructed with the same set of data: the SDFVM Data Cube.

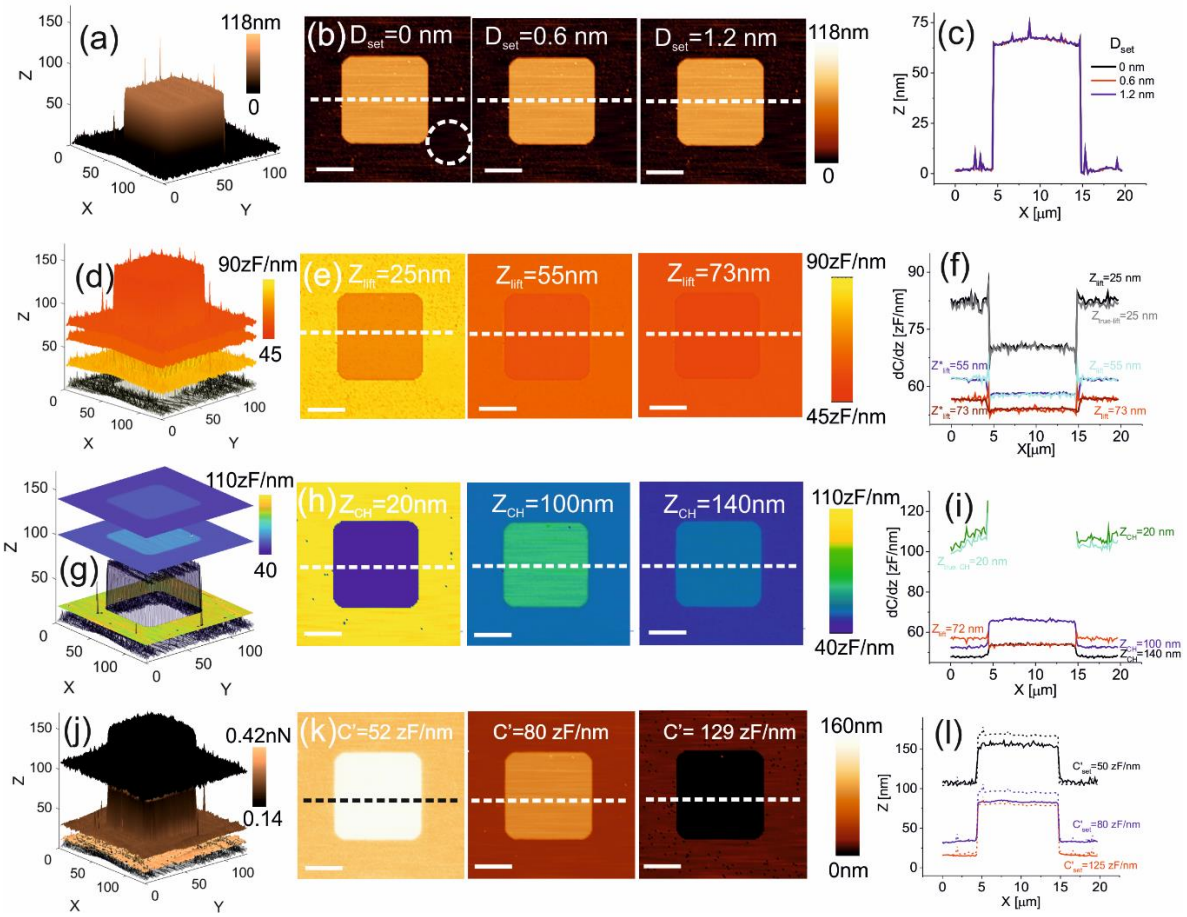

Figure 5.3: (a) Three (indistinguishable) iso-deflection surfaces at deflection set-points D_{set}=0 nm, 0.6 nm and 1.2 nm. (b) Corresponding topographic images obtained from the cuts in (a). The dashed circle represents a clean region of the substrate. (c) (continuous lines) Topographic cross-section profiles along the dashed lines in the images in (b). The dashed line represents a topographic cross-section profile obtained with 0V applied. (d) Capacitance gradient EFM cube of data with three surfaces representing the sample topography lifted at distances Z_{lift}=25 nm, 55 nm and 73 nm, and (e) corresponding obtained lift-mode EFM images. (f) (Black, dark blue and red lines) Corresponding capacitance gradient cross-section profiles along the dashed lines in (e). (light blue and magenta lines) Capacitance cross-section profiles for an image directly acquired in conventional two-pass lift mode at Z_{lift}=55 nm and 73 nm, respectively. (g) Capacitance gradient EFM cube of data with three surfaces representing constant height planes at distances Z_{CH}= 25 nm, 100 nm, and 140 nm and h) corresponding obtained constant height EFM images. At Z_{CH}=25 nm regions of the sample lower than the constant height

distance, and for which no data are available, are shown in black color. (i) (Black, dark blue and green lines) Corresponding capacitance gradient cross-section profiles along the dashed lines in (h). (j) Capacitance gradient EFM cube of data with three iso-capacitance gradient (iso-force) surfaces at values dC/dz_{set}= 52 zF/nm, 80 zF/n, 129 zF/nm and (k) corresponding obtained constant capacitance gradient (electric force) EFM images. (l) (thick lines) Constant capacitance gradient height cross-section profiles along the lines in (k). The thin lines represent the lifted topographic profiles. X-scalebar in the images is 4 μm. The range and duration of each curve is 200 nm and 150 ms, respectively. The ac applied voltage has an amplitude of 3V and frequency 5kHz. The probe is an HQ:NSC/Cr-Au probe with equivalent spring constant k~1.7 N/m, resonance frequency 80 kHz.

5.2.1 Materials and Methods

Next, I explain the EFM data acquisition and calibration. Deflection and 2ω-oscillation amplitude EFM data were recorded with a Nanowizard 4 AFM system (JPK) mounted on a T-1 Eclipse optical microscope (Nikon) and connected to an external lock-in (eLockin 204/2, Anfatec). The acquisition is performed by using the Advanced Quantitative Imaging (JPK) mode in ambient conditions at room temperature and environmental humidity ~30% RH. A set of EFM data consisted of 128x128 deflection and 2ω-oscillation amplitude approach curves, each one with 300 data points and spanning a length between 200 nm and 250 nm. The acquisition time per pixel is between 100 ms and 150 ms, and the lock-in integration time is set to 1 ms, with a gain $G_{lock\text{-}in}$=100. The ac applied voltage had amplitude v_{ac}= 4 V and frequency f_{el}=5 kHz, much smaller than half the resonance frequency of the cantilevers (f_r~70-80 kHz). We used HQ:NSC/Cr-Au conductive probes with equivalent spring constants in the range k~1.2-1.7 N/m, calibrated with the thermal noise method. Raw deflection and 2ω-oscillation amplitude approach curves were converted into calibrated deflection and capacitance gradient data as detailed earlier[34] by using the relationships:

$$D(\text{nm}) = \frac{D_{Raw}(\text{V})}{m\left(\frac{\text{V}}{\text{nm}}\right)} \qquad \text{(eq. 4.1)}$$

$$\frac{dC}{dz}(\text{aF/nm}) = \frac{4k\left(\frac{\text{nN}}{\text{nm}}\right)}{v_{ac}(\text{V})^2} \frac{A_{2\omega}(\text{V}) - A_{2\omega,offset}(\text{V})}{m\left(\frac{\text{V}}{\text{nm}}\right) G_{lock\text{-}in}\left(\frac{\text{V}}{\text{V}}\right)} \qquad \text{(eq. 4.2)}$$

where m(V/nm) is the photodiode sensitivity (i.e., the slope of the contact part of the vertical deflection approach curve), k(nN/nm) is the equivalent spring constant, and $A_{2\omega,offset}$ the

lock-in offset. The photodiode sensitivity, m, was taken as the average value of the values obtained on a bare part of the substrate (see Figure 5.4).

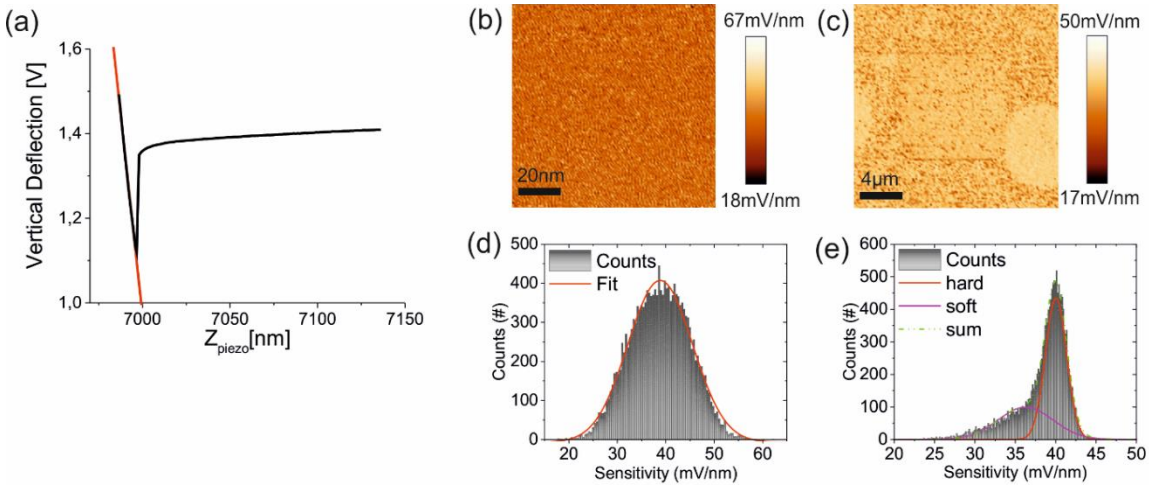

Figure 5.4: (a) Extraction of the photodiode sensitivity from a vertical deflection EFM approach curve. (b) 128x128 map of the photodiode sensitivity obtained on a freshly cleaved HOPG. (c) Idem for the case of the curves and sample in Figure 5.3. (d) The statistical distribution of the photodiode sensitivity obtained from (b). Results show a Gaussian distribution with mean m=39 ±7 mV/nm. (e) Idem obtained from (c). In this case, the distribution is fitted with a double Gaussian distribution with m=40 ±3 mV/nm and m=36 ±7 mV/nm. Experimental parameters: Z_{length}=200 nm, time per pixel 150 ms, v_{ac}=3V, f_{el}=5 kHz, HQ-NSC19/Cr-Au probes, equivalent spring constant k=1.28 N/m.

The photodiode sensitivity is calculated from each vertical deflection approach curve by determining the slope of the contact part of the curves, as usual (see Figure 5.4a). Note that since the approach curves are relatively short in SDFVM (to reduce the number of acquired points and hence the image acquisition time) both positive and negative deflection values can be considered in the least square fitting for a better statistical fit and reach good regression coefficients (e.g., R>0.9). Figure 5.4b and c show examples of maps of the photodiode sensitivity obtained from SDFVM measurements on a freshly cleaved HOPG substrate and on the sample analyzed in Figure 5.3. Figure 5.4d and e show the corresponding statistical distribution analysis of the respectively measured photodiode sensitivities. We observe that for the case of the HOPG the photodiode sensitivity shows a Gaussian distribution with mean value m=39 ±7 mV/nm, while for the case of the SiO_2 micropatterned pillar it is better represented by a double Gaussian distribution with means m=40 ±3 mV/nm and m=36 ±7 mV/nm. The sharp Gaussian distribution represents

approach curves on "clean" parts of the substrate, while the broader Gaussian distribution represents approach curves on "non-clean" parts of the sample, and hence represents both the photodiode sensitivity and the mechanical deformation of the residues. To reduce the uncertainty in the calibrated SDFVM data associated to the uncertainty in the photodiode sensitivity, which is relatively large, we used a single photodiode sensitivity for the whole set of curves, with a value corresponding to the mean value of the Gaussian distribution of the "clean" parts of the substrate.

5.2.2 Data analysis

Next, I explain how the EFM data cubes are treated: extracting the topography and generating the EFM images. EFM data cubes are built up from the 128x128 deflection and capacitance gradient approach curves (see Figure 5.5a and b).

At each position (X,Y,Z) of the cube, the value of either the deflection or the capacitance gradient is plotted. Deflection values are referred to the baseline value of the deflection approach curve. Moreover, the Z coordinate in the cube is the flattened value of the Z piezo values with respect to the zero position, determined as usual from the deflection curve.

The topographic image, $Z_{topo}(X,Y)$, is obtained by setting a positive setpoint to the deflection approach curves in the deflection EFM cube of data, D_{set}, with respect to the far distance baseline, as in conventional Quantitative Imaging[125] (see purple line in Figure 5.5c).

Lift-mode capacitance gradient EFM images, $dC/dz_{lift}(X,Y;Z_{lift})$, are obtained by setting the Z coordinate in the capacitance gradient EFM cube of data to a value representing a constant distance from the topographic surface, i.e., $Z_{lift}(X,Y)=Z_{topo}(X,Y)+Z_{lift}$ (see orange line in Figure 5.5d).

Constant height EFM images, $dC/dz_{CH}(X,Y; Z_{CH})$, are obtained by setting in the capacitance gradient EFM cube of data the Z coordinate to a fixed value with respect to a bare part of the substrate, $Z_{CH}(X,Y)=Z_{CH}$ (see red line in Figure 5.5d).

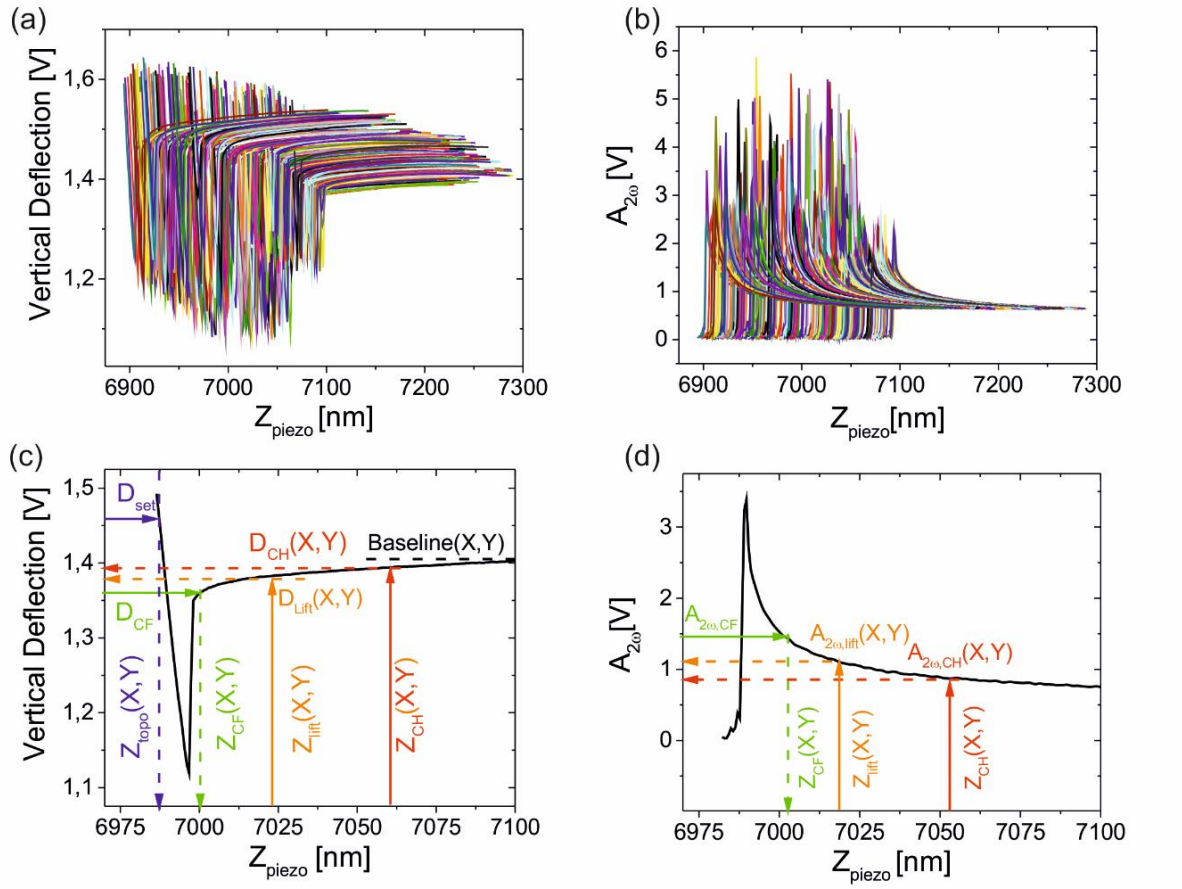

Figure 5.5: Ensemble of the N=128x128 raw approach curves for (a) the vertical deflection and (b) the 2ω-oscillation amplitude for the EFM set of data corresponding to Figure 5.3. (c) and (d) Schematic definition of the main parameters used to extract the topographic and EFM images from the EFM set of approach curves. We include the possibility to build up also dc EFM images (not considered in the manuscript) from the non-contact part of the vertical deflection approach curve in (c).

Finally, the constant capacitance gradient (force) image, $Z_{CF}(X,Y)$, is obtained by setting a constant capacitance gradient value dC/dz_{CF} to the capacitance gradient EFM cube of data (see green line in Figure 5.5d).

All this analysis allows generating many different images (see all of them in Figure 5.6) with only one SDFVM Data Cube. That is why we consider SDFVM is fully in line with the modern approach to functional SPM imaging based on big data analysis and processing[174].

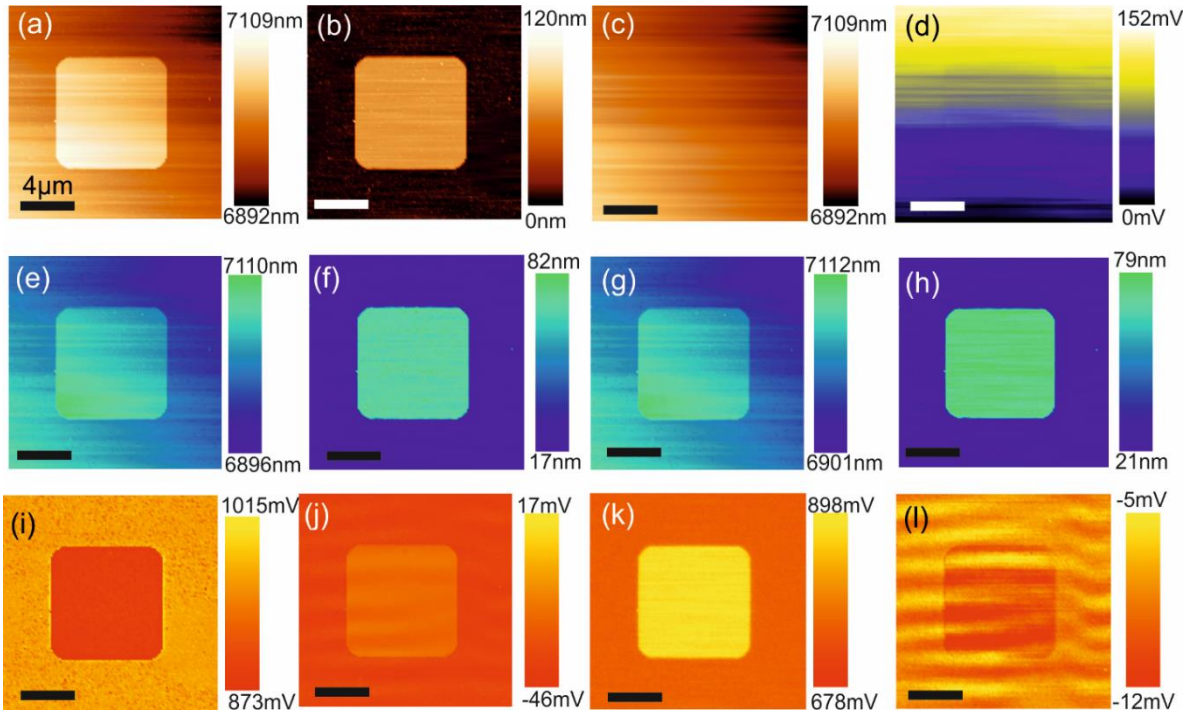

Figure 5.6: (a) Raw and (b) flattened topographic images at set point D_{set}=0 nm (with respect to the baseline value) obtained from the raw deflection EFM approach curves in Figure 5.5. (c) "Plane" subtracted to the raw topographic image in (a) to flatten it and obtain (b). (d) Baseline values calculated as the average of the furthest 30 nm of the vertical deflection curves as a function of position on the sample. (e) Raw and (f) flattened constant DC force EFM images at set point D_{CF}=-0.05 V, corresponding to a force of ~2.1 nN. (g) Raw and (h) flattened constant ac force EFM images at set point $A_{2\omega,CF}$=1.5 V, corresponding to a force of ~0.22 nN. (i) ac and (j) DC lift mode EFM images at a lift distance of 50 nm and 20 nm, respectively. (k) ac and (l) DC constant height EFM images at a substrate distance of 120 nm. Experimental parameters: Z_{length}=200 nm, time per pixel 150 ms, v_{ac}=3V, f_{el}=5 kHz, HQ-NSC19/Cr-Au probes, equivalent spring constant k=1.7 N/m. Scalebar in X is 4μm.

All these operations are performed with a custom application software written in Matlab, see Figure 5.7 (Mathworks Inc.). The application is a user-friendly app that has been built in order to perform all the data treatment explained before.

First, the user must load the RAW data extracted with the commercial AFM (Figure 5.7a). Once the data is loaded into the app, the topographic image is extracted (like it has been explained before), and the user is asked to flatten the image (a normal procedure in any AFM imaging technique), see Figure 5.7b. After that, the software is ready to cut the EFM data cube in any desired way. New windows will pop up (Figure 5.7f-h) showing the different EFM images generated, where the user can select any of the single curves acquired (Figure 5.7c and d) or perform profiles on them (Figure 5.7e).

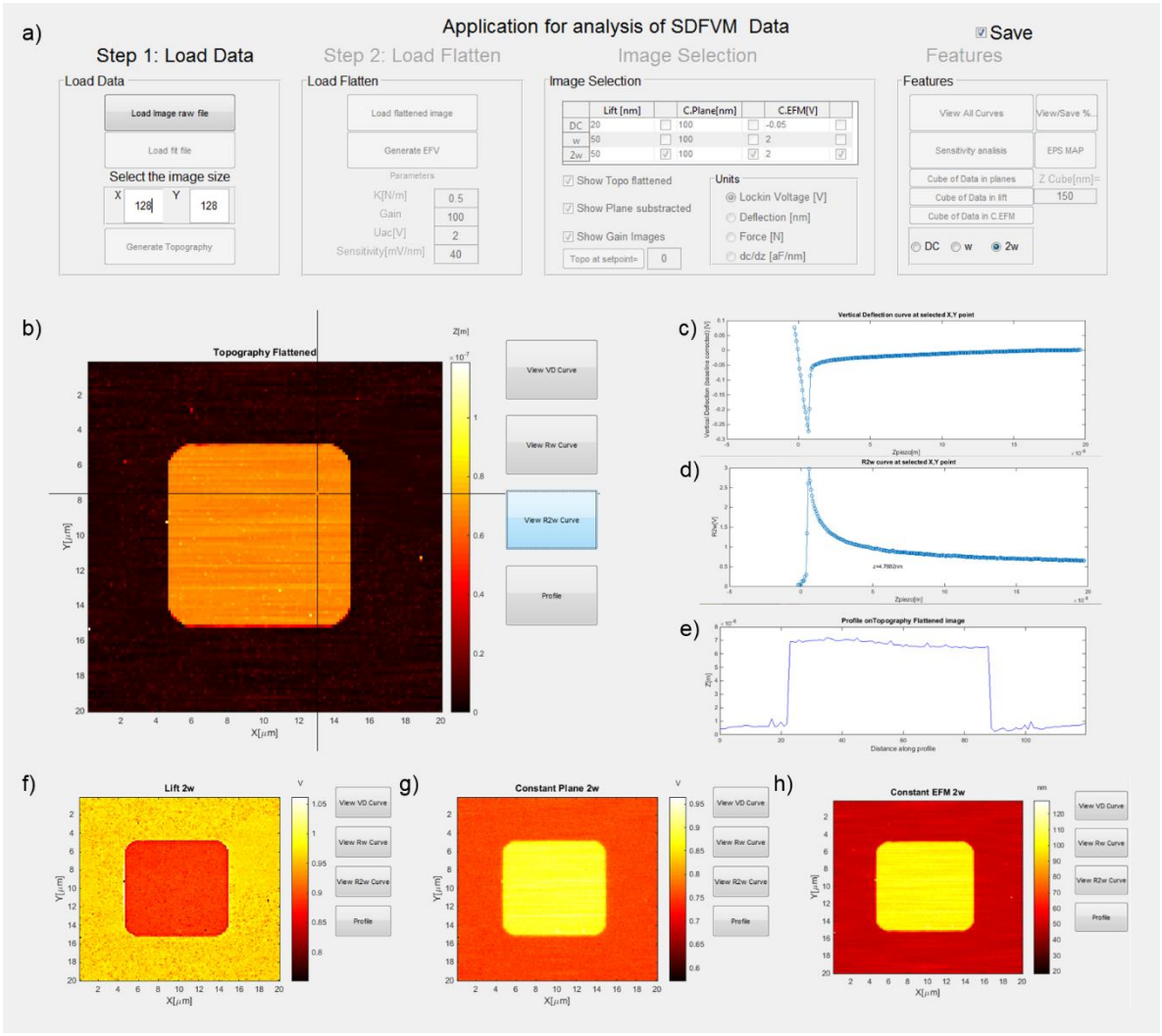

Figure 5.7: Screenshot of the different parts of the software developed for the Data analysis of SDFVM Data. a) Main window. b) Topographic image generated and different buttons to select individual vertical curves c) or 2ω oscillation curves d), or image profiles e). Electrical images generated in the different classical modes from the Data cube: f) Lift Mode, g) Constant Height, h) Constant Force.

5.2.3 Quantification

The quantification of the EFM set of data to derive the dielectric constant images was done by using finite element numerical calculations following the principles and calibration protocols shown elsewhere[28], except for the treatment of the sample topography (explained below). Briefly, the tip was modeled as a truncated cone with height H, and half-cone angle θ ended with a tangent sphere of radius R. On the top part of the cone, a "cantilever" disc of thickness W and radius L_c=L+H.tan(θ) modeled tip cantilever effects. The lever part of the probe was not explicitly modeled, and it was included through a phenomenological

capacitance gradient offset constant, dC/dz_{offset}. The tip radius and cone angle used in the theoretical model were determined by a calibration procedure detailed elsewhere[28]. In a nutshell, calculated capacitance gradient approach curves obtained numerically from a tip-metal model were fitted to the measured capacitance gradient EFM approach curves measured on a bare part of the metallic substrate, with the tip radius, half cone angle and capacitance gradient offset as free parameters. To reduce the variability of the obtained parameters, the half cone angle was determined from the fitting of few approach curves, and then left fixed, leaving only the tip radius and capacitance gradient offsets as free parameters. The microscopic parts of the tip were set to the nominal values given by the manufacturer, i.e., H=12.5 µm, W=3 µm and L=2 µm.

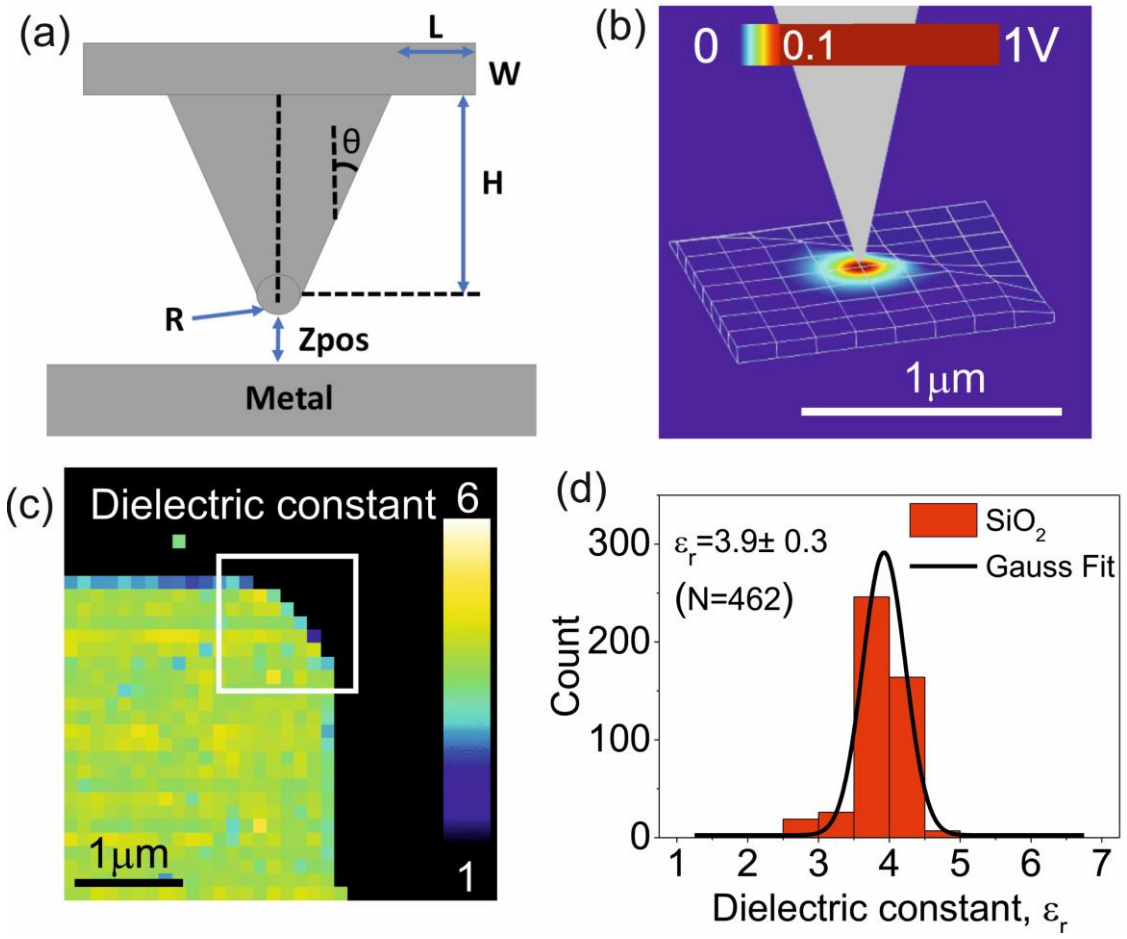

Figure 5.8: a) Sketch of the geometrical parameters for the tip calibration. b) Electric potential map of the simulated zone with the topographic reconstruction. c) Dielectric Map obtained for each pixel. d) Histogram of the pixels in c) and Gaussian Fit, for the dielectric constant extraction.

Hundreds of approach curves were considered for tip calibration (N=441), offering a high statistical significance of the results. For each tip position, a local sample geometry was obtained from the measured sample topography by selecting an area of nxm pixels around the pixel position of the tip, with nxm being smaller than the total number of pixels, NxM. The local geometric models were built by assigning the measured height at the center of the pixel and interpolating linearly between consecutive pixels, giving rise to a smooth enough surface for adequate and efficient meshing and finite element numerical calculation. The remaining part of the simulation area, of radius 10 µm, not included in the local geometric model, was set to zero height and at ground potential. The local geometric models ensure locality, consider all the geometric effects and are computationally manageable. The local sample geometric models were assumed to have a uniform dielectric constant. The electrostatic force acting on the tip calculated for the given local geometrical model was determined by solving Poisson's equation with an applied voltage V, and integrating the Maxwell stress tensor on the tip surface, by using COMSOL Multiphysics 5.3 and custom codes written in Matlab (The Mathworks), as in previous works[28]. EFM approach curves were simulated for different dielectric constants of the local geometrical model and fitted to the experimental EFM approach curve acquired in the corresponding pixel. The value of the dielectric constant obtained was the value assigned to the corresponding pixel position. Following this procedure, to map the dielectric constant of an area of NxM pixels, a total of NxM different reduced geometrical models of nxm pixels were built. For each geometrical model E capacitance gradient approach curves corresponding to the different possible values of the dielectric constant and p data points per curve were calculated. Therefore, a total of NxMxExp voltage potential distributions were calculated to map an NxM area (e.g., for an area of 32x32 pixels, the total number of potential distributions calculated was ~10^5). The computing time per pixel was ~1 hour in a computer with a CPU of Intel® Core™ i7 4.20 GHz and 64 GB of RAM. The pixels corresponding to the substrate were identified by a height threshold and were not explicitly included in the calculations.

5.3 Discussion

With the results reported here, we have enlarged the nanoscale physicochemical information that can be obtained with Scanning Probe Microscopy techniques[176–180]. Furthermore, we have provided a route to develop a novel nanoscale label-free composition mapping technique instrumentally and labor much less intensive than existing alternative techniques based on cryo-Transmission Electron (cryo-TEM)[181] or X-Ray[182] Microscopies (see next chapter for the full nanoscale label-free composition map of a bacterial cell).

There is still some room for improvement in the approach presented here. As we mentioned before, tip convolution effects are not subtracted in the geometrical models built to quantify the local dielectric constant, which can give rise to underestimated dielectric constant values for very small-scale objects. One could overcome this effect by applying some tip deconvolution process to the measured topography[183] and applying a height correction to the affected pixels. This procedure is difficult to implement in an automatic way, and further work is necessary to deal with it. We minimize these effects by using very sharp tips, which induce small tip convolution effects.

On the other side, the local dielectric constant values reported here represent an average dielectric constant value over an area of lateral dimensions a few times the tip radius, which in the present case can be a few tens of nanometers. Achieving dielectric information on smaller scales would require assigning, in the theoretical model, different dielectric constants to each pixel of the local geometrical model and developing an inverse recursive reconstruction algorithm to determine them. Such complex algorithms adapted to dielectric scanning probe techniques have not been developed yet.

Finally, there is also room for improvement in the time required to obtain a nanoscale dielectric constant image. This time is determined by both the time required to acquire a full set of SDFVM experimental data and the time required to compute the theoretical data to fit the experimental results. In the validation work, these times were around ~100 ms and ~1 hour per pixel, respectively. The acquisition pixel time is limited by the frequency of the

applied voltage f_{el}, the number of periods used by the lock-in detection $n_{periods}$, and the number of points per approach curve, N_Z, i.e. $\tau_{pixel} = N_Z\, n_{periods}/(2f_{el})$ (in the present work N_Z=300, $n_{periods}$~3, f_{el}=5 kHz from where τ_{pixel} =100 ms). The number of points per curve is given by $N_Z = L_Z/\Delta L_Z$, where L_Z and ΔL_Z are the length of the approach curves and the spacing between data points. L_Z must be long enough to have a proper range in the non-contact region to set a well-defined baseline for the deflection curves (typically L_Z~100 nm-300 nm above the highest point of the sample). Moreover, the data spacing, ΔL_Z, should be small enough so that the non-linear variations in the Z direction are well captured (typically ΔL_Z~1 nm at the closest distances). Therefore, typically N_Z ~100-300, for equally spaced points. To reduce this number, one could consider non-equally spaced data points (e.g., logarithmically spaced), which still will reproduce well the trend of the approach curves. To implement it, however, one would need instruments able to measure non-constant velocity approach curves. Concerning, the frequency of the applied voltage, it must satisfy $2f_{el}=\alpha f_{res}$, with $\alpha<1$ (here α~0.125), where f_{res} is the resonance frequency of the cantilever (here f_{res}~80 kHz) so that the 2ω harmonic sits on the flat part of the mechanical response spectra (see Figure 2.4d). Therefore, in order to increase the frequency of the electrical signal one must increase the resonance frequency of the cantilever. The use of high resonance frequency probes, with f_{res}~5 MHz, could result in a large improvement in the acquisition times, with the possibility of obtaining complete sets of SDFVM data in less than one minute. The reduction in the computing time per pixel could be obtained by parallelizing the computations, increase the computational power, and developing specific and optimized finite element algorithms adapted to this type of problem. One could also use other fitting approaches that require less theoretical input data, an alternative to least-square fitting procedures[184,185].

5.4 Conclusions

We have shown that nanoscale dielectric constant images free from topographic artifacts can be derived with Scanning Dielectric Force Volume Microscopy (SDFVM) including the real measured topography in the modeling. A full example of all the steps needed to obtain the nanoscale dielectric map have been explained deeply, from the experimental part to the final quantification. In the following chapters, the more relevant applications of SDFVM to biologically interesting samples is shown, as well as the first steps towards its implementation in liquid environment.

6. Sub-cellular label-free composition mapping of single bacterial cells from nanoscale dielectric constant images

This chapter explains the application of Scanning Dielectric Force Volume Microscopy to achieve sub-cellular label-free composition mapping of a single bacterial cell from nanoscale dielectric constant images. It is based on the article: "Mapping the Dielectric Constant of a Single Bacterial Cell at the Nanoscale with Scanning Dielectric Force Volume Microscopy[141]*". Regarding the contributions of the different authors, M. Checa, did the experiments, prepared the sample, and analyzed the data, Nuria Blanco-Cabra cultured the cells, E.Torrents supervised the biological aspects, R. Millan-Solsona developed the quantification methods, R. Fabregas helped in the theoretical modeling, and G. Gomila, wrote the manuscript and supervised the work.*

6.1 Introduction

The dielectric properties of bacterial cells have been the subject of intense research over the years due to its relevance in many fundamental and applied microbiological problems. For instance, the first models on the internal structure of bacterial cells were developed to interpret dielectric spectroscopy measurements performed on bacterial cells suspensions[186]. Moreover, electrokinetic techniques, such as dielectrophoresis, electrorotation, or impedance cytometry, exploit the dielectric properties of bacterial cells to count, sort, test the viability, or identify pathogenic bacterial cells in on-chip technologies[187–193]. Finally, in recent years,

the dielectric properties of bacterial cells have been correlated to the extracellular electron transfer capabilities of some bacterial cell types[194], to Gram type of bacterial cells[35] and to the resistance of single bacterial endospores to humid environments[36].

In the existing studies on the dielectric properties of bacterial cells, homogeneous core-shell dielectric bacterial cell models have been invariably considered to interpret the experimental results[195–197]. These models, however, offer a limited description of the dielectric properties of bacterial cells in the cases in which spatial variations take place along the bacterial cell surface or inside the cytoplasmatic region. Such variations could occur due to changes in the local composition of the cell wall and cytoplasm or to the presence of bacterial nanostructures, such as membrane vesicles[198], cytoplasmic filaments, and inclusions[181]. Furthermore, the existing dielectric bacterial cell studies have neglected the contribution of the small-scale bacterial cell appendages, such as pili, flagella, or membrane cell extensions. These appendages can show, in some cases, specific electrical properties, like in the case of the so-called electrogenic bacteria[199], which are of utmost current interest. In order to access the dielectric properties of bacterial cells at the sub-cellular level, techniques able to image the dielectric constant of a single bacterial cell with nanoscale spatial resolution are necessary, which are currently not available. Developing such techniques, besides its intrinsic interest for dielectric bacterial studies, would also open the possibility to obtain sub-cellular composition maps of single bacterial cells in a label free-way[34].

In this chapter, we address this issue and present the first sub-cellular dielectric constant image of a single bacterial cell and its relationship with the sub-cellular cell composition. To achieve it, we make use of the previously exposed Scanning Dielectric Force Volume Microscopy (SDFVM), which exceeds the capabilities of single point Scanning Dielectric Microscopy methods developed in recent years for nanoscale dielectric studies in single bacterial cells[35,36]. The dielectric constant images of single-bacterial cells obtained with SDFVM show an unparalleled spatial resolution, quantitative accuracy, statistical significance, and are free from topographic effects. From these images, we show that maps

of the local composition of the bacterial cell can be obtained at the subcellular level and without the use of any labeling or staining agents. The presented results open important avenues in Microbiology and in other fields of research, such as Materials Science, Biology, or Nanomedicine.

6.2 Sample preparation

The substrate sample consisted of silicon dioxide square pillars of thickness ~60 nm and width ~10µm micropatterned on a highly doped silicon substrate fabricated on demand (AMO Gmbh), similar to the one used in the previous chapter for the validation. *Pseudomonas aeruginosa* PAO1 (ATCC 15692) were cultivated overnight at 37ºC in LB broth (Sharlab) under aerobic conditions and deposited on the substrate sample. A drop of the culture solution was deposited onto the silicon dioxide pillars sample and left it to rest for 10 min. Afterward, the sample was rinsed with miliQ water to remove weakly adhered cells and residues. Finally, the sample was dried in a desiccator for 2-3 hours and imaged in ambient conditions.

6.3 Dielectric Imaging

Figure 6.1a shows the topographic image of the sample obtained from the D-EFM cube of data (see Figure 6.2a) for a set-point D_{set}=0 nm. A topographic cross-section profile along the dashed line in Figure 6.1a is shown in Figure 6.1g (black line). The topographic image shows the presence of: (1) a portion of a SiO_2 pillar of thickness ~60 nm; (2) a network of nanofilaments ~15 nm high corresponding to (broken) bacterial polar flagella; and (3) a single bacterial cell body ~200 nm high, ~1 µm long and ~0.5 µm wide. The bacterial cell dimensions agree well with those corresponding to bacterial cells in ambient conditions[200].

Figure 6.1b and Figure 6.1c show constant gradient (force) and lift-mode EFM images obtained from the corresponding C'-EFM cube (see Figure 6.2b) for a set point dC/dz_{set}=62 zF/nm and a lift distance Z_{lift}=50 nm, respectively. The corresponding cross-section profiles

along the dashed line in Figure 6.1a are shown in Figure 6.1g-h (red and orange lines, respectively).

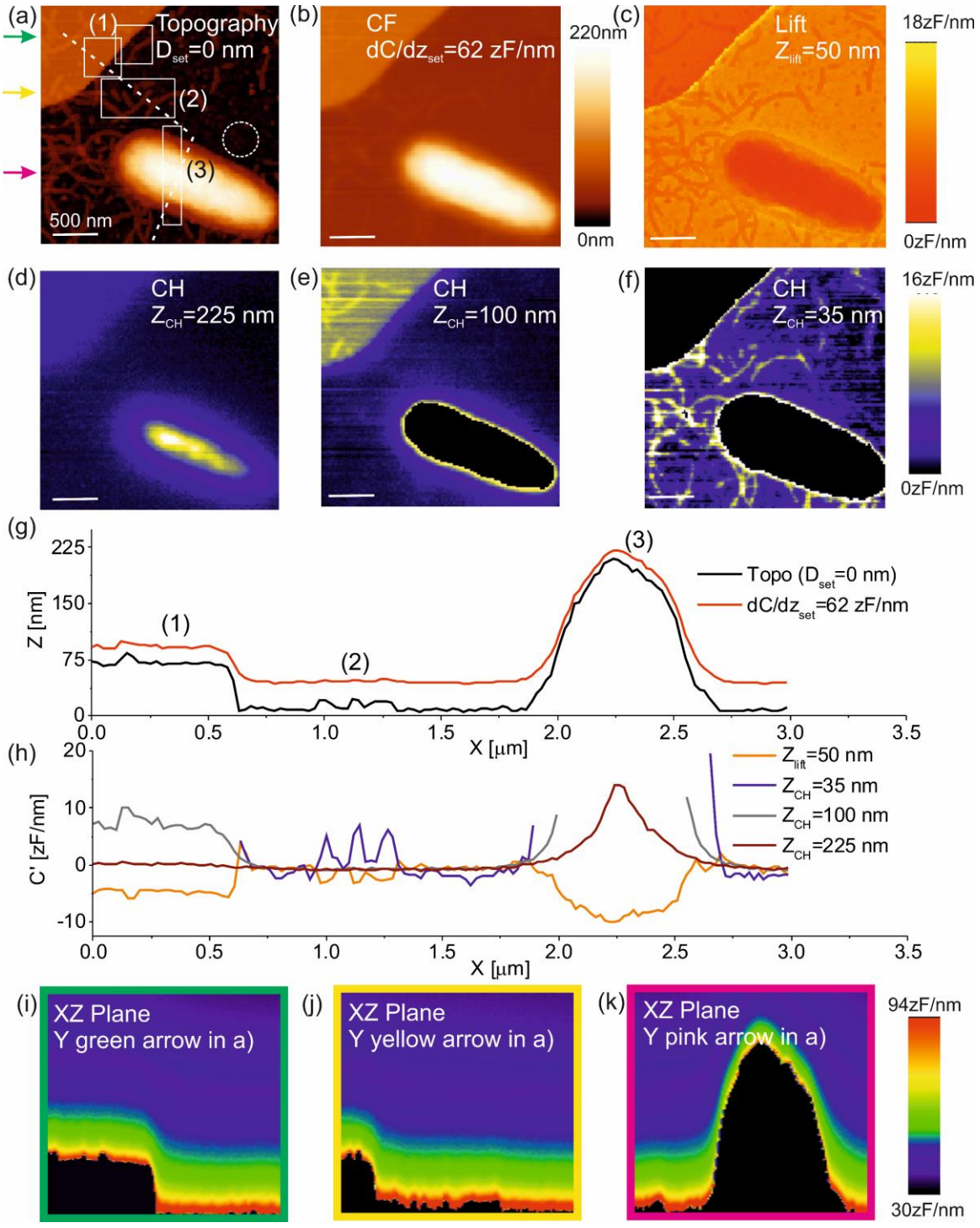

Figure 6.1: (a) Topographic image obtained from the D-EFM cube of data of a *Pseudomonas aeruginosa* bacterial cell adsorbed on a substrate containing micropatterned SiO_2 pillars (set-point D_{set}=0 nN). The rectangles correspond to the areas quantitatively analyzed in Figure 6.3 and the dashed circle to the region used for tip

geometry calibration. (b) and (c) Constant capacitance gradient and lift-mode EFM images obtained from the C'-EFM cube of data at set-point dC/dz_{set}=62 zF/nm and lift distance Z_{lift}=50 nm, respectively. (d)-(f) Constant height EFM images obtained from the C'-EFM cube of data at heights Z_{CH}=225 mn, 100 nm, and 35 nm, respectively. (g) Height profiles corresponding to (a) and (b) along the dashed line in (a). (h) Capacitance gradient profiles corresponding to (c)-(f) along the dashed lines in (a). (i)-(k) Electric signal along the XZ planes for different Y lines (see arrows in a)). Parameters of the acquisition: pixels 128x128, range of the curves 250 nm and data points 300, time per curve 100 ms, ac voltage amplitude 4 V, voltage frequency 5 kHz, HQ:NSC/Cr-Au probes, equivalent spring constant k~1.2 N/m, resonance frequency 80 kHz.

Both types of EFM images show an apparent good dielectric resolution of the different parts of the bacterial cell, including the flagella. These EFM images, however, contain topographic crosstalk contributions[166–168], and hence they do not allow to unambiguously conclude that the variations observed in the EFM images correspond solely to variations in the local electric polarization of the sample.

To determine this, constant height EFM images are much more convenient[34]. Figure 6.1d-f shows three constant height EFM images obtained from the same C'-EFM cube of data at heights Z_{CH}=225 nm, 100 nm, and 35 nm, respectively. These images, which are free from topographic crosstalk effects, show that the bacterial cell body (Figure 6.1d, Z_{CH}=220 nm), the thin dielectric film (Figure 6.1e, Z_{CH}=100 nm) and the bacterial polar flagella (Figure 6.1f, Z_{CH}=35 nm) can all be dielectrically resolved, and, hence, that their dielectric constants can be quantified (see also Figure 6.1h for the respective capacitance gradient cross-section profiles along the dashed line in Figure 6.1a). With SDFVM, constant height EFM images at tip-substrate distances smaller than the maximum height of the sample can be obtained, something that is not possible in conventional constant-height EFM imaging[35].

Finally, in Figure 6.1i, j, k, different electrical XZ planes are shown. In there, we can clearly see the different electrical signal coming from the different objects present on the sample. Such mode of presenting the data (only available in force-volume like modes) can be very interesting, as in one picture one can have an idea of the different signal coming from the different objects, as well as compare the electrical signal of the objects relative to their topographic height.

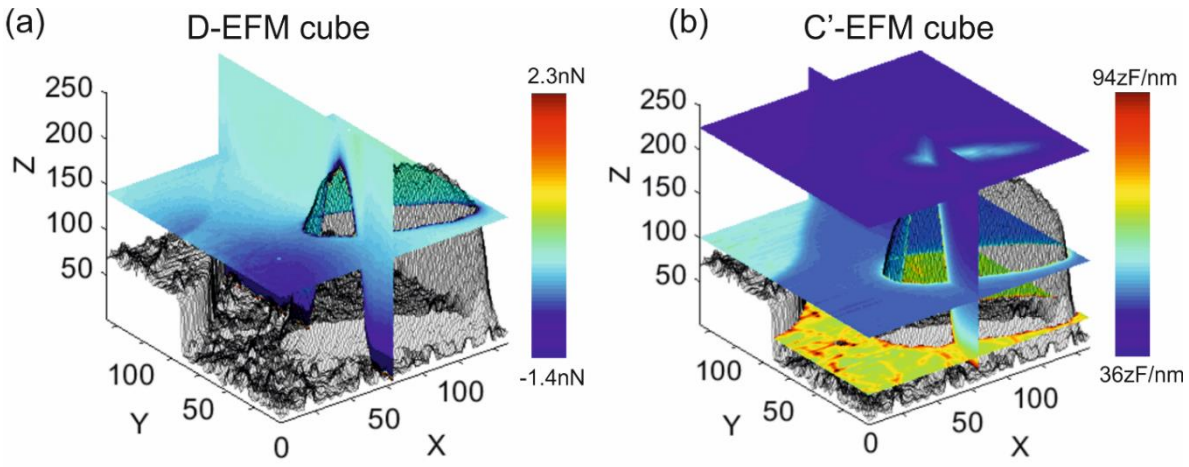

Figure 6.2: (a) Deflection and (b) capacitance gradient (2ω-oscillation amplitude) EFM cubes of data corresponding to Fig. 2 of the manuscript. Each cube of data contains 128x128x300 voxels. Experimental parameters: range and duration of each curve 250 nm and 120 ms; ac applied voltage amplitude and frequency 4 V and 5 kHz; HQ:NSC/Cr-Au probe with equivalent spring constant k=1.2 N/m and resonance frequency 66 kHz. To see the animation of the full Data Cube, go to the supplementary material of [141].

6.4 Single Cell Dielectric Map

The quantitative analysis (dielectric constant map) of the dielectric images shown in Figure 6.1 is shown in Figure 6.3. Figure 6.3a-c show examples of local sample geometric models built up to determine the local dielectric constant of the sample corresponding to the pixel positions (41,103), (68,78) and (74,32) of the topographic image in Figure 6.1a. They correspond, respectively, to the thin SiO_2 pillar, the bacterial polar flagella, and the bacterium cell body.

The local geometrical models include 17x17 pixels around the pixel position for the SiO_2 pillar and flagella and 41x41 for the bacterial cell. The number of pixels is the minimum necessary to ensure that the geometric effects on the electric polarization are accounted for correctly in the numerical calculations. A total of 40x20 different local geometrical models are built for each of the regions analyzed on the SiO_2 pillar and on the flagella, while 13x57 are built for the bacterial cell region.

The sample geometrical models are complemented with a tip geometrical model[97], whose dimensions are calibrated by using the EFM approach curves measured on the bare part of

the substrate located in the 21x21 pixel area within the dashed circle in Figure 6.1a. We obtain R=12 ± 3 nm, θ=5° and C'_{offset}= 10 ± 1 zF/nm (N=441), where the errors represent the standard deviation of a Gaussian fit to the data (see Figure 6.4).

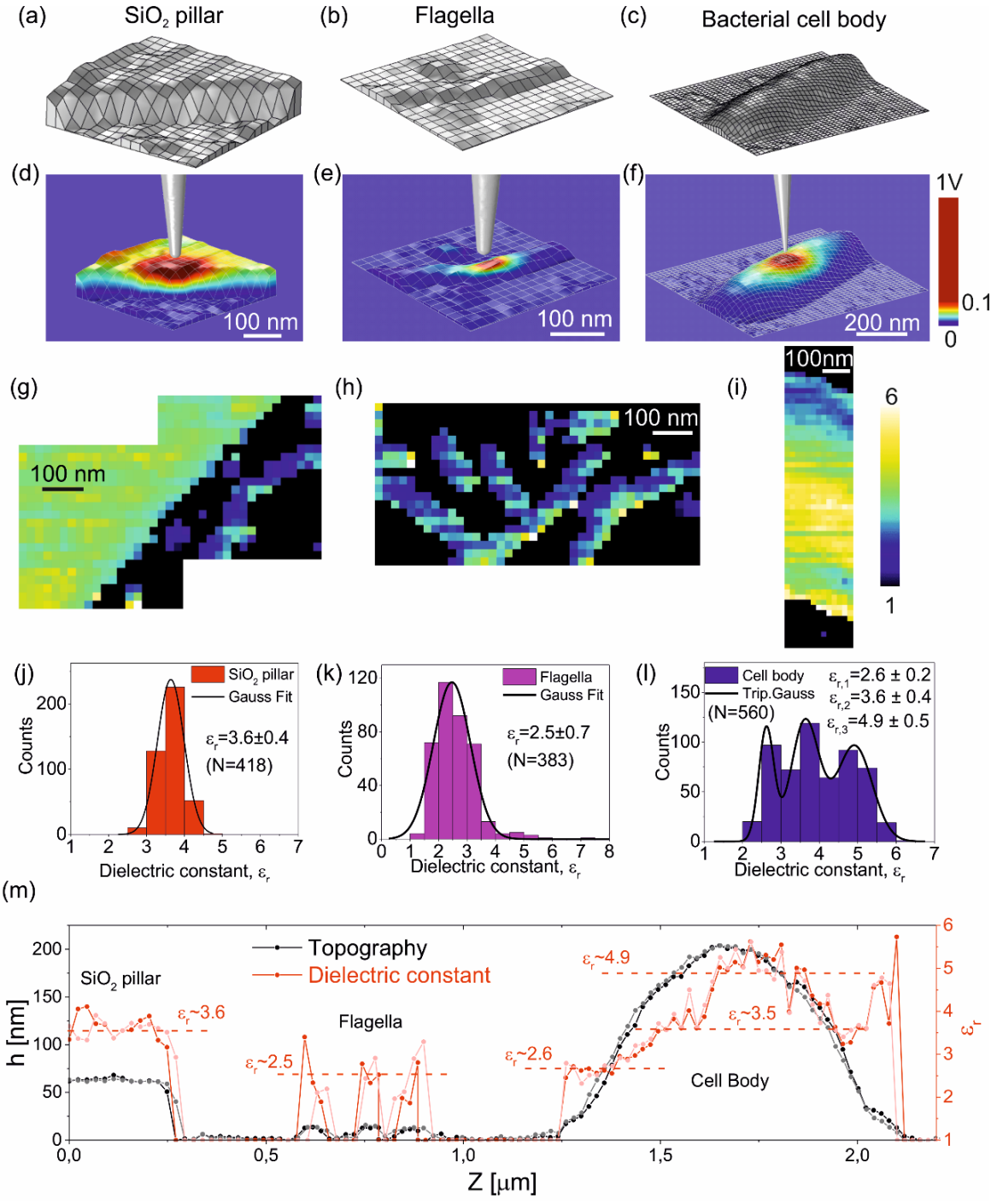

Figure 6.3: (a)-(c) Examples of local geometrical models imported from the measured topography used to calculate the dielectric constant maps on the SiO_2 pillar, the flagella, and the bacterial cell, respectively. The

number of pixels of the local geometrical models are 17x17, 17x17, and 41x41, respectively. (d)-(f) Examples of calculated electric potential distributions for a dielectric constant of 4. Calibrated tip geometry: R=12 nm, θ=5º. (g)-(i) Dielectric constant maps calculated for the regions enclosed in the squares and rectangle in Figure 6.1a. Number of pixels: 40x20 in (g) and (h) and 13x57 in (i). The dielectric constant of the pixels on the substrate has been set to unity. (j)-(l) Histogram representation of the dielectric constant values in the maps for the SiO_2 pillar, the flagella, and the cell body, respectively, together with a Gaussian (or triple Gaussian) fit to the data. The mean dielectric constants obtained from the fittings are shown in the figures, together with the error corresponding to the standard deviation of the fits. (m) Topographic (right axis, black symbols) and dielectric constant (left axis, red symbols) cross-section profiles obtained along the dashed lines in Figure 6.1a.

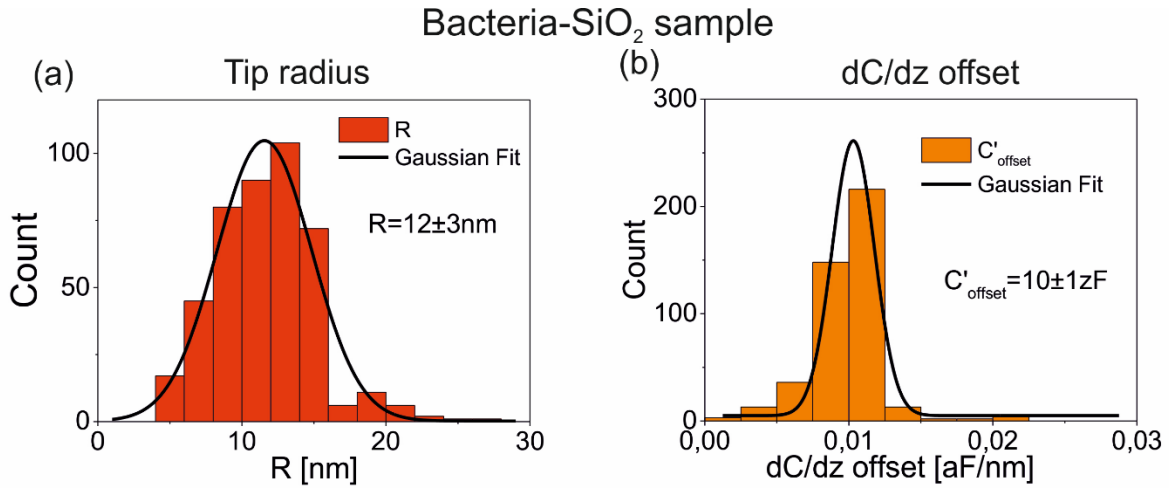

Figure 6.4: (a) and (b) Statistical distribution of the radii and capacitance gradient offsets obtained by calibrating the tip geometry in the area inside the highlighted dashed circle in Figure 6.1a. From a Gaussian fit of the data, we obtain the mean values of R=12 ± 3 nm, θ=5º and C'_{offset}= 10 ± 1 zF/nm. The remaining tip parameters are set to their nominal values, i.e., H=12.5 µm, W=3 µm, L=3 µm.

Figure 6.3d-f shows examples of electric potential distributions calculated for the different local geometries shown in Figure 6.3a-c (see Figure 6.5). The electric potential distributions show the strong effect that the geometry and size of the different parts of the bacterial cell, and of the tip position, have on the local electric polarization of the sample, and, hence, on the electric polarization force acting on the probe. Figure 6.3g-i shows the local dielectric constant images obtained on the selected regions of the areas enclosed in the squares and rectangle of Figure 6.1a, corresponding, respectively, to the SiO_2 pillar, the bacterial flagella and the body of the bacterial cell.

The SiO_2 pillar region (Figure 6.3g) shows an almost uniform distribution of dielectric constant values, eventually slightly modified locally by the presence of some flagella on top of the pillar. The statistical analysis of the distribution of dielectric constant values (Figure

6.3j) shows a mean value $\varepsilon_{r,SiO2}$=3.6±0.4 (N=418) in excellent agreement, again, with the nominal value of high-quality SiO_2 (ε_r ~4), hence demonstrating the correct quantitative implementation of SDFVM for this particular sample.

The bacterial flagella also show a fairly uniform distribution of dielectric constant values (Figure 6.3h), with a mean value $\varepsilon_{r,flag}$=2.5±0.7 (N=383) (Figure 6.3k).

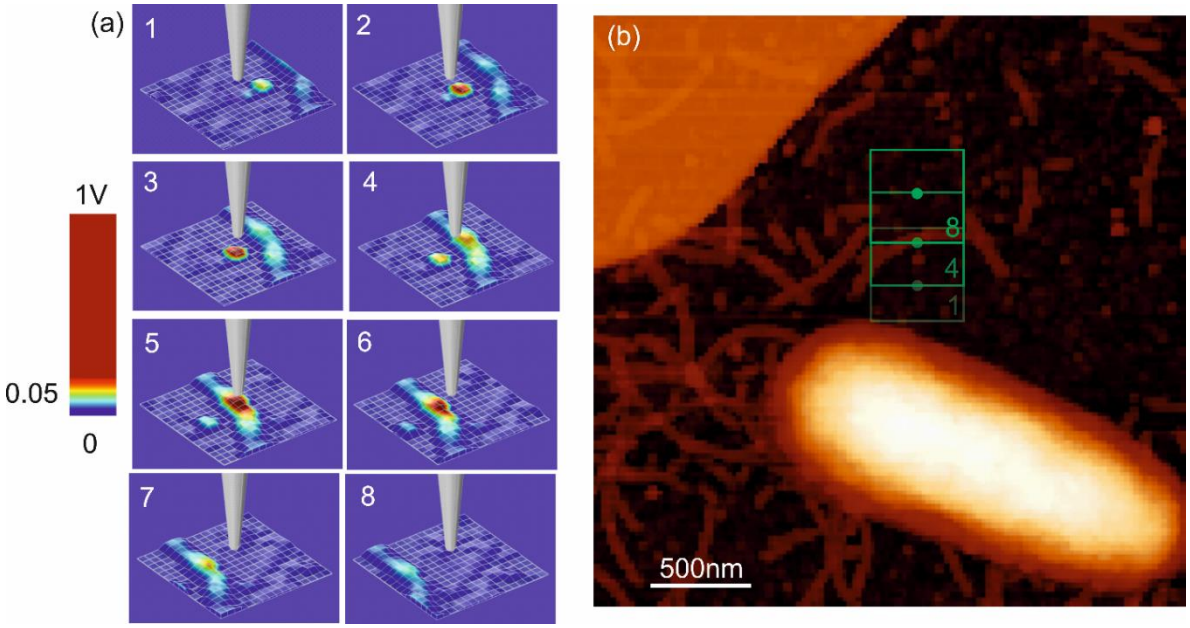

Figure 6.5: (a) Examples of dynamic reconstruction of the local geometry corresponding to a vertical line along the range of pixels (72,71) (1) to (72,86) (8) in the AFM topographic image shown in (b). The green squares show different positions of the tip and of the area included in the local topographic models.

Finally, the bacterial cell (Figure 6.3i) shows a non-uniform distribution of dielectric constant values spanning the range $\varepsilon_{r,bac}$ ~2-6 (see Figure 6.3l). Three characteristic values have been identified, namely, $\varepsilon_{r,bac1}$=2.6±0.2, $\varepsilon_{r,bac2}$=3.6±0.4 and $\varepsilon_{r,bac3}$=4.9±0.5 (N=560), by fitting the statistical distribution of dielectric constants by a triple Gaussian (see Figure 6.3l). The spatial distribution of dielectric constants on the bacterial cell, in correlation with its topography, is explicitly shown in Figure 6.3m, where cross-section profiles of the dielectric constant (red symbols) and topography (black symbols) along the dashed line in Figure 6.1a are displayed. In the figure, the characteristic dielectric constant values identified from the statistical analysis in Figure 6.3j-l are shown by horizontal dashed lines. Figure 6.3m shows

that bacterial cells show a highly non-uniform distribution of dielectric constants when mapped at the sub-cellular level.

6.5 Discussion

The highly non-uniform distribution of dielectric constants in the bacterial cell body reflects the non-uniform composition of the bacterial cell at the sub-cellular level. The first source of composition heterogeneity comes from the internal structure of the bacterial cell, which consists of the bacterial cell wall and the cytoplasmatic region. This internal heterogeneity will give rise to a non-uniform distribution of (equivalent) dielectric constants measured by means of the proposed technique (the measured dielectric constants represents the value a uniform bacterial cell would have in order to give a force on the tip equal to the one measured at the given tip position). As a first approximation, the effect of this internal structure on the measured dielectric constant can be described by using a homogeneous dielectric core-shell model[195–197], with a shell of thickness, δ_{shell}, and shell and core dielectric constants ε_{shell} and ε_{core}, respectively.

Figure 6.6a and b show, respectively, surface and cross-section images of the core shell-model used, with an example of the electric potential distribution calculated for the given tip position. Figure 6.6c shows the calculated (equivalent) dielectric constant profiles predicted from the homogeneous core-shell model for the case in which δ_{shell}=25 nm, ε_{shell}=3, and ε_{core} =1-80 (continuous lines).

The calculated dielectric constant profiles show, indeed, a non-uniform distribution that reflects the internal core-shell structure of the bacterial cell. However, the calculated dielectric constant variation cannot explain the higher variability observed in the measured dielectric constants (see Figure 6.3m). This implies that an additional source of dielectric heterogeneity should be present in the sample. In order to account for it, we considered a heterogeneous core-shell dielectric model, in which the dielectric constant of the shell and/or the core are allowed varying in space at the sub-cellular level. Figure 6.6d shows the spatial variations of the dielectric constant of the shell (blue symbols), able to account for the

experimentally measured dielectric constant (empty red symbols), by assuming that the core is homogeneous with dielectric constant ε_{core}=4. At the same time, it also shows the spatial variations of the dielectric constant of the core (grey symbols), able to account for the experimentally measured dielectric constant (empty red symbols), by assuming that the shell is homogeneous with dielectric constant ε_{shell}=3.

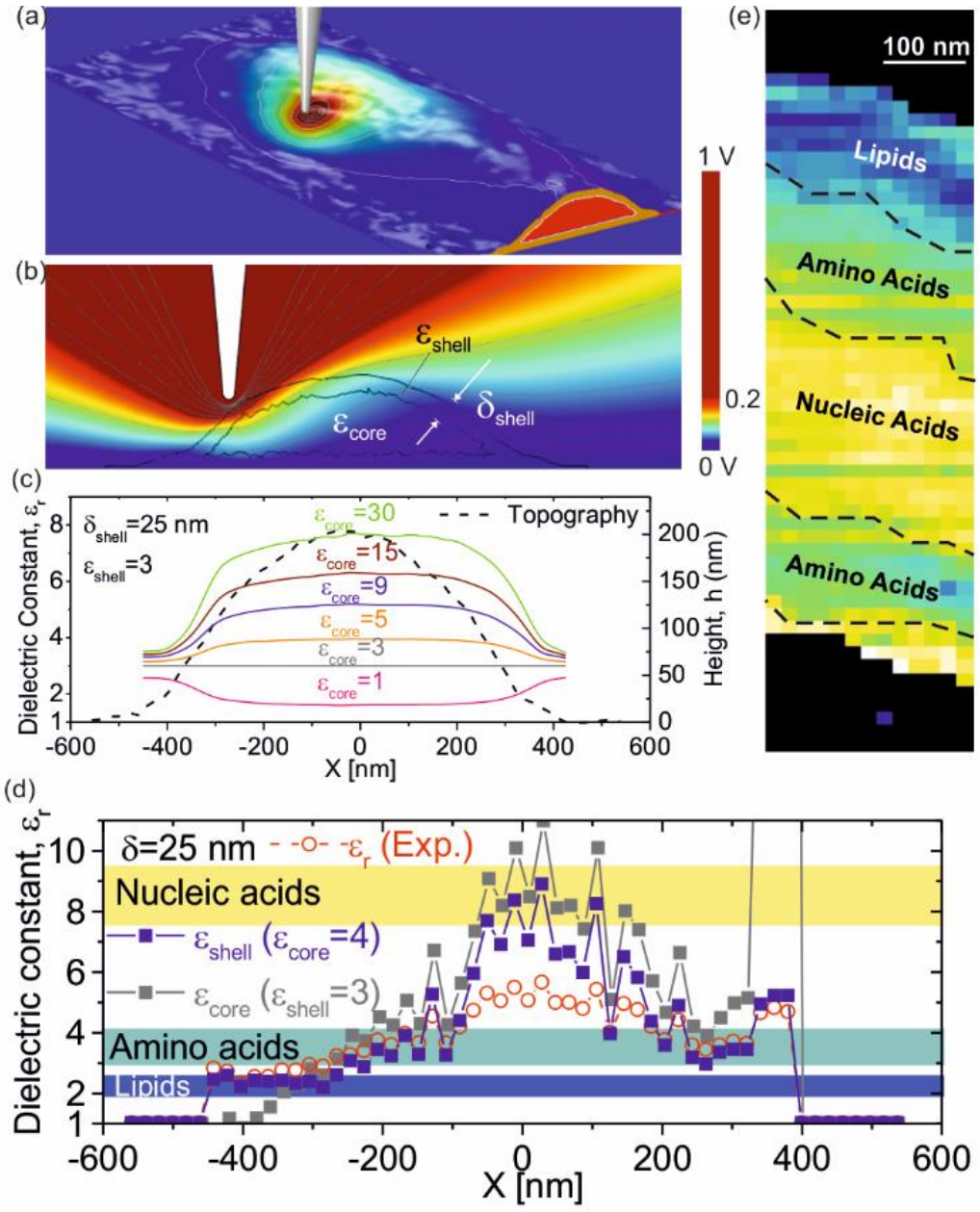

Figure 6.6: (a) Surface and (b) cross-section electric potential distribution for a homogeneous bacterial core-shell dielectric model. Parameters: ε_{shell}=2, ε_{core}=5, ε_{shell}=25 nm. Tip and remaining bacterial cell parameters are the same as in Figure 6.3. (c) (Continuous lines left axis) Bacterial dielectric constant variation predicted by the homogeneous core-shell dielectric model for the case ε_{shell}=3, δ_{shell}=25 nm, and ε_{core}=1-80. The black dashed line

represents the topographic cross-section profile (right axis, same data as in Figure 6.3m). (d) (Blue and grey symbols) Local dielectric constant values for the shell and core compatible with the measured dielectric constant (red symbols, same as in Figure 6.3m) for the case that ε_{core}=4 and ε_{shell}=3, respectively. In both cases, δ_{shell}=25 nm. The shadowed bands represent the characteristic dielectric constant values of the main cell components (lipids, amino acids, and nucleic acids). (e) Predominant shell composition superimposed on the dielectric constant map Figure 6.3i, according to the analysis performed in (d).

The values ε_{core}=4 and ε_{shell}=3 respectively, have been chosen to represent the average dielectric constant of a protein/nucleic acids (for the case of the core) and lipid/amino acids (for the case of the shell) mixture in the proportion found in the cytoplasm and cell wall of bacterial cells, with the dielectric constant of lipids, proteins (or amino acids) and nucleic acids being $\varepsilon_{r,lipids}$~2, $\varepsilon_{r,protein}$~3 and $\varepsilon_{r,nucleic}$~8 [3,31,34] (shadow bands in Figure 6.6d).

For the shell thickness, we have taken δ_{shell}=25 nm, as in previous works[35], in agreement with the known structure of the bacterial cell wall for Gram-negative bacterial cells. According to these results, the shell will show at one of its edges a dielectric constant around ~2 compatible with a rich lipidic composition. On the middle side of the bacterial cell, the shell dielectric constant would increase to ~3-4, compatible with a richer composition of proteins (or amino acids). Finally, in the central part, either the shell or core dielectric constants would increase to values up ~8-9, compatible with a predominant contribution from nucleic acids. On the other side of the cell, a similar behavior is observed, except on the very edge, where a small region with a shell dielectric constant in between proteins (or amino acids) and nucleic acids is found. Figure 6.6e shows the composition map derived, superimposed on the dielectric constant image of the bacterial cell reported in Figure 6.3i. In the above description, we have ruled out potential effects due to the hydration of the bacterial cell due to the ambient moisture, since experiments have been performed under low humidity conditions (<30% RH) for which Gram-negative bacterial cells are hardly hydrated, as we showed elsewhere[35].

The dielectric constant images derived in the present work also include the small-scale bacterial appendages, in this case (broken) polar bacterial flagella. According to the data in Figure 6.3k, we obtained a dielectric constant for the flagella, $\varepsilon_{r,flag}$=2.5±0.7. This value

constitutes a slight underestimation of the actual dielectric constant value of bacterial flagella, due to tip convolution effects present in the measured topography, and hence included in the geometric models used for the quantitative analysis. Nevertheless, our group has shown in the past that assuming a wider geometry for a nanoscale object than its actual geometry provides lower dielectric constant values[99]. This effect can be corrected following a similar approach to the one detailed in[99] for nanoparticles but adapted to the cylindrical geometry of bacterial flagella (see Figure 6.7). We obtain a corrected dielectric constant for the flagella $\varepsilon_{r,flag}^{*}$=4±2, close to the value obtained from single point SDM measurements ($\varepsilon_{r,flag}$~4.5±0.7)[169], and in agreement with the protein composition of bacterial polar flagella[201].

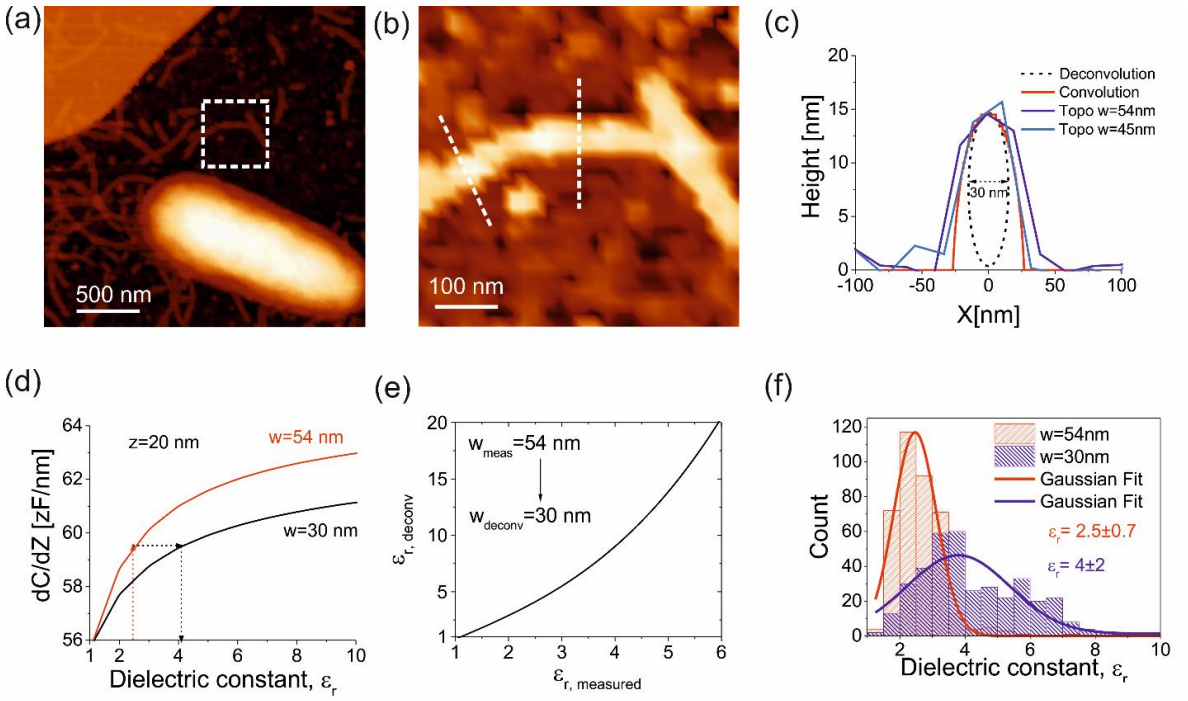

Figure 6.7: (a) Topographic image of the sample analyzed with a highlighted region used for the tip convolution analysis. (b) Digital zoom-in of the topographic image in the region highlighted in (a). (c) (blue lines) Cross-section topographic profile along the dashed lines in (b); (red line) calculated tip-convoluted profile, giving a deconvoluted width w_{deconv}=30 nm; (dashed line) deconvoluted cross-section of the flagellum. (d) Numerically calculated capacitance gradient for a tip at a distance z=20 nm from a cylindrical wire of height h=15 nm, length l= 1 µm, and widths w=54 nm and 30 nm. The dashed line arrows indicate how the conversion of the measured dielectric constant into tip-deconvoluted dielectric constants is performed. (e) The relation between the deconvoluted dielectric constant values and the measured ones. (f) Distribution of tip deconvoluted dielectric constant values (blue bars) and of measured dielectric constant values (red bars). The continuous lines represent Gaussian fits to the distributions giving $\varepsilon_{r,meas}$=2.5±0.7 and $\varepsilon_{r,deconv}$=4±2.

Regarding the limitations of thin-film dielectric models applied to heterogeneous topographically complex samples: Figure 6.8a and b show the dielectric constant maps that would be obtained by using analytical and numerical thin-film models, respectively, applied to the measurements reported Figure 6.1 (for details on the models see[97]).

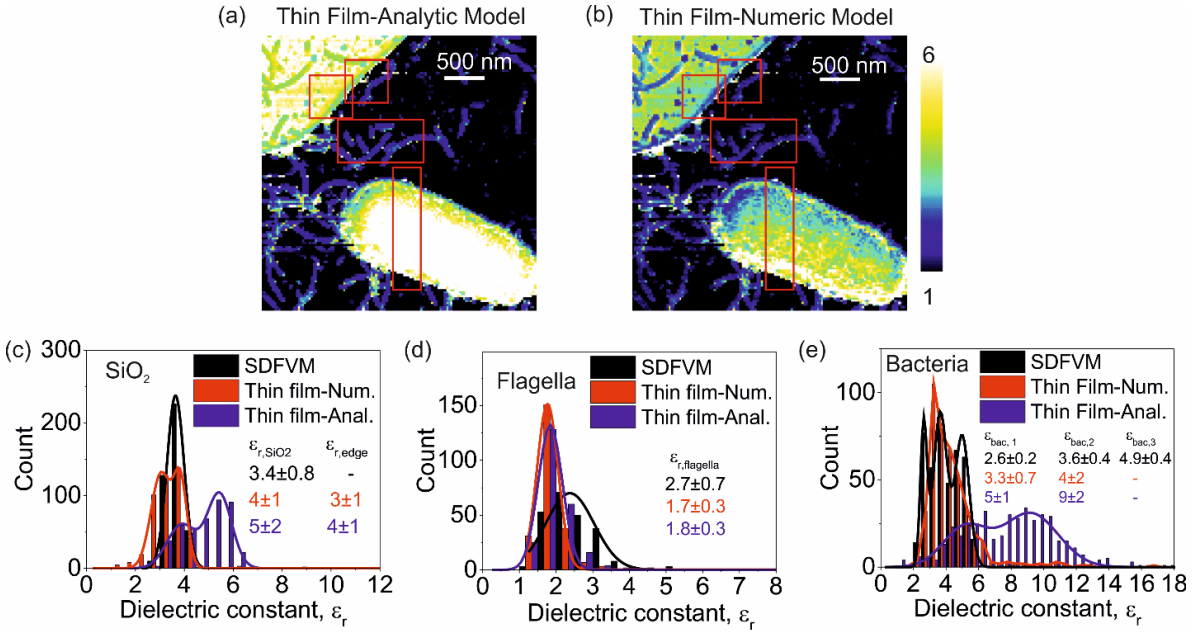

Figure 6.8: Dielectric constant maps obtained by applying (a) analytical and (b) computational local thin-film theoretical models to quantify the C'-EFM cube of data obtained on the sample of Figure 6.1. The square and rectangular highlighted regions correspond to the areas statistically analyzed and compared with the predictions of the manuscript. (c)-(e) (red and blue bars) Histogram analysis of the dielectric constant values corresponding to the highlighted regions in (a) and (b), respectively. The black bars correspond to the data obtained with the method of the present work and reported in Figure 6.3. The continuous lines represent Gaussian (or double Gaussian) fits to the data. The mean values obtained in each case are shown in the figures.

The first aspect to highlight is that at the edges of the micro/nanostructures, the dielectric constant values provided by the thin film models are not correct. This fact is observed in the statistical distribution of dielectric constant values for the SiO_2 part of the sample (Figure 6.8c), which shows two peaks, corresponding, respectively, to the edge and bulk part of the thin film pillar, instead of a single peak as we obtained with the realistic model used in SDFVM (black bars). This artifact is due to the relevance of lateral forces at the edges, which are not included in the thin-film models, and which are compensated by increasing (or decreasing) the value of the local dielectric constant, depending on the tip position with

respect to the edge. In some cases, the lateral force effects are so strong that there is no possible value of the dielectric constant able to mimic these effects, which constitutes a clear signature of the limited applicability of thin-film models. By contrast, the quantification approach followed in our study, by using the actual sample geometry naturally includes the lateral force effects, and hence provides well defined dielectric constant values at the edges of the micro/nanostructures (see Figure 6.3g-i).

Concerning the values of the dielectric constant obtained on the bulk part of the SiO_2 pillar, the numerical thin-film model provides similar values to SDFVM, as expected. Instead, the analytical thin-film model tends to provide larger values, since this model is not accurate for thin films with thicknesses larger than the tip radius, as in the present case.

For the bacterial flagella, the dielectric constant values provided by the thin film models (Figure 6.8d) tend to be smaller than the values obtained with the model based on the measured topography. This result, which has been already highlighted in the past, is a consequence of the thin film models providing the electric polarization force corresponding to an extended thin film of thickness equal to the local height of the nanoscale object. As a result, for small objects, the thin-film models consider larger areas and hence predict higher forces, which is compensated by providing smaller dielectric constants. In some cases, again, no real value can be found to mimic this effect, showing the limited applicability of the thin-film models again.

Finally, in the case of the bacterium cell the distribution of dielectric constant values predicted by the analytical thin-film model is very far from the distribution obtained with a realistic geometrical model, while the predictions of the numerical thin-film model are closer, but they fail to identify the three different contributions that we have identified and discussed in our study (Figure 6.8e), again due to the relevance of the lateral force effects on topographically complex samples. Again, in several pixels, no dielectric constant value can be obtained with these models. We then conclude that thin-film dielectric models do not provide realistic quantitative dielectric constant values when applied to bacterial cells or

provide values that are affected by the topography of the sample, and hence, they cannot be used to infer information on the sub-cellular bacterial cell composition.

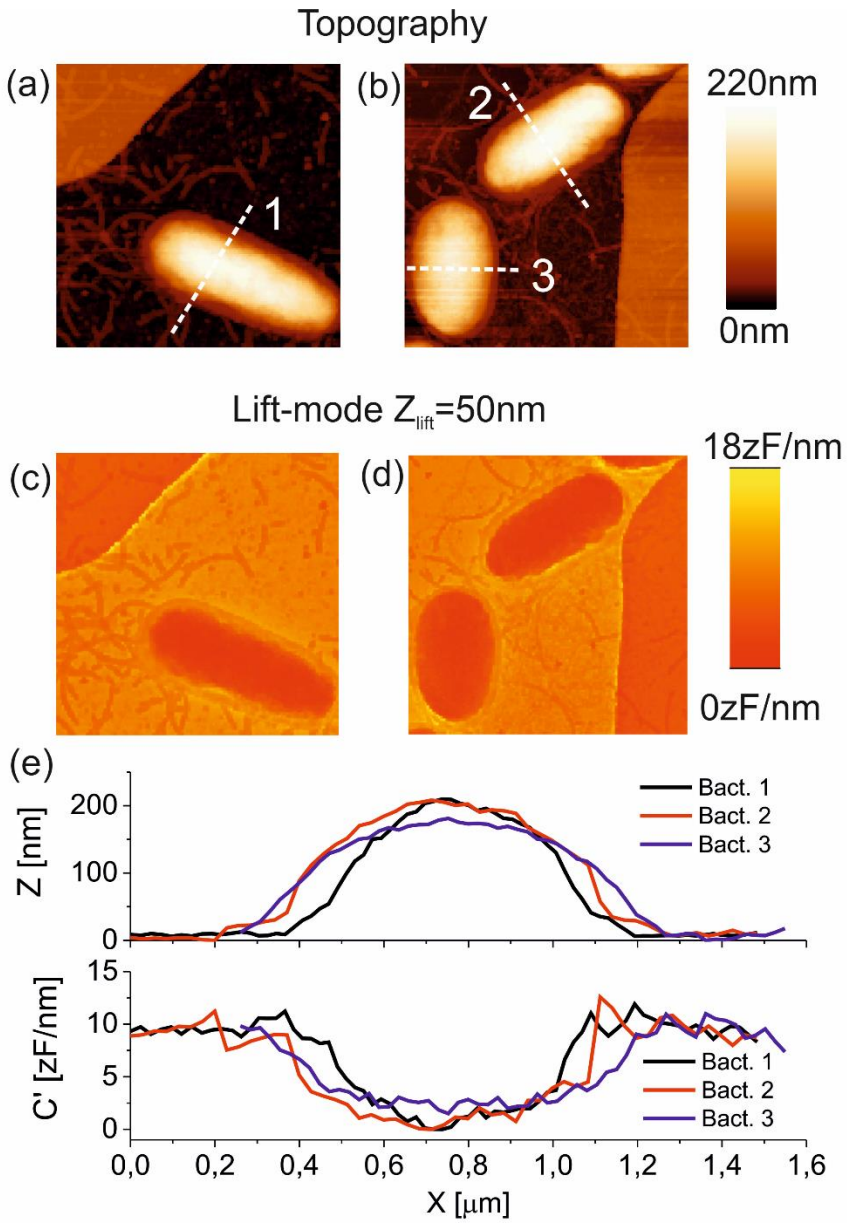

Figure 6.9: Comparison of the topographic and lift mode EFM images between different bacterial cells on the same sample. (a) and (c) correspond to the bacteria discussed in the main text. (b) and (d) correspond to two additional bacterial cells. Both the topography and the electric response is similar.

Finally, to show the reproducibility of the results reported during this chapter, in Figure 6.9, one can see the image of two more bacteria. As it can be seen, similar results to the ones shown have been obtained on the different cells measured. Figure 6.9a and c correspond to the bacteria discussed in the main text. Figure 6.9b and d correspond to two additional

bacterial cells. Figure 6.9e shows the topographic and lift-mode profiles, where one can see that for the bacteria with similar height, the lift mode contrast at the same distance shows very similar contrast along the bacteria's profile, which suggest that the numerical values of the dielectric constant we would obtain in such bacteria will be very similar to the ones obtained during this chapter.

6.6. Conclusions

We have demonstrated the possibility to obtain dielectric constant maps of single bacterial cells with nanoscale spatial resolution by means of Scanning Dielectric Force Volume Microscopy. The proposed method offers the possibility to map the local dielectric constant of any sample irrespectively of the complexity of its topography. The dielectric constant maps obtained reflect the distribution of the basic cell components (lipids, amino acids, and nucleic acids) inside and along the cell, providing much richer information than that offered by simple homogeneous core-shell models. The presented results open the route for the development of a novel nanoscale label-free composition mapping technique for Biology and Materials Science based on the local dielectric response of the samples.

7. Dielectric imaging of topographically complex samples

This chapter shows the application of Electrostatic Force Volume Microscopy (EFVM) for the acquisition of all types of EFM images in different topographically complex samples. It shows the capabilities of EFVM to obtain nanoscale electrical images in a variety of systems like small sized metallic nanowires, buried metallic structures (subsurface imaging), or bigger systems like eukaryotic cells in dry conditions.

7.1 Introduction

Like it has already been explained in previous chapters, despite the achievements that dielectric SPM techniques have accomplished[156], they still face difficulties when applied to topographically complex samples such as non-planar nanocomposite materials, 3D electronic devices, or biological samples (e.g., cells). The imaging modes for dielectric imaging currently implemented, e.g., constant height with respect to the substrate, constant distance with respect to the sample surface (or *lift-mode*), or constant magnitude (e.g., electric force), all present important limitations when applied to this type of samples. Lift-mode, for instance, introduces topographic cross-talk contributions in the dielectric image, which cannot always be completely removed by post-processing[166,168]. Constant height imaging, on its side, is not adequate for samples showing large topographic variations since the tip-substrate distance must be set too high. Finally, imaging at constant magnitude (force, current, etc.) provides images that mix dielectric and topographic information, which are, again, difficult to separate by post-processing.

In this chapter, we will show the application of the experimental technique developed during this work of thesis to three different systems of great interest in the field of nanotechnology. Namely (see Figure 7.1): metallic nanowires (NWs), subsurface properties of buried metallic pillars, and eukaryotic cells in dry environment. Here, we exploited the powerful tool of EFVM to obtain EFM images in all the available modes in a quick and automated way.

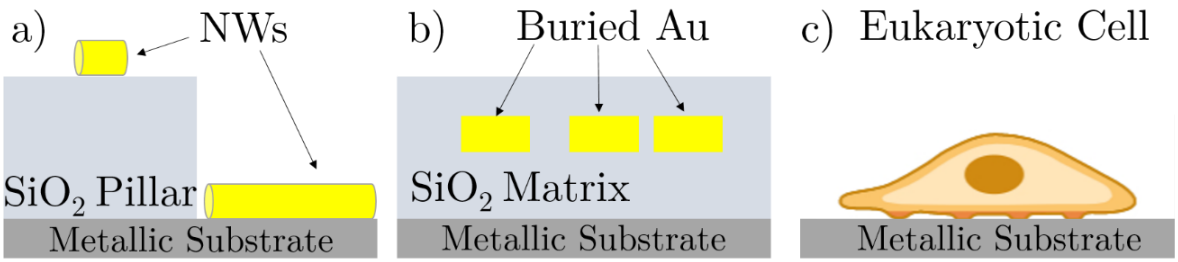

Figure 7.1: Sketch of the samples imaged in this chapter. a) Metallic NW's deposited on top of thin dielectric pillars. b) Metallic pellets buried into a dielectric matrix. c) Eukaryotic cells.

We want to differentiate between EFVM and SDFVM. EFVM is only referred to the acquisition of EFM images through the force-volume approach presented in chapter 5. However, SDFVM is referred to the coupling EFVM data to the numerical simulations in order to obtain the detailed local dielectric constant map of the sample (like the one presented in chapter 6).

7.2 Nanowires

In the nanotechnology field, sometimes samples containing different topographical features of both conductive and nonconductive nature are found. In such cases, the study of their dielectric properties can be of major relevance. Here we show an example for the case of nanowires (NWs) in the presence of SiO_2 pillars.

The sample consists of silicon dioxide square pillars of thickness ~60 nm and width ~10 µm micropatterned on a highly doped silicon substrate fabricated (AMO Gmbh), where ~40 nm silver nanowires (acquired commercially from Novarials) have been deposited on top, just by drop-casting the solution containing the nanowires and allowing the solvent to evaporate.

Figure 7.2 shows the application of EFVM to this type of sample. Figure 7.2a shows a topographic image at a set-point D_{set}= 0 nm obtained from the deflection EFVM cube. It shows two silver nanowires (~38 nm and ~48 nm in diameter, respectively) crossing from the Si^{++} substrate to the top of the SiO_2 pillar (see also the topographic cross-section profile along the dashed line in Figure 7.2g, black line).

Figure 7.2b and Figure 7.2c show constant capacitance gradient (dC/dz_{set}=44 zF/nm) and lift-mode capacitance gradient EFM (Z_{lift}=50 nm) images obtained from the corresponding capacitance gradient EFVM cube of data. Both images are represented with relative values (contrast) with respect to the value on the bare substrate. Moreover, Figure 7.2d-f shows three constant height EFM images at Z_{CH}=120 nm, 73 nm and 58 nm, respectively, also plotted in relative values with respect to the substrate. Finally, Figure 7.2g shows the cross-section profiles of all images along the dashed lines.

These images illustrate several advantages of using EFVM for the nanoscale dielectric imaging of this type of samples containing different topographical features of both conductive and nonconductive components. First, it enables obtaining EFM images in all conventional EFM modes at any desired distance with no sample perturbation (silver nanowires are weakly adsorbed to the substrate), since to obtain all the EFM images only one topographic image is acquired. Second, because it allows obtaining EFM images that cannot be obtained by conventional EFM imaging without sample or tip damaging (e.g., constant height EFM images below the maximum height, such in Figure 7.2e and f). And third, because it allows a better qualitative interpretation of the images. For instance, of the three types of EFM images shown, only the constant height EFM image allows concluding unambiguously that the two nanowires can be resolved *dielectrically*. The apparent better resolution shown by the lift-mode and constant capacitance gradient EFM images is due to the cross-talk contribution from the topographic image always present in this type of image.

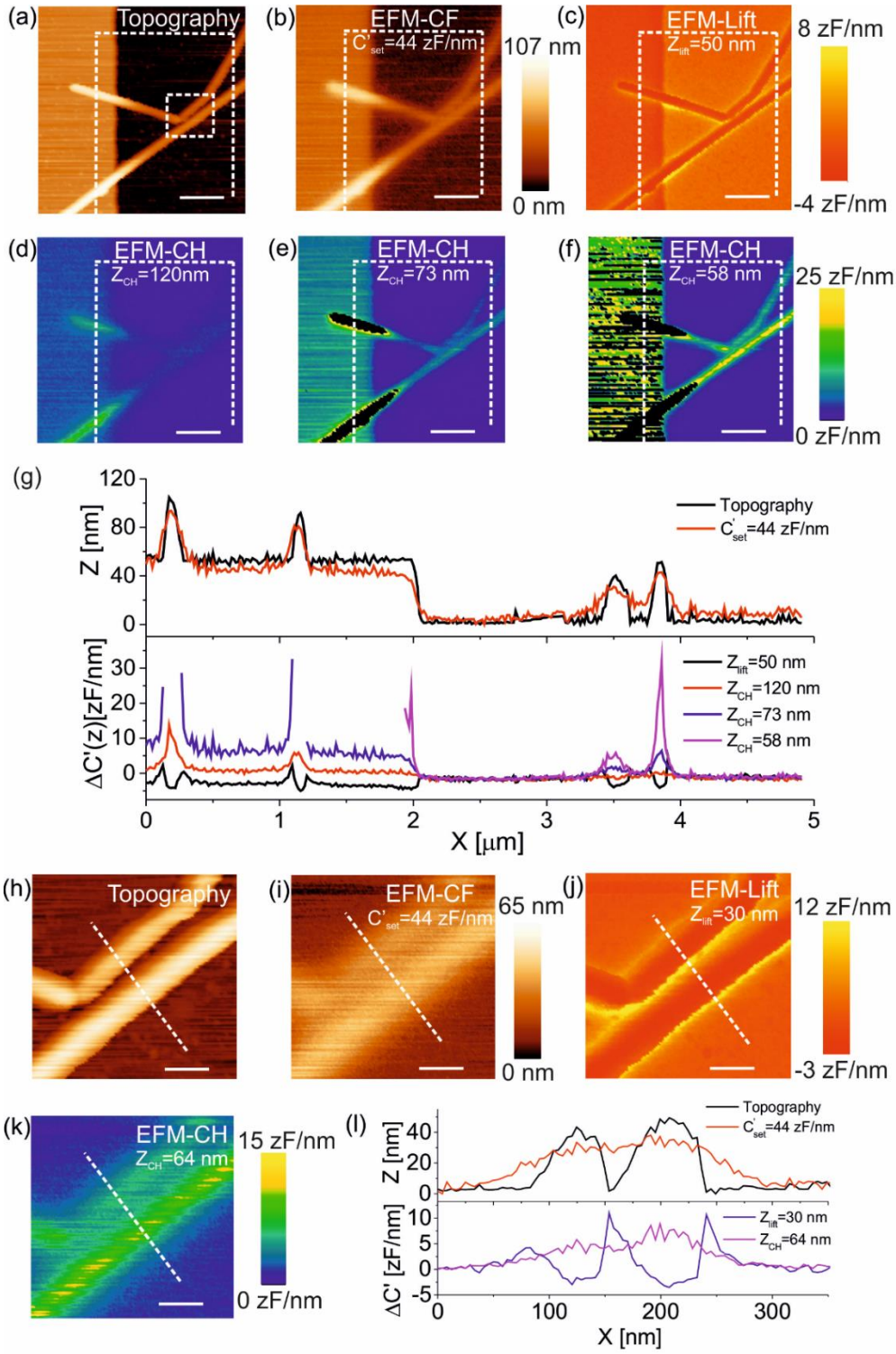

Figure 7.2: (a) Topographic image of silver nanowires ~38 nm and ~48 nm in diameter on ~60 nm thin SiO_2 micropatterned pillars on Si^{++} obtained from the deflection SDVFM cube of data at a set-point D_{set}=0 nm. (b) Constant capacitance gradient (force) EFM image obtained from the capacitance gradient EVFM cube of data at set-point C'_{set}=44 zF/nm. (c) Lift-mode EFM image obtained from the capacitance gradient EVFM cube at a lift distance Z_{lift}=50 nm. (d)-(f) Constant height EFM images obtained from the capacitance gradient EVFM cube of data at a height distances Z_{CH}=120 nm, 73 nm and 58 nm. (g) Cross-section profiles along the dashed

lines in (a)-(c) and (d)-(f). (h)-(k) Topographic (D_{set}=0 nm), constant capacitance EFM (C'_{set}=44 zF/nm), lift-mode EFM (Z_{lift}=30 nm) and constant height EFM (Z_{CH}=64 nm) images of the region of (a) showing the two silver nanowires close together (dashed square), respectively. (l) Cross-section profiles along the lines in (h)-(k). Parameters of the acquisition: pixels 128x128x300 data points, range of the curves 300 nm, time per pixel 150ms, ac voltage amplitude 2.5V, voltage frequency 5 kHz, HQ:NSC/Cr-Au probes, equivalent spring constant k=1.28 N/m, resonance frequency 80 kHz. Image size in a)-f) is: 4.5µm · 4.5µm. Image size in h)-k) is: 1µm · 1µm.

7.3 Buried dielectric microstructures

One of the main limitations of AFM is that it is normally restricted to imaging surface features. Nevertheless, some of the AFM electric modes, such as KPFM or EFM, have shown the capabilities to image subsurface properties[37,202,203], as the magnitude to which they are sensitive is the capacitance gradient (strongly dependent on geometric and electric properties of the specimen placed between the tip and the metallic substrate). Groups working in that field, claim that KPFM or EFM, coupled with non-trivial deconvolution algorithms could be used to perform tomographic imaging[204]. The images in Figure 7.3, illustrate the capabilities of EFVM for the nanoscale characterization of subsurface properties, giving a new tool to acquire in 3D the spatial dependence of the capacitance gradient, which is the magnitude of interest for such studies.

The sample consists of 50nm thick Ti/Au metallic pellets of different shapes buried into a 100nm thick SiO_2 matrix, acquired commercially. As the sample is thought to probe the subsurface capabilities of EFM, consecutive pellets are separated differently to probe the resolution limit.

Figure 7.3a shows a topographic image at a set-point D_{set}= 0 nm obtained from the deflection EFVM cube. It shows the surface of the matrix containing the buried metallic pellets. Even if the pellets are 50nm thick, the fabrication process of the sample allows obtaining a quite flat surface, with some bumps on the order of 2 or 3 nm (see also the topographic cross-section profile along the dashed line in Figure 7.3g, black line).

Figure 7.3b and Figure 7.3c show constant capacitance gradient (dC/dz_{set}=110 zF/nm) and lift-mode capacitance gradient EFM (Z_{lift}=50 nm) images obtained from the corresponding

capacitance gradient EFVM cube of data. Both images are represented with relative values (contrast) with respect to the value on the bare substrate. Moreover, Figure 7.3d-f shows three constant height EFM images at Z_{CH}=100nm, 60nm, and 40nm, respectively, also plotted in relative values with respect to the substrate. Finally, Figure 7.3g shows the cross-section profiles of all images along the dashed line.

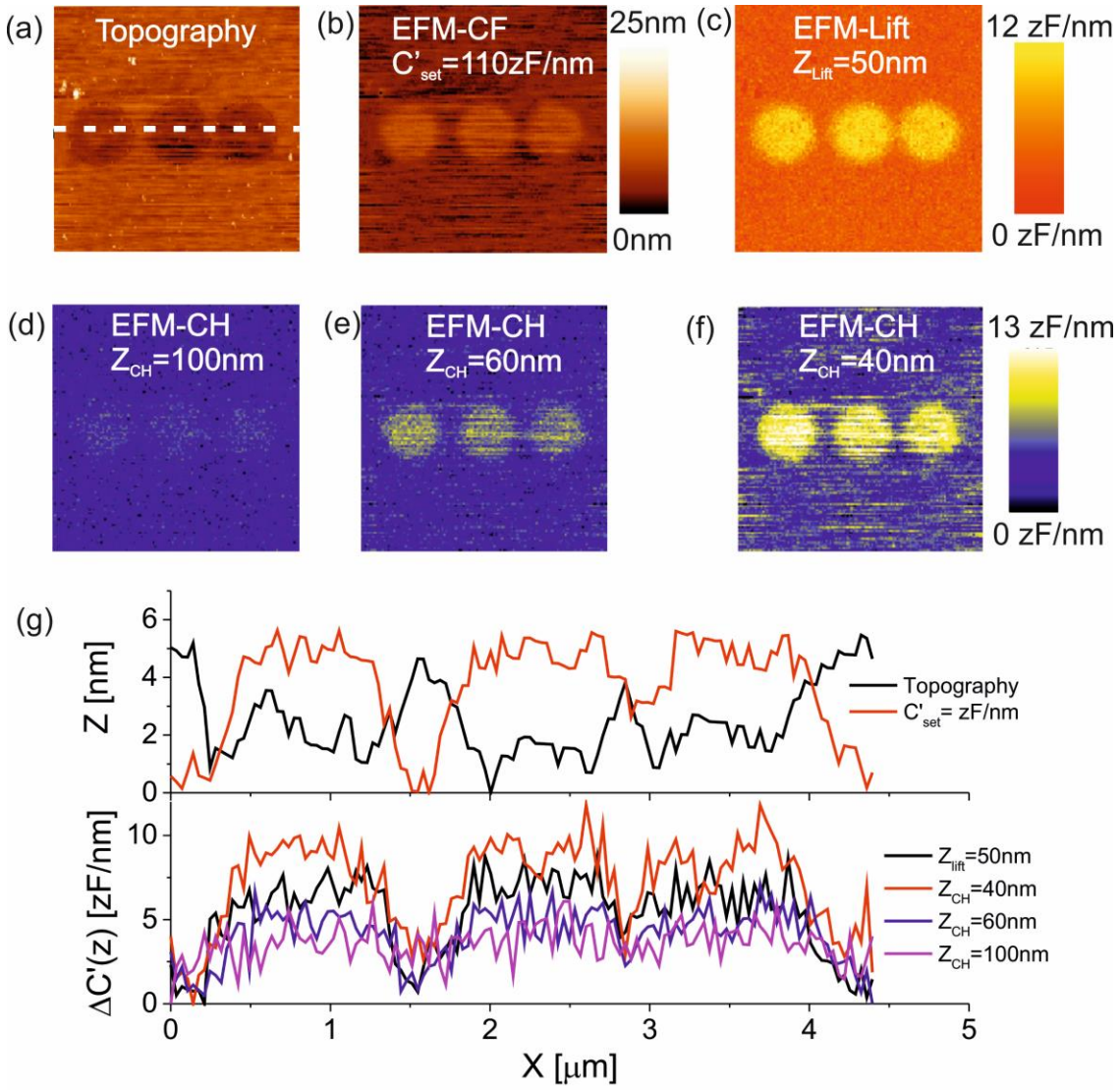

Figure 7.3: (a) Topographic image of the SiO_2 matrix with the buried metallic pellets obtained from the deflection SDVFM cube of data at a set-point D_{set}=0 nm. (b) Constant capacitance gradient (force) EFM image obtained from the capacitance gradient EVFM cube of data at set-point C'_{set}=110 zF/nm. (c) Lift-mode EFM image obtained from the capacitance gradient EVFM cube at a lift distance Z_{lift}=50 nm. (d)-(f) Constant height EFM images obtained from the capacitance gradient EVFM cube of data at a height distances Z_{CH}=100 nm, 60 nm, and 40 nm. (g) Cross-section profiles along the dashed line in (a)-(c) and (d)-(f). (Parameters of the acquisition: pixels 128x128x300 data points, range of the curves 300 nm, time per pixel 150ms, ac voltage amplitude 3V,

voltage frequency 5 kHz, HQ:NSC/Cr-Au probes, equivalent spring constant k=1.9N/m, resonance frequency ~80 kHz. Image size is: 4.5µm · 4.5µm.

Such images show the capabilities of EFVM to detect the subsurface dielectric changes in buried structures, whose surface topography is only 2 or 3nm tall, and they are around 50nm buried into a dielectric matrix.

7.4 Eukaryotic cells: HeLa cells

Like we have been commenting through the development of this work, cells are an example of topographically complex systems that can show dielectric heterogeneities of interest. Here, we show the application of EFVM for the imaging of fixed HeLa cells on top of a gold substrate in dry environment.

The cells are seeded at 50k cells/mL onto the gold substrates placed in the petri dish. After 24h of incubation in 5%CO_2 and 37ºC, the cells are observed and seem completely attached and spread on the gold substrate, and hence ready for fixation. The medium was washed away with PBS, and the sample was incubated with 2.5% glutaraldehyde in PBS for 10 min. After fixing, the sample was washed with PBS, ready for the drying process. The sample was washed consecutively with different solutions: 75%, 50% and 25% PBS and ultrapure MiliQ water, and 25%, 50%, 75%, 85%, 95%, and 100% Ethanol for 5 min each. Finally, the sample was immersed for 5 min in Hexamethyldisilazane (HMDS) and let dry in the desiccator before imaging. The protocol was optimized from the different options shown in[205]. The sample preparation was done by Adrianna Glinkowska from Nanoscopy for Nanomedicine Group (IBEC), led by Dr. Lorenzo Albertazzi.

In Figure 7.4, we can see the optical image of the dryed sample during the experiment. We can observe the density of the cells is optimal for our type of study, as we are interested into single-cell imaging, and it is easy to find them with such density. We can see the AFM cantilever and chip as well. The optical image is as well the tool that we use experimentally to locate the tip at the position where we want to perform the EFVM imaging. The white dotted square is highlighting the region that we are going to image in Figure 7.5.

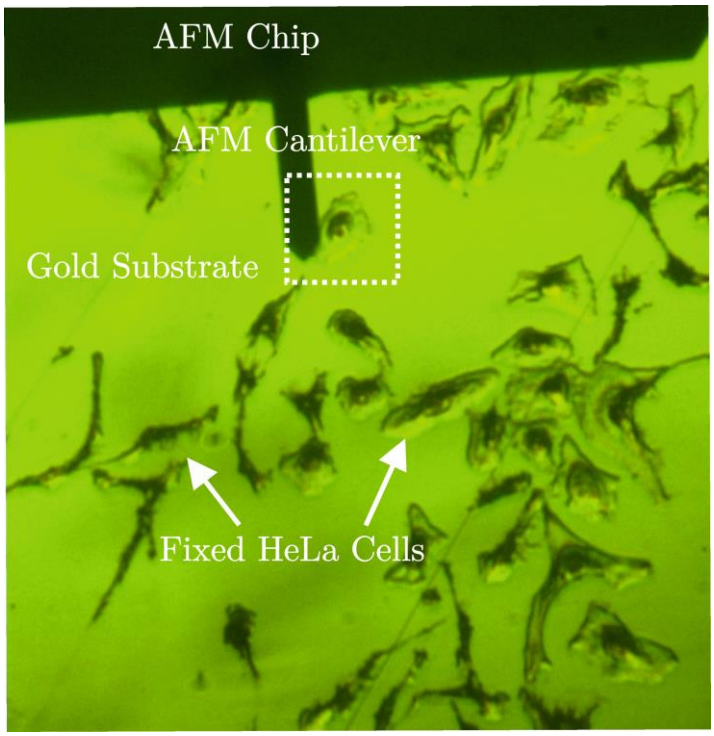

Figure 7.4: Optical Image of the previously fixed and dehydrated HeLa Cells, where one can see them as well as the AFM chip and cantilever. The white dotted rectangle is highlighting the cell imaged in Figure 7.5.

Figure 7.5a shows a topographic image at a set-point D_{set}= 0 nm obtained from the deflection EFVM cube. It shows one fixed HeLa cell of around 40 µm diameter where it is easy to identify the nucleus in the central part of the cell body (between 1 µm and 2 µm tall, see also the topographic cross-section profile along the dashed line in Figure 7.5g, black line).

Figure 7.5b shows the lift-mode capacitance gradient EFM (Z_{lift}=50 nm) image obtained from the corresponding capacitance gradient EFVM cube of data. The image is represented with relative values (contrast) with respect to the value on the bare substrate.

Moreover, Figure 7.5c-f shows four constant height EFM images at Z_{CH}=180nm, 500nm, 1µm, and 1.75µm, respectively, also plotted in relative values with respect to the substrate. Finally, Figure 7.5g shows the cross-section profiles of all images along the dashed line. Figure 7.5 h-m show the corresponding topographic and EFM images of a zoomed part of the cell (highlighted with the red dotted rectangle in Figure 7.5a).

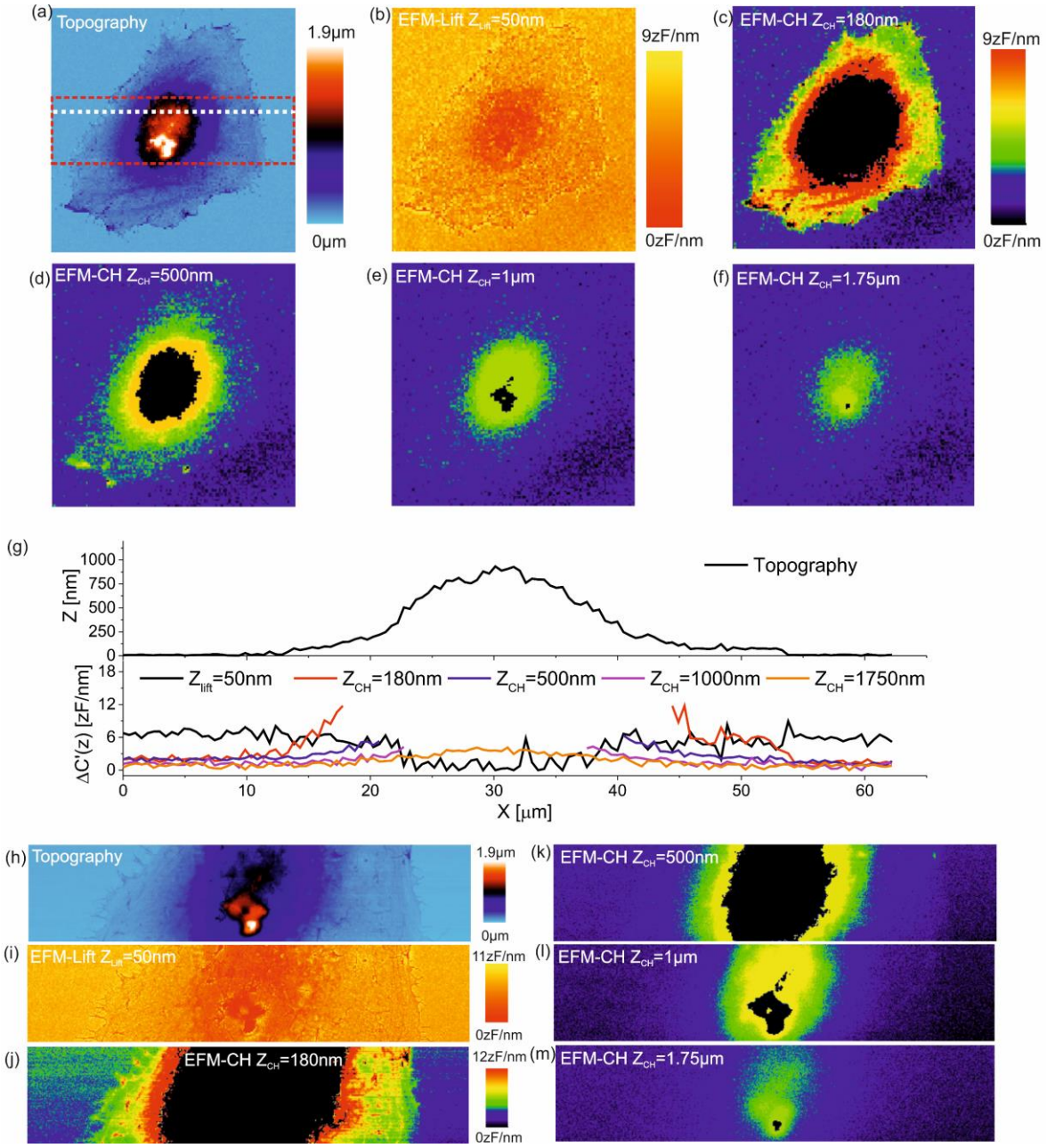

Figure 7.5: (a) Topographic image of the fixed and dehydrated HeLa cells obtained from the deflection EVFM cube of data at a set-point D_{set}=0 nm. (b) Lift-mode EFM image obtained from the capacitance gradient SDVFM cube at a lift distance Z_{lift}=50 nm. (d) Cross-section profiles along the dashed lines in (a)-(c) and (e)-(g). (c) and (e)-(g) Constant height EFM images obtained from the capacitance gradient SDVFM cube of data at a height distance Z_{CH}=180 nm, 500 nm, 1µm, and 1.75µm respectively. (h) Topography (D_{set}=0 nm) of the zoomed image (red rectangle in (a). (i), Lift-mode EFM (Z_{lift}=50 nm), (j)-(m) Constant height EFM (Z_{lift}=180 nm, 500 nm, 1µm and 1.75µm). Parameters of the acquisition: pixels 128x128x300 data points, range of the curves 2.5µm, time per pixel 150ms, ac voltage amplitude 3V, voltage frequency 5 kHz, HQ:NSC/Cr-Au probes, equivalent spring constant k=1.58 N/m, resonance frequency 80 kHz. The image (a) size is 63µm · 63µm. The image (h) size is 63µm · 14µm.

Furthermore, this is a good system to see the advantages of EFVM over conventional EFM. It can be clearly seen in the zoom images in Figure 7.5 h-m, that the lift mode image (Figure 7.5 i), seems to appear nicer in the sense that shows a much better resolution and the ultrastructure of the cell seems to be more clearly distinguish as compared to the constant height images (Figure 7.5 j-m). This is due to the fact that lift mode imaging convolutes the electrostatic signal with the topography of the sample, and if such crosstalk contributions are not removed (which is not always easy to perform by post-processing), they can bring to wrong quantitative analysis. Nevertheless, with EFVM, the constant height cuts (Figure 7.5 j-m), allow us to have images with less influence from the topography of the sample (as explained before). This is more explicitly seen in samples with big topographical variations like cells (they go from 30nm tall features at the edges to the 1μm height of the nucleus in dry conditions).

We use such a cell system (fixed) because it represents a good first approximation to the final goal of the project of performing EFM in living cells but in the always more controllable environment of air (specially for electrical measures). When cells are dried with no fixation protocol, they suffer and die, disabling the chance to study their morphology, mechanical or electrical properties in a nice way. They normally detach from the substrate, and if they do not detach, they completely lose their morphology. In addition, eukaryotic cells are much more complex and heterogeneous than prokaryotic cells, and so they become more interesting and challenging to image from the electrostatic point of view as the internal structure could be distinguished electrostatically. The nucleus is richer in DNA ($\varepsilon_r \sim 8$), which is more polarizable than proteins ($\varepsilon_r \sim 4$) and lipids ($\varepsilon_r \sim$ 2-3), principal components of the membrane and cytoskeleton. This fact opens a road to use EFM imaging and specifically intrinsic dielectric mapping as a label-free technique for compositional and structural mapping of cells. Nevertheless, it is unknown how the fixation process will affect the polarization properties of the biological components of the cell. That is why we want to push forward towards the EFVM imaging in physiological conditions with live cells.

7.5 Conclusions

We have shown that Electrostatic Force Volume Microscopy (EFVM) enables acquiring EFM images of topographically complex samples with an unparalleled efficiency that cannot be matched by any currently implemented EFM imaging mode in existing instruments (such as lift-mode, constant-height or constant force modes).

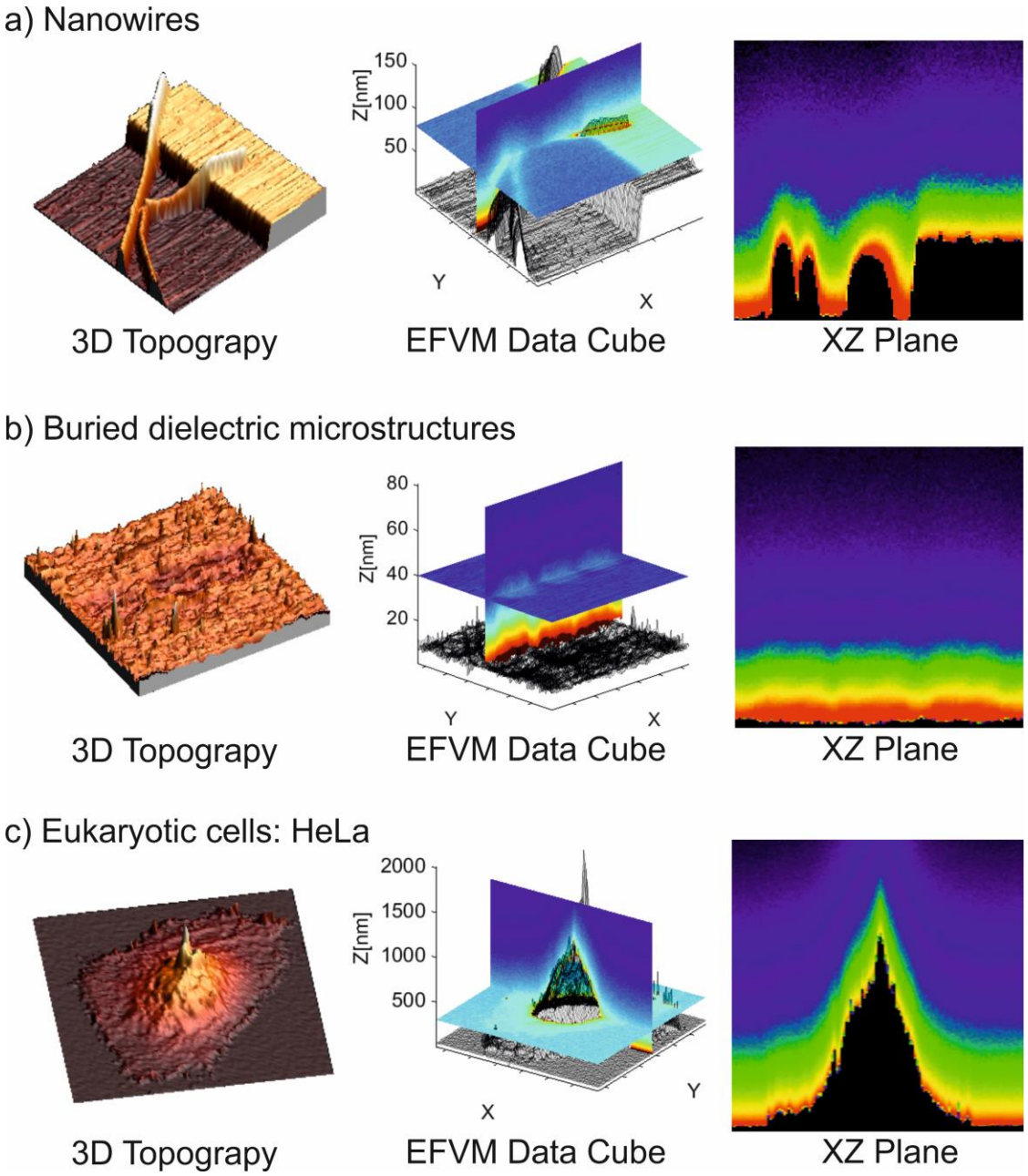

Figure 7.6: 3D Topographies, EFVM Data cubes and XZ Planes of the three systems imaged in this chapter, from where the different EFM images are extracted. a) Thin-film oxides and NWs. b) Buried dielectric microstructures. c) HeLa cells.

By acquiring the EFVM cubes of data (see Figure 7.6), one can obtain all the desired EFM images at any distance or any imaging mode with no need to pre-set them *a priori* during the image acquisition. The imaging distance and imaging mode are set *a posteriori* once the EFVM data have been acquired and can, hence, be fully customized to the specific characteristics of the sample.

We highlight, also, the possibility to obtain new images not accessible with the conventional EFM setups (like constant height at distances lower than the topography) as well as to access the close imaging distances (<20 nm of tip-sample distance), where the higher contrasts are obtained, and which are difficult to access experimentally with conventional EFM imaging modes, where usually unwanted tip collapses or tip-sample lateral hits occur. In addition, other complementary data acquisition and visualization like the XZ or YZ EFM data planes are as well exclusive from this 3D mode implementation. All these characteristics are fundamental to analyze the dielectric properties of topographically complex samples as those considered in this chapter.

The quantification and extraction of dielectric constant maps from the EFVM data is not trivial and needs finite element simulations and computer power as we showed in the previous chapter.

8. Towards Scanning Dielectric Force Volume Microscopy in liquid environment

This chapter explains the steps performed to extend Scanning Dielectric Force Volume Microscopy to the liquid environment, and its application to fixed and living eukaryotic cells in physiological conditions. It is based on the article in preparation: "Electrostatic force microscopy of HeLa cells in liquid environment". Regarding the contribution of the PhD candidate to the studies reported in that chapter, M.Checa, design and performed the experiments and analyzed the data, A.Glinkowska cultured and seeded the HeLa cells, and G.Gomila, supervised the work.

8.1 Introduction

In the previous chapters, we have shown the possibility to use EFVM and SDFVM to image and map the dielectric properties of single cells in air environment. Here we show the steps performed to extend this method to the much more relevant case of liquid environment.

The interest of having access to the electric field distribution at the nanoscale and the possibility to characterize the electrical properties of matter at the micro and nanoscale has been largely shown and commented during this work of thesis (see previous chapters). Such relevance becomes even more important when this characterization can be performed under liquid conditions. Especially when the subject of study is a biological sample, as these ones are normally found in liquid environments.

The explanation of how EFM in liquid measurements are done can be found in the introduction chapter. The experimental setup does not change with respect to other EFM

in liquid measurements[90,91], but instead of acquiring images, we will acquire the typical fast-force volume data cubes of EVFM.

First, we will expose the differences between air and liquid EFM force-distance curves. Second, we will validate the EFVM method with the same sample used previously (micropatterned pillars of silicon oxide thin film on top of silicon doped substrate). Third, we are going to show the application of EFVM to obtain EFM images of fixed eukaryotic cells for the first time (to our knowledge) in liquid environment, unambiguously showing dielectric contrast. Last, we will show some preliminary work done to achieve EFM imaging in living cells.

8.2 Differences in EFVM between air and liquid environments.

As explained in previous chapters, EFVM is based on the simultaneous acquisition of vertical deflection and electric oscillation force-distance curves in each individual pixel of the image, generating the so-called vertical deflection and derivative of capacitance Data cubes respectively. The operation of EFVM in liquid environment is ruled the same way, but using the EFM-in liquid setup, where the voltage wave sent to the sample is a high frequency voltage wave modulated by a low frequency voltage wave (used for the detection): $V(t)=V_0(1+\cos(\omega_m t))\cos(\omega_{el} t)$ (see the section 2 for details of EFM in liquid). Now, the first harmonic of the modulation frequency is the measured one, which relates to the derivative of the capacitance through the following relationship: $F_{el,\omega_m,liquid}(t)=\frac{V_0^2}{2}\frac{dC(z)}{dz}\cos(\omega_m t)$, only valid if the applied frequency falls into the high frequency regime (see modeling chapters).

There are two main qualitative difference between the curves measured in dry conditions with respect to the ones measured in liquid. The first one is the usual absence of the "snap-in" point or "jump-to-contact" point in the vertical deflection curves in liquid environment (Figure 8.1a-b). When working in liquid, the Van der Waals forces are not dominant any more at close distances, and electrostatic repulsion generally turns into vertical deflection

curves without the "snap-in" point (snap-in can also be found if the electrostatic interaction is attractive, mainly depending on the pH of the solution[206]). However, the electrostatic repulsion can sometimes be confused with the indentation of the tip into a soft sample, as both will show up as a progressive increase of the vertical deflection.

The second one is the shape of the capacitance gradient curves (Figure 8.1c-d). On the one hand, in dry conditions, EFM curves are strongly Z dependent, and the highest point of the curves is always the point where the tip touches the sample at the snap-in. On the other hand, in liquid conditions, the point of highest electrical oscillation is not always found at the closest tip-sample distance (especially for thick dielectric samples). This issue is not fully understood yet, but it has to do with two different aspects.

First, the fact that in liquid, as the relative permittivity of water is much higher (ε_r~80) compared to the air one (ε_r~1), the range of the electrostatic force extends to longer distances, turning into a higher relevance of the force acting to the cone as compared with the air case (where the majority of the force comes from the apex part of the tip which is the closest to the sample). This fact turns into a less Z dependent (or flatter) capacitance gradient curves for the case of liquid.

Second, the fact that some spurious interfacial capacitances develop both at the tip/liquid interface and the sample/liquid interface, due to space charge layers and the reordering or adsorption of molecules at the surface. This second aspect of the interfacial capacitances developing at the tip-sample/liquid interfaces has good and bad implications. On the one hand, it makes the quantification of EFM in liquid measurements (in terms of dielectric characterization and mapping) much more difficult, since additional parameters have to be included in the quantification models to obtain meaningful results. But on the other hand, the sample/liquid capacitive coupling is of major interest for many different scientific fields like electrochemistry or biosensors, and the fact that the EFM in liquid curves are dependent on those opens a route for in-liquid interfacial capacitance determination through EFM measurements.

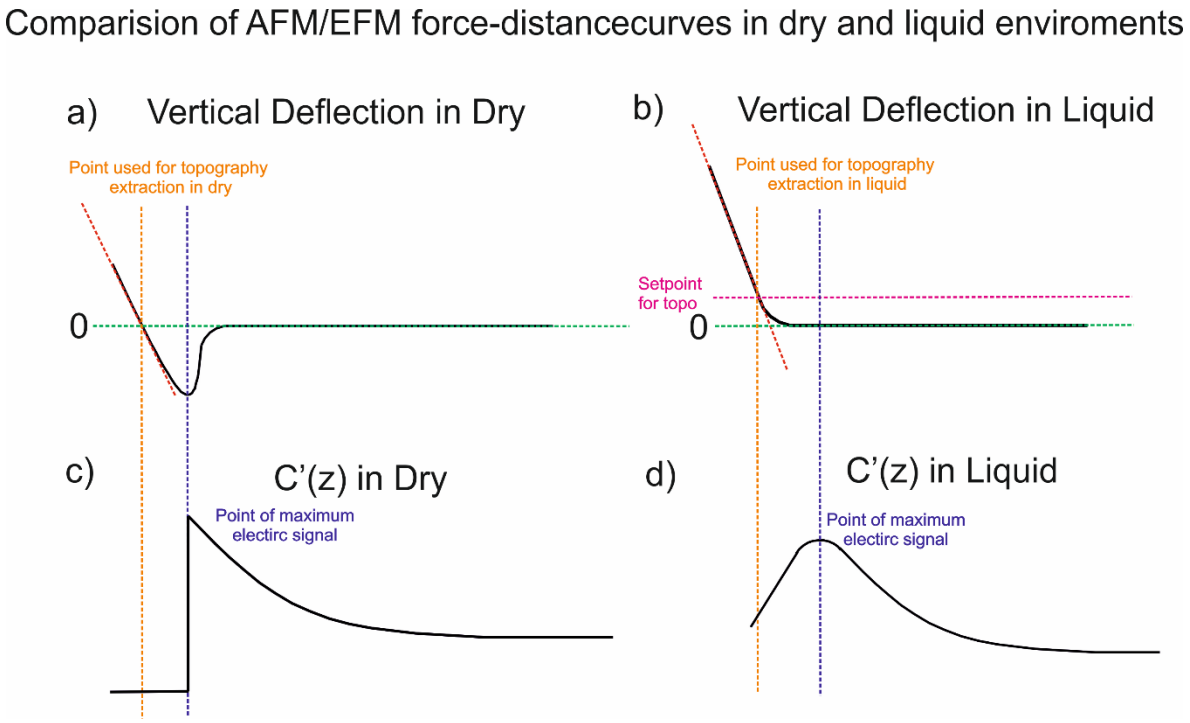

Figure 8.1: Comparison of vertical deflection and EFM force-distance curves in liquid as compared to the dry case. a) Sketch of a vertical deflection curve in dry conditions (continuous black line), baseline determination (green dotted line), linear fit for the contact region (red dotted line), and the point used for the topography (orange dotted line). b) Sketch of a vertical deflection curve in liquid media (continuous black line), baseline determination (green dotted line), the setpoint for the topography determination (pink dotted line), linear fit for the contact region (red dotted line) and the point used for the topography (orange dotted line). c) Sketch of an EFM force-distance curve in dry conditions (continuous black line), in dotted blue the point of maximum electric signal, which coincides with the contact point of the vertical deflection curves. d) Sketch of an EFM force-distance curve in liquid conditions (continuous black line) in dotted blue the point of maximum electric signal, which does not coincide with the contact point of the vertical deflection curves.

Besides these aspects, when working in liquid with biological samples like eukaryotic cells (which are normally soft), the contact region of the vertical deflection curves, can be different with respect to the harder parts of the sample (like the substrate). In the softer parts, the tip can induce unwanted deformations or even indentation in the sample, which can be misleading for the topography determination from the vertical deflection curves, as they can provoke the appearance of weird features in the vertical deflection curves or sample damaging. This is why, in soft samples, it is crucial to determine very well the setpoint used for the topographic determination (pink line in Figure 8.1b). Otherwise, "fake" or "under pressure" topographies can be obtained. The best would normally be to use the softer setpoint possible (perturbating the sample the least), and we usually define it as the point

where the signal surpasses noise of the baseline part of the vertical deflection curve, but this criterion sometimes gives great uncertainty in the topography determination. After all these considerations regarding the differences between dry and liquid EFM, we are ready to start with the results.

8.3 Validation with SiO_2 pillars

To validate the application of EFVM in liquid environment, we are going to use the same sample as we did for the validation of the method in air: thin SiO_2 micropatterned pillars on top of a doped silicon substrate. In Figure 8.2a, we show the capacitance gradient Data Cube of such sample, from where one can extract both the topography (Figure 8.2b) and all the different EFM images (lift-mode Figure 8.2c or constant height-mode Figure 8.2d-e), by following the same data analysis procedures explained deeply in previous chapters. Note that in this case units are shown in raw data (output voltage of the lock-in, as the measurements are not quantified with numerical simulations). In Figure 8.2f we show two curves of the EFVM, one on top of the metallic surface, and another one on top of the pillar, where the aspects discussed in Figure 8.1 can be observed. The profiles of the four images in Figure 8.2b-e are found in Figure 8.2g.

The first thing to point out here is the fact that we are able to obtain EFM contrast (difference in signal between the metallic region and the dielectric pillar), especially in the images in constant height mode (free from topographic crosstalk). This fact unambiguously ensures the ability to detect dielectric changes in liquid media by EFVM in liquid. The second thing to highlight (especially when compared to EFM in air environment) is the higher lateral effects seen on the signal (see Figure 8.2) and the inferior Z dependence of the curves found in liquid. The cause of such behavior (as explained previously) is the high dielectric constant of water (ε~80), which increases the importance of the cone with respect to the apex in the total signal recorded.

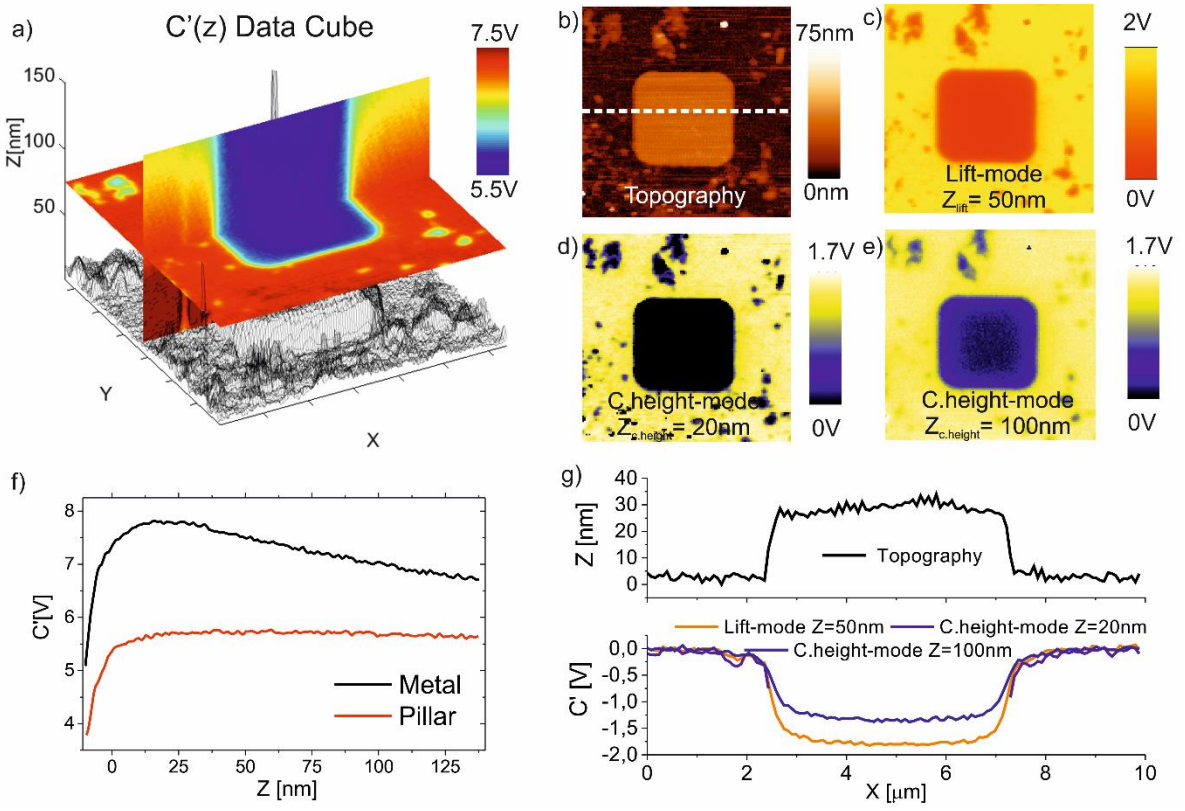

Figure 8.2: Validation of the EFVM technique in liquid environment. a) C'(z) Data Cube for the sample of SiO_2 pillars on top of the silicon doped substrate. b) Topography image extracted from the Deflection Cube of data (not shown). c) EFM Lift-mode image at 50nm lift height. d) EFM Constant-height mode image at 20nm height. e) EFM Constant-height mode image at 100nm height. f) Two different EFM force approach curves of the EFVM Data Cube, one on top of the metal and one on top of the pillar. g) Profiles of the images in b-e. EFM profiles are plotted in relative value (setting the value on top of the metal at 0V) for a better comparison. Parameters of the acquisition: pixels 128x128, range of the curves 250 nm and data points 300, time per curve 100 ms, $\omega_{modulation}$ ac voltage amplitude $2V_{pp}$, frequency 5 kHz, $\omega_{high\ frequency}$ ac voltage amplitude $2V_{pp}$, frequency 20MHz. HQ:NSC/Cr-Au probes, equivalent spring constant k~1.2 N/m.

Moreover, we can observe that contrary to what happens in dry conditions, constant height images present a negative contrast (less signal in the sample than in the metal). This is again a consequence of the high polarizability of water (ε~80). Since EFM is sensitive to the effective polarization found between tip and substrate, in the metallic parts of the sample, the polarization comes exclusively from water (ε~80). On top of the pillar, instead, we have contributions to the effective polarization coming from both the water (ε~80) (present between the tip and the pillar), and the dielectric pillar itself (ε~4), turning in a lower effective dielectric constant.

As we said before, the models for the dielectric quantification in liquid environment are still under development by other group members. The main issue here is to be able to model properly the previously mentioned interfacial capacitances happening at the tip/liquid and sample/liquid interfaces. That explains why we do not show the quantitative dielectric characterization (only the qualitative contrast) for the case of liquid images.

Next, I present the three preliminary results we have for the application of SDFVM in liquid environment. Namely, measurements in fixed eukaryotic cells, first steps for measurements in living cells, and nanoscale electrical characterization of a fully functional EGOFET.

8.4 Electric images of cells in liquid

8.4.1 Fixed cells

As a first approximation towards the living system, we have used fixed eukaryotic cells (HeLa cells) seeded on top of a gold electrode used as the metallic substrate. We used such a cell line in liquid media also for two main reasons. First, because of their good attachment to metallic surfaces like gold without the need of any special coating that could increase the sample preparation difficulty and interfere with the electric signal. Secondly, HeLa cells withstand harsh conditions and are quite resistant comparing to some other cell lines, being able to maintain alive for some time not only in the culture media, but also in some different buffers (like the ones we need to perform the EFM in liquid measurements, see section of living cell measurements).

Regarding the substrates, we have used rough gold instead of the typical atomically flat gold preferentially used in other AFM experiments, as cells have shown to grow better on rough substrates[207].

As a buffer for the measurements, we used 10mM MOPS (3- 3-(*N*-morpholino) propane sulfonic acid). It is chemically similar to HEPES buffer, and they are both often used as a buffering agent for biological systems at near-neutral pH[208]. The reasons to avoid MiliQ as a solution (where we would have more electric signal), is first to avoid shrinking/enlarging or

bursting of the cell due to osmotic shock, and second to be closer to the living conditions of the cells, where ions will be present. The use of buffers with high salt concentration (e.g. 100mM) is not performed in this work, since they would require a too high electrical excitation frequency (>100 MHz) not achievable in our set-up.

Figure 8.3 shows the aspect of the sample during the measurement.

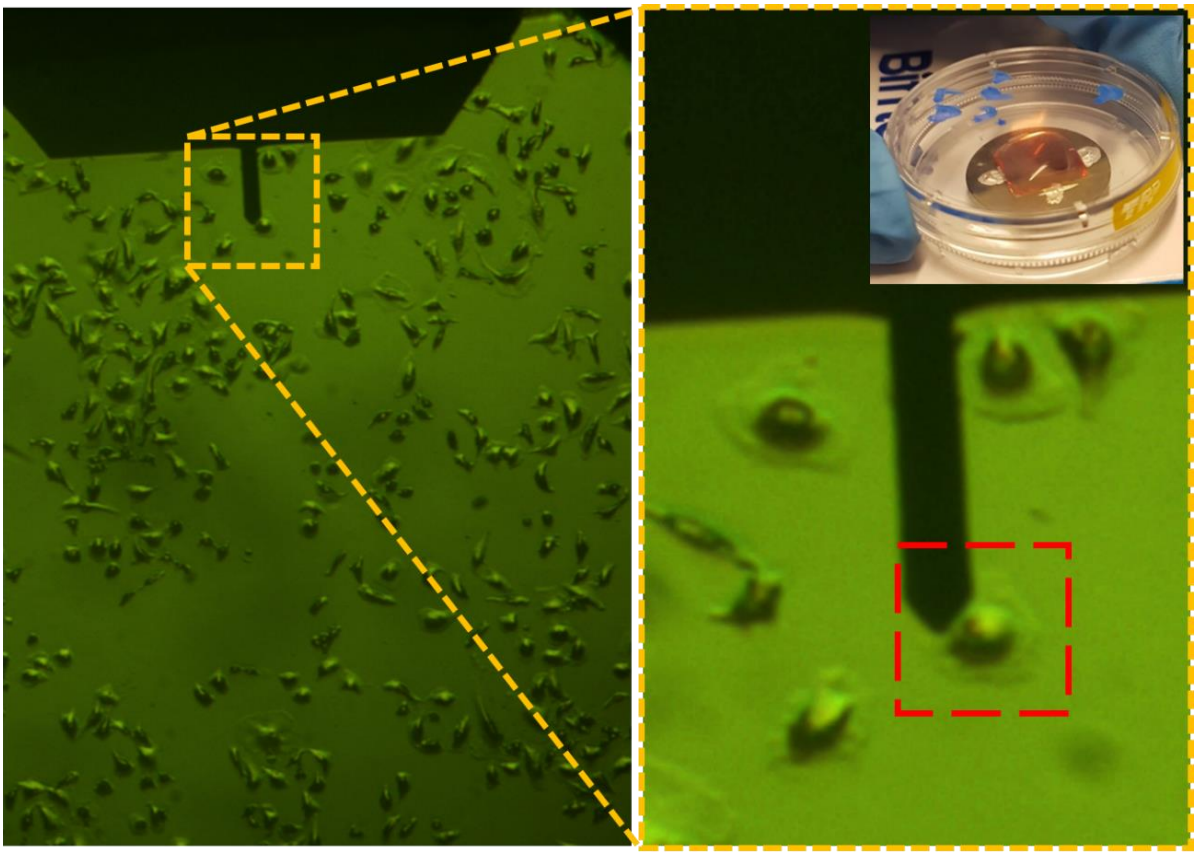

Figure 8.3: Left: Optical image of the sample containing the fixed Hela cells in 10mM MOPS once placed in the AFM stage. In black, the AFM cantilever and chip can clearly be distinguished. Right: Optical zoom of the yellow rectangular zone in left. The red rectangle indicates the optical zone imaged in Figure 8.4. On the top right angle, there is a picture of how the sample looks like after the cell seeding.

To prepare the sample, the cells are seeded at 50k cells/mL onto the gold substrates placed in the petri dish (see right-top inset in Figure 8.3) and covered by cell culture medium. After 24h of incubation in 5%CO_2 and 37ºC, the cells are observed and its complete attachment and spread on the gold substrate is verified, so that they are ready for fixation. Medium is washed away with PBS. Then, incubation with 2.5% glutaraldehyde in PBS for 10 min.

After, the sample is washed with PBS and ready to perform the change to the MOPS buffer (the buffer used for the SDFVM measurements in liquid). Again, consecutive washes with 75%, 50%, and 25% PBS in MiliQ were performed (3min each), and 2 final washes in MiliQ water for 3 min as well. Directly after that, 2 washes with 10mM MOPS buffer let the sample ready for measurement. We want to highlight that the sample has always been wet during all the processes to maintain as much as possible the shape and size of the living cell, as the drying process induces big topographical changes. Then, this is not a "rehydrated" sample, but a wet one. The protocol is optimized from the different options shown in[205]. Optical images showing the cell aspect and density can be seen in Figure 8.3. The sample preparation is done by Adrianna Glinkowska from Nanoscopy for Nanomedicine Group (IBEC), led by Dr. Lorenzo Albertazzi.

In Figure 8.4, we have the EFVM analysis of a single fixed cell. Figure 8.4a shows the topography of the cell in liquid environment. It is easy to see that the size of the cell is increased by 5 times with respect to its size in dry conditions (around ~ 1 µm at the highest point, even after fixation), where (even if proper drying processes are performed) the evaporation of water, induces important morphological changes. In the image, the nucleus (~3-6 µm) can be clearly differentiated from its surroundings (still ~1µm thick) formed by the membrane, the organelles and the cytoplasm.

Figure 8.4b shows the EFM lift-mode image at 75nm lift height extracted from the EFVM data cube. In the lift mode image, all the cell features present in the topography are also resolved (as lift mode has important topographic crosstalk effects[98]) with similar resolution to the one in the topographic image. As it has been said before, such images are easier to perform experimentally, but extracting relevant information from them (both qualitative and quantitative) is much more difficult.

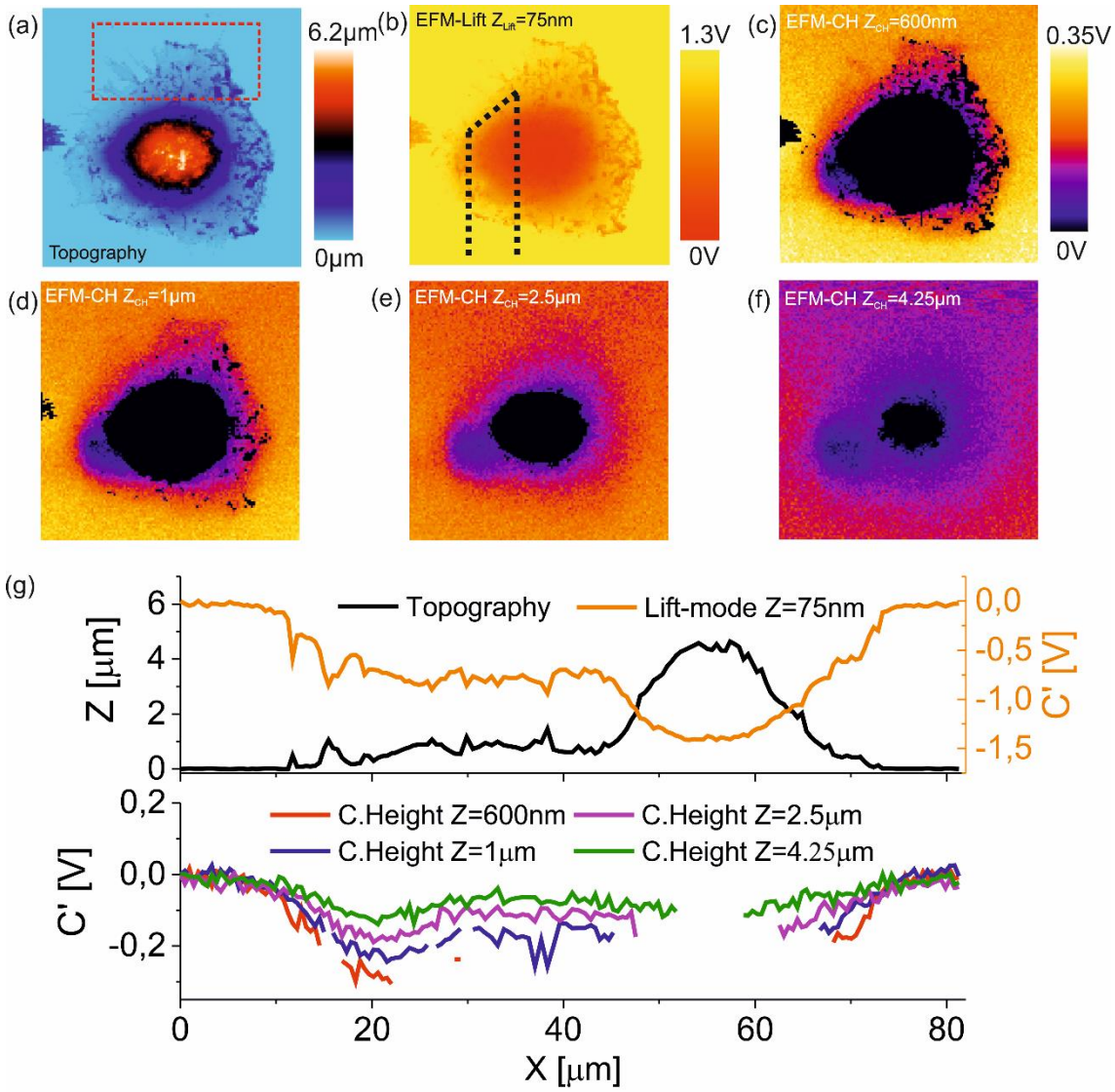

Figure 8.4: EFVM full imaging of a fixed single HeLa cell in 10mM MOPS. a) The topography of the cell. The red dotted square highlights the image shown in Figure 8.5 . b) Lift-mode EFM image at a lift height of 75nm. c-f) Constant height mode images at 600nm, 1µm, 2.5µm, and 4.25µm, respectively. g) Profile along the black dotted line in b) of the images in a-f. Profiles are shown in relative value with respect to the metal value (set to 0) for a better comparison. Imaging parameters: $1V_{pp}$ amplitude of the high frequency at $\omega_{high\ frequency}$=5MHz, a modulation frequency of ω_{mod}=5kHz, 300ms of pixel duration, and 5µm of curve length. HQ:NSC/Cr-Au probe with equivalent spring constant k=1.2 N/m. The image size is 60µm · 60µm.

Figure 8.4c-f shows the constant-height mode images at a tip-substrate distance of 600 nm, 1 µm, 2.5 µm, and 4.25 µm respectively. A change in the capacitance gradient (C'(z)) is found in the regions where there is the cell with respect to the metal regions. Nevertheless, the cell features appeared to the eye less resolved as compared to the topography and lift-mode images. This lost in resolution is a consequence of the absence of crosstalk in constant

height imaging, which highly increases the contrast of the lift-mode images. As we mentioned before, constant-height images are the most relevant for our studies, as they unambiguously reveal whether a part of the cell can be dielectrically resolved in liquid or not. If there is a contrast in constant height image, it unambiguously means that the capacitance gradient of the system has changed due to a dielectric change in the sample under study (as they are not affected by any crosstalk effect because the tip-metal distance is maintained constant during the scan). In Figure 8.4g we show the profiles of the previous images.

We would like to highlight that those images are exclusive from the EFVM imaging technique, as other "state of the art" EFM modes would provoke tip-crashing or cell destruction when trying to perform such images. Instead, EFVM achieves it by post-processing the Data Cubes measured where the inaccessible parts of the cell (the interior) appear in black.

We want to stand out that the electrical images shown in Figure 8.4, and next are just some images we decided to post-process *a posteriori*, from the measured Data Cubes. But the lift-mode, constant height, and even constant force images at any desired distance or force can be reconstructed in case of interest with the same set of data (a big advantage of Data Cube imaging with respect to conventional imaging).

With the goal of testing the resolution of the technique (as one of the main limitations of electric characterization techniques for single-cell is their poor spatial resolution), two consecutive zooms of the same image shown in Figure 8.4 are shown in Figure 8.5 and Figure 8.6. As the nucleus is quite tall (preventing good SNR on top of it as the tip-metal distance is set very high), we focused our attention in the surrounding regions (red dotted square in Figure 8.4a) and on its membrane extensions used for cell attachment and migration (red dotted square in Figure 8.5a).

With this, we want to highlight the powerfulness of the technique developed, able to image from big multicellular structures on the ~100µm X-Y range and ~10µm Z range, to small cell features such as neurons axon or filopodia below ~0.1µm X-Y range and ~0.1µm Z range.

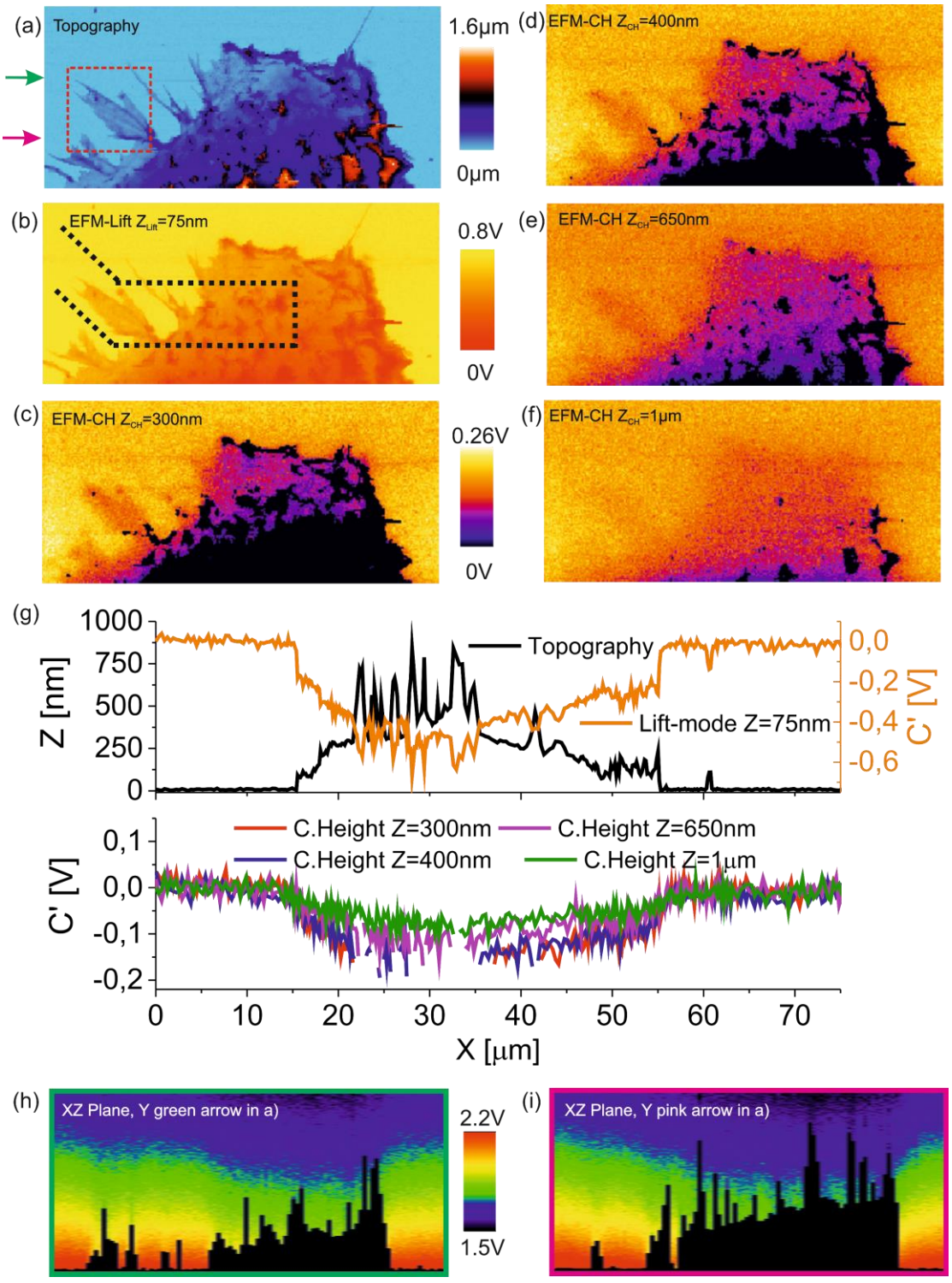

Figure 8.5: EFVM zoom in the red rectangle in Figure 8.4a. a) Topography of the cell. Red dotted rectangle indicates zone of Figure 8.6. b) Lift-mode EFM image at lift height of 75 nm. c-f) Constant height mode images at 300 nm, 400 nm, 650 nm and 1 µm respectively. g) Profile along the black dotted line in b) of the images in a-f. h-i) Electric signal along the XZ planes for different Y lines (see color arrows in a)). Imaging parameters: $1V_{pp}$ amplitude of the high frequency at $\omega_{high\ frequency}$=5 MHz, a modulation frequency of ω_{mod}=5 kHz, 300 ms of

pixel duration, and 1.2 µm of curve length. HQ:NSC/Cr-Au probe with equivalent spring constant k=1.2 N/m. Image size is 38µm · 17 µm.

In Figure 8.5a, we show the topography of the membrane region highlighted in red in Figure 8.4a.

In Figure 8.5b, a lift-mode image at 75nm of lift height is shown, and in Figure 8.5c-f, the subsequent constant height images at 300nm, 400nm, 650nm, and 1µm respectively. The profiles are found in Figure 8.5g. From them, one can observe the much lower topography of the membrane region as compared to the nucleus region. The expected dielectric contrast in the constant plane images is recovered, showing us again that we are able to detect dielectric changes in liquid conditions.

Finally, in Figure 8.6a we show the topography of one membrane extension (probably a filopodia) highlighted in red in Figure 8.5a. In Figure 8.6b, a lift-mode image at 75nm of lift height is shown and in Figure 8.6c-f the subsequent constant height images at 125nm, 150nm, 200nm and 300nm respectively. The profiles are found in Figure 8.6g. From them one can observe that, as we zoom to the edges of the cell, a much lower topography (now on the 100nm range) is found. Nevertheless, again we find the expected dielectric contrast in the constant plane images, showing us that we are able to detect dielectric changes even in the smallest cell features. Such contrast is even more clearly seen in Figure 8.6h and i, where we show the electric signal along an XZ plane, for different Y lines (see color arrows in Figure 8.6a).

Cells are not rigid objects at all. There are a lot of studies regarding cell mechanical properties, and their correlation to disease[209,210]. Not only by stiffness measurements, but also regarding the energy dissipation during the tip-sample interaction[56]. Even if the mechanical studies of cells are out of the scope of this work, I want to roughly show that the mechanical properties of the cells could also be studied with EFVM, by using the vertical deflection curves.

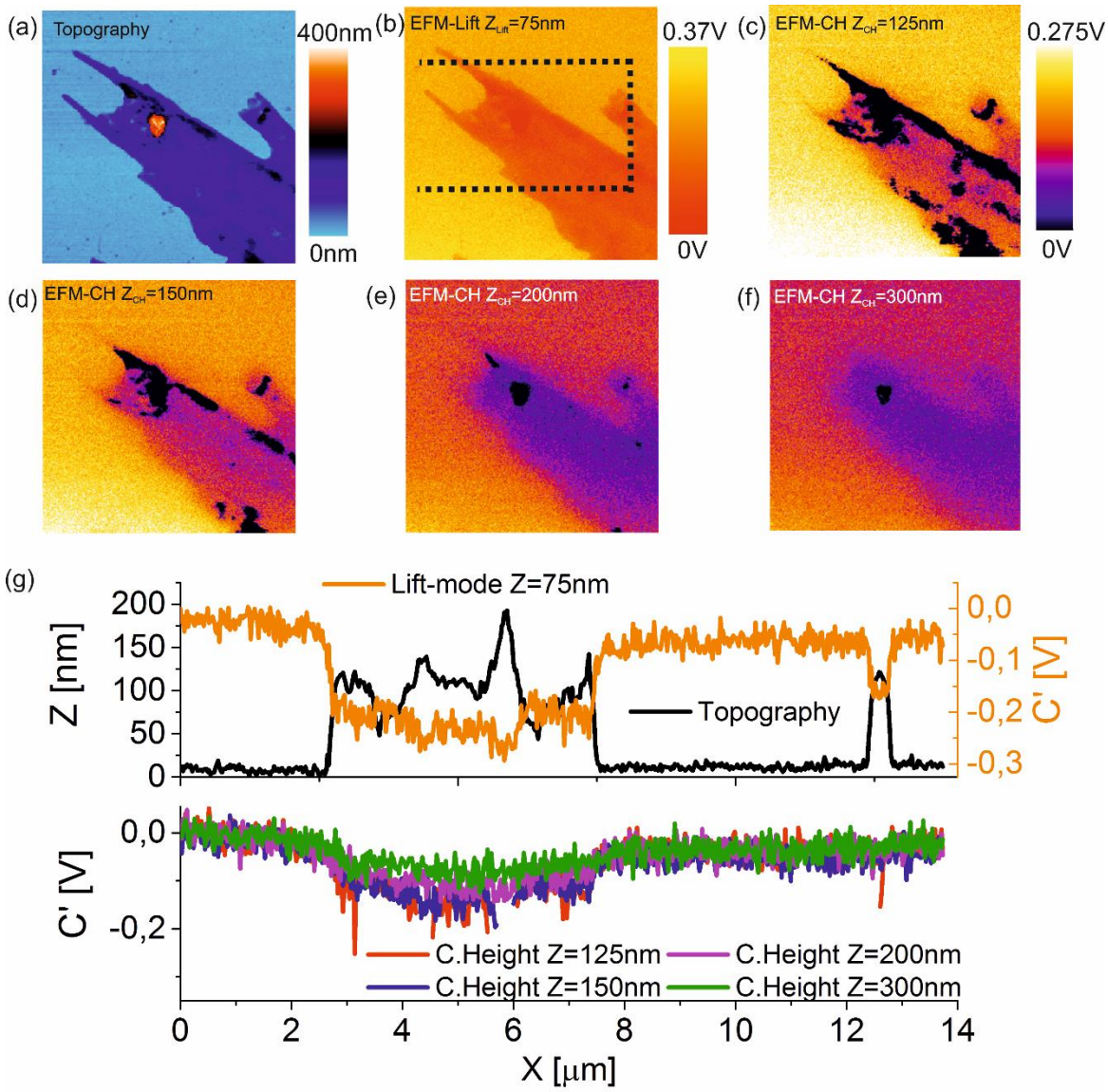

Figure 8.6: EFVM zoom in the red dotted rectangle in Figure 8.5a. a) Topography of the cell. b) Lift-mode EFM image at lift height of 75nm. c-f) Constant height mode images at 125 nm, 150 nm, 200 nm and 300 m respectively. g) Profile along the black dotted line in b) of the images in a-f. Imaging parameters: $1V_{pp}$ amplitude of the high frequency at $\omega_{high\ frequency}$=5 MHz, a modulation frequency of ω_{mod}=5 kHz, 300 ms of pixel duration, and 1.2µm of curve length. HQ:NSC/Cr-Au probe with equivalent spring constant k=1.2 N/m. Image size is 6µm · 6µm.

To briefly illustrate this possibility, in Figure 8.7a, we observe the aspect of two vertical deflection curves (one on top of the metal and one on top of the cell). A fitting of a linear function to the contact region is normally used in hard surfaces to calculate the sensitivity of the setup. In our case we also fit the linear function into the contact region of the cell curves, generating the subsequent "sensitivity maps" (Figure 8.7b, d, e,).

In the maps two zones are clearly identified. A softer zone (lower sensitivity), and a stiffer zone (higher sensitivity). A Double gaussian function can be fitted over the counts on the images (see Figure 8.7b, d,e).

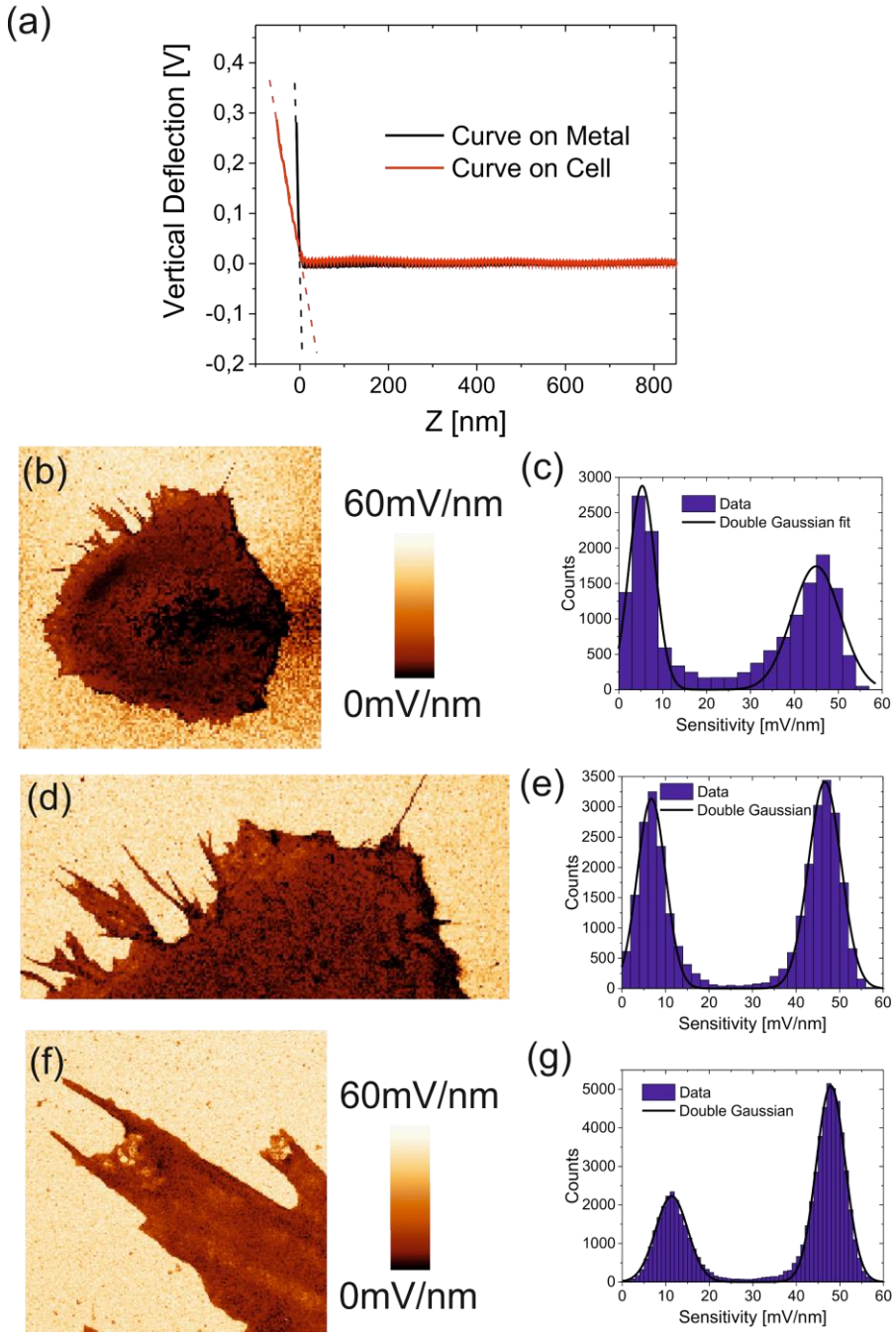

Figure 8.7: a) EFVM vertical deflection force-distance curves on top of metal and cell. b) Sensitivity Map of cell in Figure 8.4. c) Corresponding histogram of the pixel sensitivity and double Gaussian fit of the data to show the two different regions: soft (cell) and stiff (metal). d) Sensitivity Map of cell in Figure 8.5. e) Corresponding histogram of the pixel sensitivity and double Gaussian fit of the data to show the two different regions: soft (cell)

and stiff (metal). f) Sensitivity Map of cell in Figure 8.6. g) Corresponding histogram of the pixel sensitivity and double Gaussian fit of the data to show the two different regions: soft (cell) and stiff (metal).

The softness difference between the cells and the substrate is showing that even if the cells are fixed, their mechanical properties are still much softer than the metallic substrate. With further work on the quantification process, even some modification of the Hertz model (which should include the electrical oscillation of the tip) could be adjusted to every curve achieving simultaneous mechanical/electrical characterization in the same data set. Another possibility would be to use the electrical excitation of the tip to study the rheology of the cells, but as said before, we did not exploit that route so far as it is out of the interest of this work.

Regarding the range of the forces applied to the cells during the acquisition of the images, the setpoint was always in the range between 1nN and 10nN, in order to not damage the cells but to have some information in the contact region (note that figures are in volts but force can be easily calculated with the known sensitivity and spring constant of the lever).

As a summary of this section, I want to highlight that the first ever (to our knowledge) EFM in liquid images of eukaryotic cells have been obtained after their fixation. Even though fixed cells are a good morphological and structural approximation to living cells, they have lots of differences. The fixation agent (glutaraldehyde) induces a crosslinking between the proteins in the cell by creating covalent chemical bonds between them[211]. Thus, even if the fixation process preserves the biological structures from putrefaction and autolysis, and it has been proved to maintain even the membrane molecules mobility[212], it terminates all biochemical reactions taking place inside the cell (killing the fixed specimens) and inducing mechanical strengthening of the cell components[213]. To overcome these limitations, we have explored the possibility to perform EFM imaging on live cells.

8.4.2 Living cells

Once the EFM imaging of fixed eukaryotic cells has been achieved, the last step of the project was to be able to perform EFM measurements on living cells. The relevance of accomplishing such challenging goal would be huge. It would open the door to perform many

different experiments, going from label-free compositional mapping of living cells, to force-based electrophysiological recordings with nanoscale spatial resolution.

To start with, many aspects must be considered before doing the experiments, as compared to the measurements in fixed cells. The first one refers to the solution to be used for the measurements. The media has to be low concentrated enough to have EFM signal (remember that EFM measurements on high molarity solutions would need too high applied frequencies to avoid the electrostatic double layer screening of the signal), but at the same time, it has to contain the salts necessary (isotonic fluid) to maintain cells alive (too low molarity solutions would cause osmotic shock and/or other cell damages). In addition, the cells are very sensitive to pH variations, and normally the solutions used for their culture contain some pH controlling agent. For long experiments, also temperature control and CO_2 constant levels or pH buffering agent should be considered.

To assess the best media for doing the measurements, we selected 6 different solutions (see Figure 8.8) that though could be a good combination between having EFM signal but allowing the cells to maintain alive. Then, we cultured the cells, and after 24h in culture (when they already showed good surface attachment, and even reproduction started happening), we changed their culture media for the different solutions that we though could work. After the medium change, we evaluated their morphology by optical microscopy imaging during the following hours. Besides, the EFM signal of each of the 6 solutions was measured (by acquiring an EFM force-distance curve on top of a metallic substrate). This procedure allowed us to decide which is the better solution to be used.

The 6 media that we tested (shown in Figure 8.8), are chosen for the following reasons. First Dulbecco's Modified Eagle Medium (DMEM), is used as a control sample, as it is the normal culture medium where HeLa cells are grown. Also, a 10 times dilution of DMEM is tried, as at this concentration we started to observe local EFM electrical signal. Nevertheless, after 45 minutes in x0.1 DMEM, cells started detaching from the surface and/or starting to

present morphological bumps together with rounding shapes, a typical signal from apoptosis (see Figure 8.8e).

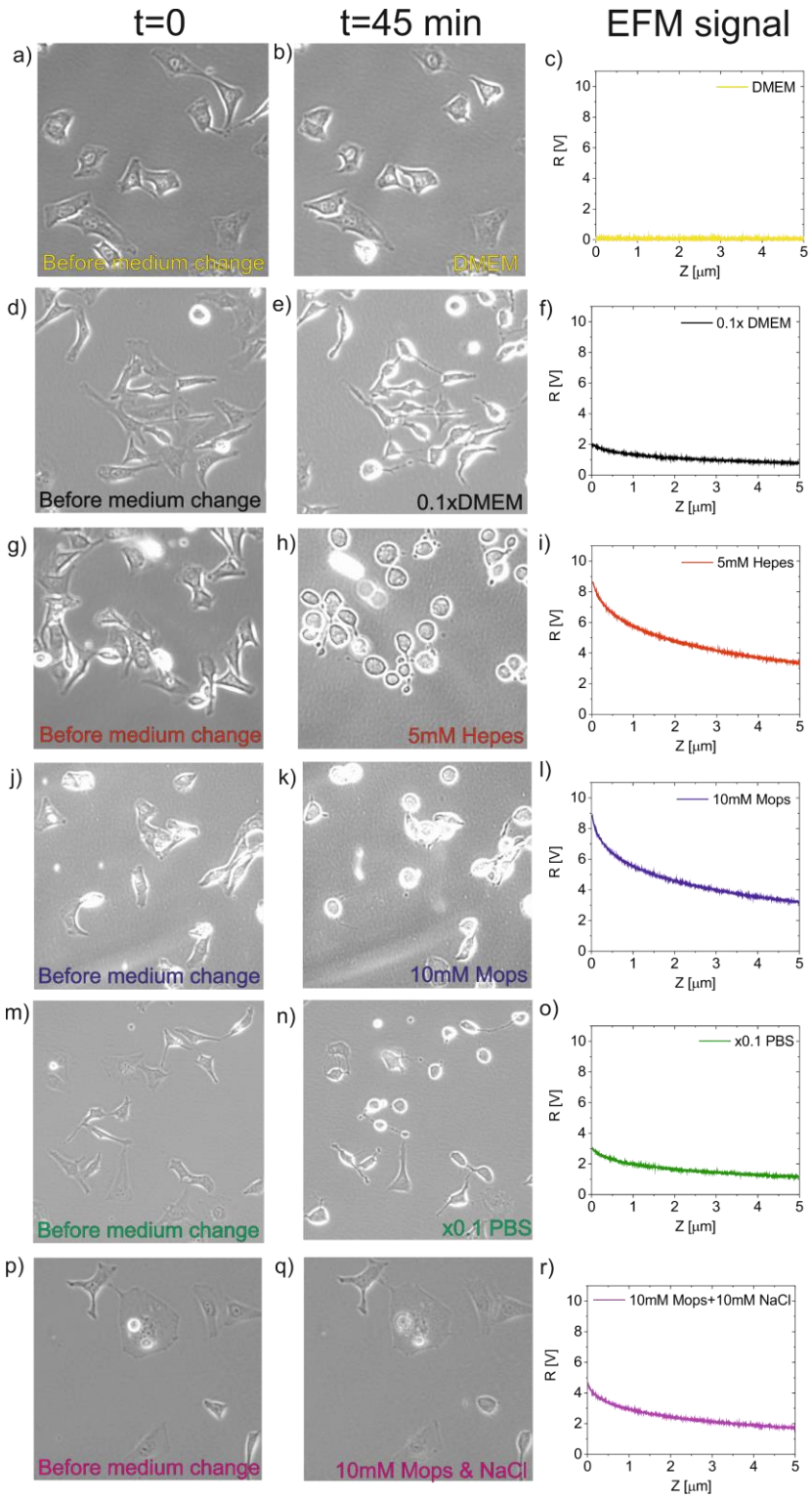

Figure 8.8: Left column: images of the cell culture before the medium change. Middle column: images of the cell culture after 45 min of solution change in b) DMEM control medium, e) 0.1x DMEM control medium, h) 5mM

HEPES buffer, k) 10mM MOPS buffer, n) 0.1xPBS, q) 10mM MOPS +10mM NaCl. Right column: EFM force distance curve on the gold substrate at 20 MHz high frequency of: c) DMEM control medium, f) 0.1x DMEM control medium, i) 5mM HEPES buffer, l) 10mM MOPS buffer, o) 0.1xPBS, r) 10mM MOPS +10mM NaCl.

Then, low concentrated solutions of HEPES and MOPS buffers were also tried (higher concentrations showed almost null electrical contrast, so they are not tried in cells). We selected them, as they are sometimes used as buffers in cell culture, to prevent pH changes[208], but the cells seemed to need something more than that to be maintained alive. Again, after 45 minutes in that buffers, they started detaching from the surface and/or starting to present morphological bumps together with rounding shapes, a typical signal from apoptosis (see Figure 8.8h,k).

Besides, 0.1x Phosphate buffered saline solution (PBS) was also tried, as 1x PBS is normally used to perform live cell washings or even live cell imaging (but it is too conductive for the EFM in liquid measurements). But again, cells presented dying features after 45 min of medium change (see Figure 8.8n).

Finally, an optimal combination was found, by adding 10mM NaCl to the 10mM MOPS buffer. In this case, even if cells seemed to shrink a little bit from their initial morphology, they looked well attached to the surface, presenting no signs of dying (see Figure 8.8q). At the same time, even if the buffer presented less EFM electrical signal as compared with some of the other media tried, it is enough to perform EFM imaging.

Based on this study, we decided to continue with the solution of 10mM MOPS + 10mM NaCl for the EFM in living cell experiments.

The second aspect to consider is the mechanical properties of the living cells. In the case of the fixed cells (see Figure 8.7), we have already seen that the cell biological structure is soft. In the case of living cells, we expected them to be even softer, as fixation normally involves hardening of the mechanical properties[213]. Even if the mechanical properties are not our focus of interest, as it has been said before, they are extremely important in order to obtain a "true" topographic image to be used for the building of the EFM images. The deformation or indentation produced by the tip during the scan, makes difficult to determine the realistic

topography of the cell when it is not pressed. This problem is of major importance in cell nano mechanics as well, because the errors in the determination of the contact point are propagated, increasing the error determination of the young modulus. There are methods used to determine well that contact point (see[214,215]), but in our case, added to the conventional issue, there are other problems. First, the oscillations produced by the laser interference on the flat region of the force-distance curves is important (this issue is strongly enhanced by the need of using a metallic substrate and probably an AFM with a low coherence laser detection system would help solving that problem). Second the big tip oscillation due to the electrical signal excitation increases the difficulty of the contact point determination. Third, the tips normally used in mechanics (k<<1N/m) are much softer than in EFM. Nevertheless, we are limited in that aspect, as such softer probes normally show a lower resonance frequency (closer to the one we need for the electrical excitation).

Thus, the issue of the true topography determination from force curve measurements is relevant, as we need to determine when the tip gets in contact with the cell surface to avoid having fake dielectric contrast (we cannot evaluate the EFM signal with the tip and sample in contact).

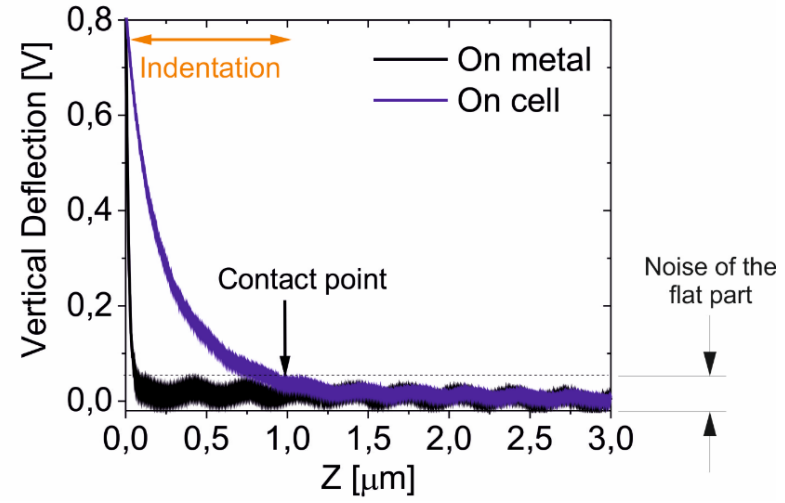

Figure 8.9: Vertical Deflection curves on the solid metallic surface (black), and on top of a living cell (blue).

To illustrate that aspect, in Figure 8.9, I show how the vertical deflection curves on top of the living cell look like, as compared to the curves on top of metal. The slow increase of the vertical deflection of the tip in the case of the living cell is a clear footprint of the tip indentation and the induced deformation of the cell. The deformation can be huge (on the micron range), which makes it difficult for us to determine in an accurate way the realistic topography (which we need to determine with at least 5 nm or 10 nm precision) to ensure unambiguously the dielectric contrast. As previously mentioned, people interested in live cell imaging or nano mechanics, can also improve the contact point determination by using very soft cantilevers (k~0.05N/m). In that case, the bending is more clearly seen, and there is less force acting on the cell deformation per unit length of piezo displacement. Nevertheless, we are limited in using such cantilevers, as the resonance frequency of them is normally on frequency the range that we need to perform the EFM recording.

Not only that, but living cells are dynamic objects that can move and/or release chemicals which also could affect the electrical measurements. As a summary, added to the complexity of the realization of EFM in liquid experiments, the aspects of live cell AFM imaging have to be considered.

As a first approximation, (knowing that the method has still a lot of room for improvement), we took the contact point the same way that we did with the fixed cells: considering that the contact point is when the vertical deflection surpasses the noise of the flat part of the vertical deflection curves.

In order to test these developments, we consider a sample consisting of living HeLa cells on top of a fibronectin coated gold substrate. The fibronectin coating (even if not needed) was used to enhance the cell adhesion to the substrate. Measures have also been done without the coating but cells are much weekly adhered and sometimes even detached from the substrate while scanning with the AFM tip. Figure 8.10b shows that the coating has a very low relevance for the EFM signal, as EFM curves appear similar to those ones acquired in clean gold.

The procedure for coating of the surfaces is done by covering the clean gold surface with a 50µg/mL fibronectin solution and left it for incubation for 24h. After the incubation, the substrates are washed twice in sterile x1 PBS. Next, the cells are seeded at 30k cells/mL onto previously coated gold substrates and covered with cell culture medium. The procedure is optimized from the one shown in[216]. After 24h of incubation in 5%CO_2 and 37ºC, the cells are observed and seem completely attached and spread on the gold substrate: Then, After a 2 min wash in x1 PBS, the sample is changed to the medium selected previously (10mM MOPS+10mM NaCl) and placed into the AFM stage for the EFM imaging.

Optical images showing the cell aspect and density can be seen in Figure 8.10a. The sample preparation is done by Adrianna Glinkowska from Nanoscopy for Nanomedicine Group, led by Dr. Lorenzo Albertazzi.

In Figure 8.10a, an optical microscopy image of the sample on the AFM stage with the 10mM MOPS+10mM NaCl medium can be seen. Cells look stretched and well attached to the fibronectin coated gold. The white dashed rectangles numbered 1 and 2, are highlighting the zones imaged later in Figure 8.11 and Figure 8.12 respectively.

In Figure 8.10b, the comparison of the electrical curves on top of the metal and on top of the cells is shown. We observe that as expected, when the tip is far away from the sample, both curves overlap. Nevertheless, as the tip gets closer, there is a zone where the two curves do not have the same shape (ensuring some dielectric contrast can be found). However, the experimental noise is more or less on the order of magnitude of the dielectric contrast, which will lead to a very noisy EFM-CH images. A smoothing of the electrical curves is performed and plotted on top of the raw data to enhance the existing contrast to the eye.

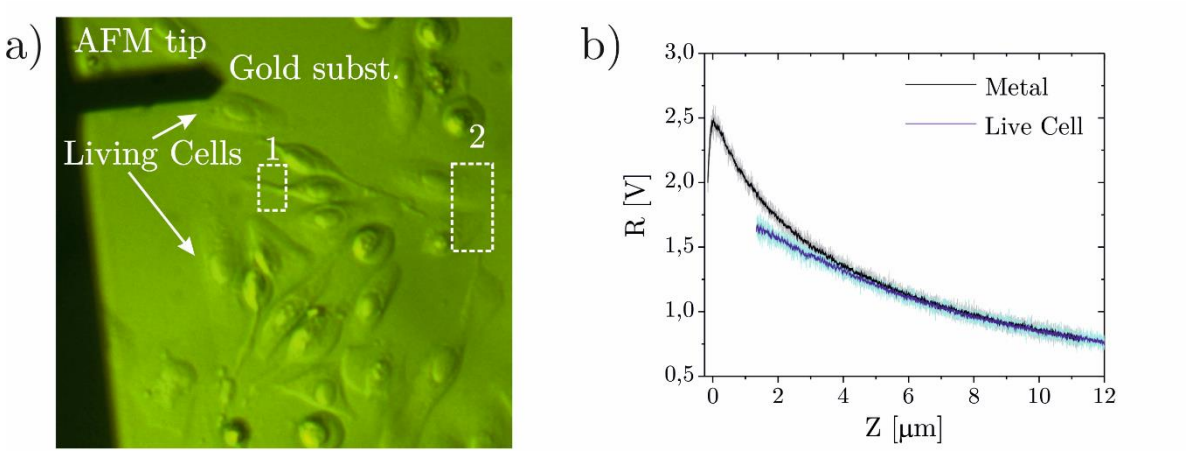

Figure 8.10: a) Optical image of the living cells seeded on the coated gold substrates b) Comparison of EFM force-distance curves on top of the coated metal and on top of the cell. A smooth data procedure is performed, highlighting the dielectric contrast.

Next we show the EFVM images of some parts of the living cells. For EFVM we have discarded the taller parts of the cells, as we have seen that they show very low contrast due to the long tip-meltal distances. In Figure 8.11a, we can see the topography of one of the arms of the cell highlighted with a the white dashed rectangle number one in Figure 8.10a.

It is around 2 µm tall. In Figure 8.11b-d, the EFM images of the living cell are shown in both lift-mode and in constant height, respectively. We can see that while the lift-mode contrast is clear (but again highly convoluted by the topographic crosstalk), the constant height mode images show a very low contrast (see profiles in Figure 8.11e). This is because the value of the expected contrast is more or less of the order of magnitude of the noise of the measurements (see Figure 8.10b).

In both cases we can see a progressive change in the background signal in the direction of the scan, which we relate first to the evaporation of the liquid due to the longer acquisition time per curve (which induces an increase of the solute's concentration during the evaporation, and thus reducing the EFM signal). Such a longer acquisition time of the image is needed due to the longer curves acquired in taller objects like cells. And second to the much narrow colorscale used in the constant height measurements in order to see the low contrast better. The progressive contamination of the tip while scanning could also add to

these issues, which in the case of live systems is increased due to their higher dynamism (excretion of chemicals, cell movement etc.).

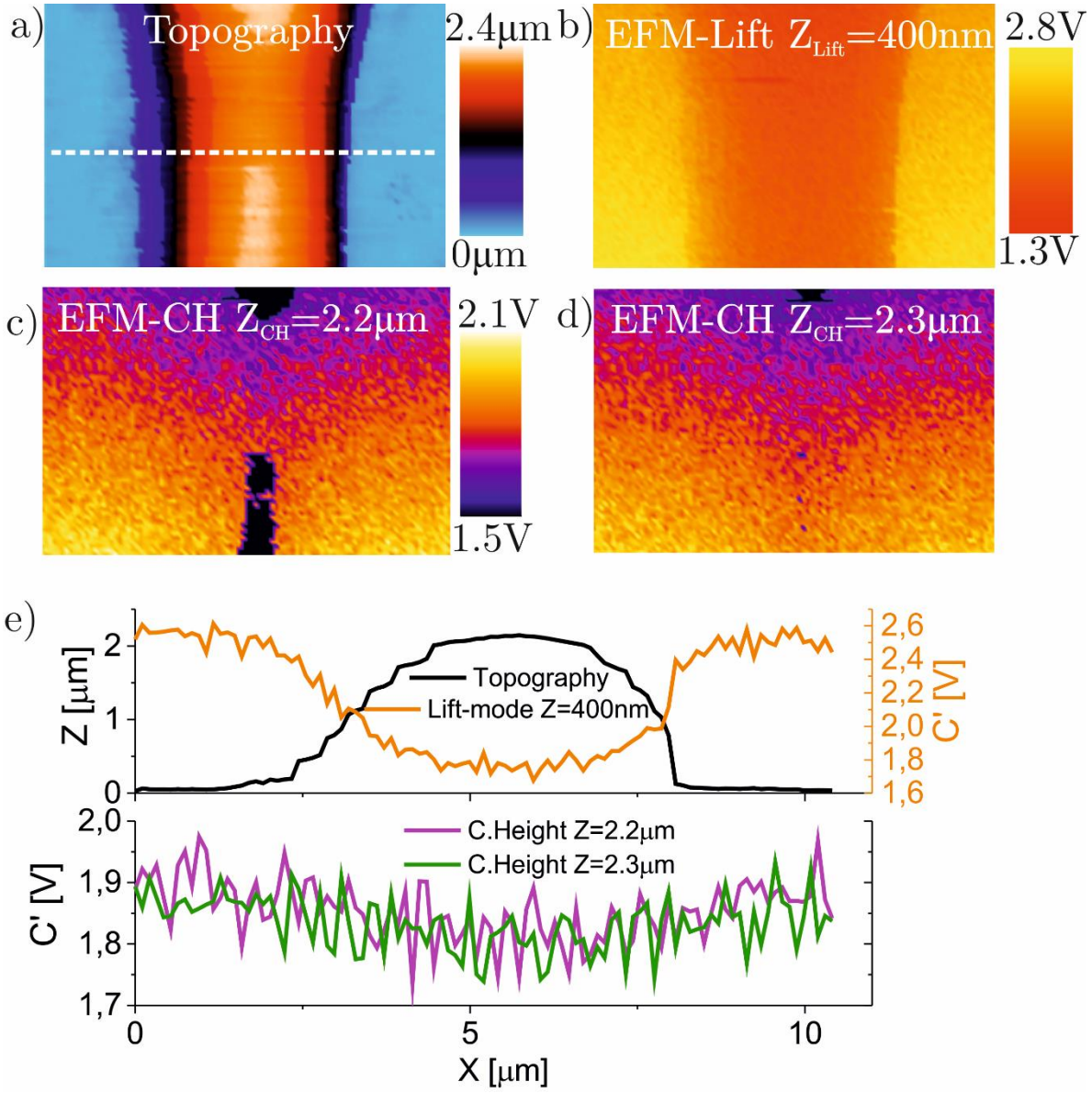

Figure 8.11: EFVM images of the rectangle 1 in Figure 8.10a. a) Topography of the cell. b) Lift-mode EFM image at lift height of 400 nm. c-d) Constant height mode images at 2.2 µm and 2.3 µm respectively. e) Profile along the white dashed line in a) of the images in a-d. Imaging parameters: $1.5V_{pp}$ amplitude of the high frequency at $\omega_{high\ frequency}$=20 MHz, a modulation frequency of ω_{mod}=5 kHz, 320 ms of pixel duration, and 7 µm of curve length. HQ:NSC/Cr-Au probe with equivalent spring constant k=1.2 N/m. Image size is 10µm · 7µm.

With the goal of having a higher dielectric contrast, we looked around for a thinner structure in order to reduce the tip-metal distance and placing ourselves in the sharpest region of the

EFM curves. In Figure 8.12 we show the EFVM imaging of the white dashed rectangle number 2 in Figure 8.10a., where the membranes of two different cells placed closely can be distinguished. Similarly to previous figures, Figure 8.12a shows the topography, and Figure 8.12b-e the subsequent EFM images in lift and constant height modes respectively.

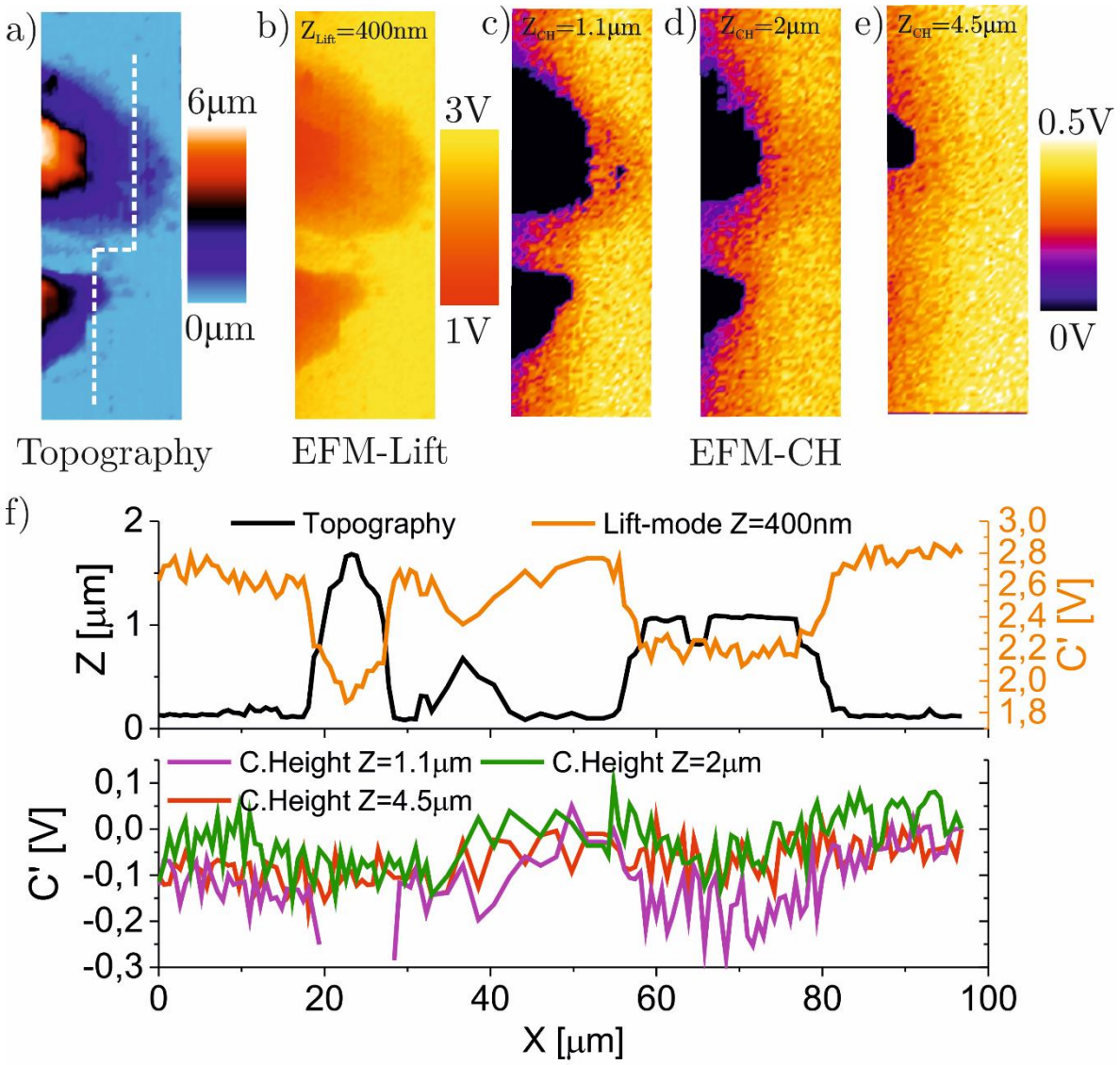

Figure 8.12: EFVM images of the rectangle 2 in Figure 8.10a. a) Topography of the cell. b) Lift-mode EFM image at lift height of 400 nm. c-e) Constant height mode images at 1.1 µm, 2 µm and 4.5 µm respectively. f) Profile along the white dashed line in a) of the images in a-d. Imaging parameters: $1.5V_{pp}$ amplitude of the high frequency at $\omega_{high\ frequency}$=20 MHz, a modulation frequency of ω_{mod}=5 kHz, 320 ms of pixel duration, and 8.5µm of curve length. HQ:NSC/Cr-Au probe with equivalent spring constant k=1.2 N/m. Image size is 80µm · 28µm.

It is relevant here to focus on Figure 8.12c, where a clear dielectric constant is found (see profiles in Figure 8.12f). In this case as we are closer, we can see the contrast better.

All this are preliminary results, that need to be analyzed and discussed more deeply but show the possibility of achieving EFM imaging of living eukaryotic cells. With this few steps towards future achievements we conclude the section of EFM live cell imaging.

8.5 Conclusions

We have shown the main differences between EFM approach curves in dry and liquid environment. We have validated the application of EFVM in liquid environment with a known robust sample, consisting of SiO_2 pillars on top of a silicon doped substrate. We have demonstrated the possibility to use EFVM to obtain for the first time (to our knowledge) EFM in liquid images of eukaryotic fixed cells, showing dielectric constant unambiguously. Quantification of such measurements needs of more complex models that are being developed by the group at the moment. Achieving quantitative dielectric mapping of cells in liquid condition (living or fixed), would be of great interest as it could be used as a label-free technique for chemical and structural composition. At the same time, the measurements in living cells would open the door towards a new force-based electrophysiological technique for the recording of active electrical cell processes. To that end, the first preliminary results on live cell EFM imaging have been shown and their main problematic issues discussed. At the moment, the main bottleneck is the realistic topography determination, needed to build the EFVM data cubes for the image extraction.

9. Conclusions

The objective of my thesis was to develop theoretically and experimentally an Scanning Force Microscopy technique (based in the multidimensional SPM approach) able to perform EFM measurements of "whatever" samples (irrespectively of their topography, mechanical properties, chemical composition, and environment they are in), focusing the interest particularly on eukaryotic cells in liquid environment, which are topographically complex, and structurally and dielectrically heterogeneous, not measured yet with nanoscale spatial resolution.

The final outcome of all this work is: On the one hand, the development of the full theoretical framework (including diffusion) needed to understand the electrostatic force microcopy technique when operated into liquid environment. On the other hand, the successful development of a new technique named Scanning Dielectric Force Volume Microscopy (SDFVM), which enables to study the nanoscale dielectric properties of whatever sample regardless of its topographical complexity, mechanical properties, chemical composition or environment conditions.

First, modelling the physical system of on an EFM tip when operating in liquid environment (which contains ionic charges), has enabled us to fully understand the physical system dynamics (considering for the first time the osmotic force contribution, and the diffusion of charges) and thus, discussing the frequency, distance, ionic concentration, and nanoscale resolution dependence of the force acting on the tip under such conditions. We have proved, that by applying a high frequency voltage wave (higher than the dielectric relaxation frequency of the system) for the excitation of the tip, the electrostatic screening of the charge space layers (also known as Electrostatic Double Layers) vanishes. Because of this, the electrostatic interaction is extended to a longer range (much larger than the short Debye length found at lower frequencies). This fact allows to easily measure experimentally the

capacitance gradient of the tip-sample system, from which the dielectric properties of the sample can be determined (with the help of numerical simulations).

Second, the development of SDFVM, a new electric SPM mode for dielectric characterization, has been achieved. It is based on the multidimensional and data oriented new SPM modes, and consist on the acquisition of EFM approach curves at each point of a sample and its post-processing and quantification by using theoretical models that include the actual measured sample topography. SDFVM technique not only improves the state-of-the-art EFM modes in lots of ways (acquisition time, sample damage, quantification process...), but also enables obtaining images which were not possible before (like constant height images at distances shorter than the topography of the sample). We have validated the technique with a known sample, tested its imaging capabilities with many different interesting nanoscale systems, and applied it to the sub-cellular mapping of a single bacterial cell, achieving for the first time (to our knowledge), the quantitative dielectric mapping of a single cell with an unparalleled spatial resolution, accuracy and statistical significance irrespectively of the complexity of the sample topography. The bacterial cell showed three characteristic equivalent dielectric constant values, namely, $\varepsilon_{r,bac1}$=2.6±0.2, $\varepsilon_{r,bac2}$=3.6±0.4 and $\varepsilon_{r,bac3}$=4.9±0.5, which enable identifying different dielectric properties of the cell wall and of the cytoplasmatic region, as well as, the existence of variations in the dielectric constant along the bacterial cell wall itself.

Last, important steps to the extension of SDFVM to liquid environment, have also been achieved. EFVM in liquid has been tested with a known sample and applied to a soft complex heterogeneous sample like a eukaryotic cell. The first ever (to our knowledge) EFM images of fixed eukaryotic cells in liquid environment have been acquired, showing a qualitative dielectric contrast in the different parts of the cell. More complex theoretical models needing the incorporation of the specific interface capacitances of all the elements of the system need to be finished to quantify such measurements. Also, the firsts EFM measures of living cells have been recorded. The main bottleneck of the data analysis is the softness of

biological tissues, which makes them a challenging system for realistic topographical measurements, strongly relevant to unambiguously determine the dielectric contrast in EFM imaging. The presented progress opens a route for nanoscale dielectric characterization in liquid of whatever sample.

10. Future perspectives

Research is always an ongoing career with no end. As all PhD projects, mine is as well embedded inside a bigger project: our research group. In my work, a new technique has been developed, validated in a known sample, tested in a variety of samples and applied to some interesting biological systems to map their dielectric properties. It is explicitly because of that, that the development and application of SDFVM brings to the end of my PhD but to the beginning of new projects related to it. Here, I try to list the most interesting and direct (from my point of view) continuations of my work as well as I show some preliminary work done.

1. **Compute the dielectric mapping in dry conditions of more heterogeneous biological and non-biological systems**. Like fixed eukaryotic cells or new materials like graphene or organic polymers used in electronic devices. In some of the cases, we have already performed the experiments needed for such quantification during my PhD but we didn't go further in the quantification process (only for the case of the bacterial cell), as we thought it was much more interesting to try to focus our efforts in applying the technique to liquid environment where cells can be live.
2. **Finish the development of the quantification modelling for liquid EFM measurements**, what will bring the possibility of quantitative dielectric mapping in liquid environments. Such achievement could lead to a new label-free technique for chemical composition and structural mapping of living cells with very easy sample preparation and relatively simple experimental setup.
3. **Improve the detection of the contact point determination for soft sample showing very high deformation**. It can be done experimentally, by acquiring low coherence laser detection systems to avoid having the laser oscillations at the flat

part of the vertical deflection curves. And by post-processing, by analyzing the methods present in the literature in more detail.

4. **Explore the range of applicability to the technique, by measuring, not only passive electrical samples**, but moving to electrically active biological (or non-biological) systems, such as neuron cells (where we have started some first tests, that are not included on this thesis) Next steps of the research project, once the real topographic determination in living cells is achieved in an unambiguous way (by improving the contact point determination) will go towards the studying of electrically excitable cells such as neurons. Neurons are cells which communicate between each other and with the other cell types using electrical signals called action potentials. Action potentials occur when the membrane of a neuronal cell depolarizes and polarizes rapidly due to the opening and closing of the ionic channels embedded in it (normally as a response to a chemical or physical perturbation). The opening and closing of the ionic channels, provoke a cascade of ionic currents going in and out the cell, which induce electric field changes in the intracellular and extracellular compartments. On the one hand the EFM in liquid measurements of non-activated cells would give the possibility to determine the effective dielectric constant of the cell membrane, which is determinant in the speed of propagation of the action potential. On the other hand, the induced changes on the electrical field surrounding the cell in activated cells would ideally as well induce a force in the EFM tip. Nevertheless, lots of other aspects like the temporal resolution or the control of the cell excitation should be tuned.

   At this stage, we have started by testing the viability to seed neuronal cells on gold substrate and check their topographical morphology in 20mM MOPS performing classic AFM topographic images of them (see Figure 10.1), but the experiments regarding the EFM recordings have not been achieved yet. One of the main advantages of our electrical measurements is the extremely fine spatial resolution, which at the same time is one of the main limitations of the state-of-the-art

electrophysiological techniques (see introduction for more details). Thus, in the case of living cells, we are not interested in their big structures (which imply very long tip-substrate distances, so low EFM signal). But we are focused in achieving nice images of the neurites (the cell body projections, consisting of two types: axons or dendrites) where the electrical signal movement takes place. The neuronal cells in Figure 10.1 are cortical neurons from primary cultures, and we can see that their neurites are cylinder-like structures with a cross-sectional radius around 400nm and 500nm, which are much smaller than the big cellular structures observed previously.

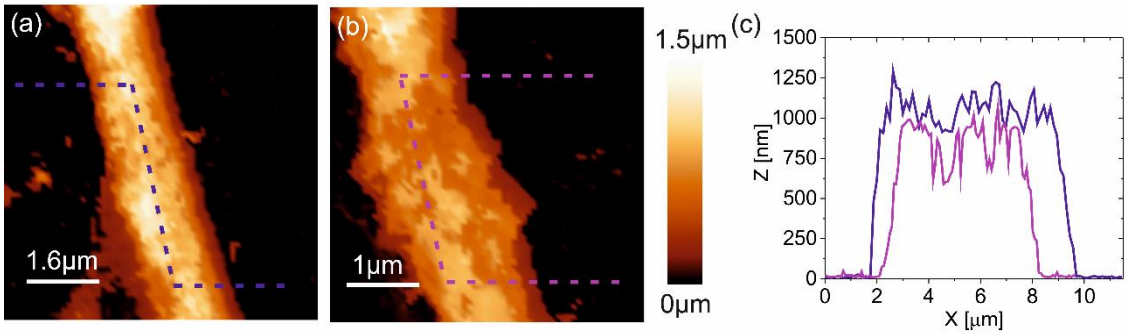

Figure 10.1: a) Topography of a neurite in a living cortical neuron seeded in a laminin coated gold substrate in 20mM MOPS. b) another image on the same sample. c) Cross-section profiles along the dashed lines in a) and b), where it is seen that the neurites have a cylinder like topography of around 500nm radius.

To prepare this type of samples, embryonic mouse cortices were dissected at embryonic day 16.5 and collected in a cold dissection medium. Tissues were mechanically chopped and dissociated with trypsinEDTA. Once cells settled down to the bottom of the tube, the supernatant was removed, re-suspended in DNAse I and incubated for 10 min at 37ºC. Fragments were mechanically dissociated by means of a pipette tip. Neurobasal medium was added and followed by centrifugation at 800 rpm for 5 min. The pellet re-suspension in new neurobasal medium was ready for seeding. The cells were seeded in the gold substrates, previously coated previously coated with Poly-L-ornithine and laminin. The sample preparation has been performed by Miriam Segura, from the group of Molecular and Cellular Neurobiotechnology lead by Prof. Jose Antonio Del Rio at IBEC.

Regarding the next steps of this project, two ideas are in mind. First, the dielectric characterization of the non-activated cells, which would give an important insight into the speed of propagation of the action potential (directly related to the membrane's capacitance).

Second, the stimulation of the activated cells should be tunned. Mainly, the triggering of the action potentials in neurons can be achieved by the release of some chemical that induces the membrane depolarization, or by light illumination in optogenetically modified cells (cells modified genetically to express light-switchable ion channels). In our case the best scenario should be to work with the second possibility (even if it requires a more complex/expensive sample preparation), it would prevent increasing dramatically the electrolyte solution molarity, which would strongly affect the EFM signal).

5. **Extend the application of SDFVM in liquid beyond biological samples.**

   In order to show the application of SDFVM to material science and device characterization, (especially its performance in liquid environment), we report the preliminary results of the EFVM imaging for nanoscale electrical characterization of a fully operating device like an Electrolyte Gated Organic Field Effect Transistor (EGOFET). The contribution of Martí Checa to this preliminary work is only the development of the experimental technique, and the performing the data analysis, but the experiments were designed and carried out by another group member. Briefly, EGOFETs are organic field effect transistors, that use the electrolyte solution to gate the transistors. On applying a potential to the gate electrode immersed in the solution, the electric double layer is formed at the electrolyte/semiconductor interface resulting in the accumulation of charges in the channel of the transistor. Such electrolyte gate transistors have been exploited as transducers in the field of bioelectronics as the active organic material is biocompatible in nature and mechanically soft and flexible.

Although such transistors have been explored largely in bio-applications, the fundamental understanding on the transduction mechanism at the nanoscale is so far missing due to a lack of techniques able to characterize the charge transport properties with nanoscale spatial resolution in liquid conditions (there are plenty of studies regarding the sister family of organic transistors working in dry conditions with KPFM or EFM[217–219]). Moreover, EGOFETS can present complex rough topographies, complicated labyrinth like electrode positioning, or different mechanical properties on the same sample, which is challenging for the state of the art EFM in liquid modes, but it is perfect for the use of SDFVM. The aim of this work is to correlate the global response of the EGOFET measured in the macroscale with the nanoscale electrical characteristics measured by EFM in liquid.

In Figure 10.2a, we show the experimental setup, which differs from the typical EFM in liquid setup. Briefly, the EFM tip is used as Gate electrode for the transistor. A DC voltage (V_{GS}) is applied between the source and gate (tip) added to the high frequency modulated voltage wave (V_{EFM}) needed for EFM in liquid: $V_{Tip\text{-}Source} = V_{GS} + V_{EFM}$. An additional DC voltage (V_{DS}) is applied between Source and Drain to have the device in operating mode (current flowing from source to drain). In this configuration, V_{GS} is used to charge the transistors channel, V_{EFM} is used for EFM in liquid recording, and V_{DS} for current driving.

In Figure 10.2b the topography of the sample is shown, a step is found at the electrodes (even if the organic semiconductor is everywhere. In Figure 10.2c EFM approach curves at different V_{GS} are found, where the charging of the channel is translated into an increase of the derivative of the capacitance. Last, Figure 10.2d shows the constant height EFM images of the of the same channel region as in in Figure 10.2b. One can see the spatial distribution of the derivative of the capacitance in the channel that clearly increases with V_{GS}, which is transduced macroscopically in a source drain current, correlating the nanoscale electric properties with the macroscopic device output (Figure 10.2e).

I want to highlight the versatility of EFVM, being able to show preliminary results as well in device characterization. Constant height images, extremely useful to extract qualitative and quantitative information in a topographically complex sample (like the one in Figure 10.2) are obtained easily, showing that the application of SDFVM in liquid is expected to have great impact in material science and device characterization.

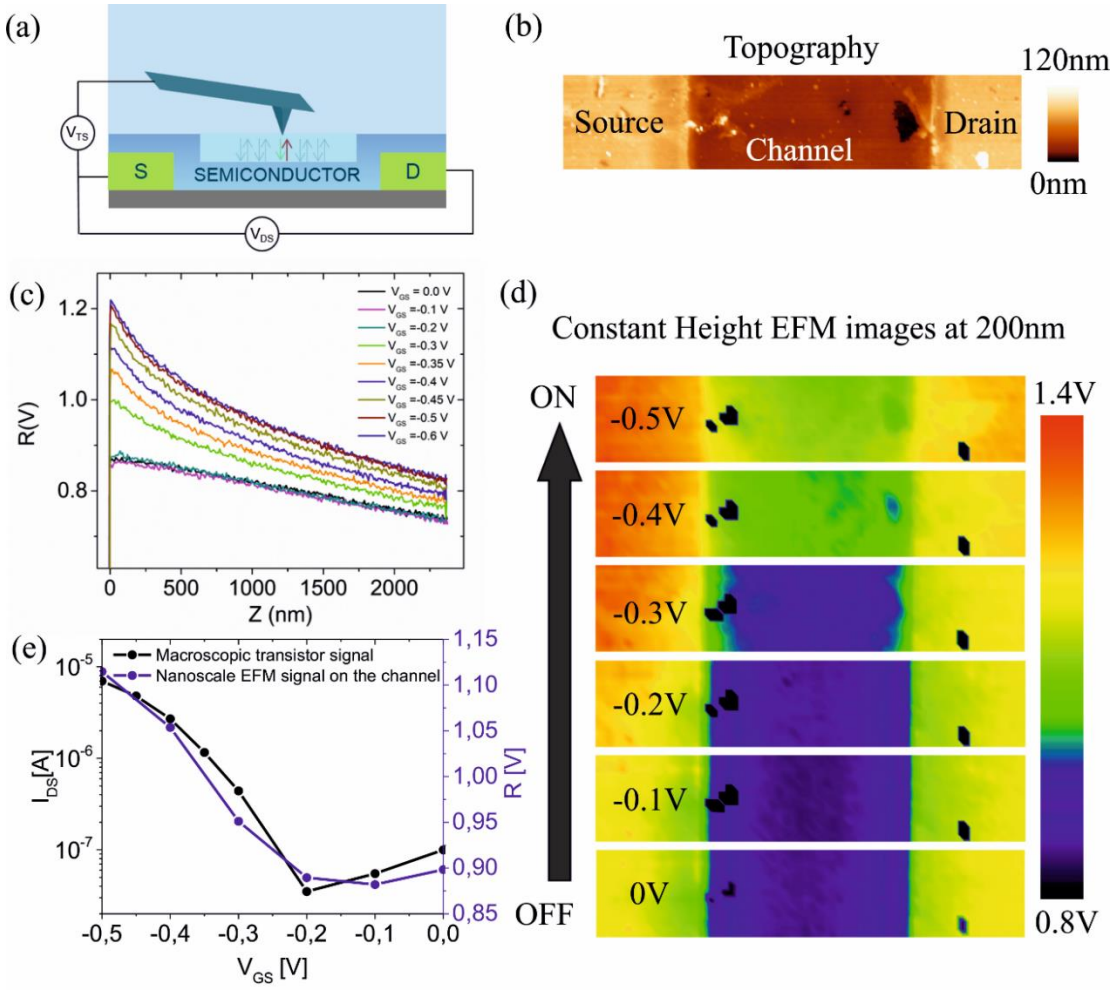

Figure 10.2: a) Experimental setup. b) Topographic image of the EGOFET channel. c) EFM approach curves for different V_{GS} applied voltages. d) Constant Height EFM images at 200nm height of the in the operando EGOFET transistor for different V_{GS} applied voltages.

6. **Coupling SDFVM with some of the advanced optical super-resolution techniques** like Photo-activated localization microscopy (PALM) or Stochastic optical reconstruction microscopy (STORM), which both need of staining agents but

could provide additional information of structural or chemical composition. Helping to evidence the correlation between chemical or biological structures and their dielectric properties.

7. **The possibility to use other quantification procedures, based on pseudo-phenomenological models, using the new data-driven approach techniques of machine learning and artificial intelligence**, could be of great interest to try to reduce the computation time necessary for the extraction of quantitatively relevant physical parameters from the SDFVM measurements. This fact becomes specially interesting in the case of SDFVM as lots of data are measured in each dataset, and correlations between data of the same experiment and within different experiments could remain hidden.

11. Resumen en castellano

Una nueva técnica de microscopio de sonda de barrido para el estudio de propiedades nanoeléctricas de células.

Las células son las unidades morfológicas y funcionales de todo ser vivo. Su habilidad para percibir y responder ante estímulos tanto externos como internos, les permite realizar sus funciones y comunicarse entre ellas. Tales estímulos, pueden tener orígenes muy diversos (reacciones químicas, presiones físicas, corrientes eléctricas…) y estar aplicados en escalas temporales y espaciales que cubren desde procesos muy pequeños y rápidos (como puede ser la conducción de un ion a través de una proteína de membrana) hasta procesos muy lentos y de grandes dimensiones (como puede ser el movimiento de toda una fibra muscular).

En esta tesis doctoral, estamos interesados en estudiar cuales son las propiedades eléctricas de las células, es decir como son capaces de conducir electricidad o polarizarse bajo la aplicación de un campo eléctrico. Para poder llevar a cabo tal caracterización a nivel de una única célula (escala micro) o incluso a nivel subcelular (escala nano), se necesitan técnicas capaces de medir las propiedades capacitivas y conductivas con gran resolución espacial y temporal.

El conocimiento actual de las propiedades de las células está basado en mediciones electrofisiológicas, usando pequeños microelectrodos que puedan medir las corrientes (o los voltajes) que suceden en diferentes procesos biológicos tanto extracelulares[8] como intracelulares[6,7], o bien en mediciones ópticas que usan tintes cuyas emisiones fluorescentes dependen de las propiedades químicas o físicas del medio que les rodea[10]. Las técnicas actuales, tienen mucho margen de mejora tanto en el ámbito de la estabilidad temporal o la no-invasividad como en lo que se refiere a su resolución espacial o la cuantificación de las propiedades físicas medibles. Es por eso por lo que el objetivo de esta tesis es desarrollar un nuevo método de caracterización eléctrica capaz de caracterizar las propiedades eléctricas

que sea estable, no invasivo, sin necesidad de usar ningún marcador y con resolución a escala nanométrica.

Es en este punto, en el que las diferentes técnicas de caracterización eléctrica que están emergiendo dentro de la familia de los microscopios de fuerzas atómicas (AFM[45]), son un buen candidato para desarrollar nuestros objetivos. Las técnicas de microscopia de sonda de barrido son capaces de caracterizar topográficamente las muestras de interés con una resolución subnanométrica a la par que obtienen información sobre otras propiedades fisicoquímicas de interés. Además, su habilidad para manipular muestras a escala nano y funcionar en condiciones fisiológicas, las está convirtiendo en una de las principales técnicas de caracterización tanto en la física de nanomateriales como en la nanobiologia[112]. En concreto el microscopio de fuerzas electrostáticas (EFM), una adaptación del AFM donde el grupo de investigación del profesor Gabriel Gomila tiene una más que demostrada experiencia[21,28,32,34,90,95,97,99], es la técnica escogida en este trabajo.

En EFM se mide la fuerza electrostática que aparece entre una punta conductora y un substrato metálico al aplicar una diferencia de potencial alterna entre ellas. Esta fuerza depende altamente (entre otras cosas) de las propiedades eléctricas (concretamente la constante dieléctrica) de la muestra que se coloca entre la punta y el substrato, cosa que permite su cuantificación, con ayuda de modelos matemáticos y simulaciones. Cuando se aplica un campo eléctrico a un material, los dipolos (inducidos o permanentes) que lo forman, se alinean con el campo, creando un campo adicional dentro del material, que apantalla totalmente (en el caso de los materiales conductores) o parcialmente (en caso de los materiales aislantes) el campo externo. La constante dieléctrica (ε_r) es la propiedad física intrínseca que nos dice como de grande es la polarización de cada material, es decir su capacidad para apantallar el campo eléctrico. El agua líquida, por ejemplo, al ser una molécula con un fuerte dipolo eléctrico que puede rotar, tiene una $\varepsilon_r \sim 80$, un valor bastante alto, en cambio el aire (mucho menos polarizable) tiene una $\varepsilon_r \sim 1$.

Existen diferentes tipos de técnicas para calcular la constante dieléctrica en materiales macroscópicos, pero no hay muchas técnicas que permitan su caracterización a escala nanométrica. El interés científico en poder medir la constante dieléctrica a escala nanométrica con resolución espacial, recae en primer lugar en el hecho de que, aunque sea una propiedad usualmente definida macroscópicamente, su naturaleza depende de sus componentes microscópicos. En segundo lugar, porque es altamente desconocido como las dimensiones pequeñas de los nanomateriales y sus diferentes relaciones de volumen-superficie pueden afectar la manera en que se polarizan. Y, en tercer lugar, porque hay materiales que solo existen en su forma nanométrica como puede ser el ADN.

En este punto es donde destaca el EFM, que, acoplado a simulaciones de elementos finitos, es capaz de medir cuantitativamente la constante dieléctrica con resolución nanométrica, siendo un buen indicador para realizar estudios de higroscopicidad[36] o composición química[34] de una manera no invasiva y sin necesidad de marcar fluorescentemente el espécimen bajo estudio ni usar otros procesos complejos de preparación de la muestra. De todos modos, los resultados que se encuentran en la literatura normalmente tienen una relevancia estadística baja debido por un lado a la complejidad de obtener resultados libres de contribuciones espurias y por otro lado a los complejos métodos de cuantificación (no automatizados), que necesitan un análisis especifico diferente en cada muestra dependiendo de su morfología o sus propiedades mecánicas.

Además, son pocos los grupos de investigación en el mundo han desarrollado durante la última década, adaptaciones del montaje experimental para poder hacer mediciones de EFM en medio líquido. Este hecho, es muy relevante para nuestro proyecto, ya que las células, para mantenerse vivas, necesitan normalmente estar en medio líquido y condiciones ambientales (temperatura, CO_2 etc) controlados. Tanto la realización de medidas relevantes de EFM en medio líquido, como su interpretación, es (además de altamente novedosa), compleja. La cuantificación de las medidas necesita modelos físicos complejos que tengan en cuenta no solamente las interacciones puramente electrostáticas, sino también las derivadas

de la difusión de las especies químicas en la solución, y las propias de las interfases metal/muestra/líquido donde se produce un reordenamiento de las moléculas en la superficie y una acumulación de carga eléctrica.

Es pues en este contexto, que estamos preparados para definir el objetivo de esta tesis: el desarrollo (tanto teórico como experimental) de una técnica de caracterización nanoeléctrica basada en el microscopio de fuerzas atómicas, enfocada a caracterizar las propiedades eléctricas de cualquier tipo de muestra de una forma automática, y sin importar el medio en el que se encuentran, focalizándonos particularmente en las células, que son topográficamente complejas, estructuralmente interesantes y dieléctricamente heterogéneas. Con el desarrollo de esta técnica, (que tendrá que mapear el campo eléctrico que rodea la muestra de estudio) pretendemos también abrir nuevas rutas para superar las principales desventajas de las técnicas actuales de electrofisiología a escala nanométrica.

A continuación, me dispongo a exponer los resultados obtenidos en esta tesis doctoral.

Desde un punto de vista teórico, mediante la resolución numérica de las ecuaciones de Poisson-Nernst-Plank, he desarrollado un modelo físico para estudiar las fuerzas que actúan sobre las superficies conductoras donde se aplica un potencial eléctrico alterno en contacto con una solución electrolítica[127]. Los resultados obtenidos, prueban que la fuerza total que actúa sobre los electrodos (que es la resultante de la fuerza eléctrica y la fuerza osmótica), presenta una compleja dependencia con la distancia entre los electrodos, la frecuencia del voltaje aplicado, la concentración iónica y las propiedades de las capas interfaciales que se producen tras el reordenamiento de moléculas y la acumulación de cargas en la superficie. Tales dependencias, difieren de las que se predicen con los modelos puramente electrostáticos o basados en análisis de circuitos equivalentes (normalmente usados para analizar los resultados en sistemas electromecánicos, o medidas eléctricas en sistemas AFM), debido a la relevancia de la fuerza osmótica en casi todo el rango frecuencial.

A grandes rasgos, se encuentra que la dependencia en frecuencia de la fuerza que sufren los electrodos se divide en 3 rangos:

1. La frecuencia baja, donde la acumulación de carga en la superficie produce un rápido decaimiento del potencial eléctrico llegando a la anulación del campo eléctrico entre los electrodos, es decir, presentando un comportamiento capacitivo que apantalla la interacción electrostática para separaciones entre electrodos mayores que la longitud característica de Debye.
2. La frecuencia intermedia, en la que hay una acumulación parcial de carga en los electrodos, pero que no llega a apantallar totalmente la interacción electrostática, lo que produce un comportamiento resistivo, para todo el rango de separación entre electrodos debido al campo eléctrico no nulo entre los electrodos.
3. La frecuencia alta, donde los iones no tienen tiempo de reaccionar a la aplicación del campo eléctrico externo, y quedan "congelados". Sin jugar ningún papel en la fuerza resultante en los electrodos, y originando una caída de potencial lineal entre estos. Éste es el rango frecuencial donde hacemos las medidas de EFM en líquido, y el único donde los modelos puramente electrostáticos son válidos.

El desarrollo de estos modelos se ha llevado a cabo en primer lugar para una geometría 1D, donde el problema es más sencillo y además también tiene solución analítica en algunos casos, y luego se ha aplicado a sistemas 3D, para dos tipos de geometría de los electrodos: esfera-plano y punta-plano. Es en este último caso, donde el estudio coge una relevancia mayor, ya que, en primer lugar, nos permite justificar el uso de altas frecuencias para las medidas de EFM en líquido y nos prueba que para el rango de altas frecuencias en el que los iones no juegan ningún papel, es posible usar modelos puramente electrostáticos para la cuantificación de las medidas.

Desde un punto de vista experimental, durante esta tesis se ha desarrollado una nueva técnica de microscopía de fuerzas atómicas a la que llamamos: *Scanning Dielectric Force Volume Microscopy* (SDFVM)[141]. El método se basa en la adquisición de una curva de

aproximación de fuerza electrostática en cada punto de la muestra y su postratamiento y cuantificación usando métodos computacionales que incorporan la topografía real medida durante el escaneo. SDFVM proporciona imágenes cuantitativas de la constante dieléctrica local de la muestra con una precisión, resolución espacial y relevancia estadística sin igual. Constituye la contraparte dieléctrica a las técnicas volumétricas modernas para el mapeo de propiedades mecánicas a escala nanométrica[173] y sigue la línea de la nueva aproximación hacia el AFM funcional, basado en el análisis y procesado de grandes cantidades de datos[174].

En primer lugar, la técnica ha sido validada con una muestra de calibración que consiste en pilares de dióxido de silicio encima de un substrato conductor, en el que se ha comprobado que la nueva forma de adquisición de la imagen y el procesado de los datos recupera los resultados esperados en las muestras conocidas y donde se ha podido comprobar que las principales ventajas de la técnica son:

1. La posibilidad de obtener mapas de la constante dieléctrica a escala nanométrica sin importar la complejidad topográfica de la muestra de una forma semiautomática.
2. La posibilidad de acceder a todos los diferentes métodos de imagen de EFM (elevación constante, plano constante, fuerza constante) e incluso nuevos métodos de imagen inaccesibles con las técnicas actuales (plano constate a una altura inferior a la de la muestra, o planos XZ o YZ) en solo una medida experimental, mediante el postproceso de los datos.
3. La minimización del daño a la punta y a la muestra durante la adquisición, debido a que solamente es necesario obtener una imagen topográfica para disponer de todas las imágenes eléctricas.
4. La minimización de las fuerzas laterales aplicadas a la muestra especialmente importante en muestras adheridas débilmente al substrato) , al mover la punta solo verticalmente y no lateralmente como otros métodos de imagen (contacto, *tapping* etc.).

5. El acceso simultáneo a las propiedades mecánicas de la muestra (no ha sido muy explotado en nuestro caso, ya que nuestro interés se centra en las propiedades eléctricas), pero la técnica permite mapear propiedades eléctricas y mecánicas simultáneamente.

Las principales desventajas del método son: por un lado, el largo tiempo de computación necesario para la cuantificación de las medidas en forma de mapa de constante dieléctrica local (estamos empezando a plantear la posibilidad de trabajar en técnicas alternativas basadas en AI para suplantar las simulaciones de elementos finitos, mucho más costosas computacionalmente hablando). Y, por otro lado, el hecho de que la señal eléctrica está aplicada durante toda la adquisición de datos (hecho que podría inducir cambios en la topografía medida, especialmente para muestras conductoras). Respecto a este segundo hecho, para los sistemas en los que hemos trabajado nosotros, no hemos visto que tenga mucha relevancia, por eso no nos ha preocupado mucho, pero quizás el método podría ser mejorado experimentalmente para cortar el señal eléctrico al tocar la muestra.

En segundo lugar, la técnica se ha probado en aire (donde las medidas en EFM son más sencillas y conocidas) para varios sistemas diferentes, todos interesantes en el campo de la nanociencia, como son mezcla de materiales nanoestructurados como nanohilos conductores y capas finas dieléctricas, nanomateriales conductores enterrados en matrices aislantes, que prueban las capacidades de caracterización subsuperficiales del EFM o sistemas celulares tanto procariotas como eucariotas. Los resultados prueban el poder de la técnica y las ventajas listadas anteriormente.

En tercer lugar, el método ha sido aplicado a obtener por primera vez el mapa de constante dieléctrica local de una célula, en este caso una bacteria de la especie *Pseudomonas aeruginosa* y de sus pequeños apéndices, los flagelos (ver Figura 11.1). Como principal resultado del estudio, hemos visto que el cuerpo celular de la bacteria muestra tres valores característicos de constante dieléctrica ($\varepsilon_{r,bac1} = 2.6 \pm 0.2$, $\varepsilon_{r,bac2} = 3.6 \pm 0.4$ y $\varepsilon_{r,bac3} = 4.9 \pm 0.5$), que nos permiten identificar diferentes propiedades dieléctricas de la pared celular y

de la región citoplasmática a la vez que (por primera vez) identificar variaciones en la constante dieléctrica a lo largo de la pared celular en sí misma.

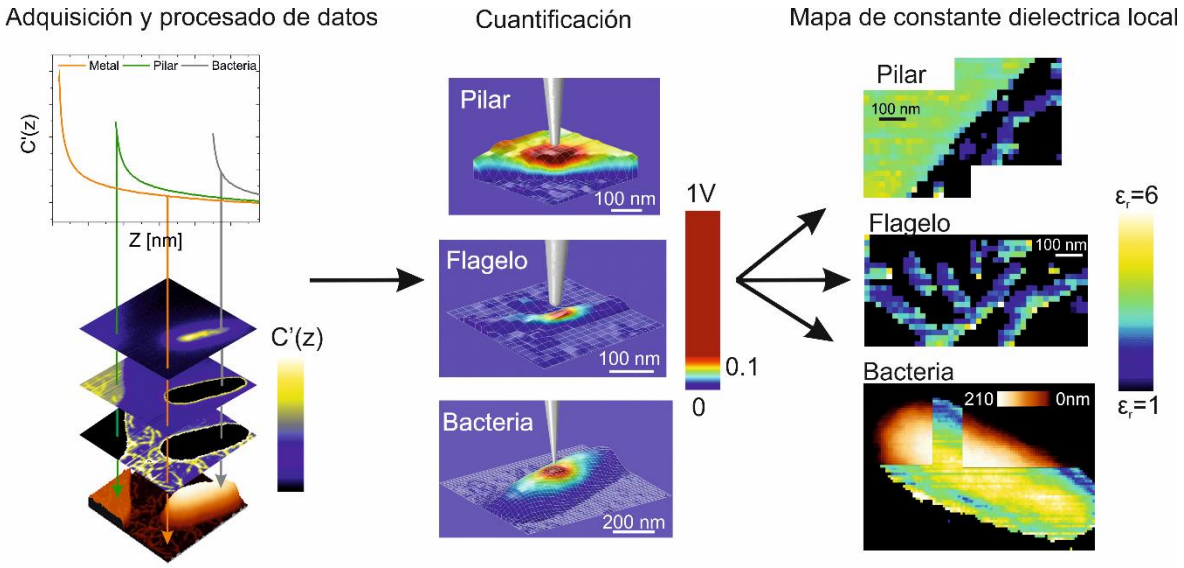

Figura 11.1: Esquema de la aplicación de SDFVM al mapeo de constante dieléctrica local de una célula bacteriana y sus apéndices.

En cuarto lugar, se han dado los primeros pasos para conseguir aplicar SDFVM en ambiente líquido, tanto en agua MiliQ, como en soluciones electrolíticas poco concentradas (<10mM). Primero, se ha utilizado la misma muestra de calibración que en el caso del aire (pilares de dióxido de silicio), para probar que se reproducen los resultados conocidos. Después, se ha aplicado a dos sistemas que completan el objetivo de la tesis y muestran el potencial de la técnica, que se espera que tenga un alto impacto en el ámbito de ciencias de la vida, donde mapear la constante dieléctrica local a escala nanométrica sin importar la complejidad de la muestra, ni el ambiente en que se encuentre (vacío, aire o líquido) es muchas veces necesario.

Estos sistemas son, por un lado, células eucariotas fijadas, donde se ha conseguido por primera vez, obtener contraste dieléctrico en tales muestras en líquido, probando la alta sensibilidad de la técnica y abriendo la puerta a observar variaciones dieléctricas (como las mencionadas anteriormente para el caso de la bacteria en aire), para sistemas altamente más heterogéneos e interesantes como una célula eucariota. Y, por otro lado, células eucariotas vivas, donde por primera vez se han superado diferentes dificultades experimentales

necesarias para la realización de medidas EFM (que medio realizar las medidas, como afectan las propiedades mecánicas blandas de las células a nuestro método etc.).

Por último, en el apartado de perspectivas futuras del proyecto, se muestran los resultados preliminares realizados para poder hacer la caracterización de transistores EGOFET en pleno funcionamiento. Para este proyecto, se ha conseguido correlacionar la señal eléctrica nanométrica con la respuesta macroscópica del dispositivo en forma de corriente, demostrando el amplio campo de aplicaciones de SDFVM, que cubre desde la biología celular, hasta la caracterización de dispositivos electrónicos.

Por todo lo comentado, damos por completado el objetivo de la tesis de desarrollar un método de caracterización eléctrica a escala nanométrica basado en microscopia de fuerzas atómicas, muy versátil; capaz de trabajar con cualquier tipo de muestra sin importar en qué ambiente se encuentre, como sea su topografía o cuales sean sus propiedades mecánicas; enfocado principalmente al estudio de las propiedades eléctricas de células.

12. Acknowledgements

The journey of undertaking a PhD is very heterogeneous. From the innocence of the first's days until the extreme wise realism of the last months, there is a long bumpy road. In my case, it would not have been possible without the heartwarming moments of good scientific results, but also without the social accompaniment surrounding me during the last four years and before. The time of thanking everyone who has made this thesis possible has arrived.

In the first place, I am very thankful to my supervisor Prof. Gabriel Gomila, for being such a good and patient mentor to me. Thank you for the freedom and the trust deposited on me from the first day, and for putting my feet on the ground when I was too optimistic but cheering me up when I was too pessimistic, by making me enjoy while learning the (so often painfully mentioned) "circle of science".

Secondly a special acknowledgement to the best technician in the world, my friend Rubén Millàn-Solsona. I only have one supervisor on the paper, but you have been my hands-on supervisor on so many practical aspects, that you can consider a big part of this thesis as yours.

After the two bosses, it comes Ricardo Hidalgo. With Richi I have spent the happiest days of my PhD. No doubt. So many conversations about the good and the bad, the pretty and the ugly, the love and the hate, the all and the nothing. From day one, a special connection was built which I am sure will last forever.

To my PhD partner Helena Lozano, with whom I have walked through this road of experiments and bureaucracy together. We came from very different worlds, but we have found a wonderful way to understand each other. Thank you.

To the "A team": René, Marc and Maria Chiara. For making me feel at home in the Nanobioelec group from day one. For making me feel that, apart from coming to work, I was every day going to IBEC to meet my friends. Your guidance has been very useful to me from all the points of view.

To the "queen" Adrica Kyndiah. Thank you for being our young mum at work. The day you leave the lab, it will still have his brain (GG) and hands (RM), but it will lose its heart.

To the SPM 2.0 generation of PhDs Martina and Hari. The good energy that you brought to the group has made both the good and bad moments a lot better. Tontolina, thank you for not killing me every day even if I deserve it. Hari, thank you for your smile and kindness. To both of you for the next year, only one advise: breath in, breath out.

To the newbies Shubham and Larissa, thanks for joining with such a good energy and vitality. Good luck.

To the biologists who have provided me the best samples I could get, and have watered me with the necessary realism, always willing to help: Thank you Miriam, Núria, Adrianna and Arnau. Also, to their bosses Prof. Toni Del Rio, Dr. Eduard Torrents and Dr. Sílvia Pujals.

To all the IBEC community, with whom I have shared a lot of experiences, from mountain trekking to salsa dancing, a special mention to Maider, Claudia, Natalia, Berta, Fabio, Carlos, Javi, Agata, Gizem, Edgar, Lucas, Carlos, Victor. As well to all my IRB friends, Jürgen, Carla, Marina, Leyre, Lorena, Adrián and Simone.

To Prof. Javier Tejada and all the Group of Magnetism of the University of Barcelona, where I did my BsC and MsC final projects. Thank you for introducing me to the world of research, sending me to Berlin under the great supervision of Alberto Hernández-Mínguez. Your optimism and the trust you deposited on me were really important to my decision of doing a PhD and showed me that one could do research while playing the ukulele.

To the best roommates one can have Giorgio, Gerard and Felipe, for being there every day (or once every two weeks, depending the season). Giorgio, I seriously don't know what I will do the day we leave Grassot. You have shown me so many things, among them all, I want to highlight your leitmotiv "que bien vivir". Gerard, you left us before time, but it was for a good reason, I am sure Agata will look after you very well, but since that day we lack the backwards Mercedes cup and Franz Sinatra t-shirt dancing Bruno Mars on the cleaning Sunday. Felipe, you are the best of all the people I list here. You have been my best friend since so long ago. Keep showing us the way with your drawings. Keep being always there to help solve all *quilombos*.

The feeling of belonging to a group is hard to generate, but once it is there is more powerful than anything. In my case I only belong to two groups. One is Betis (the best soccer team in the world), the other one is the BBM. Thank you all, Quim, Guillem, Alex, Pol, Sergio, Ruxi and those mentioned above. We are the envy of all group friends ever existed. I think we have the right combination of joy, trust, love and responsibility. Thank you all. You are my adopted family. Thank you as well to the WAGs of the BBM, you have found your place in a group the best way.

Thank you to the friends from University: Edgar, Busquets, Sotiris, Genís and Pols. Our meetings are not as often as Edgar would like to, but they are always a peak of joy and laugh necessary to break the routine. We should pay more attention to Edgar and meet more often. Thank you for the help during the Uni years, preparing the exams, presentations and homework next to you made the way much more enjoyable.

Thank you to my fencing and childhood friends: Blai, Clara, Carles, Albert, Víctor and Nil and the aforementioned Guillem. And to my fencing coaches: Juanjo and Dani. I grew up with you. I developed my personality in my times with you during competitions, trainings, travels etc. Thank you all.

Thank you to my Australian family Barbara and Desmond. You have been much more than English teachers for me. You are always there to help. The payed English lessons first, and the unpaid practical conversation hours later, have been extremely useful for me, as English is the language of science. Thank you as well for so many awesome unexpected dinners and wines together, while chatting about trying to make the world a better place.

To Javi, Loli and Ivan for opening me the doors of their house with trust and respect.

Thank you to all my family members, above which I want to highlight my grandparents Paco, Miquel, Luisa and Maria Helena, they showed me the correct way of behaving. They gave me difficult combination of love and freedom necessary to become a good human being. My Andalusian uncles and cousins, with a special remark to Luis and Amalia, who looked me and my brother after so many times when we were kids. But also, to Paco, Lina, Isa, Paquito, Pablo and Juanillo. Thank you for the best Christmas and summer laughs. My Catalan uncles and cousins: Maria, Xavi, Joan, Dora, Adrià and Ignasi, thank you all for the good moments in the family trips and Can Nadal lunches. For making me laugh, doing the best imitations of avi Miquel and avia Maria Helena.

To my parents, Bet and Andrés, for creating the best family. The best ambient for growing and becoming who I am. For looking me after without pressing too much. This thesis is yours. To Carles, although normally it is said the other way around, it has always been me who admires you since May 6th, 1996.

Finally, to Noemi for being patient during the last months, for striving in every aspect, for being the best teammate to go with.

Thank you all.

13. Appendix

List of publications and congress presentations

13.1. Publications

Checa, M., Millan-Solsona, R. & Gomila, G. Frequency-dependent force between ac-voltage-biased plates in electrolyte solutions. *Phys. Rev. E* **100**, (2019).

Checa, M., Millan-Solsona, R. & Gomila, G. Mapping the Dielectric Constant of a Single Bacterial Cell at the Nanoscale with Scanning Dielectric Force Volume Microscopy. *Nanoscale*, (2019).

Checa, M., Millan-Solsona, R. & Gomila, G. Modeling Electrostatic Force Microscopy in electrolyte solutions. *In preparation.*

Millan-Solsona, R., **Checa, M.**, & Gomila, G. Dielectric properties of sub-nanometer ultrathin molecular layers at the metal/electrolyte interface by electrochemical force microscopy. *In preparation.*

Kyndiah, A., Leonardi, F., Di Muzio, M., **Checa, M.**, Millan-Solsona, R. & Gomila, G. Nanoscale electrical characterization of Electrolyte Gate Organic Field Effect Tranistor. *In preparation.*

Checa, M., Glinkowska, A., Millan-Solsona, R. & Gomila, G. Electrosttic force microscopy of HeLa cells in lquid enviroment. *In preparation.*

13.2 Congress Presentations

13.2.1 Posters

Checa, M., Segura-Feliu, M., Del Rio , J.A. & Gomila, G. Imaging living cortical neurons with Atomic Force Microscopy. *XVIII. Annual Linz Winter Workshop: Advances in Single-Molecule Research for Biology and Nanoscience. Linz, Austria (2016).* (Awarded 3rd best poster of the conference).

Checa, M., Segura-Feliu, M., Urrea, L., Del Rio , J.A. & Gomila, G. Imaging living cortical neurons with Atomic Force Microscopy. *9th IBEC Symposium: Bioengineering for Active Ageing. Barcelona, Spain. (2016).*

Checa, M., Millan-Solsona, R. & Gomila, G. Electric forces under non-static conditions measured with Atomic Force Microscopy. *10th IBEC Symposium: Bioengineering for Future Medicine. Barcelona, Spain. (2017).*

Checa, M., Millan-Solsona, R., Fabregas, R. & Gomila, G. Nanoscale Dielectric Imaging by Electrostatic Force Volume Microscopy. *11th IBEC Symposium: Engineering solutions for health. Barcelona, Spain. (2018).*

Checa, M., Millan-Solsona, R., Blanco-Cabra, N., Torrents, E., Fabregas, R. & Gomila, G. Sub-cellular dielectric mapping of a bacterial cell by Scanning Dielectric Force Volume Microscopy. *12th IBEC Symposium: Bioengineering for Active Ageing. Barcelona, Spain. (2019).*

13.2.2 Oral

Checa, M., Millan-Solsona, R. & Gomila, G. Nanoscale Dielectric Imaging by 3D-Electrostatic Force Microscopy. *IBEC PhD Seminars. Barcelona, Spain (2019).*

Checa, M., Millan-Solsona, R. & Gomila, G. Modelling of electric forces acting on Atomic Force Microscopy in electrolyte solutions. *Fuerzas y Túnnel. Jaca, Spain (2018).*

Checa, M., Millan-Solsona, R. & Gomila, G. Mapping the Dielectric properties of topographically complex samples at the nanoscale with Electrostatic Force Volume Microscopy. *International Scanning Probe Microscopy (ISPM) Conference. Louvain-la-Neuve, Belgium (2019).*

14. List of acronyms and abbreviations

AC	Alternating current
AC-EFM	Alternating Current Electrostatic Force Microscopy
AFM	Atomic Force Microscopy
AI	Artificial Intelligence
AM-EFM	Amplitude Modulated Atomic Force Microscopy
C-AFM	Conductive Atomic Force Microscopy
DC	Direct Current
DC-EFM	Direct Current Electrostatic Force Microscopy
DH-KPFM	Dual Harmonic Kelvin Probe Force Microscopy
DNA	Deoxyribonucleic Acid
DMEM	Dulbecco's Modified Eagle Medium
ε_r	Dielectric constant
EcFM	Electrochemical Force Microscopy
EDL	Electrostatic Double Layer
EET	Extracellular Electron Transfer
EFM	Electrostatic Force Microscopy
EFVM	Electrostatic Force Volume Microscopy
EGOFET	Electrolyte-gated organic field-effect transistor

ESM	Electrochemical Strain microscopy
FM-EFM	Frequency Modulated Atomic Force Microscopy
HMDS	Hexamethyldisilazane
IHP	Inner Helmholtz Plane
KPFM	Kelvin Probe Force Microscopy
MOPS	3- 3-(*N*-morpholino) propane sulfonic acid
NIM	Nanoscale Impedance Microscopy
NPP	Nernst-Planck-Poisson
NWs	Nanowires
OHP	Outer Helmholtz Plane
OL-KPFM	Open Loop Kelvin Probe Force Microscopy
PALM	Photo-activated localization microscopy
PBS	Phosphate buffered saline
SCM	Scanning Capacitance Microscopy
SDFVM	Scanning Dielectric Force Volume Microscopy
SDM	Scanning Dielectric Microscopy
SEM	Scanning Electron Microscopy
SECM	Scanning Electrochemical Microscopy
SICM	Scanning Ion Conductance Microscopy
SMM	Scanning Microwave Microscopy
SPFM	Scanning Polarization Force Microscopy
SPM	Scanning Probe Microscopy

STM	Scanning Tunneling Microscopy
STORM	Stochastic optical reconstruction microscopy

15. References

1. Madigan, M., Bender, J., Kelly, M., Buckley, D. and David Stahl. *Brock Biology of Microorganism*. (Pearson, 2015).

2. Hille, B. Ionic channels in excitable membranes. *Biophys. J.* 283–294 (1978).

3. Cuervo, A. *et al.* Direct measurement of the dielectric polarization properties of DNA. *Proc. Natl. Acad. Sci.* **111**, E3624–E3630 (2014).

4. Guest, W. C., Cashman, R. and Plotkin, S. S. A theory for the anisotropic and inhomogeneous dielectric properties of proteins. *Phys.Chem.Chem.Phys.* **13**, 6286–6295 (2011).

5. Dunlop, J., Bowlby, M., Peri, R., Vasilyev, D. and Arias, R. High-throughput electrophysiology : an emerging paradigm for ion-channel screening and physiology. *Nat. Rev. Drug Discov.* **7**, (2008).

6. Kodandaramaiah, S. B., Franzesi, G. T., Chow, B. Y., Boyden, E. S. and Forest, C. R. Automated whole-cell electrophysiology of neurons in vivo. *Nat. Methods* **9**, (2012).

7. Hamill, O. P., Marty, A., Neher, E., Sakmann, B. and Sigworth, F. J. Improved Patch-Clamp Techniques for High-Resolution Current Recording from Cells and Cell-Free Membrane Patches. *Eur. J. Physiol.* 85–100 (1981).

8. Obien, M. E. J., Deligkaris, K., Bullmann, T. and Bakkum, D. J. Revealing neuronal function through microelectrode array recordings. *Front. Neurosci.* **8**, 1–30 (2015).

9. Novellino, A. and Zaldívar, J.-M. Recurrence Quantification Analysis of Spontaneous Electrophysiological Activity during Development : Characterization of In Vitro Neuronal Networks Cultured on Multi Electrode Array Chips. *Adv. Artif. Intell.* **2010**, (2010).

10. Grienberger, C. and Konnerth, A. Imaging Calcium in Neurons. *Neuron* (2012).

11. Lab, M. J., Bhargava, A., Wright, P. T. and Gorelik, J. The scanning ion conductance microscope for cellular physiology. *Am. J. Physiol. Circ. Physiol.* **304**, H1–H11 (2013).

12. Davey, C. L. and Kell, D. B. The Dielectric Properties of Cells and Tissues: What Can They Tell Us About the Mechanisms of Field/Cell Interactions? in *Emerging Electromagnetic Medicine* (1990).

13. Afsar, M. N., Birch, J. R., Clarke, R. N. and Chantry, G. W. The measurement of the properties of materials. *Proc. IEEE* **74**, 183–199 (2008).

14. Janezic, M. D. and Williams, D. F. Permittivity characterization from transmission-line measurement. *IEE MTT-S Int. Microw. Symp. Dig.* 1343–1346 (1997).

15. Jacob, M. V., Mazierska, J., Leong, K. and Krupka, J. Microwave properties of low-loss polymers at cryogenic temperatures. *IEEE Trans. Microw. Theory Tech.* **50**, 474–480 (2002).

16. Mekhannikov, A. I., Myl'nikov, A. V. and Maslennikova, L. P. Calibration of a coaxial antenna-probe for microwave dielectric measurements. *Meas. Tech.* **50**, 425–428 (2007).

17. Martinez, A., Byrnes, A. P., Survey, K. G. and Avenue, C. Modeling Dielectric-constant values of Geologic Materials: An Aid to Ground-Penetrating Radar Data Collection and Interpretation. *Curr. Res. Earth Sci.* **1**, (2001).

18. Kaatze, U. Complex Permittivity of Water as a Function of Frequency and Temperature. *J. Chem.*

Eng. Data **34**, 371–374 (1989).

19. Arauz-Garofalo, G. Prospects of microwave spectrometry for vascular stent monitoring Towards a non-invasive and non-ionizing follow-up alternative. *PhD Thesis* (2017).

20. Gabriel, S., Gabriel, C. and Lau, R. W. The dielectric properties of biological tissues: II. Measurements in the frequency range 10 Hz to 20 GHz. *Phys. Med. Biol.* **41**, 2251–2269 (1996).

21. Fumagalli, L. *et al.* Anomalously low dielectric constant of confined water. *Science.* **360**, 1339–1342 (2018).

22. Paul, R. Dielectric constant of biological systems. *Phys. Rev. A* **30**, (1984).

23. Nymeyer, H. and Zhou, H. X. A method to determine dielectric constants in nonhomogeneous systems: Application to biological membranes. *Biophys. J.* **94**, 1185–1193 (2008).

24. Abeyrathne, C. D., Halgamuge, M. N., Farrell, P. M. and Skafidas, E. An ab-initio computational method to determine dielectric properties of biological materials. *Sci. Rep.* **3**, 1–5 (2013).

25. Raabe, G. and Sadus, R. J. Molecular dynamics simulation of the dielectric constant of water: The effect of bond flexibility. *J. Chem. Phys.* **134**, (2011).

26. Klymchenko, A. S. Solvatochromic and Fluorogenic Dyes as Environment-Sensitive Probes : Design and Biological Applications. *Acc. Chem. Res.* (2017).

27. Signore, G., Abbandonato, G., Storti, B. and Sto, M. Imaging the static dielectric constant in vitro and in living cells by bioconjugable GFP chromophore analog†. *Chem. Commun.* 2–4 (2013).

28. Fumagalli, L. and Gomila, G. Probing Dielectric Constant at the Nanoscale with Scanning Probe Microscopy. in *Capacitance Spectroscipy of Semiconductors* (Pan Stanford Publishing, 2018).

29. Coffey, D. C. and Ginger, D. S. Time-resolved electrostatic force microscopy of polymer solar cells. *Nat. Mater.* **5**, 735–740 (2006).

30. Moser, J., Verdaguer, A., Jiḿnez, D., Barreiro, A. and Bachtold, A. The environment of graphene probed by electrostatic force microscopy. *Appl. Phys. Lett.* **92**, (2008).

31. Dols-Perez, A., Gramse, G., Calò, A., Gomila, G. and Fumagalli, L. Nanoscale electric polarizability of ultrathin biolayers on insulating substrates by electrostatic force microscopy. *Nanoscale* **7**, 18327–18336 (2015).

32. Fumagalli, L., Ferrari, G., Sampietro, M. and Gomila, G. Quantitative Nanoscale Dielectric Microscopy of Single-Layer Supported Biomembranes. *NanoLetters* **9**, 1604–1608 (2009).

33. Riedel, C. *et al.* Nanodielectric mapping of a model polystyrene-poly(vinyl acetate) blend by electrostatic force microscopy. *Phys. Rev. E* **81**, 1–4 (2010).

34. Fumagalli, L., Esteban-Ferrer, D., Cuervo, A., Carrascosa, J. L. and Gomila, G. Label-free identification of single dielectric nanoparticles and viruses with ultraweak polarization forces. *Nat. Mater.* **11**, 808–816 (2012).

35. Esteban-Ferrer, D., Edwards, M. A., Fumagalli, L., Juarez, A. and Gomila, G. Electric Polarization Properties of Single Bacteria Measured with Electrostatic Force Microscopy. *ACS Nano* **8**, 9843–9849 (2014).

36. Van Der Hofstadt, M. *et al.* Internal Hydration Properties of Single Bacterial Endospores Probed by Electrostatic Force Microscopy. *ACS Nano* **10**, 11327–11336 (2016).

37. Cadena, M. J., Reifenberger, R. G. and Raman, A. High resolution subsurface imaging using resonance-enhanced detection in 2nd-harmonic KPFM. *Nanotechnology* **29**, (2018).

38. Castañeda-Uribe, O. A., Reifenberger, R., Raman, A. and Avila, A. Depth-sensitive subsurface imaging of polymer nanocomposites using second harmonic Kelvin probe force microscopy. *ACS Nano* **9**, 2938–2947 (2015).

39. Jespersen, T. S. and Nygard, J. Mapping of individual carbon nanotubes in polymer / nanotube composites using electrostatic force microscopy. *Appl. Phys. Lett.* **90**, (2007).

40. Lozano, H., Fabregas, R. and Gomila, G. Sizing single nanoscale objects from polarization forces. *Sci. Rep.* 1–12 (2019).

41. Zhao, W., Cheong, L., Cui, W., Xu, S. and Cai Shen. A case study of the electrical properties of astrocytes by multimode AFM. *J. Microsc.* **275**, 75–81 (2019).

42. Zhao, W., Cui, W., Xu, S., Cheong, L. and Wang, D. Nanoscale Advances Direct study of the electrical properties of PC12 cells and hippocampal neurons by EFM and KPFM. *Nanoscale Adv.* 537–545 (2019).

43. Valavade, A. V., Date, K. S., Press, M. R. and Kothari, D. C. Scanning Dielectric Constant Microscopy for imaging single biological cells. *Biomed. Phys. Eng. Express* **4**, 55023 (2018).

44. Binnig, G. and Rohrer, H. Scanning tunneling microscopy. *Helv. Phys. Acta* **55**, 726–735 (1982).

45. Binnig, G., Quate, C. F. and Gerber, C. Atomic Force Microscope. *Phys. Rev. Lett.* **56**, (1986).

46. Kawai, S. *et al.* Van der Waals interactions and the limits of isolated atom models at interfaces. *Nat. Commun.* **7**, 1–7 (2016).

47. Jang, J., Schatz, G. C. and Ratner, M. A. Capillary force in atomic force microscopy. *J. Chem. Phys.* **120**, 1157–1160 (2004).

48. Lim, R., Li, S. F. Y. and Shea, S. J. O. Solvation Forrces Using Sample-Modulation Atomic Force Microscopy. *Langmuir* 6116–6124 (2002).

49. Durkan, C. and Welland, M. E. Investigations into local ferroelectric properties by atomic force microscopy. *Ultramicroscopy* **82**, 141–148 (2000).

50. Bhushan, B., Israelachvili, J. N. and Landman, U. Nanotribology: friction, wear and lubircation at the atomic scale. *Nature* (1995).

51. Oesterhelt, F. *et al.* Unfolding pathways of individual bacteriorhodopsins. *Science.* **288**, 143–146 (2000).

52. Schilcher, K., Schindler, H., Gruber, H. J., Baumgartner, W. and Hinterdorfer, P. Detection and localization of individual antibody-antigen recognition events by atomic force microscopy. *Proc. Natl. Acad. Sci.* **93**, 3477–3481 (2002).

53. Pastré, D., Joshi, V., Curmi, P. A. and Hamon, L. Detection of single DNA molecule hybridization on a surface by atomic force microscopy. *Small* **9**, 3630–3638 (2013).

54. Müller, D. J. and Dufrêne, Y. F. Atomic force microscopy: A nanoscopic window on the cell surface. *Trends Cell Biol.* **21**, 461–469 (2011).

55. Li, X. *et al.* Quantitatively probing the magnetic behavior of individual nanoparticles by an AC field-modulated magnetic force microscopy. *Sci. Rep.* **6**, 1–8 (2016).

56. Guerrero, C. R., Garcia, P. D. and Garcia, R. Subsurface Imaging of Cell Organelles by Force Microscopy. *ACS Nano* **13**, 9629–9637 (2019).

57. Ito, T., Kodera, N. and Ando, T. A high-speed atomic force microscope for studying biological macromolecules. *Seibutsu Butsuri* **41**, S92 (2017).

58. Ge, G. *et al.* MAC mode atomic force microscopy studies of living samples, ranging from cells to fresh tissue. *Ultramicroscopy* **107**, 299–307 (2007).

59. Garcia, R. Phase Imaging Atomic Force Microscopy. in *Amplitude Modulation Atomic Force Microscopy* (2010).

60. Niimi, Y. *et al.* Scanning tunneling microscopy and spectroscopy of the electronic local density of states of graphite surfaces near monoatomic step edges. *Phys. Rev. B - Condens. Matter Mater. Phys.* **73**, 1–8 (2006).

61. Nirmalraj, P. N., Thompson, D. and Riel, H. E. Capturing the embryonic stages of self-assembly - Design rules for molecular computation. *Sci. Rep.* **5**, 1–9 (2015).

62. Alexeev, A., Loos, J. and Koetse, M. M. Nanoscale electrical characterization of semiconducting polymer blends by conductive atomic force microscopy (C-AFM). *Ultramicroscopy* **106**, 191–199 (2006).

63. Barrett, R. C. and Quate, C. F. Charge storage in a nitride-oxide-silicon medium by scanning capacitance microscopy. *J. Appl. Phys.* **70**, 2725–2733 (1991).

64. Williams, C. C. Two-dimensional dopant profiling by scanning capacitance force microscopy. *Annu. Rev.Mater. Sci* **29**, 471–504 (1999).

65. Naitou, Y. *et al.* Spatial fluctuation of dielectric properties in Hf-based high- k gate films studied by scanning capacitance microscopy. *Appl. Phys. Lett.* **87**, 1–3 (2005).

66. Shao, R., V.Kalinin, S. and A.Bonell, D. Local impedance imaging and spectroscopy of polycrystalline ZnO using contact atomic force microscopy. *Appl. Phys. Lett.* **82**, 1869–1871 (2003).

67. Gramse, G. *et al.* Quantitative sub-surface and non-contact imaging using scanning microwave microscopy. *Nanotechnology* **26**, (2015).

68. Biagi, M. C. *et al.* Nanoscale electric permittivity of single bacterial cells at gigahertz frequencies by scanning microwave microscopy. *ACS Nano* **10**, 280–288 (2016).

69. Gramse, G. *et al.* Calibrated complex impedance and permittivity measurements with scanning microwave microscopy. *Nanotechnology* **26**, (2015).

70. Perez-Martinez, C. S. and Perkin, S. Surface forces generated by the action of electric fields across liquid films †. *Soft Matter* 4255–4265 (2019).

71. Bard, A. J., Fan, F. R. F., Kwak, J. and Lev, O. Scanning Electrochemical Microscopy. Introduction and Principles. *Anal. Chem.* **61**, 132–138 (1989).

72. Lee, Y., Ding, Z. and Bard, A. J. Combined scanning electrochemical/optical microscopy with shear force and current feedback. *Anal. Chem.* **74**, 3634–3643 (2002).

73. Hansma, P. K., Drake, B., O.Marti, S.A.C.Gould and C.B.Prater. The Scanning Ion-Conductance. *Science.* **243**, 1–3 (1987).

74. Simeonov, S. and Schäffer, T. E. High-speed scanning ion conductance microscopy for sub-second

topography imaging of live cells. *Nanoscale* **11**, 8579–8587 (2019).

75. Page, A. *et al.* Fast Nanoscale Surface Charge Mapping with Pulsed-Potential Scanning Ion Conductance Microscopy. *Anal. Chem.* (2016) doi:10.1021/acs.analchem.6b03744.

76. Nonnenmacher, M., O'Boyle, M. P. and Wickramasinghe, H. K. Kelvin probe force microscopy. *Appl. Phys. Lett.* **58**, 2921–2923 (1991).

77. Knapp, H. F., Mesquida, P. and Stemmer, A. Imaging the surface potential of active purple membrane. *Surf. Interface Anal.* **33**, 108–112 (2002).

78. Kholkin, A., Kalinin, S., Roelofs, A. and Gruverman, A. Review of Ferroelectric Domain Imaging by Piezoresponse Force Microscopy. in *Scanning Probe Microscopy: Electrical and Electromechanical Phenomena at the Nanoscale* (2007).

79. Black, J. M. *et al.* Fundamental aspects of electric double layer force-distance measurements at liquid-solid interfaces using atomic force microscopy. *Sci. Rep.* **6**, 1–12 (2016).

80. Sotres, J. and Baró, A. M. AFM imaging and analysis of electrostatic double layer forces on single DNA molecules. *Biophys. J.* **98**, 1995–2004 (2010).

81. Raiteri, R., Grattarola, M. and Butt, H. J. Measuring electrostatic double-layer forces at high surface potentials with the atomic force microscope. *J. Phys. Chem.* **100**, 16700–16705 (1996).

82. Haag, A. L., Schumacher, Z. and Grutter, P. Sensitivity measurement of a cantilever-based surface stress sensor. *J. Chem. Phys.* **145**, (2016).

83. Raiteri, R., Butt, H. J. and Grattarola, M. Changes in surface stress at the liquid/solid interface measured with a microcantilever. *Electrochim. Acta* **46**, 157–163 (2000).

84. Takeuchi, O., Ohrai, Y., Yoshida, S. and Shigekawa, H. Kelvin probe force microscopy without bias-voltage feedback. *Jpn. J. Appl. Phys.* **46**, 5626–5630 (2007).

85. Kobayashi, N., Asakawa, H. and Fukuma, T. Nanoscale potential measurements in liquid by frequency modulation atomic force microscopy. *Rev. Sci. Instrum.* **81**, (2010).

86. Collins, L. *et al.* Probing charge screening dynamics and electrochemical processes at the solid-liquid interface with electrochemical force microscopy. *Nat. Commun.* **5**, 1–8 (2014).

87. Nina Balke, S. J. and S. K. ESM of Li-ion Conductive Materials for Energy Generation and Storage Roger. *Asylum Research* 1–6.

88. Nellist, M. R. *et al.* Potential-sensing electrochemical atomic force microscopy for in operando analysis of water-splitting catalysts and interfaces. *Nat. Energy* **3**, 46–52 (2018).

89. Morozovska, A. N., Eliseev, E. A., Balke, N. and Kalinin, S. V. Local probing of ionic diffusion by electrochemical strain microscopy: Spatial resolution and signal formation mechanisms. *J. Appl. Phys.* **108**, (2010).

90. Gramse, G., Edwards, M. A., Fumagalli, L. and Gomila, G. Dynamic electrostatic force microscopy in liquid media. *Appl. Phys. Lett.* **101**, (2012).

91. Gramse, G., Dols-Perez, A., Edwards, M. A., Fumagalli, L. and Gomila, G. Nanoscale measurement of the dielectric constant of supported lipid bilayers in aqueous solutions with electrostatic force microscopy. *Biophys. J.* **104**, 1257–1262 (2013).

92. Umeda, K. I. *et al.* Practical aspects of Kelvin-probe force microscopy at solid/liquid interfaces in

various liquid media. *J. Appl. Phys.* **116**, (2014).

93. Gramse, G., Casuso, I., Toset, J., Fumagalli, L. and Gomila, G. Quantitative dielectric constant measurement of thin films by DC electrostatic force microscopy. *Nanotechnology* **20**, (2009).

94. Garcia, R. and Perez, R. Dynamic atomic force microscopy methods. *Surface Science Reports* vol. 47 197–301 (2002).

95. Fumagalli, L., Gramse, G., Esteban-Ferrer, D., Edwards, M. A. and Gomila, G. Quantifying the dielectric constant of thick insulators using electrostatic force microscopy. *Appl. Phys. Lett.* **96**, 2008–2011 (2010).

96. Hudlet, S., Saint Jean, M., Guthmann, C. and Berger, J. Evaluation of the capacitive force between an atomic force microscopy tip and a metallic surface. *Eur. Phys. J. B* **2**, 5–10 (1998).

97. Gomila, G., Gramse, G. and Fumagalli, L. Finite-size effects and analytical modeling of electrostatic force microscopy applied to dielectric films. *Nanotechnology* **25**, (2014).

98. Hofstadt, M. Van Der *et al.* Nanoscale dielectric microscopy of non-planar samples by lift-mode electrostatic force microscopy. *Nanotechnology* **27**, (2016).

99. Gomila, G., D Esteban-Ferrer and Fumagalli, L. Quantification of the dielectric constant of single non-spherical nanoparticles from polarization forces: Eccentricity effects. *Nanotechnology* **24**, (2013).

100. Pfeffer, C. *et al.* Filamentous bacteria transport electrons over centimetre distances. *Nature* **491**, 218–221 (2012).

101. Israelachvili, J. N. *Intermolecular and Surface Forces*. *Amsterdam: Academic Press* (2011). doi:10.1021/ie50534a061.

102. Gramse, G., Edwards, M. A., Fumagalli, L. and Gomila, G. Theory of amplitude modulated electrostatic force microscopy for dielectric measurements in liquids at MHz frequencies. *Nanotechnology* **24**, (2013).

103. Umeda, K. I. *et al.* Analysis of capacitive force acting on a cantilever tip at solid/liquid interfaces. *J. Appl. Phys.* **113**, (2013).

104. Radmacher, M., Fritz, M., Cleveland, J. P., Walters, D. A. and Hansma, P. K. Imaging Adhesion Forces and Elasticity of Lysozyme Adsorbed on Mica with the Atomic Force Microscope. *Langmuir* **10**, 3809–3814 (1994).

105. Hertz, H. Über die Berührung fester elastischer Körper. *J. für die reine und Angew. Math.* **171**, 156–171 (1881).

106. Rico, F. *et al.* Probing mechanical properties of living cells by atomic force microscopy with blunted pyramidal cantilever tips. *Phys. Rev. E* **72**, 1–10 (2005).

107. Vinckier, A. and Semenza, G. Measuring elasticity of biological materials by atomic force microscopy. *FEBS Lett.* **430**, 12–16 (1998).

108. Pimpang, P. *et al.* Atomic force microscopy adhesion mapping: Revealing assembly process in inorganic systems. *J. Phys. Chem. C* **117**, 19984–19990 (2013).

109. Alsteens, D. *et al.* Imaging G protein-coupled receptors while quantifying their ligand-binding free-energy landscape. *Nat. Methods* **12**, 845–851 (2015).

110. Belianinov, A. *et al.* Big data and deep data in scanning and electron microscopies: deriving

functionality from multidimensional data sets. *Adv. Struct. Chem. Imaging* **1**, 1–25 (2015).

111. Alsteens, D., Trabelsi, H., Soumillion, P. and Dufrêne, Y. F. Multiparametric atomic force microscopy imaging of single bacteriophages extruding from living bacteria. *Nat. Commun.* **4**, 4–5 (2013).

112. Dufrêne, Y. F. *et al.* Imaging modes of atomic force microscopy for application in molecular and cell biology. *Nat. Nanotechnol.* **12**, 295–307 (2017).

113. Medalsy, I., Hensen, U. and Muller, D. J. Imaging and quantifying chemical and physical properties of native proteins at molecular resolution by force-volume AFM. *Angew. Chemie - Int. Ed.* **50**, 12103–12108 (2011).

114. Söngen, H. *et al.* Resolving Point Defects in the Hydration Structure of Calcite (10.4) with Three-Dimensional Atomic Force Microscopy. *Phys. Rev. Lett.* **120**, 116101 (2018).

115. Uhlig, M. R., Martin-Jimenez, D. and Garcia, R. Atomic-scale mapping of hydrophobic layers on graphene and few-layer MoS2 and WSe2 in water. *Nat. Commun.* **10**, 2606 (2019).

116. Umeda, K., Kobayashi, K., Minato, T. and Yamada, H. Atomic-Scale 3D Local Hydration Structures Influenced by Water-Restricting Dimensions. *Langmuir* **34**, 9114–9121 (2018).

117. Umeda, K. *et al.* Atomic-resolution three-dimensional hydration structures on a heterogeneously charged surface. *Nat. Commun.* **8**, 1–9 (2017).

118. Miyazawa, K., Watkins, M., Shluger, A. L. and Fukuma, T. Influence of ions on two-dimensional and three-dimensional atomic force microscopy at fluorite-water interfaces. *Nanotechnology* **28**, (2017).

119. Martin-Jimenez, D. and Garcia, R. Identification of Single Adsorbed Cations on Mica-Liquid Interfaces by 3D Force Microscopy. *J. Phys. Chem. Lett.* **8**, 5707–5711 (2017).

120. Martin-Jimenez, D., Chacon, E., Tarazona, P. and Garcia, R. Atomically resolved three-dimensional structures of electrolyte aqueous solutions near a solid surface. *Nat. Commun.* **7**, 1–7 (2016).

121. Miyazawa, K. *et al.* A relationship between three-dimensional surface hydration structures and force distribution measured by atomic force microscopy. *Nanoscale* **8**, 7334–7342 (2016).

122. Fukuma, T. *et al.* Mechanism of atomic force microscopy imaging of three-dimensional hydration structures at a solid-liquid interface. *Phys. Rev. B - Condens. Matter Mater. Phys.* **92**, 1–7 (2015).

123. Herruzo, E. T., Asakawa, H., Fukuma, T. and Garcia, R. Three-dimensional quantitative force maps in liquid with 10 piconewton, angstrom and sub-minute resolutions. *Nanoscale* **5**, 2678–2685 (2013).

124. Kominami, H., Kobayashi, K. and Yamada, H. Molecular-scale visualization and surface charge density measurement of Z-DNA in aqueous solution. *Sci. Rep.* **9**, 1–7 (2019).

125. Chopinet, L., Formosa, C., Rols, M. P., Duval, R. E. and Dague, E. Imaging living cells surface and quantifying its properties at high resolution using AFM in QI^{TM} mode. *Micron* **48**, 26–33 (2013).

126. Gutierrez, J., Mondragon, I. and Tercjak, A. Quantitative nanoelectrical and nanomechanical properties of nanostructured hybrid composites by peakforce tunneling atomic force microscopy. *J. Phys. Chem. C* **118**, 1206–1212 (2014).

127. Checa, M., Millan-Solsona, R. and Gomila, G. Frequency-dependent force between ac voltage biased plates in electrolyte solutions. *Phys. Rev. E* **100**, 022604 (2019).

128. Mukundan, V. and Pruitt, B. L. MEMS electrostatic actuation in conducting biological media. *J. Microelectromechanical Syst.* **18**, 405–413 (2009).

129. Sounart, T. L., Panchawagh, H. V and Mahajan, R. L. Frequency-dependent electrostatic actuation in microfluidic MEMS. *Microelectromechanical Syst. J.* **96**, 3–5 (2010).

130. Lim, J., Whitcomb, J., Boyd, J. and Varghese, J. Transient finite element analysis of electric double layer using Nernst-Planck-Poisson equations with a modified Stern layer. *J. Colloid Interface Sci.* **305**, 159–174 (2007).

131. Honbo, K. *et al.* Visualizing Nanoscale Distribution of Corrosion Cells by Open-Loop Electric Potential Microscopy. *ACS Nano* **10**, 2575–2583 (2016).

132. Kobayashi, N., Asakawa, H. and Fukuma, T. Quantitative potential measurements of nanoparticles with different surface charges in liquid by open-loop electric potential microscopy. *J. Appl. Phys.* **110**, (2011).

133. Kobayashi, N., Asakawa, H. and Fukuma, T. Dual frequency open-loop electric potential microscopy for local potential measurements in electrolyte solution with high ionic strength. *Rev. Sci. Instrum.* **83**, (2012).

134. Umeda, K. I., Kobayashi, K., Matsushige, K. and Yamada, H. Direct actuation of cantilever in aqueous solutions by electrostatic force using high-frequency electric fields. *Appl. Phys. Lett.* **101**, 1–5 (2012).

135. Marchand, D. J., Hsiao, E. and Kim, S. H. Non-contact AFM imaging in Water using electrically driven cantilever vibration. *Langmuir* **29**, 6762–6769 (2013).

136. Bazant, M. Z., Thornton, K. and Ajdari, A. Diffuse-charge dynamics in electrochemical systems. *Phys. Rev. E - Stat. Physics, Plasmas, Fluids, Relat. Interdiscip. Top.* **70**, 24 (2004).

137. Parsegian, V. A. and Gingell, D. On the Electrostatic Interaction across a Salt Solution between Two Bodies Bearing Unequal Charges. *Biophys. J.* **12**, 1192–1204 (1972).

138. Panchawagh, H. V., Sounart, T. L. and Mahajan, R. L. A model for electrostatic actuation in conducting liquids. *J. Microelectromechanical Syst.* **18**, 1105–1117 (2009).

139. Collins, L. *et al.* Dual harmonic Kelvin probe force microscopy at the graphene-liquid interface. *Appl. Phys. Lett.* **104**, (2014).

140. Kumar, B. and Crittenden, S. R. Stern potential and Debye length measurements in dilute ionic solutions with electrostatic force microscopy. *Nanotechnology* (2013).

141. Checa, M. *et al.* Mapping the dielectric constant of a single bacterial cell at the nanoscale with scanning dielectric force volume microscopy. *Nanoscale* **11**, 20809–20819 (2019).

142. Barber, P. *et al.* Polymer Composite and Nanocomposite Dielectric Materials for Pulse Power Energy Storage. *Materials (Basel).* 1697–1733 (2009).

143. Dang, Z., Yuan, J., Yao, S. and Liao, R. Flexible Nanodielectric Materials with High Permittivity for Power Energy Storage. *Adv. Mater.* 6334–6365 (2013).

144. Roy, M. *et al.* Polymer Nanocomposite Dielectrics – The Role of the Interface. *IEEE Trans. Dielectr. Electr. Insul. Vol.* **12**, (2005).

145. Schwan, K. R. F. H. P. Dielectric properties of tissues and biological materials: a critical review. *Crit. rev. Biomed. Eng* **17**, 25–104 (1989).

146. R. Pethig. *Dielectric and electronic properties of biological materials*. (Wiley: New York, 1979).

147. Huang, Y., Wang, X., Gascoyne, P. R. C. and Becker, F. F. Membrane dielectric responses of human

T-lymphocytes following mitogenic stimulation. *Biochim. Biophys. Acta* **1417**, 51–62 (1999).

148. Sun, T., Tsuda, S., Zauner, K. and Morgan, H. On-chip electrical impedance tomography for imaging biological cells. *Biosens. Bioelectron.* **25**, 1109–1115 (2010).

149. Dharia, S., Ayliffe, E. and Rabbitt, R. D. Single cell electric impedance topography : Mapping membrane capacitance. *Lab Chip* 3370–3377 (2009).

150. R., P. and Barr, R. . *Bioelectricity: A Quantitative Approach*. (Plennum Press: New York, 1982).

151. Kotnik, T., Kramar, P., Pucihar, G. and Tarek, M. Cell Membrane Electroporation — Part 1 : The Phenomenon. *IEEE Electr. Insul. Mag.* (2012).

152. Hussain, B. S. M. *et al.* Toxicity Evaluation for Safe Use of Nanomaterials : Recent Achievements and Technical Challenges. *Adv. Mater.* **78216**, 1549–1559 (2009).

153. Reich, E. S. Nano rules fall foul of data gap. *Nature* 8–9 (2013).

154. Schrurs, F. and Lison, D. Focusing the research efforts. *Nat. Nanotechnol.* **7**, (2012).

155. Asami, K. The scanning dielectric microscope. *Meas. Sci. Technol* (1994).

156. Kalinin, S. V. and Gruveman, A. *Scanning Probe Microscopy: Electrical and Electormechamical Phenomena at Nanoscale*. (Springer Science: New York, 2007).

157. Lee, D., Pelz, J. P. and Bhushan, B. Scanning capacitance microscopy for thin film measurements. *Nanotechnology* (2006).

158. Pingree, L. S. C. and Hersam, M. C. Bridge-enhanced nanoscale impedance microscopy. *Appl. Phys. Lett* **233117**, (2005).

159. Lai, K., Kundhikanjana, W. and Shen, M. A. K. Z. Nanoscale microwave microscopy using shielded cantilever probes. *Appl Nanosci* 13–18 (2011).

160. Biagi, M. C., Badino, G., Fabregas, R. and Gramse, G. Direct mapping of the electric permittivity of heterogeneous non-planar thin films at gigahertz frequencies by scanning microwave microscopy. *Phys.Chem.Chem.Phys.* 3884–3893 (2017).

161. Hu, J., Xiao, X. and Salmeron, M. Scanning polarization force microscopy: A technique for imaging liquids and weakly adsorbed layers. *Appl. Phys. Lett* **476**, 1–4 (1995).

162. Crider, P. S., Majewski, M. R., Zhang, J., Oukris, H. and Israeloff, N. E. Local dielectric spectroscopy of polymer films. *Appl. Phys. Lett* **013102**, 2–5 (2010).

163. Krayev, A. V and Talroze, R. V. Electric force microscopy of dielectric heterogeneous polymer blends. *Polymer (Guildf).* **45**, 8195–8200 (2004).

164. Kumar, B., Bonvallet, J. C. and Crittenden, S. R. Dielectric constants by multifrequency non-contact atomic force microscopy. *Nanotechnology* (2012).

165. Lu, W., Wang, D. and Chen, L. Near-Static Dielectric Polarization of Individual Carbon Nanotubes. *NanoLetters* (2007).

166. Tevaarwerk, E., Keppel, D. G., P.Rugheimer, M.G.Lagally and M.A.Eriksson. Quantitative analysis of electric force microscopy : The role of sample geometry. *Rev. Sci. Instrum* **053707**, (2016).

167. Biagi, M. C. *et al.* Nanoscale Electric Permittivity of Single Bacterial Cells at Gigaherts Frequencies by SMM. *ACS Nano* (2016).

168. Hofstadt, M. Van Der, Fabregas, R., Biagi, M. C., Fumagalli, L. and Gomila, G. Nanoscale dielectric microscopy of non- planar samples by lift-mode electrostatic force microscopy. *Nanotechnology* (2016).

169. Lozano, H. *et al.* Dielectric constant of flagellin proteins measured by scanning dielectric microscopy. *Nanoscale* 19188–19194 (2018).

170. Yang, Y. *et al.* Size Dependence of Dielectric Constant in a Single Pencil-Like ZnO Nanowire. *NanoLetters* 10–13 (2012).

171. Peng, S. *et al.* Local Dielectric Property Detection of the Interface between Nanoparticle and Polymer in Nanocomposite Dielectrics. *Sci. Rep.* 1–9 (2016) doi:10.1038/srep38978.

172. Cherniavskaya, O., Chen, L., Weng, V., Yuditsky, L. and Brus, L. E. Quantitative Noncontact Electrostatic Force Imaging of Nanocrystal Polarizability. *J. Phys. Chem. B* 1525–1531 (2003).

173. Dufrêne, Y. F., Martínez-martín, D., Medalsy, I., Alsteens, D. and Müller, D. J. Multiparametric imaging of biological systems by force-distance curve – based AFM. *Nat. Methods* **10**, 847–854 (2013).

174. Kalinin, S. V *et al.* Big, Deep, and Smart Data in Scanning Probe Microscopy. *ACS Nano* (2016).

175. Fumagalli, L., Ferrari, G., Sampietro, M. and Gomila, G. Dielectric-constant measurement of thin insulating films at low frequency by nanoscale capacitance microscopy. *Appl. Phys. Lett* **243110**, (2007).

176. Dufrêne, Y. F. Using Nanotechniques to explore microbial surfaces. *Nat. Rev. Microbiol.* **2**, 1–10 (2004).

177. Dufrêne, Y. F. Towards nanomicrobiology using atomic force microscopy. *Nat. Rev. Microbiol.* **6**, (2008).

178. Liu, S. and Wang, Y. Application of AFM in Microbiology : A Review. *Scanning* **32**, 61–73 (2010).

179. Webb, H. K., Truong, V. K., Hasan, J., Crawford, R. J. and Ivanova, E. P. Physico-mechanical characterisation of cells using atomic force microscopy — Current research and methodologies. *J. Microbiol. Methods* **86**, 131–139 (2011).

180. Cheong, L., Zhao, W., Song, S. and Shen, C. Acta Biomaterialia Lab on a tip : Applications of functional atomic force microscopy for the study of electrical properties in biology. *Acta Biomater.* (2019).

181. Milne, J. L. S. and Subramaniam, S. Cryo-electron tomography of bacteria : progress , challenges and future prospects. *Nat. Rev.* **7**, 666–675 (2009).

182. Gros, M. A. Le, Mcdermott, G. and Larabell, C. A. X-ray tomography of whole cells. *Curr. Opin. Struct. Biol.* 593–600 (2005).

183. Markiewicz, P. and Goh, M. C. Atomic Force Microscopy Probe Tip Visualization and Improvement of Images Using a Simple Deconvolution Procedure. *Langmuir* 5–7 (1994).

184. Borodinov, N. and Neumayer, S. Deep neural networks for understanding noisy data applied to physical property extraction in scanning probe microscopy. *npj Comput. Mater.* 1–8 (2019).

185. Sacha, G. M., Varona, P., Sacha, G. M. and Cardellach, M. An inverse problem solution for undetermined electrostatic force. *Nanotechnology* 5–10 (2009).

186. Fricke, H., Schwan, H., P.H, Li, K. and Bryson, V. A dielectric study of the Low-Contuctance Surface Membrane in E.Coli. *Nature* 134–135 (1956).

187. Bernabini, C., Holmes, D. and Morgan, H. Micro-impedance cytometry for detection and analysis of micron-sized particles and bacteria. *Lab Chip* **d**, 407–412 (2011).

188. Haandbaek, N., With, O., Heer, F. and Hierlemann, A. Resonance-enhanced microfluidic impedance cytometer for detection of single bacteria †. *Lab Chip* 3313–3324 (2014).

189. Mannoor, M. S., Zhang, S., Link, A. J. and Mcalpine, M. C. Electrical detection of pathogenic bacteria via immobilized antimicrobial peptides. *Proc. Natl. Acad. Sci.* **107**, 19207–19212 (2010).

190. Yang, L. and Bashir, R. Electrical / electrochemical impedance for rapid detection of foodborne pathogenic bacteria. *Biotechnol. Adv.* **26**, 135–150 (2008).

191. David, F., Hebeisen, M., Schade, G. and Berardino, M. Di. Viability and Membrane Potential Analysis of Bacillus megaterium Cells by Impedance Flow Cytometry. *Biotechnol. Bioeng.* **109**, 483–492 (2012).

192. Samitier, J., Castellarnau, M., Errachid, A., Madrid, C. and Jua, A. Dielectrophoresis as a Tool to Characterize and Differentiate Isogenic Mutants of Escherichia coli. *Biophys. J.* **91**, 3937–3945 (2006).

193. Park, S., Koklu, M. and Beskok, A. Particle Trapping in High-Conductivity Media with Electrothermally Enhanced Negative Dielectrophoresis. *Anal. Chem.* **81**, 2303–2310 (2009).

194. Wang, Q., Iii, A. D. J., Gralnick, J. A., Lin, L. and Buie, C. R. Microfluidic dielectrophoresis illuminates the relationship between microbial cell envelope polarizability and electrochemical activity. *Sci. Adv.* 1–12 (2019).

195. Holzel, R. Non-invasive determination of bacterial single cell properties by electrorotation. *Biochim. Biophys. Acta* **1450**, 53–60 (1999).

196. Sanchis, A. *et al.* Dielectric Characterization of Bacterial Cells Using Dielectrophoresis. *Bioelectromagnetics* **401**, 393–401 (2007).

197. Asami, K., Hanai, T. and Koizumi, N. Dielectric analysis of esterichia coli suspensions in the light of the theory of interfacial polarization. *Biophys. J.* **31**, 215–228 (1980).

198. Toyofuku, M., Nomura, N. and Eberl, L. Types and origins of bacterial membrane vesicles. *Nat. Rev. Microbiol.*

199. Lovley, D. R. and Malvankar, N. S. Seeing is believing : novel imaging techniques help clarify microbial nanowire structure and function. *Environ. Microbiol.* **17**, 2209–2215 (2015).

200. Hofstadt, M. Van Der, Hüttener, M., Juárez, A. and Gomila, G. Nanoscale imaging of the growth and division of bacterial cells on planar substrates with the atomic force microscope. *Ultramicroscopy* **154**, 29–36 (2015).

201. Wang, F. *et al.* A structural model of flagellar filament switching across multiple bacterial species. *Nat. Commun.*

202. Reifenberger, R. *et al.* Depth-Sensitive Subsurface Imaging of Polymer Nanocomposites Using Second Harmonic Kelvin Probe Force. *ACS Nano* 2938–2947 (2015).

203. Cadena, M. J. *et al.* Sub-surface imaging of carbon nanotube–polymer composites using dynamic AFM methods. *Nanotechnology* (2013).

204. Riedel, C., Schwartz, G. A., Arinero, R., Colmenero, J. and Sa, J. J. On the use of electrostatic force microscopy as a quantitative subsurface characterization technique : A numerical study. *Appl. Phys. Lett.* **023101**, 227–229 (2011).

205. C.J.Wright *et al.* Optimized sample preparation for high-resolution AFM characterization of fixed human cells. *J. ofMicroscopy* **240**, 111–121 (2010).

206. Butt, H. Measuring electrostatic, van der Waals and hydrationh forces in electrolyte solutions with an atomic force microscope. *Biophys. J.* **60**, (1991).

207. Gentile, F. *et al.* Cells preferentially grow on rough substrates. *Biomaterials* **31**, 7205–7212 (2010).

208. Michl, J. and Park, K. C. Evidence-based guidelines for controlling pH in mammalian live-cell culture systems. *Commun. Biol.* 1–12.

209. Raman, A. *et al.* Mapping nanomechanical properties of live cells using multi-harmonic atomic force microscopy. *Nat. Nanotechnol.* **6**, 4–9 (2011).

210. Haase, K., Pelling, A. E. and Haase, K. Investigating cell mechanics with atomic force microscopy. *J. R. Soc. Interface* (2015).

211. Hopwood, D. Theoretical and practical aspects of glutaraldehyde fixation. *Histochem. J.* **4**, 267–303 (1972).

212. Tanaka, K. A. K. *et al.* Membrane molecules mobile even after chemical fixation. *Nat. Methods* **7**, (2010).

213. Yamane, Y., Shiga, H., Haga, H., Kawabata, K. and Abe, K. Quantitative analyses of topography and elasticity of living and fixed astrocytes. *J. Electron Microsc. (Tokyo).* **471**, 463–471 (2000).

214. Gavara, N. Combined strategies for optimal detection of the contact point in AFM force-indentation curves obtained on thin samples and adherent cells. *Sci. Rep.* 1–13 (2016).

215. Benítez, R., Moreno-flores, S., Bolós, V. J. and Toca-Herrera, J. L. A new automatic contact point detection algorithm for AFM force curves. *Microsc. Res. Tech.* **76**, 870–876 (2013).

216. Cooke, M. J., D.S.H.Shah, S. R. P., D.Athey, J.H.Lakey and S.A.Przyborski. Enhanced cell attachment using a novel cell culture surface presenting functional domains from extracellular matrix proteins. *Cytotechnology* **56**, 71–79 (2008).

217. J.Murawski *et al.* Tracking speed bumps in organic field-effect transistors via pump-probe Kelvin-probe force microscopy. *J.Appl.Phys* **244502**, (2015).

218. Tal, O. and Rosenwaks, Y. Electronic Properties of Doped Molecular Thin Films Measured by Kelvin Probe Force. *J.Phys.Chem. B* 25521–25524 (2006).

219. Yamagishi, Y., Kobayashi, K., Kimura, T., Noda, K. and Yamada, H. Local carrier dynamics in organic thin fi lm transistors investigated by time- resolved Kelvin probe force microscopy. *Org. Electron.* **57**, 118–122 (2018).

“Mañana más, pero no mejor, porque es imposible.”

El Gran Wyoming